# Generation of Hydroxyapatite Nanomaterial through Biomineralization for Potential Biomedical Applications

*A Thesis*

*Submitted in Partial Fulfillment of the Requirements for the Degree of*

**DOCTOR OF PHILOSOPHY**

*by*

**PRIYA MULLICK**


**Department of Biosciences and Bioengineering**
**Indian Institute of Technology Guwahati**
**Guwahati-781039, Assam, India**

**December 2020**

# Generation of Hydroxyapatite Nanomaterial through Biomineralization for Potential Biomedical Applications

*A Thesis*

*Submitted in Partial Fulfillment of the Requirements for the Degree of*

**DOCTOR OF PHILOSOPHY**

*by*

**PRIYA MULLICK**


**Department of Biosciences and Bioengineering**
**Indian Institute of Technology Guwahati**
**Guwahati-781039, Assam, India**

**December 2020**

*Dedicated to My Parents*

*And*

*Almighty God*

**INDIAN INSTITUTE OF TECHNOLOGY GUWAHATI**

**DEPARTMENT OF BIOSCIENCES AND BIOENGINEERING**

## STATEMENT

I do hereby declare that the research findings of this thesis is the result of research work carried out by me in the Department of Biosciences and Bioengineering, Indian Institute of Technology Guwahati, Guwahati, India, under the supervision of Professor Aiyagari Ramesh.

As per the general norms of reporting research findings, due acknowledgements have been made, wherever the research findings of other researchers have been cited in this thesis.

Priya Mullick

**Date:** 31.12.2020

**Priya Mullick**

**INDIAN INSTITUTE OF TECHNOLOGY GUWAHATI**

**DEPARTMENT OF BIOSCIENCES AND BIOENGINEERING**

## CERTIFICATE

It is certified that the work described in this thesis entitled "***Generation of Hydroxyapatite Nanomaterial through Biomineralization for Potential Biomedical Applications***" by Ms. Priya Mullick for the award of degree of Doctor of Philosophy is an authentic record of the results obtained from the research work carried out under my supervision in the Department of Biosciences and Bioengineering, Indian Institute of Technology Guwahati, India, and this work has not been submitted elsewhere for the award of any other degree.

Priya Mullick

**Priya Mullick**
**(Candidate)**
**Roll No. 156106004**

**CERTIFIED**

Aiyagari Ramesh

**Aiyagari Ramesh**
**(Thesis Supervisor)**
**Date:** 31/12/2020

# ACKNOWLEDGEMENT

First and foremost, I would like to express my sincere and heartfelt gratitude towards my PhD thesis supervisor, Professor Aiyagari Ramesh during my PhD tenure. I sincerely express my deepest sense of regards to Prof. Ramesh for giving the opportunity to work under him and his valuable guidance, encouragement and support in every step of my work. His praiseworthy dedication towards research and teaching and the extensive knowledge was a constant inspiration for me. His invaluable guidance, support, freedom, suggestion and kindness during my PhD program has helped me to grow as an independent researcher, decision maker and a good human being. I am really blessed and fortunate to work with him.

I am extremely grateful to my doctoral committee members, Professor Ranjan Tamuli, Dr. S. Senthilkumar and Dr. Lal Mohan Kundu whose valuable suggestions and motivation has led a new perception to improve my research work.

I would like to acknowledge Professor Gopal Das, Department of Chemistry, for giving me an opportunity to learn basics of the biomineralization process and essence of interdisciplinary science. I owe him my sincere gratitude for his valuable suggestions, patience, student friendly behavior and giving me the opportunity to work in collaboration, which has made my stay at IIT Guwahati all the more meaningful.

My sincere gratitude goes towards Professor Latha Rangan, Head of the Department of Biosciences and Bioengineering, IIT Guwahati, and Professor Kannan Pakshirajan and Professor V.V. Dasu, Former Heads of the Department Biosciences and Bioengineering, IIT Guwahati for providing me the necessary facilities that helped me to pursue my research at IIT Guwahati.

I am grateful to Professor Siddhartha Sankar Ghosh, Professor Pranab Goswami, Professor Lingaraj Sahoo and Dr. Biplab Bose for giving me an opportunity to work with the DBT program support team at the Centre for Excellence, Dept. of Bioscience and Bioengineering, IIT Guwahati which enabled me to develop my skills and complete my Ph.D. work.

I am also thankful to all the faculty members and our Department of Biosciences and Bioengineering staff Mr. Dipankar, Mr. Binay, Mrs. Prarthana, Mr. Niranjan, Mr. Nurul and Mr. Pankaj for supporting me throughout my Ph.D. tenure. I would like to thank Department of Biosciences and Bioengineering for providing departmental instrumentation facility for my research work. I would also like to thank Central Instruments Facility (CIF) of IIT Guwahati for providing ambient atmosphere of research and high-end equipments to accomplish my experiments. I would also like to acknowledge Department of Chemistry and Centre for the Environment, IIT Guwahati for providing high-end equipment for my experiments.

I acknowledge the state-of-art facility at the Center for Excellence under the aegis of Program Support Grant provided by Department of Biotechnology (DBT), Government of India. I am grateful to Department of Biotechnology (DBT) and Science and Engineering Board (SERB) for supporting my research through grants. I am also grateful to Ministry of

Human Resource Development (MHRD) and IIT Guwahati for providing research fellowship.

I would like to extend sincere gratitude to Dr. Rupinder Singh, Ms. Senjuti Halder, Ms. Megha Basak Department of Chemistry and Mr. Arnab Ghosh, Mr. Partha Protim Bakal Centre for the Environment, IIT Guwahati for their help regarding various instrument handling.

It is my pleasure to thank my seniors, Dr. Thiyagarajan Durairaj, Dr. Sandipan Mukherjee and Dr. Poulomi Dey for their help and encouragement during my initial days of PhD work. It is my pleasure to thank my current lab members Basu Bhattacharjee and Barlina Konwar. I am also gratified to my former lab members Preeti, Tabassum, Narahari, Dipanjali, Gopika for their support and friendship during my PhD tenure.

I also wish to thank my departmental seniors, Dr. Poulami Dutta, Dr. Namami Goswami, Dr. Mahesh Agarwal, Dr. Neha Arora, Dr. Babina Chakma and Dr. Mohitosh Dey for all the valuable suggestions, advice and motivation.

I wish to thank my friends, Srijita, Ruma, Gargi, Madonna, Anasua, Sreeja, Srirupa, Muthuvel, Anil Kumar, Swapna, Anisha, Sheuly, Smita, Rajib, Vinay, Krisnakanta, Anirban, Anurag, Avishek, Manisha, Jon Jyoti, Sanjana for whom my stay at IIT Guwahati was always memorable and wonderful. I shall always remain thankful to Poulami, Sheuly, Srijita, Ruma, Gargi, Srirupa, Muthuvel and Krisnakanta with whom I had fun and have spent my best days at IIT Guwahati.

I would like to thank Dr. Abhijit Manna for his constant support, motivation, encouragement and helping me in all possible ways to complete the research work.

Lastly, and also most importantly, I am extremely grateful to my living god, my parents Mrs. Chandrani Mullick and Mr. Prabir Kumar Mullick. They have showered my life with their unconditional love and blessings. I am really grateful for their support, freedom, trust and affection. I would like to take this opportunity to offer my heartfelt gratitude to my parents and my teachers whose support and help have made this journey more worthy and wonderful.

**Priya Mullick**

# CONTENTS

# ABBREVIATIONS

| | |
|---|---|
| **µg** | Microgram |
| **µL** | Microliter |
| **µM** | Micromolar |
| **Å** | Armstrong |
| $A_{600}$ | Absorbance at 600 nm |
| **AFM** | Atomic Force Microscope |
| **ALP** | Alkaline phosphatase |
| **ANOVA** | Analysis of variance |
| **ATR-FTIR** | Attenuated total reflectance Fourier-transform infrared spectroscopy |
| **BET** | Brunauer–Emmett–Teller |
| **bp** | Base pair |
| **cFDA-SE** | 5(and 6)-carboxyfluorescein diacetate succinimidyl ester |
| **CFU** | Colony forming unit |
| **Col I** | Collagen I |
| **cps** | Counts per second |
| **CR** | Congo red |
| **$C_T$** | Cycle threshold |
| **CV** | Crystal violet |
| **DAPI** | 4′,6-diamidino-2-phenylindole |
| **DLS** | Dynamic light scattering |
| **DMEM** | Dulbecco's modified eagles medium |
| **DMSO** | Dimethyl sulfoxide |
| **DNA** | Deoxyribonucleic acid |
| **EDTA** | Ethylenediamine tetraacetic acid |
| **EDX** | Energy Dispersive X-Ray Analysis |
| **FBS** | Fetal bovine serum |
| **FESEM** | Field emission scanning electron microscope |
| **FETEM** | Field emission transmission electron microscope |
| **FTIR** | Fourier-transform infrared spectroscopy |
| **GAPDH** | Glyceraldehyde-3-phosphate-dehydrogenase |
| **GRAS** | Generally Regarded As Safe |
| **HANPs** | Hydroxyapatite nanoparticles |
| **HEK** | Human embryonic Kidney |

## Abbreviations

| | |
|---|---|
| **HEPES** | N-2-Hydroxyethyl Piperazine N-2 Ethane Sulphonic acid |
| **HRTEM** | High-resolution transmission electron microscopy |
| **$IC_{50}$** | half maximal inhibitory concentration |
| **ITC** | Isothermal Titration Calorimetry |
| **$K_a$** | Association constant |
| **kDa** | Kilo Dalton |
| **LAB** | Lactic acid bacteria |
| **MA** | Malonic acid amphiphile |
| **MALDI-TOF** | Matrix Assisted Laser Desorption Ionization-Time of Flight |
| **MBC** | Minimum bactericidal concentration |
| **MBEC** | Minimum Biofilm Eradication Concentration |
| **MBIC** | Minimum Biofilm Inhibitory Concentration |
| **mg** | Milli grams |
| **MG-63** | Human osteosarcoma cells |
| **MIC** | Minimum inhibitory concentration |
| **MKC** | Minimum killing concentration |
| **mL** | Milliliter |
| **mM** | Millimolar |
| **MRS** | de Man, Rogosa and Sharpe |
| **MS** | Mass Spectrometry |
| **MTCC** | Microbial Type Culture Collection, Institute of Microbial Technology (IMTECH), Chandigarh, India |
| **MTT** | 3-(4,5-Dimethylthylthiazol-2-yl)-2,5-diphenyltetrazolium bromide |
| **MWCO** | Molecular weight cut-off |
| **NB** | Nutrient Broth |
| **NCIM** | National Collection of Industrial Microorganism, National Chemical Laboratory (NCL), Pune, India |
| **nm** | Nanometer |
| **NPN** | 1-N-phenylnaphthylamine |
| **NPs** | Nanoparticles |
| **OCN** | Osteocalcin |
| **$OD_{600}$** | Optical density at 600 nm |
| **PBS** | Phosphate buffered saline |
| **PI** | Propidium iodide |
| **PNPP** | p-nitrophenyl phosphate |
| **PXRD** | Powder X-ray diffraction |
| **qRT-PCR** | Real-Time Quantitative Polymerase Chain Reaction |
| **RNA** | Ribonucleic acid |

## Abbreviations

| | |
|---|---|
| **rpm** | Revolutions per minute |
| **RT** | Room temperature |
| **Runx2** | Runt-related transcription factor 2 |
| **SAED** | Selected Area Electron Diffraction |
| **SBF** | Simulated body fluid |
| **SD** | Standard deviation |
| **SDS** | Sodium dodecyl sulphate |
| **TRITC** | Tetramethyl rhodamine |
| **TW** | Titanium wire |
| **w/v** | Weight/volume |
| $\lambda_{Em}$ | Emission wavelength |
| $\lambda_{Ex}$ | Excitation wavelength |

भारतीय प्रौद्योगिकी संस्थान गुवाहाटी
Indian Institute of Technology Guwahati

# LIST OF TABLES

## List of Tables

# LIST OF SCHEMES AND FIGURES

**CHAPTER 4**

Chapter 1

# Introduction and Literature Review

## Introduction

Hydroxyapatite (HA) has emerged as an important inorganic material owing to its fascinating physico-chemical properties and vast application potential in the domain of healthcare. In particular, hydroxyapatite nanoparticles (HANPs) have significant implications in bone tissue engineering scaffolds, fabrication of implant coating and in the regime of drug delivery systems. Considering their promising scope in biomedicine and to fulfill their constant demand, there is a pressing need to develop facile methods of synthesizing HANPs. A gamut of chemical methods for synthesis of hydroxyapatite nanoparticles (HANPs) have been described. However, these methods entail the use of toxic reagents and harsh reaction conditions that are not desirable. In order to leverage the potential of HANPs in translational biomedical applications, there is a critical need to develop non-toxic and environment friendly methods of generating HANPs. Conceivably, synthesis of HANPs through biomineralization is a promising framework to generate biocompatible and therapeutic materials and address this very important and contemporary healthcare issue.

In biomineralization-driven synthesis, it is paramount that the proteins or peptide templates not only favour nucleation, but are also non-toxic and biocompatible. In this regard, the choice of proteins from lactic acid bacteria (LAB) emerge as an interesting prospect given the GRAS (generally regarded as safe) status of LAB and their established probiotic attributes. Conceivably, cell-free and cell surface-associated proteins from LAB may be used for HANP synthesis as they are less likely to have toxic implications. However, given the inherent heterogeneity of LAB cell-free and cell surface-associated proteins, it is pertinent to analyse and unravel their role(s) in the mineralization process. The knowledge generated from such a study would decipher the mechanistic aspect of the process, will be a fundamental contribution towards the field and provide a guideline to select key players for nucleation and generation of HANPs. Given the labile nature of proteins as templates, there is also an interesting scope to explore rationally designed synthetic amphiphiles that can mimic the protein/peptide template actions in the mineralization process and generate HANPs for biomedical applications. It is critical that the therapeutic merit of a new nanomaterial should be validated by demonstrating its potential in mitigating a real clinical problem. HANPs hold enormous promise in drug delivery applications and in bone tissue engineering,

wherein incorporation of HANPs into a polymeric scaffold renders bone cell growth and differentiation.

Based on the aforementioned rationale, the present investigation describes a novel approach of using secreted and cell surface-associated proteins of LAB as biomineralization templates for synthesis of HANPs and unravels the mechanistic facets of the mineralization process. A biomineralization-inspired synthesis of HANPs using malonic acid amphiphile is also illustrated. The therapeutic potential of the generated HANPs is demonstrated in antibiofilm application and in developing scaffolds and implants that support bone cell growth in *in vitro* cell culture models. The following section provides a detailed literature review pertinent to the research area of the present investigation.

## Literature Review

*1.1 Hydroxyapatite as a Material for Biomedical Application*

Hydroxyapatite (HA) is a prominent inorganic material widely used in dental and orthopaedic applications because of its established biocompatibility, slow degradation rate, osteoconductivity and osteoinductive attribute. Ailments associated with bone defects are highly prevalent and globally every year 2.2 million people require bone grafting surgery in order to refurbish such bone defects (Javaid and Kaartinen, 2013). In U.S, about half a million patients suffer from bone defects annually and the treatment cost is in excess of 205 billion dollars (Amini *et al.,* 2012). Based on the emerging role of HA in the biomedical sector, it is projected that the global market for HA will reach approximately 2.62 billion euros by 2023 and achieve an annual growth rate of over 5% from 2019-2023 (Veiga *et al.,* 2020).

The major inorganic component of bone is HA. Essentially, bone is composed of type I collagen and calcinated nanosized HA (Cai and Tang, 2008). It is noteworthy that in mammals, the biological apatite mineral has a Ca/P ratio of 1.67 (Liu *et al.,* 2013). HA has been extensively used in repair of hard tissues i.e. bone repair, for bone growth, coating of implants as well as filler substitutes in bone or teeth (Zhang *et al.,* 2014; Leevengood and Zhang, 2014, Gao *et al.,* 2017; Roohani-Esfahani *et al.,* 2016). The chemical structure similarity of hydroxyapatite with bone and teeth has led to extensive research effort to ascertain the potential of HA as a substitute material (Hutmacher *et al.,* 2007; Habraken *et al.,* 2007). Synthetic biomaterial composed of HA

can be used to construct artificial bone graft. However, in this context, it is pertinent to evaluate its biocompatibility, porous structure, mechanical strength, osteoconductive and osteoinductive traits (Li *et al.*, 2017; Torgbo and Sukyai, 2018; Narayanan and Lee, 2016). For bone tissue engineering applications, HA can be incorporated into polymeric matrix or hydrogel (Jiang *et al.*, 2013; El hadad *et al.*, 2014; Li *et al.*, 2019). Especially, polymer-hydroxyapatite composites have attracted major interest as bone scaffolds for regenerative medicine (Iafisco *et al.*, 2013; Li *et al.*, 2019; Liu *et al.*, 2015; Kutikov *et al.*, 2015). Titanium metal and its alloy have significant scope as an implant in orthopaedic surgery. In order to enhance osteointegration of implant, coating of implant surface with HA is distinctly beneficial (Salinas *et al.*, 2013; Qin *et al.*, 2018; Arcos and Regi, 2020).

Bacterial infection following surgical implantation is a serious healthcare concern. Herein, HA-implant loaded with antibiotic or grafted with metals such as Ag, Zn, Cu can exhibit antibacterial properties (Bream *et al.*, 2017; Ghimire *et al.*, 2019; Wang *et al.*, 2017; Zhang *et al.*, 2018; Liu *et al.*, 2017). The porous nature, high drug loading capacity, ability to render controlled drug release and biocompatibility of HA are attributes which render the development of effective drug delivery system. HA can be explored deliver antibiotics directly to hard tissues (Ryabenkova *et al.*, 2017; Long *et al.*, 2013; Tang *et al.*, 2014). Additional therapeutic molecules delivered by HA include anti-cancer substances (Xiong *et al.*, 2016; Li *et al.*, 2016) as well as anti-inflammatory drugs (Oner *et al.*, 2011; Aghaei *et al.*, 2014; Shao *et al.*, 2012).

### *1.2. Synthesis Routes for Generation of Hydroxyapatite*

Various routes of synthesis have been described in the literature for the generation of hydroxyapatite nanoparticles (HANPs) as illustrated in Figure 1.1. The major processes, which are extensively used for synthesis of HANPs are discussed with various examples in the following sections.

#### *1.2.1. Wet Chemical Precipitation Method*

In order to synthesize HA by wet precipitation method, $Ca(NO_3)_2.4H_2O$ and $(NH_4)_2HPO_4$ solution were used as precursors and the size of the HA grain was increased as the temperature was raised from 100-1200°C. Following heat-treatment, the HA particles were monodispersed and nanometres in size (Mobasherpour *et al.*, 2007). Sub-micron sized hydroxyapatite (HA) powder have also been produced by wet

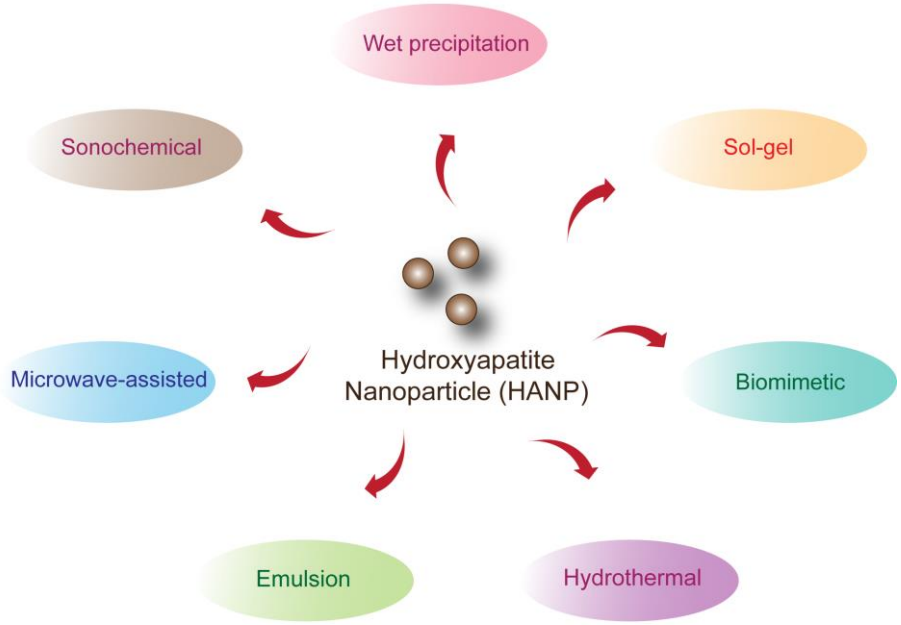


**Figure 1.1.** Scheme illustrating various methods of hydroxyapatite nanoparticle synthesis.

chemical precipitation method. Studies have revealed that HA powders heat treated at 950°C had smaller size and inferior mechanical properties as compared to HA powder obtained by heat treatment at 1250°C. Further, low reaction temperature (30°C) and rapid acid addition rate (5.5 ml/min) were favorable to yield uniform, spherical-shaped, HApowder of 0.2-0.3 μm size (Yelten-Yilmaz and Yilmaz, 2018). In another wet chemical precipitation method, crab-shells and egg-shells were used as natural source of calcium for HANP synthesis. The size of the HANP obtained from crab-shell and egg-shell were 293 nm and 183 nm, respectively (Irfan *et al.*, 2020). In order to minimize aggregation of HANPs, a low temperature precipitation reaction was proposed in conjunction with Darvan 821AVR as a dispersing agent (Cunniffe *et al.*, 2010). In a separate study, HA was precipitated using calcium hydroxide solution and orthophosphoric acid, wherein the reaction was carried out upto 95°C. In this study, the kinetics of phase transformation in the reaction was ascertained by conductometric method (Prakash *et al.*, 2006).

### *1.2.2. Sol-Gel Method*

In a particular study, HANPs were generated using the microbe *Bacillus licheniformis* and calcium chloride and potassium hydroxy phosphate were used as precursor reagents. Apparently, the *pqq* gene cluster present in *B. licheniformis* was involved in

phosphate solubilization process and the solubilized phosphate then combined with $Ca^{2+}$ in a sol-gel manner to yield HANPs (Priyam *et al.*, 2019). In another study, a pre-gel method was used for the synthesis of hydroxyapatite/ alginate (HAP@Alg) core/ shell nanoparticles. The size of HAP@Alg ranged from 160 nm to 1200 nm, while the nanoparticles displayed biocompatibility, superior drug loading capacity and drug release profile (Liang *et al.*, 2012).

*1.2.3. Hydrothermal Method*

Rod-shaped hydroxyapatite nanoparticles having a particle size range of 55-110 nm were synthesized by using a combination of high-gravity reactive precipitation and hydrothermal method (Yang *et al.*, 2010). HANPs having flower-like structure could be obtained using $CaCl_2$, $NaH_2PO_4$, and potassium sodium tartrate by a hydrothermal method at 200°C, wherein potassium sodium tartrate played a central role in the formation of nanostructured HA (Ma, 2012). In another study, calcium acetate and phosphoric acid were used for nano-hydroxyapatite (nHA) powder synthesis. Subsequently, nHA was combined with multiwalled carbon nanotube (MWCNT) by hydrothermal process at 200°C for 2 h to obtain a homogeneous composite of nHA and MWCNT (Ustundag *et al.*, 2013). In a separate study, it was demonstrated that HA particles were precipitated using calcium/ citrate /phosphate solutions at 180°C hydrothermally. Interestingly, depending on citrate: Ca ratio, rod-like, hedgehog-like and bundle-like HA particles were precipitated (Santos *et al.*, 2015).

*1.2.4. Biomimetic Process*

Ovalbumin has been used as a natural biosurfactant for the synthesis of hydroxyapatite with a low phase transformation temperature through a biomimetic strategy. The generated HA-nanocrystals were needle-shaped when synthesized at room temperature and at 550°C, HA could be transformed into β-tri calcium phosphate (Zhao *et al.*, 2008). In another study it was illustrated that graphene oxide (GO) functionalized with carrageenan (Car) can serve as a HAP nucleation centre and render biomimetic mineralization of hydroxyapatite. This hybrid material can be used as a promising substrate for bone and tissue engineering applications (Liu *et al.*, 2014). Two fusion proteins were involved in protein/peptide-mediated biomineralization, wherein nonaromatic, hydroxylated and charged amino acid residues were implicated in binding and nucleation of hydroxyapatite (Melcher *et al.*, 2016).

Additional representative examples, which describe various routes of HANP synthesis and the respective size of the HANPs obtained by these methods is shown in Table 1.1. In the current investigation, a biomineralization approach has been adopted for synthesis of HANPs. Hence, in the following section, a brief overview of the biomineralization process and various materials synthesized by the biomineralization process is discussed.

**Table 1.1.** Various methods involved in hydroxyapatite nanomaterial synthesis.

| Sl. No. | Method of Synthesis | Size of Hydroxyapatite Nanoparticle | Reference |
|---|---|---|---|
| 1. | Hydrothermal | 30–200 nm | Jiang *et al.*, 2017 |
| 2. | Microwave Synthesis | 300−500 nm | Karunakaran *et al.*, 2019 |
| 3. | Biomimetic | < 200 nm | Ryu *et al.*, 2011 |
| 4. | Wet Precipitation | 30 nm | Sheikh *et al.*, 2016 |
| 5. | Hydrothermal | 60 nm | Wang *et al.*, 2015 |
| 6. | Solvothermal | 10–40 nm | Sun *et al.*, 2018 |
| 7. | Co-precipitation | 138 ± 26 nm | Zhou *et al.*, 2020 |
| 8. | Emulsion Technique | 150 nm | Koirala *et al.*, 2015 |
| 9. | Biomimetic | 50-60 nm | Li *et al.*, 2017 |
| 10. | Wet Precipitation | > 100 nm | Ma and Qin 2015 |
| 11. | Hydrothermal | 150 nm | Wang *et al.*, 2011 |
| 12. | Co-precipitation | < 200 nm | Selvakumar *et al.*, 2017 |
| 13. | Wet Precipitation | 80 nm | Ghosh *et al.*, 2017 |
| 14. | Solvothermal | 23-27 nm | Nosrati *et al.*, 2020 |
| 15. | Wet Precipitation | 15 nm | Andres *et al.*, 2017 |

*1.3. Essential Concepts of Biomineralization*

Biomineralization is a ubiquitous phenomenon observed in living beings, starting from the microorganisms to vertebrates, wherein micro to nanoscale materials are generated. Biomineralization can follow two pathways as described by Lowenstam (1981). These pathways encompass: (a) Biologically induced biomineralization, where minerals precipitate serendipitously owing to the interaction between microorganisms and their surroundings. Herein, the type of mineral deposition depends on pH, temperature and other environmental factors and the heterogeneity of the material is manifested in morphology, water content, trace element composition and particle size (Mann, 1983). (b) Biologically controlled biomineralization is the other major route of mineral formation, which is mediated through specific regulation, as evidenced in magnetotactic bacteria (Mirabello *et. al*., 2016).

Biomineralization can also be classified depending on its location as proposed by Weiner and Dove (2003). This classification encompasses: (a) Epicellular biomineralization, which occurs on the surface of the cell. (b) Intercellular biomineralization, which takes place between two cells, wherein the epidermis of the cell can serve as nucleation center followed by mineral deposition over the cell surface (Mann, 2001). A representative example is evident in calcareous algae that render nucleation and grow calcite with a *c*-axis orientation, which is perpendicular to the cell surface (Borowitzka *et al.*, 1974; Borowitzka, 1982). (c) Intracellular biomineralization, which is inside the cells where pH and ion diffusion can be regulated for mineral formation. Representative example is the case of magnetotactic bacteria, which produce magnetic crystals inside cells (Mirabello *et al.*, 2016). The nucleation center within the cell can be vacuoles or vesicles, wherein mineralization is controlled and compartmentalized. During export of the biomineral, the vesicle(s) or vacuole(s) may migrate to the membrane and the biomineral is transported by exocytosis. Alternatively, biomineral are exported by a breach in the membrane (Watabe and Kingsley, 1989). (d) Extracellular biomineralization, which occurs outside the cells or inside the macromolecular chamber where proteins, polysaccharides are abundant. The cells can adopt two broad routes to transfer constituents to the matrix. Firstly, the cells can actively pump cations through the membrane into the surrounding exterior (Simkiss, 1986). In an alternate approach, cations may accrue within the cell as cation-loaded vesicles, which are exported through the membrane and later disrupted in the

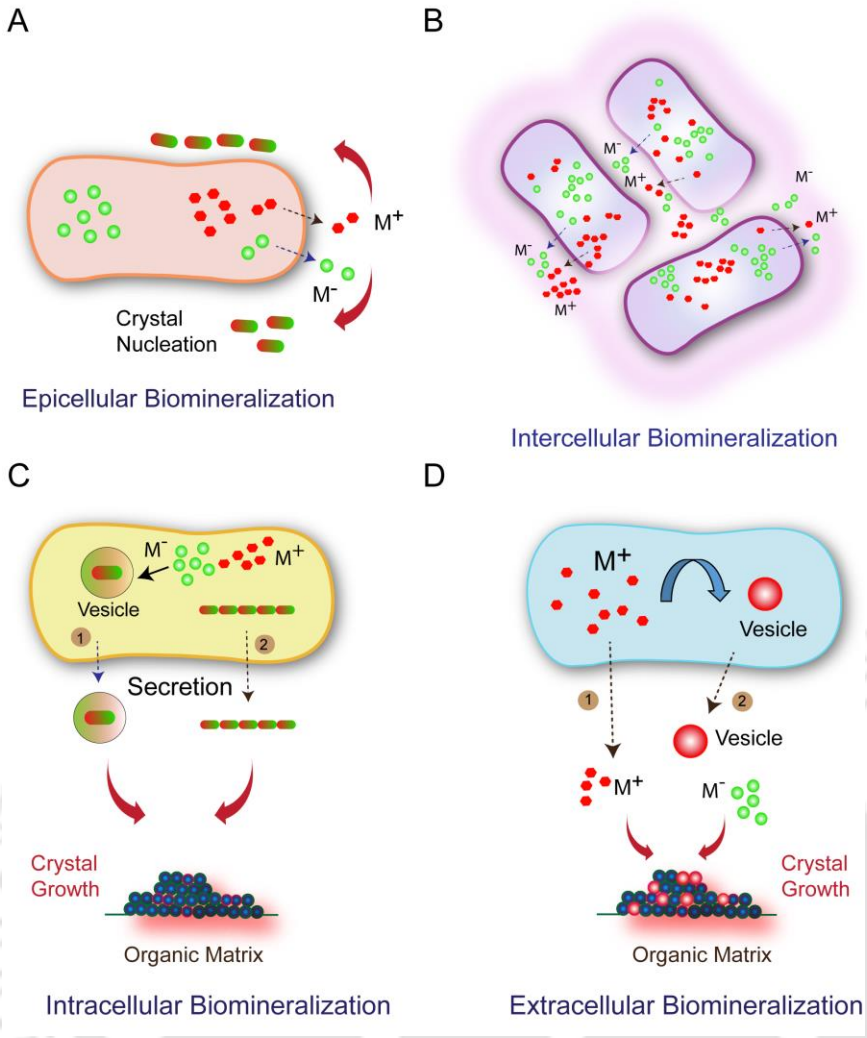


**Figure 1.2.** Cartoon illustrating the essential features of (A) Epicellular biomineralization, (B) Intercellular biomineralization, (C) Intracellular biomineralization and (D) Extracellular biomineralization.

vicinity of the organic matrix. A representative example is manifested in the mollusk shell nacreous layer, which serves as an organic matrix layer with chitin and acidic macromolecules being the predominant constituents (Levi-Kalisman *et al.*, 2001). A cartoon representing the four aforementioned routes of biomineralization is shown in Figure 1.2.

The salient examples of biomineralization that occur in nature include calcium carbonate ($CaCO_3$) in mollusk shells and sponges, hydroxyapatite [$Ca_{10}(PO_4)_6(OH)_2$] in bones and teeth of vertebrates, amorphous silica ($SiO_2$) in diatoms and sponges, magnetite ($Fe_3O_4$) nanocrystals in magnetotactic bacteria and chiton teeth (Lopez-Moreno *et al.*, 2017; Mirabello *et al.*, 2016; Arakaki *et al.*, 2015; Javaheri *et al.*, 2015; Crookes-Goodson *et al.*, 2008). These structures impart superior mechanical strength

and flexibility in the organisms (Weaver *et. al*., 2012). It has been shown that macromolecules such as proteins can act as nucleation point or template, wherein ions can be deposited in an organized manner leading to crystal formation (Uchida *et al.,* 2007).

### *1.4. Inorganic Materials Derived by Biomineralization*

#### *1.4.1. Calcium Carbonate*

Calcium carbonate is prevalent in mollusk shells and sponges. Organic biomacromolecules such as protein, glycoproteins and polysaccharides play a vital role in $CaCO_3$ biomineralization. For instance, it has been shown that the CAP-1 peptide from exoskeleton of crayfish, which contains acidic amino acids (aspartic acid) is involved in electrostatic interaction with $Ca^{2+}$ ions and calcium carbonate mineralization (Sugawara *et al.,* 2006). In a pioneering work, it was demonstrated that Pif 80 and Pif 97 acidic matrix proteins isolated from pearl oyster *P. fucata* were involved in $CaCO_3$ mineralization process (Suzuki *et al.,* 2009). Microbially induced calcite precipitation (MICP) from a supersaturated solution owing to the presence of microbial cells and their biochemical activities has been described (Bosak, 2011). In the biomineralization process, bacterial cells having negatively charged groups can act as scavengers and bind divalent cations such as $Ca^{2+}$ on their surface, leading to subsequent binding with anion (carbonate) to form insoluble calcium carbonate (Anbu *et al.,* 2016). The detailed mechanism of production of calcium carbonate biominerals by ureolytic bacteria along with role of bacteria has been discussed. A variety of marine ureolytic bacteria such as *Sporosarcina sp.*, *Bacillus sp.* and *Brevundimonas sp*. were observed to precipitate calcium carbonate minerals. Further, in case of *B. lentus* CP28, higher urease activity triggered precipitation of calcite crystals through the enzymatic hydrolysis of urea (Wei *et al.,* 2015). In a separate study, it was demonstrated that hollow rhombohedral calcite could be prepared by carbonation of calcium hydroxide solution (Kontrec *et al.,* 2013). Generation of stable vaterite microspheres was achieved by mineralization in presence of ovalbumin protein (Wang *et al.,* 2009). Vaterite mesocrystals have been generated by a biomimetic process in solution through a biomineralization approach using sodium citrate (SC) and sodium dodecyl benzenesulfonate (SDBS) (Wang *et al.,* 2015).

*1.4.2. Magnetite*

Magnetotactic bacteria exhibit the propensity to mineralize and thus magnetite nanoparticles can be produced by magnetosome-associated proteins (Lopez-Moreno *et al.,* 2017). The potential of using a bioinspired approach for magnetite synthesis has been articulated in a review article (Mirabello *et al.,* 2016). In another review article, the scope of using magnetosome-associated protein in the synthesis of biomimetic magnetic particle has been highlighted (Peigneux *et al.,* 2016). Mms6 protein from *Magnetospirillum gryphiswaldense* regulates crystal growth as well as crystal nucleation (Arakaki *et al.,* 2003; Amemiya *et al.,* 2007; Bird *et al.,* 2016). MamC protein from *Magnetococcus marinus* MC-1 has the ability to bind iron so that iron can interact with acidic amino acids to initiate mineralization (Valverde-Tercedor *et al.,* 2015). In another study, it was shown that Glu66 and Asp70 amino acids present in the α helical loop of MamC protein play a critical role for nucleation, biomineralization and magnetite crystal growth (Ubago-Rodriguez *et al.,* 2019). Arakaki *et. al*., (2003) reported that Mms6, Mms5, Mms7 proteins from *M. magneticum* play a significant role in magnetite formation. Magnetite biomineralization under bioinspired conditions could yield magnetite nanoparticles whose size ranged from 10-20 nm and 20-40 nm, in presence of arginine and lysine amino acid residues, respectively (Contreras-Montoya *et al.,* 2020). In another study, it was reported that Mad-10, a magnetite binding protein present in *Desulfamplus magnetovallimortis* BW-1 mineralizes bullet-shaped magnetite nanoparticles through its highly conserved C-terminal region (Pohl *et al.,* 2019).

*1.4.3. Silica*

Silica deposition in diatoms and sponges take place through biomineralization process (Crookes-Goodson *et al.,* 2008). Silica deposition is mediated by the silaffin protein and long chain polyamines (LCPA). These biomolecules play a critical role to form biosilica. Silaffins and LCPA form some supramolecular structures to precipitate silica and create different morphology i.e. spheres, sheets and plates. There is a H-bond formation between the amino groups of silaffin or LCPA and hydroxyl groups present in silicic acid, which triggers the polymerization process (Poulsen and Kroger, 2004). Javaheri *et al.,* 2015 reported that when cells are in log phase and silica is present in abundance, a “mesh-like pattern” is observed whereas low silicic acid content led to “tree-like pattern”. In a review article, it was reported that the protein silicatein plays an important role in sponge silica mineralization (Schroder *et al.,* 2009). Silica

biomineralization can be possible using helical biomolecules including DNA, polypeptides, cellulose and rod like viruses. The electrostatic interactions between charged helical biomolecules and silicates leads to generation of ordered biomolecules-silica materials (Liu *et al.,* 2015). Silica nanoparticles synthesized using BSA as a template resulted in porous, monodisperse, smaller size (~250-380 nm) particles, while non-porous, heterogeneous, larger size (~700-1000 nm) particles resulted in the absence of BSA protein core (Jackson *et al.,* 2015). In another study it was reported that interaction between silicanin-1, a membrane protein and long chain polyamines (LCPA) can influence the self-assembly of bio-silica forming organic matrix in silica deposition vesicle lumen of *Thalassiosira pseudonana* (Kotzsch *et al.,* 2017).

*1.4.4. Hydroxyapatite*

The basic inorganic building blocks of bone and enamel in vertebrates are nanosized apatite. Bone consists of type I collagen and calcinated nanosized HA (Cai and Tang, 2008), wherein the principal inorganic component of bone is HA. Mineralized collagen fibril consisting of self-assembled triple helical type I collagen is the basic template for bone mineralization. Some non-collagenous proteins (NCPs) are also associated with bone mineralization. These NCPs have a high content of acidic amino acids such as aspartic acid or glutamic acid or phosphorylated serine/ threonine (Alves *et al.,* 2010). In an interesting study, artificial bone-like peptide/hydroxyapatite nanocomposite was synthesized using mussel-inspired polydopamine adhesive, wherein the polydopamine-coated peptide nanowires were mineralized to yield hydroxyapatite nanocrystals (Ryu *et al.,* 2011). In another study, a random DNA duplex was used as a biomineralization template to generate hydroxyapatite for bone tissue engineering (Yu *et al.,* 2020). In a separate study, it was shown that skeletal hydroxyapatite could be derived by mineralization of hydrogel matrices composed of various polymeric constituents. (Iwatsubo *et al*., 2015). An engineered fusion protein was designed based on *Bacillus subtilis* synthase YaaD, the *Aspergillus nidulans* hydrophobin DEWA, and the rationally designed peptide P11-4. This fusion protein was effective in driving mineralization of hydroxyapatite in artificial saliva (Melcher *et al*., 2016). Nanocapsules and crystalline nanorods of HAp were generated by biomineralization of fish sperm DNA at high pH in solutions containing $Ca^{2+}$ and $PO_4^{3-}$ ions (Bertran *et al*., 2014). The mineralization of hydroxyapatite nano-needles in the self-assembled matrix of *Bombyx mori* silk sericin protein has also been reported (Yang *et al*., 2015). Silk

microfibers (mSF) have been used as a template to support the growth of HA. Initially HA nanoplates were shown to assemble and form microspheres having flower-like appearance, followed by aggregation, which led to coverage of (mSF) (Xu *et al.*, 2016). In another study, carboxylated graphene functionalized with acidic casein phosphopeptides (CPPs) was generated, which could support facile mineralization of hydroxyapatite (Fan *et al.*, 2013).

*1.5. Templates for Biomimetic Synthesis*

Based on the principle of biomineralization, there is a strong research endeavor to adopt biomimetic approaches using macromolecules or whole cells as templates for biomimetic synthesis of inorganic and metal-based nanomaterials, which have biomedical potential. The macromolecular templates used for mineralization mostly consist of proteins, peptides, polysaccharides and lipids, while whole cell-based biomineralization process mostly engage bacterial cells, fungus or biofilms (Figure 1.3). In line with this premise, in the current investigation microbial protein templates and whole cell has been used for mineralization and generation of HANPs. The following section provides a brief overview on the use of macromolecular templates and whole cell for biomimetic synthesis of inorganic and metal-based materials.

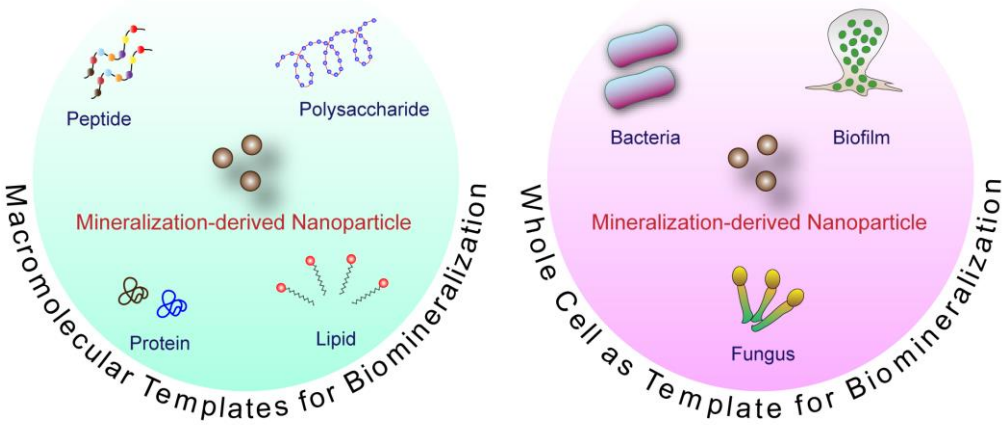


**Figure 1.3.** Cartoon illustrating template action in biomineralization for synthesis of biogenic nanomaterial.

*1.5.1. Protein/Peptide-based Template*

Proteins can regulate calcium carbonate biomineralization by controlling calcite, vaterite, aragonite phase. Amphiphilic peptides based on glutamic acid and leucine with β-sheet and α-helical structures have been shown to yield stable vaterite structure (Lu *et al.*, 2018). It has been shown that Ti-binding peptide (TBP-1) aptamer can bind to Ti, Si and Ag surfaces and support biomineralization activities under ambient condition (Sano *et al.*, 2005). The role of calcitonin (CALC)-like system as a regulatory factor in mollusk shell mineralization has been highlighted (Cardoso *et al.*, 2020). In a separate study, an eight-repeat unit consisting of Gly-Pro-Pro (GPP8) sequence similar to the central sequence of type I collagen and eight negatively charged contiguous glutamic acid residues (E8) representing the bone sialoprotein (BSP) were shown to support biomineralization of hydroxyapatite when these motifs were displayed on bacterium flagella (Li *et al.*, 2012). A heptapeptide having the sequence MLPHHGA and present in the C-terminal portion of MDG1, a 27-peptide residue, was able to induce hydroxyapatite biomineralization in hydrogel (Gungormus *et al.*, 2010). Three different amphiphilic peptide having phenylalanine-serine tail or alkyl-serine tail or serine-only tail and varying conformation from β-turn to α-helix to random coil facilitated biomineralization and generation of silica nano-ribbons, nanofibers and nanospheres, respectively (Huang *et al.*, 2014). Borah *et al.*, (2009) reported that lactic acid bacteria (LAB) protein extract can be used as crystal growth modifier and demonstrated the formation of calcium and barium minerals using cell-free extract of LAB. Uchida *et al.*, (2007) reported that mammalian iron storage protein "ferritin" has the capability to biomineralize ferrihydrite particles. Gold nanoparticles have been synthesized by using cell free supernatant of *Rhizopus oryzae* fungal extract, wherein protein concentration and $HAuCl_4$ concentration control size and shape of the nanoparticles (Das *et al.*, 2012). Jutz and Boker (2010) proposed an interesting method for the preparation of calcium-phosphate inorganic microcapsules. Following preparation of oil-in-water emulsion stabilized by BSA or ferritin protein, the water phase was exchanged with calcium-phosphate solutions, leading to the formation of nanostructured crystalline calcium phosphate in the protein stabilized interface.

*1.5.2. Polysaccharide-based Template*

Acidic polysaccharide with carboxyl functional groups can play an important role in iron oxyhydroxide mineralization and it has been reported that microbial

polysaccharide influence iron mineralization in both natural and cultured samples (Chan *et al.*, 2009). In another study it has been reported that an osmotolerant marine isolate, related to *Alteromonas macleodii* produced an exopolysaccharide, which supported the synthesis of biocompatible silver nanoparticles of around 70 nm in size (Mehta *et al.*, 2014). The inhibitory effect of branched, linear, neutral, and acidic polysaccharides comprising of alginate, polygalacturonate, amylose, dextrin and amylopectin on crystal growth was ascertained, wherein it was observed that branched, acidic polysaccharides were superior as inhibitors for calcium carbonate precipitation (Nielsen *et al.*, 2012). In an interesting study, AFM and SEM-based analysis of calcite morphology suggested that the ancient complex polysaccharide from Maastrictian chalk was still effective as a calcite growth inhibitor (Sand *et al.*, 2014). In a comprehensive review article, the role of polysaccharides and proteoglycans in the mineralization of calcium carbonate was highlighted (Arias and Fernandez, 2008).

### *1.5.3. Lipid-based Template*

Lipid is not primarily involved in the biomineralization process but it can self-assemble and contribute to compartmentalization. For instance, stimuli-responsive liposomes have been shown to mediate the formation of mineral, polymer, and mineral-polymer composite biomaterials (Collier and Messersmith, 2001). In a mechanistic study, it was proposed that a lipid/water interface is critical in inducing self-assembly and mineralization of haemozoin (β-haematin), which may hold implications in detoxification of haem by malarial parasite (Egan *et al.*, 2006).

Some representative examples of macromolecule-based approaches for biomineralization are indicated in Table 1.2.

### *1.5.4. Whole Cell-Based Synthesis*

*Bacillus megaterium* promotes carbonate mineralization by epicellular and intercellular activities. The bacterial cell wall, EPS or metabolic products help in the nucleation process for calcite development and generation of vaterite by the cell free supernatant has been demonstrated (Lian *et al*., 2006). In the diatom *C. fusiformis*, the protein silaffin and the long chain polyamine have been implicated in mineralization of silica (Pohnert, 2002). *Klebsiella pneumoniae* LH1 isolated from dolomite induce intracellular and extracellular biomineralization. Amino acids and organic groups present in EPS controlled the growth of minerals followed by metal absorption.

**Table 1.2.** Macromolecules involved in biomineralization-based synthesis of nanomaterials.

| Sl No. | Macromolecule | Source | Material | Size | Reference |
|---|---|---|---|---|---|
| 1. | Polysaccharide | *Alteromonas macleodii* | Ag nanoparticle | 50 nm | Mehta *et al.*, 2014 |
| 2. | Peptide | Poly-L-arginine | Magnetite nanoparticle | 10-40 nm | Kuhrts *et al.*, 2019 |
| 3. | Peptide | Fmoc-Phe–Phe–Asp-OH | $TiO_2$ nanofiber | 60 nm | Li *et al.*, 2018 |
| 4. | Peptide | Mms13cc/MmsFcc from *M. magneticum* AMB-1 | Magnetite nanoparticle | 30-50 nm | Rawlings *et al.*, 2019 |
| 5. | Protein | Hydrophobin fusion protein | Hydroxyapatite nanoparticle | < 200 nm | Melcher *et al.*, 2016 |
| 6. | Protein | Curli amyloid proteins | Hydroxyapatite nanoparticle | 200 nm | Abdali *et al.*, 2020 |
| 7. | Peptide | 14-mer bi-functional copolypeptide | $Fe_3O_4$ nanoparticles | 10 nm | Liu *et al.*, 2019 |
| 8. | Peptide | Amelogenin-inspired peptides | Hydroxyapatite nanoparticle | 43-66 nm | Mukherjee *et al.*, 2018 |
| 9. | Protein | Spider silk protein/osteopontin/ sialoprotein SIBLING proteins | Calcium Phosphate | 500 nm | Neubauer and Scheibel 2020 |
| 10. | Polysaccharide | Anionic heparin/ alginate | Hydroxyapatite nanoparticle | 91 nm | Coleman *et al.*, 2013 |
| 11. | Polysaccharide | EPS of *E. coli* | Gold Nanoparticle | 2-15 nm | Kang *et al.*, 2017 |
| 12. | Peptide | Statherin-derived peptide | Hydroxyapatite nanoparticle | 100 nm | Wang *et al.*, 2018 |
| 13. | Protein | Albumin | Ceria nanomaterials | 5-150 nm | Yang *et al.*, 2017 |
| 14. | Peptide | Amyloid-based Peptide | Gold Nanoparticle | 6-9 nm | Jain *et al.*, 2019 |

Ammonia and carbonic anhydrase (CA) act together to promote an ambient alkaline environment, which favours the Mg-carbonates formation (Zhao *et al.*, 2020). Carbonate hydroxyapatite (cHA) and zinc-magnesium substituted hydroxyapatite (HA) have been made via biomineralization by using *Enterobacter aerogenes* (Ahmadzadeh

*et al.*, 2016). The mechanism of biomineralization of gold by the fungus *Rhizopous oryzae* has been reported and the cytoplasmic proteins implicated in the reduction of gold and capping of the generated gold nanoparticles were identified (Das *et al*., 2012). Biologically induced mineralization of calcite and otavite by the urease-positive fungi *Neurospora crassa* has also been reported (Li *et al*., 2014). In a separate study it was reported that viable biofilm of the bacterium *Cupriavidus metallidurans* was implicated in biomineralization of gold (Fairbrother *et al*., 2013). In a separate study, growth of gold, silver, and gold-silver alloy crystals in *Lactobacillus* strains has been demonstrated. It was proposed that the crystal nucleation was mediated by nanoclusters formed within the cell or by importing nanoclusters formed extracellularly (Nair and Pradeep, 2002).

### *1.6. Biomedical Applications of Hydroxyapatite Nanomaterials*

Hydroxyapatite nanoparticles (HANPs) have come of age and are in the forefront of biomedical applications. The scope of exploring HANPs in therapy is vast and consists of application domain ranging from (i) antibacterial activity, (ii) antibiofilm activity, (iii) development of osteogenic scaffold for bone tissue engineering, (iv) coating of osteogenic implant, (v) development of therapeutics, (vi) cell labelling applications and (vii) drug delivery. A schematic representation of the major biomedical applications of HANPs is depicted in Figure 1.4. In the current investigation, the therapeutic potential of the generated HANPs is ascertained in antibiofilm application and in the development of scaffolds and implants for supporting bone cell growth. The following section provides a concise literature review pertaining to the applications of HANPs in antibacterial therapy, bone tissue engineering and some additional biomedical applications.

#### *1.6.1. Antibacterial Applications*

A samarium/gadolinium substituted hydroxyapatite (Sm/Gd-HAP) coating onto borate-passivated AISI 316L SS stainless steel has been used as an effective bioimplant for bone tissue engineering applications. The coating exhibited antibacterial activity against *Staphylococcus aureus* and *Escherichia coli* and could also render proliferation of mouse preosteoblast MC3T3-E1 cell line (Sathishkumar *et al.,* 2016). Silver-doped mesoporous hydroxyapatite nanoparticles were obtained through ascorbic acid-mediated and microwave-assisted synthesis. These nanoparticles revealed antibacterial

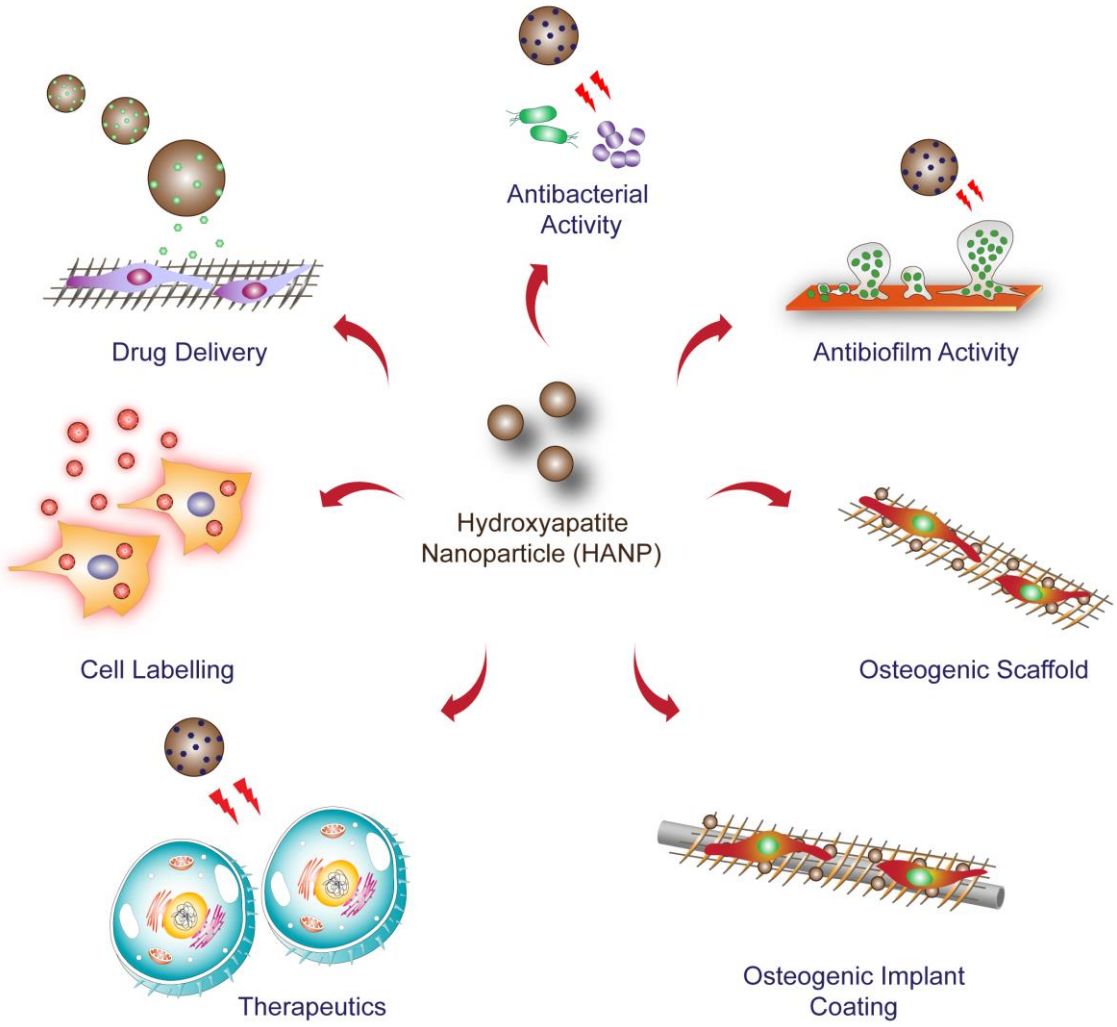


**Figure 1.4.** Schematic representation of the major biomedical applications of hydroxyapatite nanoparticles.

activity against *Streptococcus pneumoniae* MTCC 1935, *Bacillus subtilis* MTCC 1133, *Escherichia coli* MTCC 1692 and *Klebsiella pneumoniae* MTCC 7407 (Karunakaran *et al.*, 2019). A γ-polyglutamic acid and copper doped hydroxyapatite (γ-PGA/$Cu_x$HAp) nanocrystal showed antibacterial activity and supported endothelial (HUVEC) and osteogenic cell (MC3T3-E1 cell line) proliferation. With an increase in the copper content, there was an enhancement in the antibacterial activity of γ-PGA/$Cu_x$HAp against *S. aureus* ATCC 6538 (Shu *et al.*, 2020). Lactoferrin adsorbed onto biomimetic hydroxyapatite nanocrystals has been explored to mitigate *Helicobacter pylori* infection (Fulgione *et al.*, 2016). Additional representative examples on the use of HANPs for antibacterial applications are listed in Table 1.3.

**Table 1.3.** Hydroxyapatite nanomaterials in antibacterial applications.

| Sl. No. | Type of Material | Synthesis Method | Target Bacteria | Reference |
|---|---|---|---|---|
| 1. | Multifunctional HA | Microwave-assisted combustion | *S. aureus*<br>*E. coli* | Lamkhao *et al.*, 2019 |
| 2. | Ceria and AgNPs-reinforced HA | Suspension-precipitation | *S. aureus*<br>*E. coli* | Pandey *et al.*, 2018 |
| 3. | γ-polyglutamic acid and copper co-synthesized hydroxyapatite (γ-PGA/CuxHAp) | *In situ* polymerization | *S. aureus*<br>*E. coli* | Shu *et al.*, 2020 |
| 4. | HAP nanowire-AgNPs-ciprofloxacin | Solvothermal | *S. aureus*<br>*E. coli* | Xiong *et al.*, 2017 |
| 5. | Polydopamine-assisted hydroxyapatite and lactoferrin multilayer structure (PDA-HALF) | Biomimetic approach and spin-assisted layer-by-layer (LBL) assembly technique | *S. aureus*<br>*E. coli* | Shen *et al.*, 2018 |
| 6. | Cefazolin-loaded HANPs | Core−shell method | MRSA<br>*E. coli*<br>*P. aeruginosa* | Munir *et al.*, 2019 |
| 7. | BMP/CS/Ag/HA | Electrochemical deposition | *S. epidermidis*<br>*E. coli* | Xie *et al.*, 2014 |
| 8. | $Mg^{2+}$-substituted hydroxyapatite (HA) | Wet-chemical precipitation | *S. aureus*<br>*P. aeruginosa*<br>*E. coli* | Andrés *et al.*, 2018 |
| 9. | $Zn^{2+}$, $Mg^{2+}$ and $CO_3^{2-}$ ion doped-HA | Neutralization method | *E. coli*<br>*P. aeruginosa*<br>*S. aureus*<br>*C. albicans* | Sprio *et al.*, 2019 |
| 10. | Ag/ZnO/HA composite | Chemical reduction method | *S. aureus*<br>*E. coli* | Zhang *et al.*, 2018 |

### *1.6.2. Bone Tissue Engineering Applications*

A hydroxyapatite scaffold with hexagon-like column array topography was fabricated, which could support fibronectin adsorption, was biocompatible, and rendered high osteogenic gene and protein expression in human adipose-derived stem cells (ADSCs)

(Wei *et al.,* 2020). Collagen is the predominant protein in bone mineralization. A recent and comprehensive review article highlights the use of alternate proteins such as fibrin, silk proteins, keratin, sericin, fibroin in the synthesis of hydroxyapatite composite for bone tissue engineering, skin tissue engineering applications and drug delivery systems (Veiga *et al.,* 2020). A review article has described the generation of bio-inspired mineralization-based materials, which may hold considerable potential in bone tissue engineering and regenerative medicine (Alves *et al.,* 2010). In another study, 58s-Bioglass, collagen and chondroitin sulfate were used as a scaffold to grow hydroxyapatite (HAP) crystals. Plate-like and petal-like crystals were observed when these scaffolds were used. The biocompatibility of the scaffold was checked against osteoblast MC3T3-E1 cells and the composite was found to have considerable potential as a bone substitute. (Yang *et al.,* 2013). Hydroxyapatite scaffold obtained through biogenic synthesis from cuttlefish bone (*Sepia officinalis*) exhibited porous interconnected structure and favorable mechanical properties. This scaffold was biocompatible and supported cellular adhesion and proliferation of mouse osteoblast cells (MC3T3-E1) after 7 days culture (Hadagalli *et al.,* 2019). Polycaprolactone/ carbon nanofiber/ hydroxyapatite composite scaffold coated onto titanium displayed biocompatibility and supported proliferation of human osteosarcoma MG-63 cells. The composite implant material exhibited healing property and *in vivo* osteointegration was observed after 4 weeks (Elangomannan *et al.,* 2017). Hydroxyapatite nanowire as the core and magnesium silicate nanosheets as the shell was integrated into chitosan matrix (HANW@MS/CS) to generate a porous scaffold, which not only promoted cell adhesion and growth of rat bone marrow derived mesenchymal stem cells (rBMSCs) but also induced the expression of osteogenic genes and the vascular endothelial growth factor (VEGF) gene in rBMSCs. Owing to enhanced surface area and pore volume, the nanocomposite was amicable to drug delivery applications and stimulated bone regeneration *in vivo,* which led to formation of new bone and blood vessel (Sun *et al.,* 2017). A porous, composite scaffold consisting of rod-shaped nano HA core and amorphous silica sheath (Si-nHA) blended with gelatinous matrix displayed good biocompatibility, osteogenic differentiation and vascularization in bone engineering *in vitro*. Further, this composite could also support vascularization in chick chorioallantoic membrane (CAM) model and rat model, leading to new bone formation in case of a femoral segmental defect (Anitha *et al.,* 2017). Polydopamine template-assisted hydroxyapatite multi-layered nanofilms were generated, which rendered

superior bone morphogenic protein-2 (BMP-2) loading and release. This multilayer nanofilm supported high osteoconductivity *in vitro* in case of bone marrow stromal cells from rat and *in vivo* Sprague-Dawley (SD) rat implantation (Xie *et al.*, 2016). A bone biomimetic calcium deficient hydroxyapatite/collagen/plate rich plasma (PRP) containing scaffold was generated, which rendered effective cell proliferation and differentiation of preosteoblast MC3T3-E1 cells (Lee and Kim, 2018). 3D printed Fe scaffolds bearing nano-hydroxyapatite coating resulted in enhanced cell viability, alkaline phosphatase (ALP) activity and osteogenic differentiation of rabbit bone marrow mesenchymal cells. The porosity and mechanical strength of the scaffold was analogous to natural bone (Yang *et al.*, 2018). 3D porous chitosan-gelatin (C-G) scaffolds having sintered hydroxyapatite (sHA) or non-sintered (nsHA) were akin to human spongy bones. MTS assay, confocal microscopy and SEM images showed that C-G/sHA scaffold rendered higher Saos-2 cell affinity and proliferation as compared to C-G/nsHA scaffold (Isikli *et al.*, 2012). A porous interconnected alginate/HAP composite scaffold was generated, which exhibited 82% porosity, having pore size of 150 μm. It was observed that rat osteosarcoma UMR106 cells seeded onto this scaffold showed better cell attachment as compared to pure alginate scaffold (Lin and Yeh, 2004). Additional examples that describe the use of hydroxyapatite in bone tissue engineering applications is illustrated in Table 1.4.

*1.6.3. Other Biomedical Applications*

Rod like HAP nanocrystals generated through a biomolecule-assisted hydrothermal method were shown to exhibit anti-proliferative activity against cultured HeLa cells (Cao *et al.*, 2010). Studies have been conducted to ascertain the adsorption and release kinetics of anti-cancer drugs loaded onto biomimetic hydroxyapatite nanocrystals. The outcome of this study points out the therapeutic implications of the generated nanocomposite (Palazzo *et al.*, 2007). $SiO_2$ template mediated hydroxyapatite nanoparticles were prepared and surface functionalized with fluorescein isothiocyanate (FITC). These fluorescent nanoparticles were biocompatible and rendered facile cell labelling (Liu *et al.*, 2011). A hydroxyapatite/chitosan (HA/CS) composite scaffold was developed for the delivery of the antibacterial lysostaphin, which resulted in effective elimination of methicillin-resistant *Staphylococcus aureus* (MRSA) (Xue *et al*., 2014).

**Table 1.4.** Hydroxyapatite nanomaterials in bone tissue engineering applications.

| Sl. No. | Type of Material | Method of Fabrication | Application | Reference |
|---|---|---|---|---|
| 1. | Poly (lactic-co-glycolic acid), mesoporous hydroxyapatite, Poly(γ-benzyl-L-glutamate) 3D scaffold | Solvent casting/particulate leaching (SC/PL) | *In vitro* MC3T3-E1 cell proliferation, osteogenic marker differentiation. *In vivo* rapid mineralization and new bone formation in rabbit radius defect repair model | Li *et al.*, 2019 |
| 2. | Microarc oxidation-fluoridated hydroxyapatite-coated Mg−Zn−Zr−Sr alloy | Microarc oxidation followed by chemical deposition | Increased cell viability, biocompatibility and new bone formation *in vivo* | Wang *et al.*, 2019 |
| 3. | Chitosan/poly (γ-glutamic acid) /hydroxyapatite (CPH) and platelet-rich fibrin (PRF) | Electrospinning followed by electrostatic interaction | Osteoinduction, osteoconduction, osteointegration *in vitro* and *in vivo* | Zhang *et al.*, 2019 |
| 4. | Sr/Fe co-substituted HAp bio-ceramics | Sonication-assisted chemical aqueous precipitation | Drug delivery system, promotes hMSCs osteogenic differentiation | Ullah *et al.*, 2020 |
| 5. | Silk fibroin/chitosan scaffold with BMP-2-loaded HAP (mHANPs) | Freeze drying method | Sustained release of BMP-2, enhanced osteogenic marker differentiation, ALP activity, calcium mineralization | Qiu *et al.*, 2020 |
| 6. | Hydroxyapatite (HA), bioactive glass (BG), tricalcium phosphate (TCP) particles coated on poly (L-lactic acid) (PLLA) nanofibers | Electrospinning | Bone graft substitutes for bone injuries and defect in rat model | Dinarvand *et al.*, 2011 |

**Table 1.4.** Hydroxyapatite nanomaterials in bone tissue engineering applications.

| Sl. No. | Type of Material | Method of Fabrication | Application | Reference |
|---|---|---|---|---|
| 7. | Boron Nitride/Gelatin/HAP | Electrospinning | High osteoblast gene expression, and ALP activity in human bone cells (HOS) | Nagarajan *et al.*, 2017 |
| 9. | HAP/silk fibre (SF)/methylcellulose (MC) composite | Electrospinning | Cellular adhesion, proliferation and ALP activity of human osteoblast cells | Valarmathi and Sumathi, 2020 |
| 10. | Composites of poly (L-lactide) (PLLA) and nano-hydroxyapatite(nHAp) functionalized with Europium (III) | Co-rotating twin screw extrusion technique using 3D printer extruder | nHAp/PLLA@$Eu^{3+}$ scaffolds promoted osteogenesis and chondrogenesis of human adipose-derived multipotent stromal cells (hASCs). | Marycz *et al.*, 2020 |
| 11. | Hydroxyapatite/poly-(γ-benzyl-L-glutamate) (HA/PBLG) microcarriers | Emulsion/*in situ* precipitation method | Acicular HA/PBLG microcarriers rendered mineralization and osteogenic differentiation of adipose stem cells (ADSCs) | Bu *et al.*, 2020 |
| 12. | Three-dimensional chitosan (CS)/honeycomb porous carbon/hydroxyapatite composite | *In situ* deposition and vacuum freeze-drying | Osteogenesis in mouse bone marrow mesenchymal stem cells and repair of bone defect in *in vivo* experiments | Dai *et al.*, 2020 |

# MOTIVATION AND OBJECTIVES OF THE PRESENT INVESTIGATION

# MOTIVATION AND OBJECTIVES OF THE PRESENT INVESTIGATION

Based on the existing literature reports as highlighted in Chapter 1 of the thesis, it is quite evident that in order to leverage the potential of hydroxyapatite nanoparticles (HANPs) in biomedical applications, there is a pressing need to develop non-toxic and environment friendly methods of HANP synthesis. Herein, biomineralization can be conceived as a promising route to generate biocompatible HANPs for therapeutic applications. The origin of the current research investigation is based on the following cardinal points:

1. In order to facilitate therapeutic applications of biomineralization-derived HANPs, it is paramount that the proteins or peptide templates used for such bottom-up synthesis not only favor nucleation, but are also non-toxic, biocompatible and naturally abundant. To this end, it can be envisioned that microbes, which are amicable to large scale cultivation can be explored as a source of proteins or peptides, that can serve as a mineralization template. In particular, lactic acid bacteria (LAB) emerge as an interesting prospect. The rationale behind the choice of LAB and their protein extracts is: (a) LAB are probiotics and GRAS (Generally Regarded as Safe) organisms and hence it is envisaged that the secreted proteins of LAB are less likely to have toxic implications and are suitable candidates as biomineralization templates, (b) Owing to their inherent metabolism, LAB is likely to secrete acidic proteins, which favor metal chelation and template-directed mineralization process thereof.

2. Biomineralization-derived nanomaterials have been reported extensively in the literature. However, the nuances with respect to the reaction mechanism, interaction between metal ions and protein-templates, structure-activity relationship of template proteins, macromolecular assembly and mechanistic insights into the process of mineralization for generation of biocompatible nanomaterials is not fully understood as yet. Hence, it is pertinent to acquire a mechanistic insight on the biomineralization process in order to generate

HANPs with superior attributes for biomedical applications. In this Ph.D. thesis, a major endeavor has been to unravel the role of the LAB template protein(s) in mineralization of HANPs. It is conceived that this effort will bridge the knowledge-gap and provide a guideline to select appropriate LAB-based molecular templates for nucleation and mineralization in order to generate HANPs for applications in biology and medicine.

3. Literature reports suggest that LAB cell surface-associated proteins (CSPs) are acidic and hydrophobic in nature and have the propensity to self-assemble. Hence, it can be envisaged that the LAB CSPs can serve as a nucleation scaffold, through metal chelation and facilitate HANP mineralization. Metal-chelating acidic groups (like $COO^-$ and $PO_4^{3-}$) are also abundantly present in the cell envelope of Gram-positive bacteria. Thus, in addition to CSP, these metal-chelating cell surface ligands present on the Gram-positive LAB can perhaps be exploited at the whole-cell level to render high density nucleation sites and efficient metal chelation, leading to enhanced biomineralization of HANPs.

4. Given the complex and labile nature of proteins, there is a scope to design and build a repertoire of protein/peptide mimics such as synthetic amphiphiles and explore their potential in bio-inspired mineralization for facile and large-scale generation of HANPs. It is envisaged that such synthetic amphiphiles can be rationally designed, which not only support biomimetic mineralization but also enhance the scope of biomedical application by generating HANPs having superior attributes such as high surface area, which can be leveraged for developing scaffolds for regenerative medicine and tissue engineering.

5. It is critical that the therapeutic merit of a newly generated hydroxyapatite-based nanomaterial should be validated by demonstrating its potential in mitigating a real clinical problem. To this end, HANPs generated through biomineralization can be leveraged for antibacterial and orthopaedic applications.

A cartoon illustrating the essential motivating factors in the current investigation is shown in Figure 1.5.

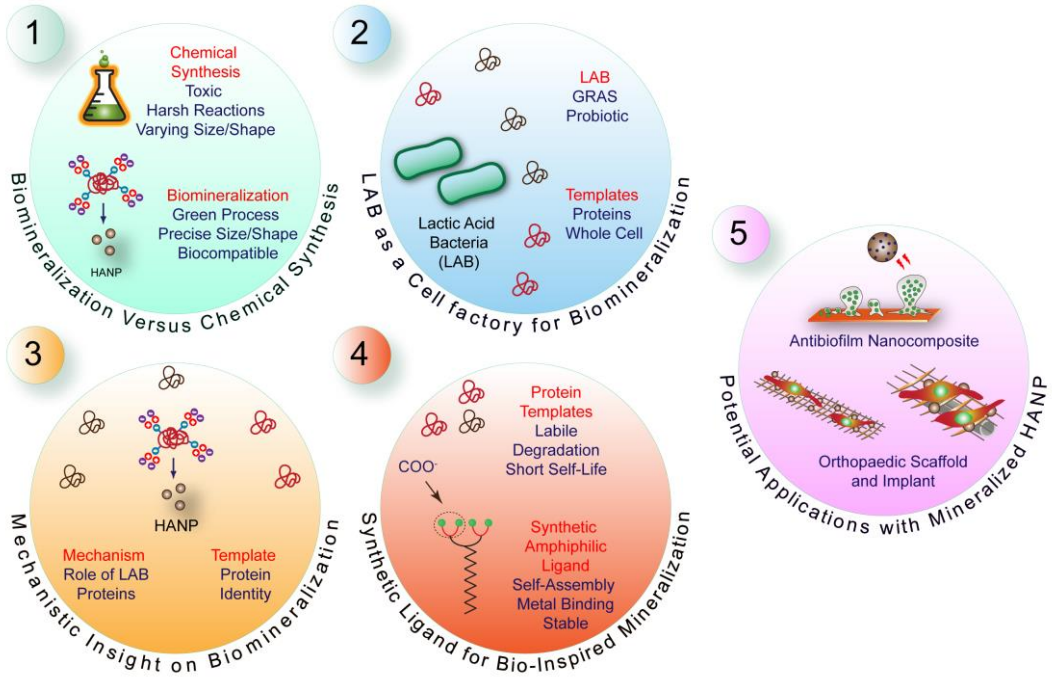


**Figure 1.5.** Schematic illustrating the principal motivating factors for the present investigation.

Based on the scope of the research work, the essential objectives of the Ph.D. thesis are as follows:

1. Generation of hydroxyapatite nanoparticle through biomineralization using cell-free protein extract of lactic acid bacteria (LAB).
2. Mechanistic studies on biomineralization to address the role of LAB cell-free proteins in hydroxyapatite synthesis and development of antibiotic-loaded hydroxyapatite nanocomposite for antibiofilm application.
3. Generation of hydroxyapatite nanoparticle by biomineralization of cell surface-associated protein from probiotic LAB.
4. Generation of macroporous scaffold grafted with LAB cell surface-associated protein mineralized hydroxyapatite nanoparticle for bone cell growth.
5. Biomineralization-inspired synthesis of hydroxyapatite nanoparticle using malonic acid amphiphile for orthopaedic implant application.

# Chapter 2

## Generation of Hydroxyapatite Nanoparticles (HANPs) Using Extracellular Proteins of Lactic Acid Bacteria

*In this chapter, the extracellular protein extract of three different LAB strains was used as an indigenous nucleation scaffold for biomineralization-based synthesis of hydroxyapatite nanoparticle. The characterization of the nanoparticles is presented in detail.*

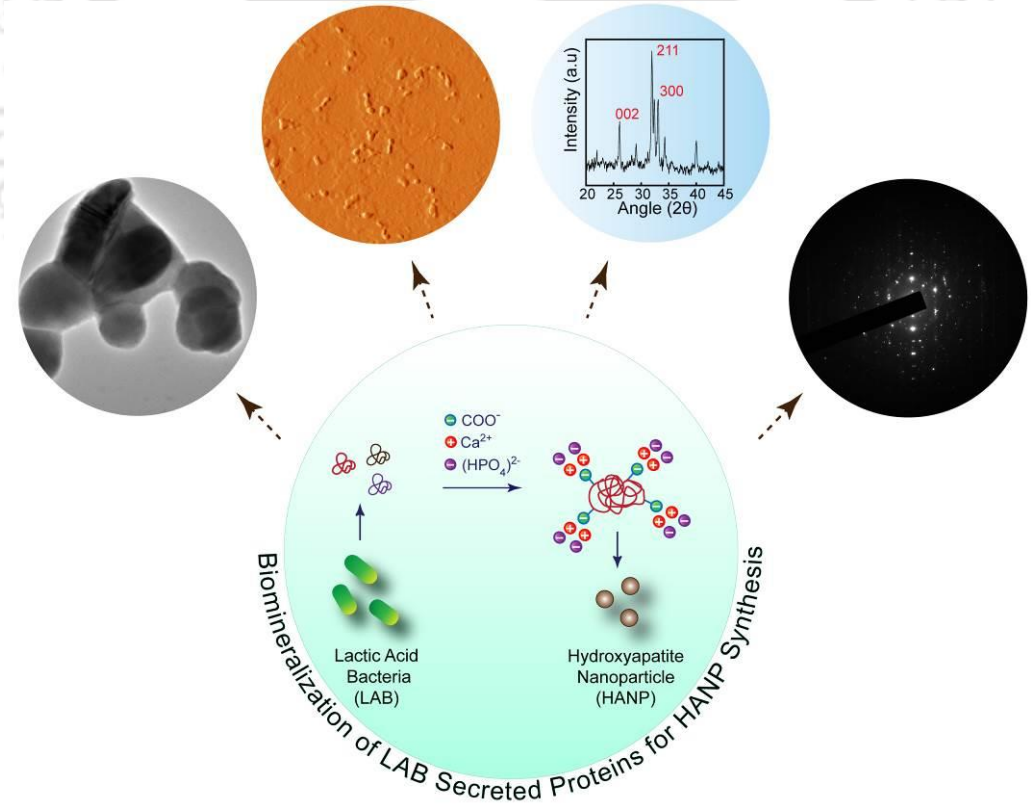

# ABSTRACT

Cell free proteins from lactic acid bacteria (LAB) referred herein as secreted LAB proteins (SLPs) were used as a biomineralization template for the generation of hydroxyapatite nanoparticles (HANPs). Synthesis of HANPs was accomplished by using SLPs from *Lactobacillus plantarum* MTCC 1325, *Lactobacillus plantarum* CRA52 and *Pediococcus pentosaceus* CRA51 in a wet precipitation method. Following synthesis, HANPs were isolated by centrifugation using varying speed and it was observed that HANPs recovered at 10,000 rpm were uniform in shape and size and crystalline in nature. FETEM analysis revealed that the HANPs obtained from SLPs of *L. plantarum* MTCC 1325 ranged from 75-100 nm in size, while HANPs obtained from SLPs of *L. plantarum* CRA52 and *P. pentosaceus* CRA51 were 50-60 nm in size. AFM analysis indicated that the average height profile of HANPs generated from the SLPs of *L. plantarum* MTCC 1325, *L. plantarum* CRA52 and *P. pentosaceus* CRA51 were approximately 2.38 nm, 3.13 nm and 4.11 nm, respectively. FTIR analysis of the synthesized HANPs revealed the presence of peaks at 3568 $cm^{-1}$, 1461 $cm^{-1}$ and 1041 $cm^{-1}$, corresponding to $OH^-$, $CO_3^{2-}$ and $PO_4^{3-}$ stretching frequencies, respectively. Evidence for the crystalline nature of HANPs was obtained by powder XRD analysis, wherein sharp peaks were observed at $2\theta = 26^0$, $31^0$ and $33^0$, which correspond to (002), (211) and (300) lattice planes. The crystalline nature of the HANPs was also supported by SAED pattern. ITC studies revealed that the secreted LAB protein (SLP) scaffold augmented the biomineralization process for growth of HANP crystal.

## 2.1. Introduction

Hydroxyapatite nanoparticles (HANPs) have emerged as materials of great potential in contemporary healthcare, given their significant propect in bone tissue engineering and regeneration, antibacterial, anti-cancer and cell labelling applications (Zia *et al.,* 2020; Valarmathi *et al.,* 2020; Haider *et al.,* 2017; Padmanabhan *et al.,* 2020; Deshmukh *et al.,* 2016). Although a large number of chemical methods are available for synthesizing HANPs (Sadat-Shojai *et al*., 2013; Degli Esposti *et al.,* 2020; Xie *et al.,* 2016) they have limited scope as they entail the use toxic chemicals as a precursor material and the reaction conditions can be quite harsh. In this context, biomineralization-directed synthesis of HANPs can offer a viable solution as it facilitates green synthesis and is perceived to render precise control of size and shape of nanoparticles (NPs). Biomineralization is a ubiquitous phenomenon evidenced across living beings from microbes to vertebrates (Weiner and Dove, 2003; Lowenstam, 1981; Mann, 1995), with natural examples such calcium carbonate ($CaCO_3$) in mollusk shells and sponges, hydroxyapatite [$Ca_{10}(PO_4)_6(OH)_2$] in bones and teeth of vertebrates, amorphous silica ($SiO_2$) in diatoms and sponges, magnetite ($Fe_3O_4$) nanocrystals in magnetotactic bacteria and chiton teeth (Addadi *et al.,* 2013; Lechner and Becker, 2015; Jabalera *et al.,* 2019; Alves *et al.,* 2010). Further, macromolecular templates such as natural and engineered proteins and peptides have been used as templates in mineralization for synthesis of NPs having significant application potential in the healthcare domain (Yang *et al.,* 2017; Ghorbani *et al.,* 2019; Li *et al.,* 2012).

Although biomineralization offers a distinct scope for NP synthesis, it is vital that the protein or peptide templates are both abundant and biocompatible in order to facilitate large-scale synthesis of NPs for translational applications. In this regard, the protein or peptide templates can be sourced from microbes, as they are amicable to large-scale cultivation, and harnessing the protein or peptides following cell growth is convenient. However, considering biomedical applications, it is pertinent that the microbial protein or peptide templates not only emerge as nucleation scaffolds, but are also non-toxic. To this end, the choice of lactic acid bacteria (LAB) as a source of such templates can be explored given the GRAS (generally regarded as safe) status of LAB. Herein, an earlier study has demonstrated the generation of hydroxyapatite (HA) crystals using extracellular protein extract of LAB as a template (Borah *et al.,* 2009).

Based on this lead, in the present work, the proteins present in the cell-free supernatant (CFS) from three different LAB strains namely *L. plantarum* MTCC 1325,

*L. plantarum* CRA52 and *P. pentosaceus* CRA51 were used as a template for HANP synthesis through a biomineralization process. The investigation provides an extensive characterization of HANPs generated by mineralization of the protein extract from the LAB strains.

## 2.2. Materials and Methods

### *2.2.1. Growth Media and Chemicals*

Lactobacillus de Man, Rogosa and Sharpe (MRS) broth, calcium nitrate and di-ammonium hydrogen phosphate were procured from HiMedia, Mumbai, India. Ammonium solution and ammonium sulfate were obtained from Merck, India. Commercially available hydroxyapatite nanoparticle [particle size <200 nm (BET)] was procured from Sigma-Aldrich, USA.

### *2.2.2. Bacterial Strains and Culture Condition*

*Lactobacillus plantarum* MTCC 1325, *Lactobacillus plantarum* CRA52 and *Pediococcus pentosaceus* CRA51 was grown in MRS media at 37°C for 18 h under static condition. All the bacterial strains were revived from frozen stock cultures and subcultured prior to the experiments.

### *2.2.3. Preparation of Secreted LAB Protein (SLP) Extract*

*Lactobacillus plantarum* MTCC 1325, *Lactobacillus plantarum* CRA52 and *Pediococcus pentosaceus* CRA51 was grown in 100 ml MRS broth at 37°C for 18 h under static condition. The culture was subjected to centrifugation at 8000 rpm for 5 min at 4°C and the cell-free supernatant (CFS) was collected. Ammonium sulfate was added to the CFS at a concentration of 40% (w/v) (Jain *et al.*, 2010) and the solution was stirred at 4°C to precipitate the proteins. The resulting mixture was centrifuged at 12000 rpm for 10 min at 4°C and the pellet was collected. Subsequently, the pellet was resuspended in sterile MilliQ water and dialyzed using a 12 kDa MWCO dialysis bag (Sigma, USA) against water for 24 h. The dialysate was referred to as secreted LAB protein (SLP) extract. The concentration of the protein in the SLP extract was estimated by Bradford reagent (Sigma-Aldrich, USA). The dialysate was lyophilized and stored at -20°C prior to further use.

*2.2.4. Synthesis of Hydroxyapatite Nanoparticle (HANP) by Biomineralization of SLP Extract*

HANPs were essentially prepared by following a previously reported wet precipitation method (Dasgupta *et al.*, 2010) Briefly, to a 6.0 ml aliquot of 5.0 M $Ca(NO_3)_2$ solution, ammonia solution was added to adjust the pH to 9.0. A 5.0 ml aliquot of SLP extract (20 µg/ml protein concentration) was added dropwise to the pH adjusted Ca-salt solution. In order to ensure proper mixing, the solution was stirred continuously at room temperature. Parallelly, a control experiment was set up in which sterile MilliQ water was added instead of SLP extract. To this reaction mixture, 0.018 molar $(NH_4)_2$ $HPO_4$ solution was added dropwise to maintain a Ca: P ratio of 1.67:1. The pH of the mixture was again adjusted to 9.0 by adding $NH_4OH$ solution and the mixture was incubated at 37°C for 24 h under static condition followed by centrifugation at 10000 rpm for 5 min and the supernatant was discarded. The recovered pellet was washed twice with sterile MilliQ water followed by lyophilization and a final calcination step at 600°C for 2 h to obtain HANPs. The HANPs were stored at -20°C prior to further use.

*2.2.5. Characterization of HANPs*

The synthesized HANPs obtained from LAB crude SLP extract and chemically synthesized HANPs (Dasgupta *et al.*, 2010) were characterized by FTIR analysis, powder XRD analysis, atomic force microscopy (AFM) and FETEM analysis. The following section provides a description of these methods:

*2.2.5.1. FTIR and Powder X-ray Diffraction (XRD)*

FTIR spectra of HANPs prepared from LAB crude protein extract, chemically synthesized HANPs and the commercially available HANPs (Sigma-Aldrich, USA) were recorded in KBr pellets at 4.0 $cm^{-1}$ resolution in an infrared spectrometer (Spectrum One, Perkin-Elmer). For every sample, eight scans were performed in the range of 4000 $cm^{-1}$ to 500 $cm^{-1}$. Powder XRD (D2 Phaser, Bruker, Germany) of the HANPs were recorded at room temperature over the 2θ range of 20°-45° with a step size of 0.02° and a count time of 2s/step.

*2.2.5.2. Atomic Force Microscopy*

Samples of HANPs were sonicated for 1 hour and 10 µl of each sample was spotted onto sterile glass cover slips (18 mm × 18 mm) and air dried inside the laminar hood overnight. Atomic force microscopic images were captured with an Agilent 5500 AFM (Agilent Technologies, Chandler, AZ, USA). Cantilevers made up of silicon nitride were used having a resonant frequency of ca. 150 to 200 kHz. Images were acquired in non-contact mode, with 10 µm × 10 µm area at a scan rate of 0.5-1.0 line/s. Analysis of the topographic images of the surface was accomplished by using the WSxM v5.0 Develop 6.5 image viewer software.

*2.2.5.3. FETEM Analysis*

HANP samples were drop-casted onto a carbon-coated copper grid and dried overnight inside a laminar hood. The samples were then subjected to FETEM analysis (INCA, JEOL JEM 2100F, Japan) and their images were recorded. The samples were also subjected to High Resolution Transmission Electron Microscope (HR-TEM) analysis and the selected area electron diffraction (SAED) pattern was recorded.

*2.2.5.4. Isothermal Titration Calorimetry (ITC) Analysis*

ITC analysis was conducted in a VP-ITC instrument (MicroCal, Northampton, USA) at 37°C. The SLP extract (20 µg/ml) from *P. pentosaceus* CRA51 and 5.0 mM $Ca(NO_3)_2$ solution was taken in MilliQ water and mixed thoroughly followed by filtration using a 0.22 µm filter. The pH of SLP extract-$Ca^{2+}$ complex mixture was adjusted to 9.0 by adding ammonia solution. Ammonified protein-$Ca^{2+}$ complex was loaded on to the cell and titrated with $(NH_4)_2HPO_4$ solution. The integrated heat effect was determined by non-linear regression using a single site-binding model (Microcal Origin, Version 5.0).

## 2.3. Results and Discussion

*2.3.1. Synthesis of HANPs by using Secreted LAB Protein (SLP) Extract as Biomineralization Template*

In the present study, the secreted LAB protein (SLP) extract present in the cell-free supernatant (CFS) of *L. plantarum* MTCC 1325, *L. plantarum* CRA52 and *P. pentosaceus* CRA51 was used as a biomineralization template for the synthesis of hydroxyapatite nanoparticles (HANPs). SLP extract from the LAB strains are likely to

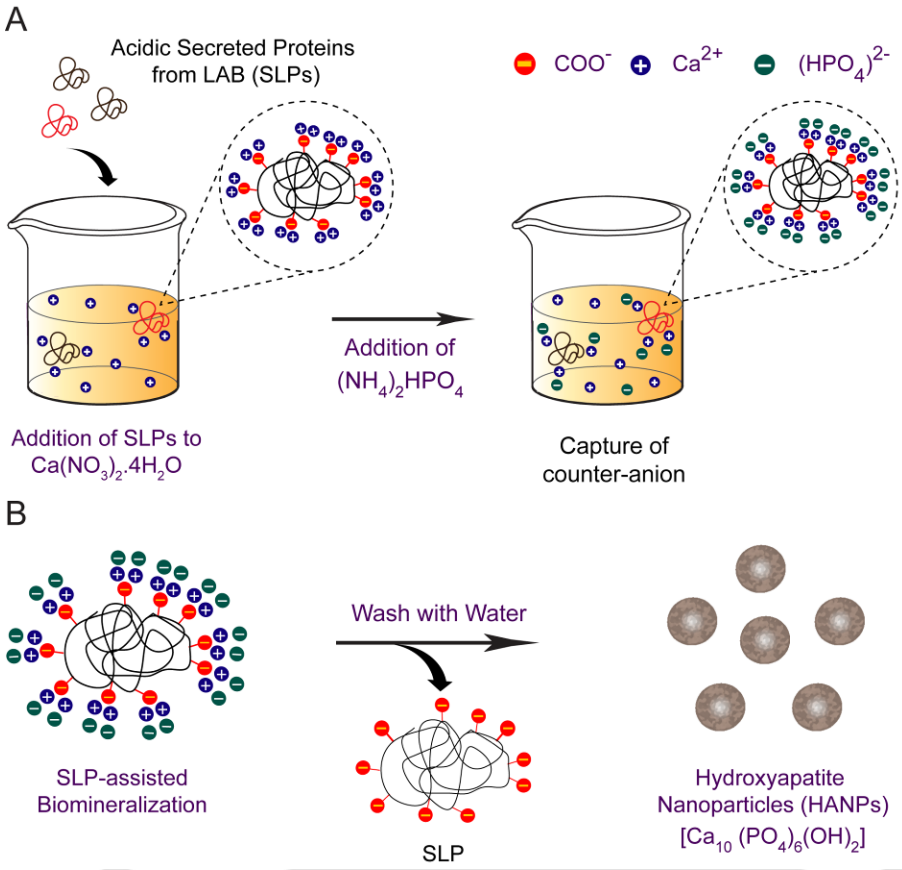


**Figure 2.1.** Schematic representation illustrating (A) role of acidic secreted proteins from LAB (SLPs) in biomineralization process and (B) generation of hydroxyapatite nanoparticles (HANPs) using acidic secreted proteins from LAB.

be biocompatible templates, given the GRAS (Generally Regarded As Safe) status of these LAB strains. Further, it can also be conjectured that the acidic LAB SLPs will be efficient as nucleation scaffolds by anchoring the cation ($Ca^{2+}$) followed by binding of counter-anion ($[HPO_4]^{2-}$) (Figure 2.1A) and direct biomineralization-based HANP synthesis (Figure 2.1B).

The concentration of the protein present in the CFS of *L. plantarum* MTCC 1325, *L. plantarum* CRA52 and *P. pentosaceus* CRA51 was 44.13 µg/ml, 15.63 µg/ml and 17.15 µg/ml, respectively, as quantified by Bradford assay. HANPs were synthesized by essentially following a wet precipitation method (Dasgupta *et al.*, 2010). The synthesized HANPs were harvested by centrifugation at various speeds. It was observed that the shape and size of HANPs harvested at 10000 rpm was quite homogeneous as compared to the HANPs recovered at other speeds by centrifugation (Figure 2.2 A, C, E, G and I). Further, SAED pattern analysis indicated that HANPs recovered at 10000 rpm also exhibited significant crystallinity as compared to other

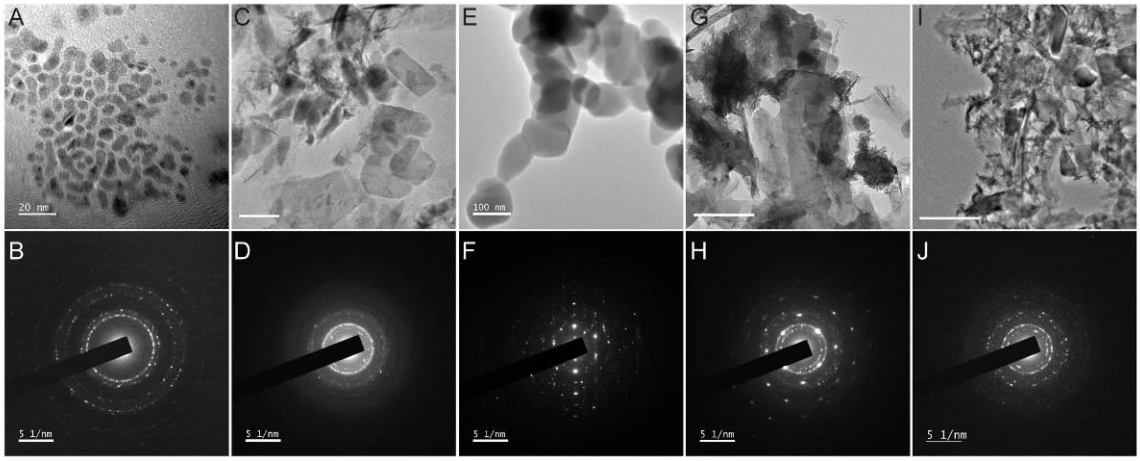


**Figure 2.2.** FETEM image and corresponding SAED pattern of HANPs generated by biomineralization using cell free extract of *L. plantarum* MTCC 1325. HANPs were recovered using various centrifugation speed. The panels represent HANPs recovered at (A-B) 6000 rpm, (C-D) 8000 rpm, (E-F) 10000 rpm, (G-H) 12000 rpm and (I-J) 14000 rpm. Scale bar for the FETEM images are: (A) 20 nm, (C) 500 nm, (E) 100 nm, (G) 1.0 μm and (I) 2.0 μm.

samples (Figure 2.2 B, D, F, H and J). Hence, in all the subsequent experiments, the synthesized HANPs were recovered by using a speed of 10000 rpm in centrifugation.

*2.3.2. Characterization of HANPs Obtained by Biomineralization*

FETEM analysis indicated that the HANPs obtained by biomineralization of SLP were mostly spheroid or oblong-shaped, along with some cuboidal particles (Figure 2.3A-C). ImageJ analysis suggested that the average particle size distribution of HANPs obtained from SLP of *L. plantarum* MTCC 1325 ranged from 75-100 nm, whereas the corresponding particle size distribution in case of *L. plantarum* CRA52 and *P. pentosaceus* CRA51 was 50-60 nm. The average particle size of HANPs obtained from the LAB extracts were comparable to the size of HANPs obtained by various other routes of synthesis (Table 2.1). HR-TEM analysis indicated that the HANPs obtained from SLPs of *L. plantarum* MTCC 1325, *L. plantarum* CRA52 and *P. pentosaceus* CRA51 were oval in shape, with a lattice distance of 2.36 nm, 1.9 nm, and 0.9 nm, respectively (Figure 2.3 D-F).

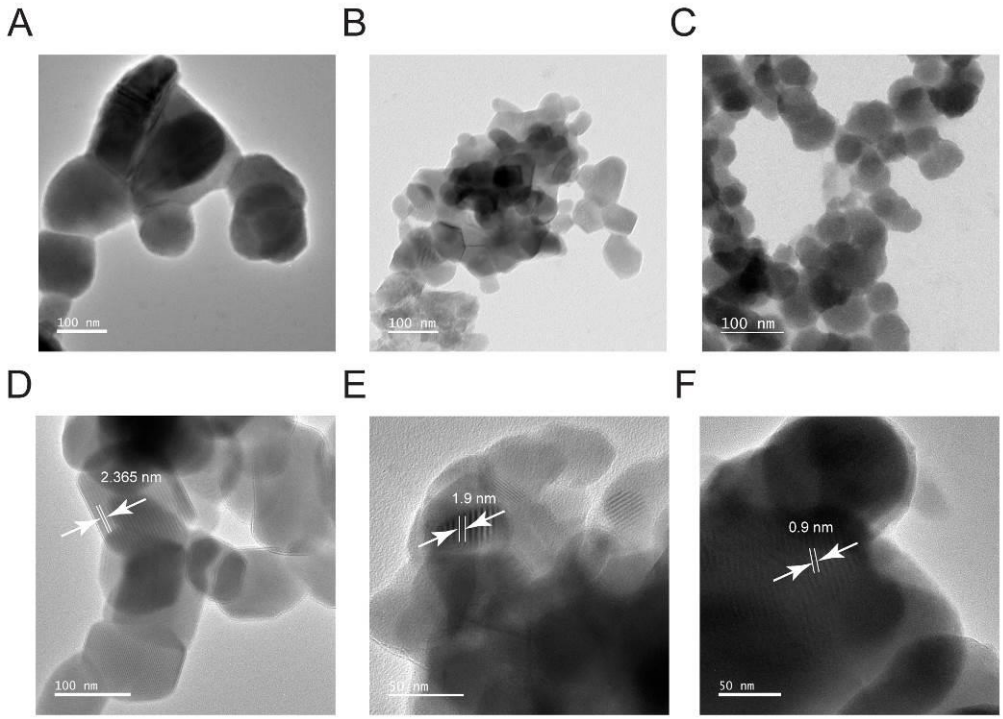


**Figure 2.3.** FETEM and HR-TEM analysis of HANPs generated by biomineralization using cell free extract of (A and D) *L. plantarum* MTCC 1325, (B and E) *L. plantarum* CRA52, and (C and F) *P. pentosaceus* CRA51, respectively.

**Table 2.1.** An overview of the size of HANPs obtained through various modes of synthesis.

| Serial No. | Mode of Synthesis | Size of HANPs | Reference |
|---|---|---|---|
| 1. | Biomimetic | 98 ± 22 nm | Gao *et al*., 2016 |
| 2. | Hydrothermal | 104 nm | Cao *et al*., 2010 |
| 3. | *In situ* precipitation | 30-110 nm | Dasgupta *et al*., 2010 |
| 4. | Biomimetic | 100-300 nm | Zhang *et al*., 2008 |
| 5. | Wet chemical | 20-50 nm | Li *et al*., 2012 |
| 6. | Biomimetic | >500 nm | Ethirajan *et al*., 2009 |
| 7. | Biomimetic | <100 nm | Cunniffe *et al*., 2016 |
| 8. | Sol-gel | >100 nm | Yang *et al*., 2018 |
| 9. | Co-precipitation | 100-300 nm | Chen *et al*., 2016 |
| 10. | Biomimetic | >500 nm | Li *et al*., 2017 |
| 11. | Hydrothermal | ~30 nm | Qi *et al*., 2020 |
| 12. | Hydrothermal | 60-70 nm | Cipreste *et al*., 2016 |

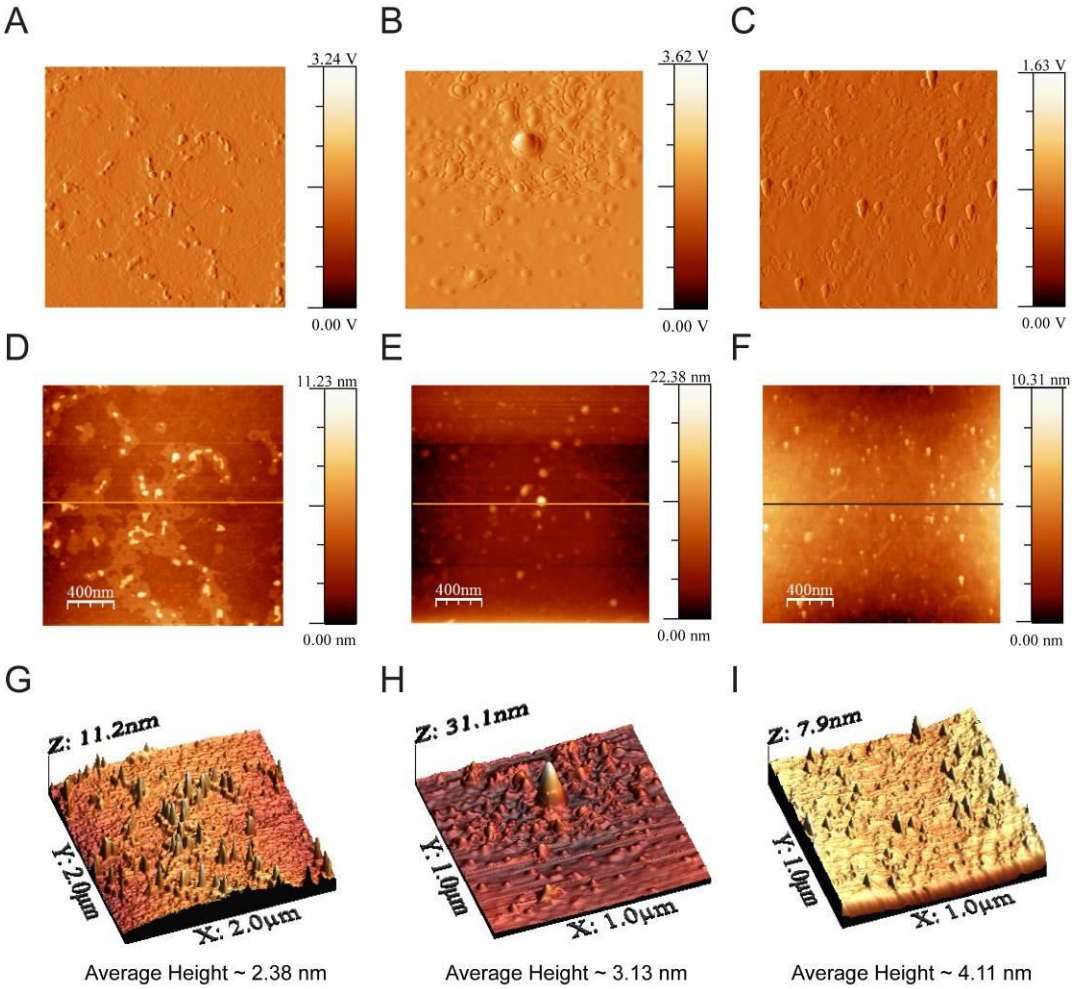


**Figure 2.4.** (A-C) Amplitude channel, (D-F) 2D topography and (G-I) 3D topography images obtained in AFM analysis of HANPs obtained from cell free extract of (A, D, G) *L. plantarum* MTCC 1325, (B, E, H) *L. plantarum* CRA52, (C, F, I) *P. pentosaceus* CRA51.

In AFM analysis, the amplitude channel and 2D topography images revealed that the HANPs obtained from the SLPs were mostly round or oblong-shaped (Figure 2.4 A-F), while 3D topography images indicated that the average height profile for the HANPs obtained from SLP of *L. plantarum* MTCC 1325, *L. plantarum* CRA52 and *P. pentosaceus* CRA51 were approximately 2.38 nm, 3.13 nm and 4.11 nm, respectively (Figure 2.4 G-I). FTIR analysis of HANPs obtained from the LAB SLPs revealed the presence of significant peaks at 3568 $cm^{-1}$, 1461 $cm^{-1}$, and 1041 $cm^{-1}$ (Figure 2.5), which correspond to $OH^-$, $CO_3^{2-}$, and $PO_4^{3-}$ stretching frequencies, respectively (Cipreste *et al.*, 2016; Dasgupta *et al.,* 2010).

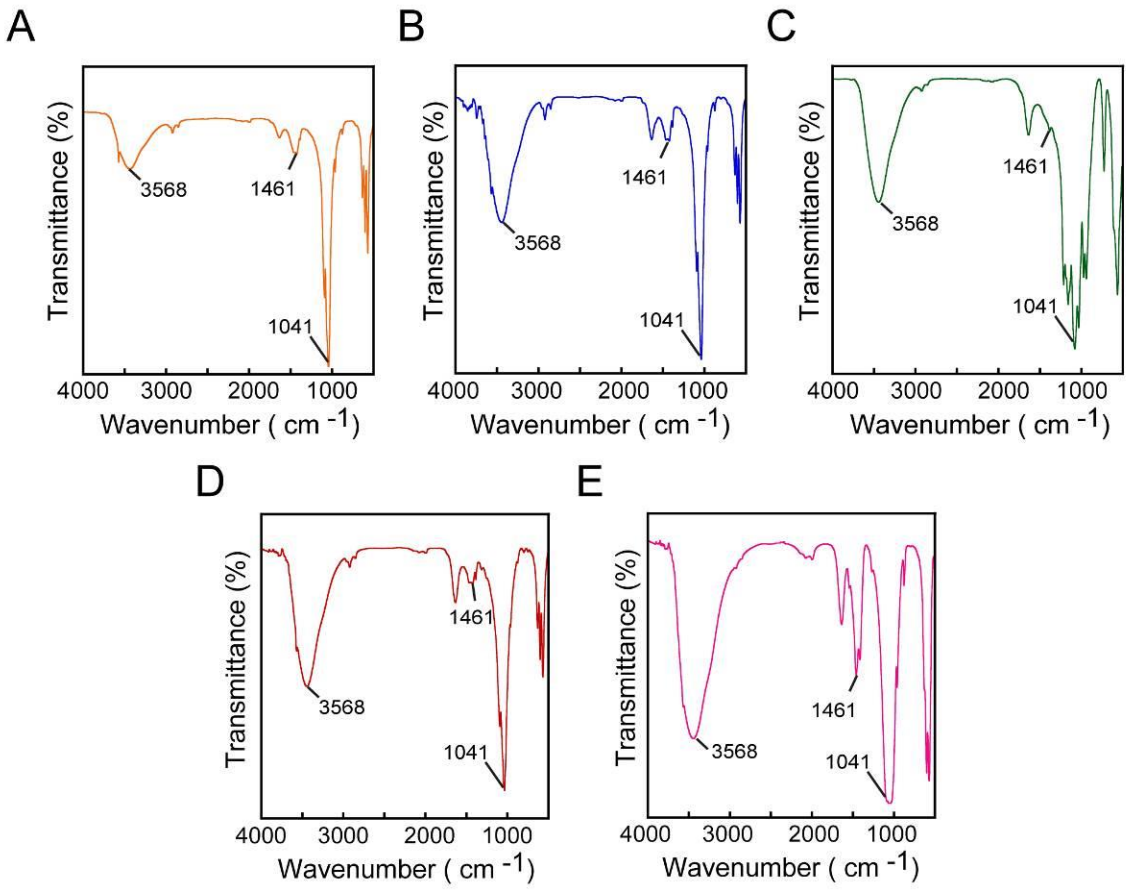


**Figure 2.5.** FTIR analysis of HANPs obtained from SLPs of (A) *L. plantarum* MTCC 1325, (B) *L. plantarum* CRA52, (C) *P. pentosaceus* CRA51. FTIR analysis of (D) HANPs obtained by chemical synthesis method and (E) HANPs procured commercially (Sigma-Aldrich, USA) are also indicated as reference samples.

The crystalline nature of the synthesized HANPs was apparent from SAED pattern analysis (Figure 2.6 A-C). In powder XRD analysis, the manifestation of sharp peaks at around 2θ = 26° corresponding to the (002) lattice plane, 2θ = 31° corresponding to (211) lattice plane and 2θ = 33° corresponding to the (300) lattice plane (Gao *et al*., 2016; Li *et al*., 2012) also suggested the presence of crystalline hydroxyapatite (Figure 2.6 D-F).

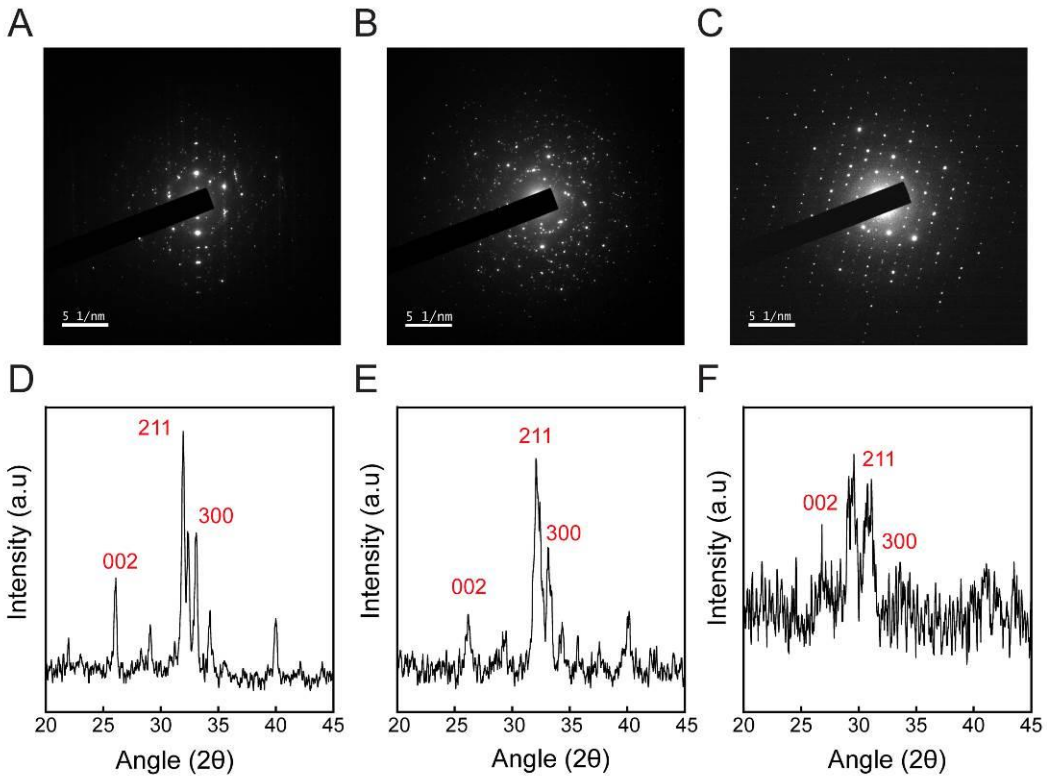


**Figure 2.6.** SAED and powder XRD pattern of HANPs generated by biomineralization using cell free extract of (A and D) *L. plantarum* MTCC 1325, (B and E) *L. plantarum* CRA52 and (C and F) *P. pentosaceus* CRA51, respectively.

Based on the characterization studies, it is worthwhile to mention here that the HANPs obtained from the SLPs were comparable to the HANPs obtained by a chemical synthesis method (Dasgupta *et al.,* 2010), which was also characterized as a reference control sample (Figure A2.1 in Appendix).

*2.3.3. ITC Studies for Analysis of Binding Isotherm*

Based on the HANPs obtained, it is apparent that the SLP extracts assume a central role as biomineralization templates, wherein it can be conceived that the initial stage of biomineralization perhaps involves the formation of a stable complex between the SLPs and the metal ion ($Ca^{2+}$ herein), which in turn facilitates the subsequent binding of the counter ion ($PO_4^{3-}$). ITC studies could validate this tenet and suggested that the presence of SLPs as template rendered biomineralization, as evidenced by the favorable binding of $PO_4^{3-}$ ion with $Ca^{2+}$-SLP complex of *P. pentosaceus* CRA51 ($K_a$ = 5.71 × $10^5$ $M^{-1}$) (Figure 2.7A). This notion is further strengthened by the

observation that the binding of $PO_4^{3-}$ ion with $Ca^{2+}$ was weaker in the absence of the SLP template ($K_a$ = 4.13 × $10^4$ $M^{-1}$) (Figure 2.7B), which reiterated the critical role of the SLP in nucleation process. It may be mentioned here that in control experiments, no interaction could be observed when the SLP was titrated with only $PO_4^{3-}$ ions, which perhaps is due to the anionic nature of both the SLP as well as $PO_4^{3-}$ ion (Figure 2.7C).

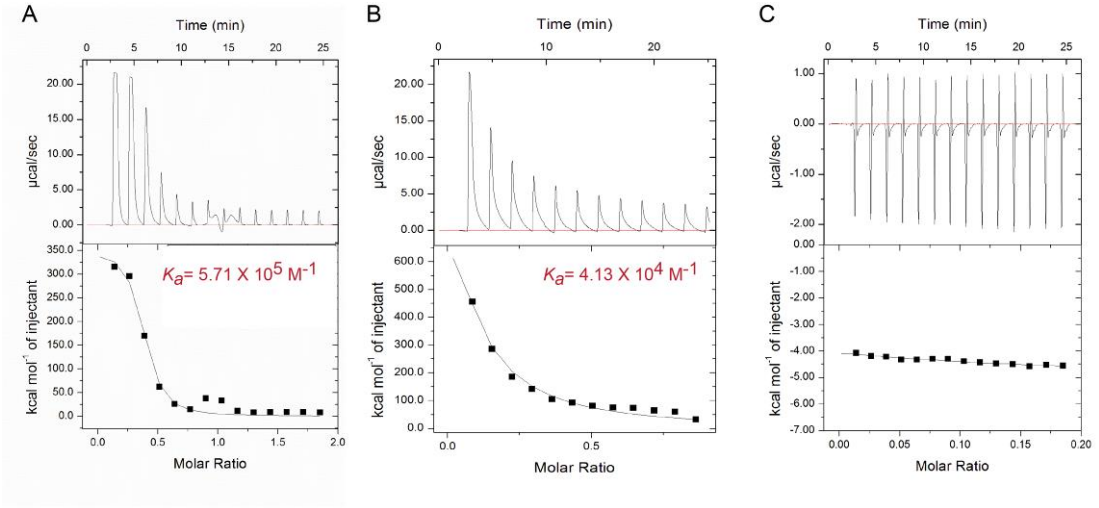


**Figure 2.7.** (A) Binding isotherm in presence of *P. pentosaceus* CRA51 SLP-$Ca^{2+}$ complex with $PO_4^{3-}$ ion. (B) Binding isotherm of $Ca^{2+}$ and $PO_4^{3-}$ ions in the absence of SLP. (C) Interaction between *P. pentosaceus* CRA51 SLP and $PO_4^{3-}$ ion.

## 2.4. Significant Findings

The salient findings of the present study can be enlisted as follows:

1. Biomineralization-based generation of hydroxyapatite nanoparticles (HANPs) was accomplished using the secreted protein extract of the LAB strains *L. plantarum* MTCC 1325, and *L. plantarum* CRA52 and *P. pentosaceus* CRA51.
2. FETEM and ImageJ analysis revealed that the average particle size of HANPs obtained from cell free supernatant of *L. plantarum* MTCC 1325 ranged from 75-100 nm, whereas in case of *L. plantarum* CRA52 and *P. pentosaceus* CRA51, the particle size was 50-60 nm.
3. FTIR analysis and powder XRD analysis validated the synthesis and crystallinity of HANPs.
4. ITC studies revealed that the secreted LAB protein (SLP) scaffold had a favorable impact in the biomineralization process for controlled crystal growth.

Although the extracellular protein extract of the LAB strains rendered biomineralization and synthesis of HANPs, the nature of the protein extract is complex and heterogenous as it is a mixture of several proteins. Hence, to acquire a mechanistic insight of the mineralization process, the role of individual secreted proteins in HANP synthesis is reported in the next chapter. Generation of an HANP-antibiotic nanocomposite for antibiofilm application is also described in the next chapter.

# Chapter 3

## Mechanistic Studies on the Role of Extracellular LAB Proteins in HANP Synthesis and Generation of HANP- Nanocomposite for Antibiofilm Application

*This chapter elucidates the potential of the individual proteins present in the cell free protein extract of LAB strains to serve as a mineralization template for synthesis of hydroxyapatite nanoparticles. Generation of an antibiotic-loaded hydroxyapatite nanocomposite for antibacterial and antibiofilm application is also illustrated.*

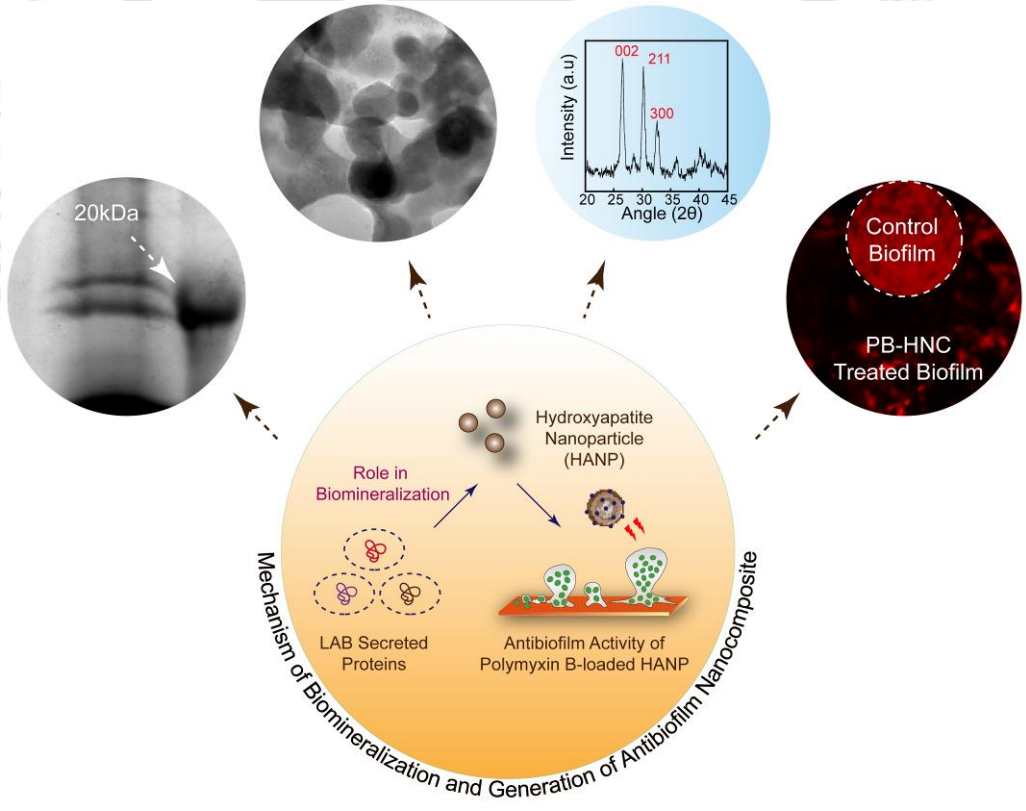

# ABSTRACT

The study highlighted in this chapter provides a mechanistic insight on the role of the individual secreted protein(s) present in the cell free extract of *L. plantarum* MTCC 1325, *L. plantarum* CRA52 and *P. pentosaceus* CRA51 in biomineralization for generation of HANPs. The major proteins present in the cell free extract of *L. plantarum* MTCC 1325, *L. plantarum* CRA52 and *P. pentosaceus* CRA51 were detected by SDS-PAGE analysis. The three major proteins from *L. plantarum* MTCC 1325 were ~75 kDa, ~25 kDa and ~20 kDa in size and these proteins were eluted from the gel as separate protein fractions (PF1-PF3). FTIR analysis of HANPs synthesized separately using the three eluted protein fractions from *L. plantarum* MTCC 1325 revealed that the characteristic peaks corresponding to stretching frequency of $OH^-$ (3568 $cm^{-1}$), $CO_3^{2-}$ (1461 $cm^{-1}$) and $PO_4^{3-}$ (1041 $cm^{-1}$) was only observed for HANPs derived from the ~20 kDa protein, which suggested that this protein perhaps served as a mineralization template and rendered HANP synthesis. FETEM analysis indicated that the HANPs obtained from the ~20 kDa protein of *L. plantarum* MTCC 1325 were spherical in shape with a particle size of 40-60 nm, while powder XRD and SAED pattern analysis confirmed the crystalline nature of the HANPs. In case of *P. pentosaceus* CRA51, powder XRD analysis and SAED pattern indicated that only the HANPs obtained from the crude extract and the ~43 kDa protein fraction were crystalline in nature. In order the explore the prospect of the synthesized HANPs in antibacterial applications, polymyxin B (PB)-loaded hydroxyapatite nanocomposite (PB-HNC) was generated. A notable decrease in the viability of *P. aeruginosa* MTCC 2488 cells (upto 2.0 $Log_{10}$ CFU) was observed upon treatment with PB-HNCs loaded with 10 µM PB. The ability of PB-HNC to inhibit as well as eradicate *P. aeruginosa* MTCC 2488 biofilm was validated by MTT assay, crystal violet assay as well as fluorescence microscope analysis. Interestingly, it was observed that PB-HNC was non-toxic to cultured HEK 293 cells at concentrations equivalent to its $BIC_{50}$ (75 µM) and $BEC_{50}$ (150 µM) against *P. aeruginosa* MTCC 2488 biofilm.

### 3.1. Introduction

Nanoscale hydroxyapatite has elicited enormous interest owing to its versatile application potential in healthcare. In the context of biomedical applications, it is paramount that non-toxic and environment friendly methods are adopted for the synthesis of hydroxyapatite nanoparticles (HANPs). Herein, it was demonstrated in the previous investigation described in Chapter 2 that the secreted protein(s) from a beneficial and GRAS microbe such as LAB can serve as mineralization templates and render facile synthesis of HANPs. The precise role of proteins in the biosynthesis of inorganic nanomaterials have also been highlighted in previous studies (Das *et al*., 2012; Jain *et al*., 2011; Bansal *et al*., 2004; Yang *et al*., 2017; Veiga *et al*., 2020). Given the native heterogeneity of the LAB cell-free protein extracts, it is pertinent to analyze the proteins and unravel their role(s) in the mineralization process during HANP synthesis.

Nanoscale hydroxyapatite has come of age especially as a functional material for bone tissue engineering, implant coating and in drug delivery (Haider *et al*., 2017; Brokesh and Gaharwar, 2020; Szczes *et al*., 2017). Fabrication of bactericidal nanocomposites based on hydroxyapatite have also been highlighted in recent studies. Emerging literature reports indicate that metal doped-hydroxyapatite exhibit osteogenic attributes and display antibacterial activity against *Staphylococcus aureus* and *Escherichia coli* (Shu *et al*., 2020; Karunakaran *et al*., 2019; Sathishkumar *et al*., 2016). *Pseudomonas aeruginosa* is an opportunistic human pathogen, which is implicated in serious life-threatening diseases (Bentzmann and Plesiat, 2011; Saedi *et al*., 2011; Breidenstein *et al*. 2011; Ang *et al*. 2016; Arevalo-Ferro *et al*., 2003). *P. aeruginosa* displays inherent resistance against antibiotics and biofilm formation by this pathogen poses an additional therapeutic challenge (Lambert, 2002; Tseng *et al*., 2013; Walters *et al*., 2003; Purdy Drew *et al*., 2009). It has been reported in literature that the antibiotic polymyxin B holds considerable promise in mitigation of *P. aeruginosa* cells as well as biofilm (Lim *et al*., 2011, Tam *et al*., 2005, Berditsch *et al*., 2015; Billings *et al*. 2013; Da Silva Carvalho and Perez, 2019).

Based on the aforementioned tenet, this chapter deciphers the role of the individual protein(s) present in the cell free extract of LAB strains in biomineralization for generation of HANPs. Generation of a polymyxin B-loaded hydroxyapatite nanocarrier (PB-HNC) for alleviation of *P. aeruginosa* biofilm is also described in this chapter.

## 3.2. Materials and Methods

### *3.2.1. Reagents and Growth Media*

Sodium dodecyl sulphate (SDS), glycine, trypsin-EDTA, 5 (and 6) carboxyfluorescein diacetate succinimidyl ester (cFDA-SE), congo red, propidium iodide, polymyxin B, potassium bromide, Dulbecco's Modified Eagle Medium (DMEM), 3-(4,5-dimethyl-2-thiazolyl)-2,5-diphenyl-2H-tetrazolium bromide (MTT) and 1-N-phenylnaphthylamine (NPN) were obtained from Sigma Aldrich, USA. Dimethyl sulfoxide (DMSO), acetic acid glacial, methanol and absolute ethanol were obtained from Merck (India). Nutrient broth (NB) and crystal violet were procured from HiMedia, Mumbai, India. N-2-hydroxyethyl piperazine N-2 ethanesulfonic acid (HEPES buffer), Coomassie Brilliant Blue R-250 and pre-stained high range protein marker was procured from Sisco Research Laboratories (SRL), Mumbai, India.

### *3.2.2. Bacterial Strains*

*Lactobacillus plantarum* MTCC 1325 (*L. plantarum* MTCC 1325), *Lactobacillus plantarum* CRA52 (*L. plantarum* CRA52) and *Pediococcus pentosaceus* CRA51 (*P. pentosaceus* CRA51) was grown in MRS broth at 37°C for 18 h under static condition. *P. aeruginosa* MTCC 2488 bacteria was grown in NB broth at 37 °C and 180 rpm for 12 h. Prior to experiments, the bacterial strains were revived from frozen stocks and subcultured.

### *3.2.3. Analysis of Secreted LAB Protein (SLP) Extract*

The SLPs were obtained from *L. plantarum* MTCC 1325, *L. plantarum* CRA52 and *P. pentosaceus* CRA51 as mentioned in section 2.2.3 of Chapter 2. The SLPs were then subjected to SDS-PAGE analysis. SLPs from the LAB strain (20 µg/mL) were loaded on a 12% denaturing gel and a pre-stained high range protein marker was also run along with the protein samples. After completion of electrophoresis, the gel was stained with Coomassie Brilliant Blue R-250 dye for 4 h in a rocker and destained with methanol: acetic acid (25:10 v/v) solution. The image of the destained gel was captured in a Geldoc system (BioRad, USA).

### *3.2.4. Gel Extraction of Secreted LAB Protein (SLP) Extract*

The prominent protein bands observed for the LAB SLPs in the SDS-PAGE analysis were extracted using IN-GEL digest protocol (Sigma, USA), without using trypsin

enzyme. The gel eluted protein fractions (PFs) were lyophilized and the concentration of protein in each fraction was estimated by Bradford's reagent.

*3.2.5. Analysis of Protein Fraction 3 (PF3) Obtained from SLPs of L. plantarum MTCC 1325*

An aliquot of the SLP and gel eluted protein fraction 3 (PF3) (both in sterile MilliQ water) obtained from *L. plantarum* MTCC 1325 was subjected to reverse phase HPLC analysis (PerkinElmer Analytical HPLC system, USA). The concentration of SLP and PF3 loaded onto the HPLC column was 20 µg/mL and 14 µg/mL, respectively. An analytical reverse phase HPLC column (Agilent Analytical C18 column) was used in conjunction with series 200 HPLC pump and series 200 UV/vis detector. The solvent system consisted of solvent A (0.1% TFA in MilliQ water) and solvent B (0.1% TFA in acetonitrile), each at a flow rate of 1.0 mL/min. The operating conditions were: 0 to 5 minutes 5% solvent A, 5 to 60 minutes a gradient of 5% to 95% solvent B. The eluted fractions were pooled from multiple runs and the solvent was evaporated in a SpeedVac concentrator (Eppendorf). The fractions were finally resuspended in sterile MilliQ water. Circular Dichroism (CD) spectra of PF3 (14 µg/mL in sterile MilliQ water) obtained from *L. plantarum* MTCC 1325 was measured from 180-300 nm in a spectropolarimeter (JASCO, J-815) with a 5.0 mm path length cuvette at 25ºC. Sterile MilliQ water was used to calibrate the baseline of the instrument. For every sample, CD spectra was recorded from three independent samples, wherein three scans were performed for every sample and the average was considered to enhance the signal-to-noise ratio. CD spectra was expressed in terms of milli degree (mdeg).

*3.2.6. Generation of HANPs with Protein Fractions (PFs) Obtained from SLPs of LAB*

The proteins fractions (PFs) obtained from SLPs of *L. plantarum* MTCC 1325 and *P. pentosaceus* CRA51 were used as templates for HANP synthesis by essentially following the wet precipitation method mentioned in section 2.2.4 of Chapter 2. The synthesized HANPs were characterized by FTIR, PXRD, FETEM, HR-TEM and SAED pattern analysis by following the protocols that are already described in section 2.2.5.1 and 2.2.5.3 of Chapter 2. The hydrodynamic radius of HANPs was also estimated by DLS analysis. Briefly, 1.0 mg/ml HANP was resuspended in sterile MilliQ water and a 0.1 ml aliquot of the solution was again dispersed in 1.0 ml sterile

MilliQ water and subjected to DLS analysis (Zetasizer, Malvern, UK). The experiments were run in three independent sets with three replicate scans.

*3.2.7. Polymyxin B-loaded Hydroxyapatite Nanocarrier (PB-HNC)*

For generation of polymyxin B (PB)-loaded hydroxyapatite nanocarrier (PB-HNC), HANPs (1.0 mg/ml resuspended in sterile MilliQ water) were incubated overnight with various concentrations of PB (25-800 µM) on a rocker at room temperature. After incubation, the solution was centrifuged at 10000 rpm for 5 min and the pellet was resuspended in sterile MilliQ water. The total volume of the solution was maintained at 0.5 mL. Subsequently, the solution was centrifuged at 10,000 rpm for 5.0 min. The supernatant from various samples was aspirated and taken in a fresh microcentrifuge tube, and the amount of polymyxin B in these samples was ascertained by following an activity-based NPN assay (Goswami *et al*., 2013). A previously generated calibration curve for polymyxin B obtained in an NPN assay was used to measure the quantity of the antibiotic adsorbed onto HANPs and for ascertaining the adsorption capacity ($q_e$) of HANPs (Saha *et al*., 2011).

*3.2.8. In Vitro Release Kinetics of Polymyxin B from PB-HNC*

PB-HNCs (1.0 mg/mL HANPs loaded with 300 µM polymyxin B) were dispersed in separate sets in 1.0 ml of (a) 10 mM HEPES buffer (pH 7.4), (b) 100 mM citrate buffer (pH 3.0), and (c) simulated body fluid (SBF) (pH 7.4). The composition of SBF was as described in an earlier study (Kokubo *et al*., 1990). The samples were incubated in a shaker at 120 rpm at 37°C, and at specific time periods (1, 3, 6, 12, 24, and 48 h) the samples were withdrawn, centrifuged at 10000 rpm for 5 min and the supernatant was collected. For each sample, the amount of PB released from PB-HNC was ascertained by measuring the amount of the antibiotic released in the supernatant by an activity-based NPN assay as mentioned before (Goswami *et al*., 2013) and expressed as % cumulative release.

*3.2.9. Minimum Inhibitory Concentration (MIC) and Minimum Killing Concentration (MKC) of PB-HNC*

*P. aeruginosa* MTCC 2488 was inoculated at 1% level in microtiter wells having NB medium and grown overnight at 37°C and 180 rpm in presence of PB-HNC having varying concentrations of loaded polymyxin B. PB-HNC used in these experiments

consisted of 1.0 mg/mL HANP loaded with 0.18 μM - 400 μM polymyxin B. In a parallel set, cells were also grown in presence of only polymyxin B at similar concentrations (0.18 μM- 400 μM). Following incubation, the growth of *P. aeruginosa* MTCC 2488 was ascertained by measuring absorbance at 600 nm in a microtiter plate reader (Infinite M200, TECAN, Switzerland). MIC of PB-HNC or polymyxin B was denoted as the lowest concentration of the antibiotic (present either in PB-HNC or singularly), which prevented cell growth and yielded an absorbance ($A_{600}$) reading of <0.1. An aliquot (1% v/v) from all the wells, where the target bacteria failed to grow ($A_{600}$ <0.1) was aspirated and used to re-inoculate separate microtitre wells having fresh NB medium and incubated overnight at 37°C and 180 rpm, without any further addition of either PB-HNC or polymyxin B singularly. MKC of PB-HNC or polymyxin B was considered as the lowest concentration of the antibiotic that inhibited the growth of *P. aeruginosa* MTCC 2488 cells following re-inoculation ($A_{600}$ <0.1). The MIC and MKC of PB-HNC and polymyxin B against *P. aeruginosa* MTCC 2488 was determined from three independent experiments, each having three replicas. Data analysis and calculation of standard deviation was performed with Microsoft Excel 2010 (Microsoft Corporation, USA). A schematic illustrating the protocol to determine MIC and MKC of PB-HNC is depicted in Scheme 3.1.

### *3.2.10. Antibacterial Activity of PB-HNC*

#### *3.2.10.1. Time Kill Curve*

Overnight grown cells of *P. aeruginosa* MTCC 2488 were harvested by centrifugation, washed twice with sterile phosphate buffered saline (PBS) and resuspended in the same ($10^6$ CFU/mL). The cell suspension was then incubated with HANPs (1.0 mg/mL) or 10 μM polymyxin B or PB-HNC (1.0 mg/mL HANP loaded with 10 μM polymyxin B) in separate sets at 37°C and 180 rpm. At intermittent time periods (3 h, 6 h, 12 h and 24 h), an aliquot (0.1 mL) from each of these samples was subjected to serial dilution and plating in NB-agar medium. The plates were incubated at 37°C for 24 h and the colonies were enumerated to ascertain the viable cell number ($Log_{10}$ CFU/mL) for each sample. The viable cell count was also determined for cells suspended in PBS alone or cells treated with only HANPs. Viable cell count was determined from three independent experiments, each having three replicas. Data analysis and calculation of standard deviation was performed with Microsoft Excel 2010 (Microsoft Corporation, USA).

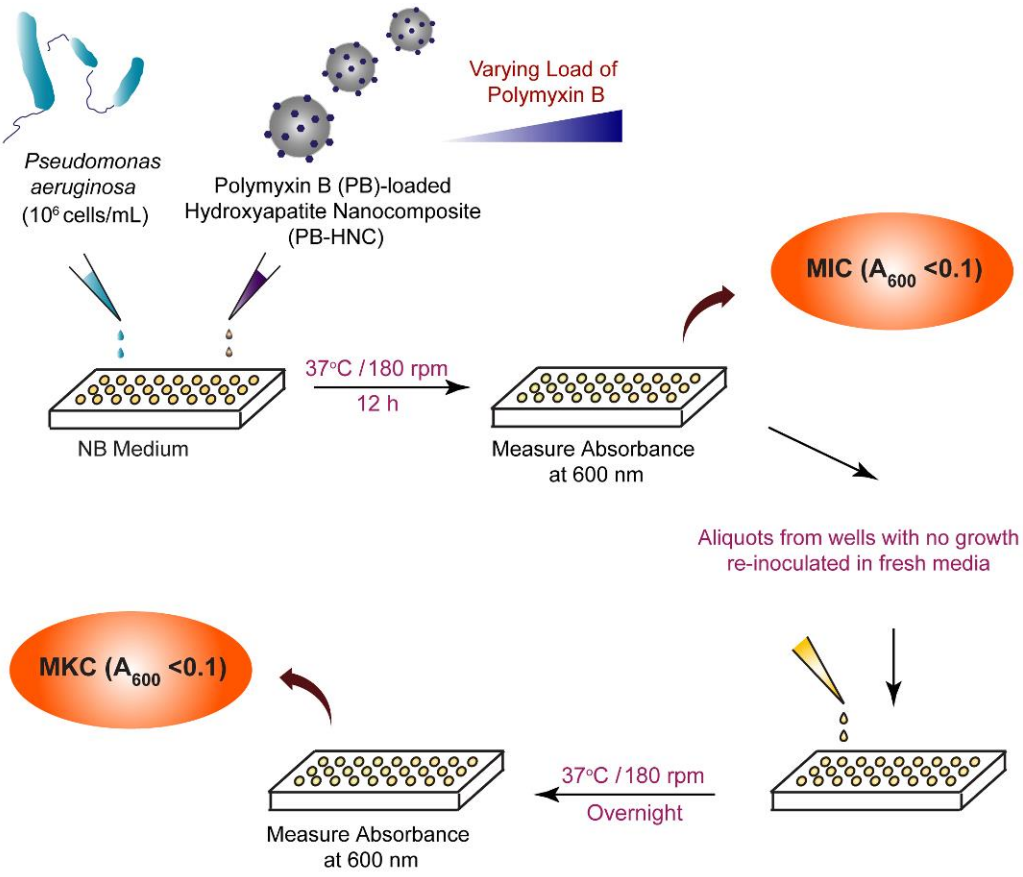


**Scheme 3.1.** Schematic representation of the protocol used for estimation of minimum inhibitory concentration (MIC) and minimum killing concentration (MKC) of PB-HNC against *Pseudomonas aeruginosa* MTCC 2488.

*3.2.10.2. cFDA-SE Leakage Assay and PI Uptake Assay*

Overnight grown cells of *P. aeruginosa* MTCC 2488 were centrifuged at 8000 rpm for 3 min. The cell pellet was washed twice with sterile phosphate buffer, resuspended in the same and labelled with cFDA-SE (final concentration of 50 µM) at 37°C for 20 min. Following incubation, the cells were again centrifuged at 8000 rpm for 3 min followed by washing twice with sterile phosphate buffer to wash off the excess dye. cFDA-SE labelled cells were then treated with (a) PB-HNC (1.0 mg/mL HANP loaded with 10 µM polymyxin B) or (b) polymyxin B alone (10 µM) or (c) HANP alone (1.0 mg/mL) in separate sets for 3 h. Following treatment, the cells were centrifuged at 8000 rpm for 3 min. The fluorescence of the cell free supernatant was measured at an excitation wavelength of 488 nm and emission wavelength of 518 nm in a spectrofluorometer (FluoroMax-3, HORIBA) in order to ascertain the leakage of

carboxyfluorescein from the treated cells. The fluorescence measurements were noted after deducting the fluorescence of effluxed dye from control samples. For each treated and control sample, fluorescence measurements were performed for three independent experimental samples, each having three replicas. A schematic representation of the cFDA-SE leakage assay is shown in Scheme 3.2.

For conducting PI uptake assay, *P. aeruginosa* MTCC 2488 cells were grown overnight and centrifuged at 8000 rpm for 3 min. The cell pellet was washed twice in sterile PBS (pH 7.4) and resuspended in the same. The cell suspension was treated in separate sets with (a) PB-HNC (1.0 mg/mL HANP loaded with 10 μM polymyxin B) or (b) polymyxin B alone (10 μM) or (c) HANP alone (1.0 mg/mL) for 3 h. Subsequently, the cells were washed with sterile PBS, resuspended in the same and incubated with PI (final concentration of 30 μM) for 30 min at 37°C in a circulating water bath incubator (Amersham, USA). Following incubation, the cells were centrifuged and the excess dye was removed by washing the cells with sterile PBS. The washed cells were subsequently resuspended in sterile PBS and their fluorescence was measured in a spectrofluorometer (FluoroMax-3, HORIBA) at an excitation wavelength of 535 nm and emission wavelength of 617 nm. The fluorescence emission intensity values obtained for untreated cells were subtracted from all experimental values. For each treated and control sample, fluorescence measurements were performed for three independent experimental samples, each having three replicas. A schematic representation of the PI uptake assay is shown in Scheme 3.3.

*3.2.10.3. Microscopic Analysis*

*P. aeruginosa* MTCC 2488 cells (~$10^6$ CFU/mL suspended in sterile PBS) were treated with PB-HNC (1.0 mg/mL HANP loaded with 10 μM polymyxin B) for 6 h. In a parallel control experiment, *P. aeruginosa* MTCC 2488 cells were also grown as control for 6 h. A 5.0 μL aliquot of the target cells treated with PB-HNC or the untreated cells was spotted on separate carbon coated TEM grid (Pacific Grid, USA) and air-dried in a laminar hood. The samples were then subjected to FETEM analysis (JEOL 2100F, Japan) and their images were recorded.

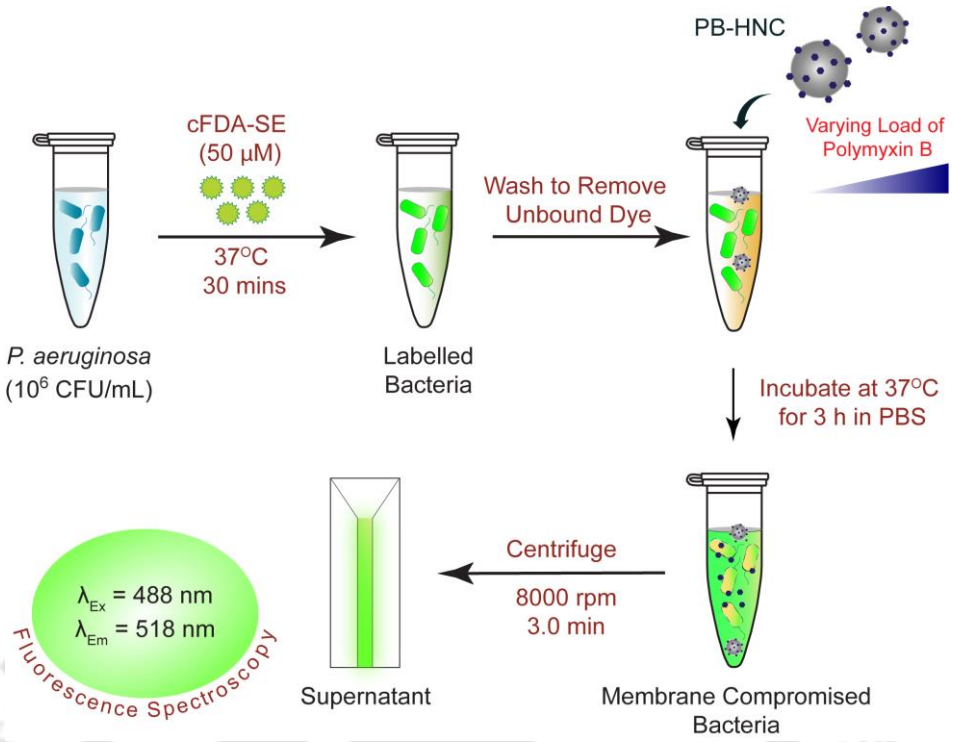


**Scheme 3.2.** Schematic representation of cFDA-SE leakage assay to determine the antibacterial activity of PB-HNC against *Pseudomonas aeruginosa* MTCC 2488.

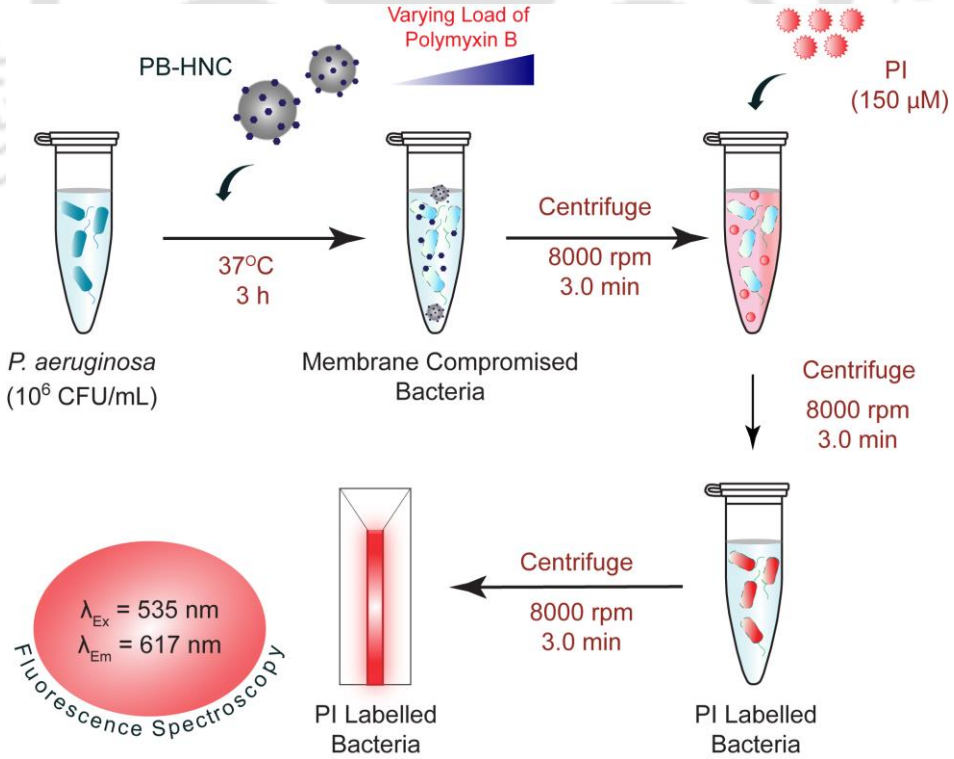


**Scheme 3.3.** Schematic representation of PI uptake assay to estimate the antibacterial activity of PB-HNC against *Pseudomonas aeruginosa* MTCC 2488.

*3.2.11. Antibiofilm Activity of PB-HNC*

*3.2.11.1. Estimation of Biofilm Metabolic Activity by MTT Assay*

*P. aeruginosa* biofilm was grown in NB media taken in a 96 well microtitre plate in static and humid condition at 37°C by essentially following a previously described method (Goswami *et al*., 2014). *P. aeruginosa* MTCC 2488 was grown in presence of PB-HNC in separate sets. The PB-HNC used in the separate sets consisted of 1.0 mg/mL HANP loaded with varying concentrations of polymyxin B (25 μM, 50 μM, 75 μM, 100 μM, 150 μM, 200 μM, 300 μM and 400 μM). Following 24 h of biofilm growth, the microtitre well plate was placed in a laminar hood and the spent media was aspirated gently and the wells were washed thrice with 200 μL of sterile PBS to remove the free non-adherent planktonic cells. The biofilm metabolic activity was then determined by MTT assay as described in an earlier study (Goswami *et al*., 2014). In the MTT assay, untreated *P. aeruginosa* biofilm was considered as the control sample. The absorbance obtained for control samples (untreated biofilm) was considered to represent 100% biofilm metabolic activity, whereas the absorbance for PB-HNC treated biofilm was compared to that of the control samples in order to determine % biofilm metabolic activity. The minimum concentration of PB-HNC which resulted in 50% inhibition in *P. aeruginosa* MTCC 2488 biofilm metabolic activity ($BIC_{50}$) as compared to untreated control sample was determined. All the experiments were performed in three independent sets and every set consisted of three replicates. Data analysis and calculation of standard deviation was performed with Microsoft Excel 2010 (Microsoft Corporation, USA).

In a separate experiment, pre-grown *P. aeruginosa* MTCC 2488 biofilm (grown in 96 well microtitre plate for 24 h) was treated in separate sets with PB-HNC for 24 h. As mentioned previously, PB-HNC used in the separate sets consisted of 1.0 mg/mL HANP loaded with varying concentrations of polymyxin B (25 μM, 50 μM, 75 μM, 100 μM, 150 μM, 200 μM, 300 μM and 400 μM). Subsequently, biofilm metabolic activity was estimated by MTT assay as mentioned previously. In the MTT assay, untreated *P. aeruginosa* biofilm was considered as the control sample. The absorbance obtained for control samples (untreated biofilm) was considered to represent 100% biofilm metabolic activity, whereas the absorbance for PB-HNC treated biofilm was compared to that of the control samples in order to determine % biofilm metabolic activity. The minimum concentration of PB-HNC which resulted in 50% eradication of pre-grown *P. aeruginosa* MTCC 2488 biofilm ($BEC_{50}$) as observed

from 50% decrease in biofilm metabolic activity compared to untreated control sample was also ascertained. All the experiments were performed in three independent sets and every set consisted of three replicates. Data analysis and calculation of standard deviation was performed with Microsoft Excel 2010 (Microsoft Corporation, USA). A schematic representation of the MTT assay performed to estimate metabolic activity of biofilm is shown in Scheme 3.4.

*3.2.11.2. Estimation of Biofilm Biomass by Crystal Violet Staining*

In separate sets, biofilm of *P. aeruginosa* MTCC 2488 was grown in 96 well microtitre plate in static and humid condition at 37°C for 24 h in presence of PB-HNC. Herein, PB-HNC used in the separate sets consisted of 1.0 mg/mL HANP loaded with varying concentrations of polymyxin B (25 μM, 50 μM, 75 μM, 100 μM, 150 μM, 200 μM, 300 μM and 400 μM). Following incubation, the microtitre well plate was placed in a laminar hood and the spent media was aspirated gently and the wells were washed thrice with 200 μL of sterile PBS to remove the free non-adherent planktonic cells. Subsequently, 1% (v/v) crystal violet solution (150 μl) was added to each well and incubated for 45 min to stain the biofilm. The crystal violet stain impregnated in biofilm was then solubilized with 95% ethanol (200 μl) and the biofilm biomass (%) was determined by aspirating the ethanol-solubilized dye solution from each well into fresh well and measuring absorbance at 595 nm in a microtiter plate reader (Infinite M200, TECAN, Switzerland). All the experiments were performed in three independent sets and every set consisted of three replicates. Data analysis and calculation of standard deviation was performed with Microsoft Excel 2010 (Microsoft Corporation, USA). A schematic representation of the crystal violet assay for estimation of biofilm biomass is shown in Scheme 3.4.

*3.2.11.3. Fluorescence Microscope Analysis*

Biofilm of *P. aeruginosa* MTCC 2488 was grown in sterile 96 well microtitre plate as described previously. The biofilm samples were then treated with PB-HNC (1.0 mg/mL HANP loaded with 100 μM polymyxin B) for 24 h. Subsequently, control (untreated)

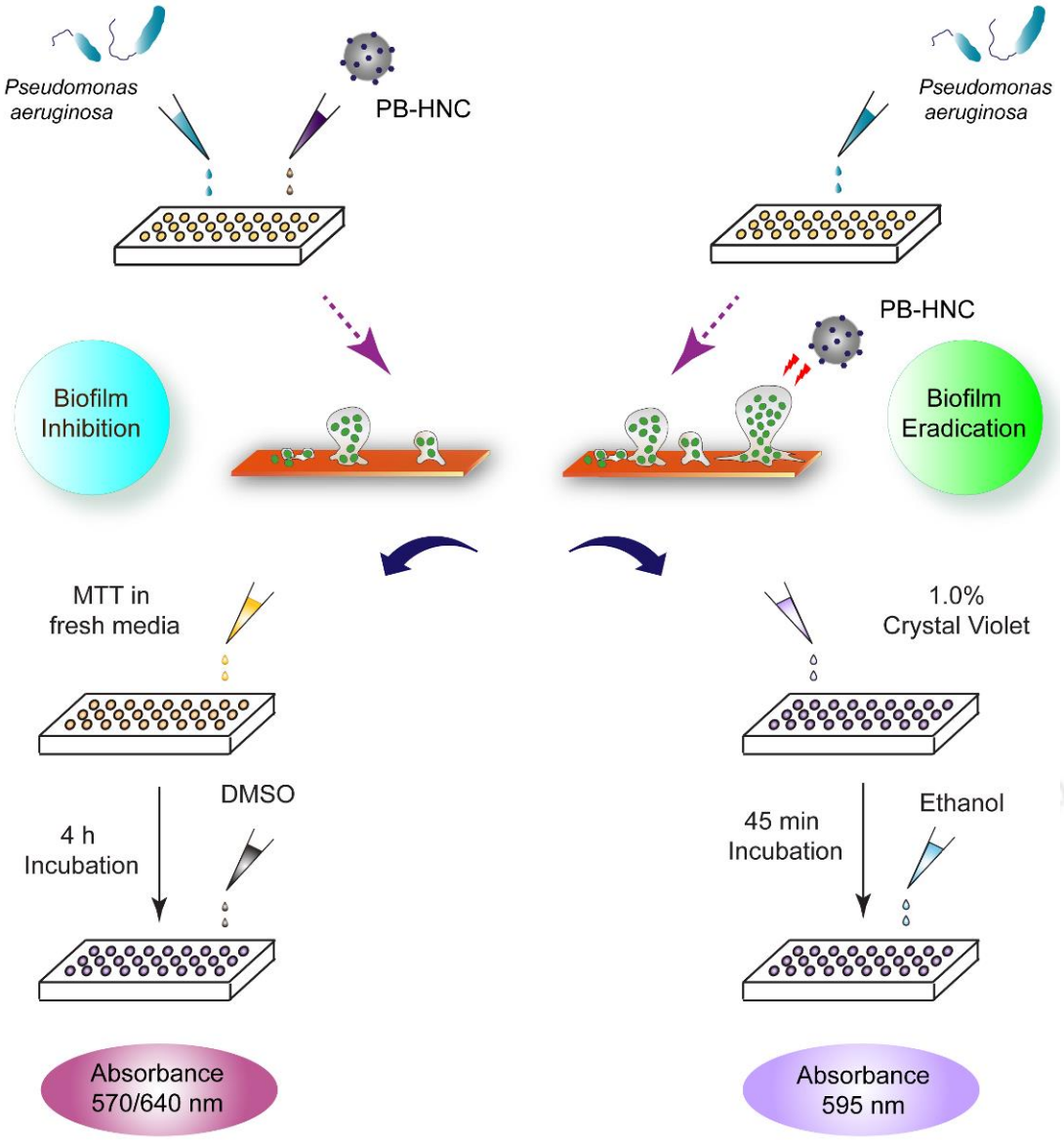


**Scheme 3.4.** Schematic representation of the protocol for MTT assay and crystal violet assay to ascertain the activity of PB-HNC against *Pseudomonas aeruginosa* MTCC 2488 biofilm.

as well as treated biofilm samples were separately labelled with cFDA-SE and congo red (CR) by following a previously described method (Goswami *et al*., 2014). The stained biofilms were then observed under a fluorescence microscope (Eclipse Ti-U, Nikon) with a filter that allowed blue light excitation for cFDA-SE and green light excitation for CR stained cells. Images of the treated and control biofilms were recorded.

*3.2.12. Cytotoxic Effect of PB-HNC*

The *in vitro* cytotoxic effect of PB-HNC was ascertained against cultured human embryonic kidney cell line (HEK 293 cells) by a standard MTT assay. HEK 293 cells were grown in tissue culture flask and then seeded onto 96-well tissue culture plates at a density of $10^4$ cells per well by following a previously described method (Goswami *et al*., 2013). The seeded HEK 293 cells were then treated in separate sets with PB-HNC (1.0 mg/mL HANP loaded with PB in the range of 0.325−400 μM) in DMEM, for a period of 24 h. Following incubation for 24 h and removal of the media, fresh DMEM having MTT solution was added to the wells and further incubated for 4 h at 37°C. The media was removed and DMSO was added to solubilize the insoluble formazan product. The absorbance of the solution was then measured in a microtiter plate reader at 570 nm against a reference of 640 nm. The absorbance obtained for the untreated control samples represented 100% cell viability. The absorbance obtained for the treated cells was compared to the control to ascertain the % cell viability. The MTT assay was conducted in six independent sets, with each set having three replicas. Data analysis and calculation of standard deviation was performed with Microsoft Excel 2010 (Microsoft Corporation, USA).

## 3.3. Results and Discussion

*3.3.1. Analysis of Proteins in SLP Extract*

It was evident in Chapter 2 that the secreted LAB protein (SLP) extract from the LAB strains *L. plantarum* MTCC 1325, *L. plantarum* CRA52 and *P. pentosaceus* CRA51 could be used as a biomineralization template for the generation of HANPs. However, given the inherent heterogeneity of the LAB cell-free protein extracts, it was pertinent to analyze the proteins and unravel their role(s) in the mineralization process in order to provide a guideline to select appropriate bio-macromolecular templates for nucleation and generation of HANPs. Hence, to identify the protein(s) present in the SLP extract, SDS-PAGE analysis was conducted. In case of *L. plantarum* MTCC 1325, the major proteins present in the SLP extracts were ~75 kDa, ~25 kDa and ~20 kDa in size (Figure 3.1, lane 1). The major proteins present in the SLP extract of *L. plantarum* CRA52 were ~25 kDa and ~20 kDa in size (Figure 3.1, lane 2), while the corresponding major proteins detected in the SLP extract of *P. pentosaceus* CRA51 were ~95 kDa and ~43 kDa in size (Figure 3.1, lane 3).

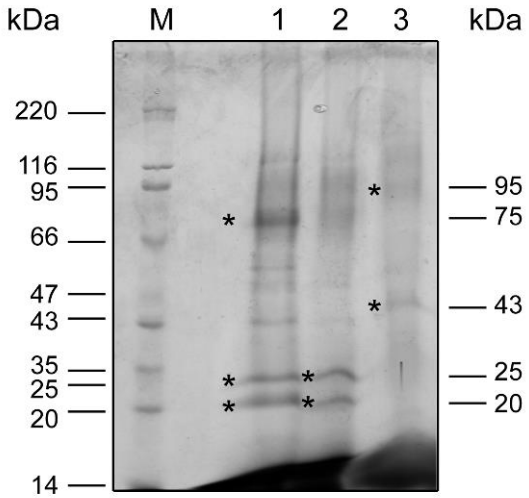


**Figure 3.1.** SDS-PAGE analysis of secreted LAB protein (SLP) extract. Lane 1: *L. plantarum* MTCC 1325. Lane 2: *L. plantarum* CRA52. Lane 3: *P. pentosaceus* CRA51. * indicates the major protein bands identified in the respective SLPs.

*3.3.2. Generation of HANPs Using Fractionated Protein of SLP Extract*

In order to ascertain whether the individual proteins present in SLP extract of *L. plantarum* MTCC 1325 could render template-directed HANP synthesis, the three major protein bands corresponding to ~75 kDa, ~25 kDa and ~20 kDa protein were individually eluted following SDS-PAGE analysis of SLP. The eluted proteins were referred to as protein fractions 1-3 (PF1-3) and they were used individually in separate sets as a template for HANP synthesis by following the wet precipitation method described earlier in Chapter 2. FTIR analysis revealed that HANPs obtained from PF3 (~20 kDa protein) revealed characteristic peaks at 3568 $cm^{-1}$, 1461 $cm^{-1}$ and 1041 $cm^{-1}$ corresponding to $OH^-$, $CO_3^{2-}$, and $PO_4^{3-}$ stretching frequency, respectively (Figure 3.2A), which indicated that the ~20 kDa protein present in the SLP extract of *L. plantarum* MTCC 1325 supported the generation of HANPs through biomineralization. The typical FTIR peaks indicative of HANP synthesis (3568 $cm^{-1}$, 1461 $cm^{-1}$ and 1041 $cm^{-1}$) were not prominent when PF1 (~25 kDa protein) or PF2 (~75 kDa protein) were used as templates in HANP synthesis (Figure A3.1, Appendix). The eluted protein fraction 3 (PF3) comprising of the ~20 KDa protein was evidenced as a single band on the gel (Figure 3.2B, lane 2). In HPLC, three prominent peaks (Peaks1-3) were obtained for the SLP extract of *L. plantarum* MTCC 1325, while PF3 present in the SLP revealed a single peak with a retention time of ~11.65 min, which was analogous to the retention time for peak 1 in the SLP extract (Figure 3.2C). Based

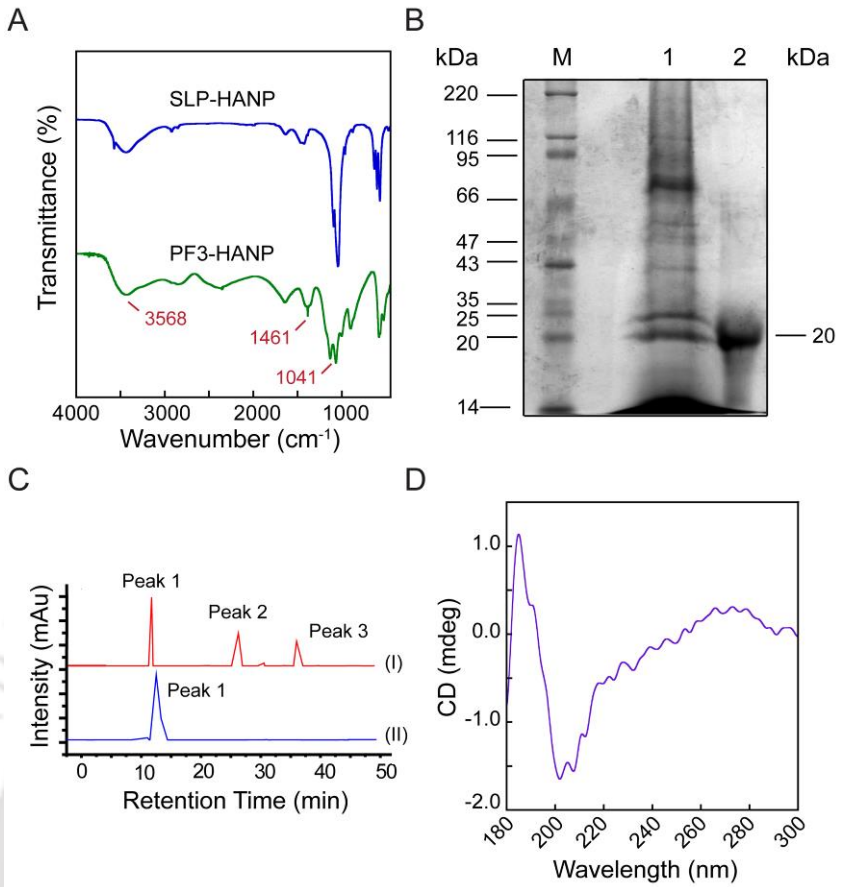


**Figure 3.2.** (A) FTIR analysis of HANPs obtained from SLP extract and gel-eluted PF3 from *L. plantarum* MTCC 1325. (B) SDS-PAGE analysis of the SLP extract (Lane 1) and the gel-eluted PF3 (Lane 2) obtained from *L. plantarum* MTCC 1325. (C) HPLC profile for SLP extract (Trace I) and the gel-eluted PF3 (Trace II) obtained from *L. plantarum* MTCC 1325. (D) CD analysis of purified PF3 obtained from *L. plantarum* MTCC 1325.

on this observation, it is likely that PF3 corresponded to the gel eluted ~20 kDa protein. CD analysis indicated that the ~20 kDa protein was essentially a β-sheet rich protein (~57%) (Figure 3.2D).

FETEM analysis of HANPs obtained from PF3 of *L. plantarum* MTCC 1325 showed that the NPs were spherical in shape with a particle size of 40-60 nm (Figure 3.3A, Panel (i)). The presence of prominent lattices in PF3-derived HANPs was captured in HR-TEM, wherein the lattice distance was ~0.37 nm (Figure 3.3A, Panel (ii)). The crystalline nature of the HANPS was evident from the SAED pattern (Figure 3.3A, Panel (iii)). DLS analysis revealed that the PF3-derived HANPs were ~354 nm in size (Figure 3.3B), while the crystalline nature of the HANPs was corroborated by powder XRD analysis, wherein the salient peaks observed at $2\theta = 26^0$, $31^0$ and $33^0$

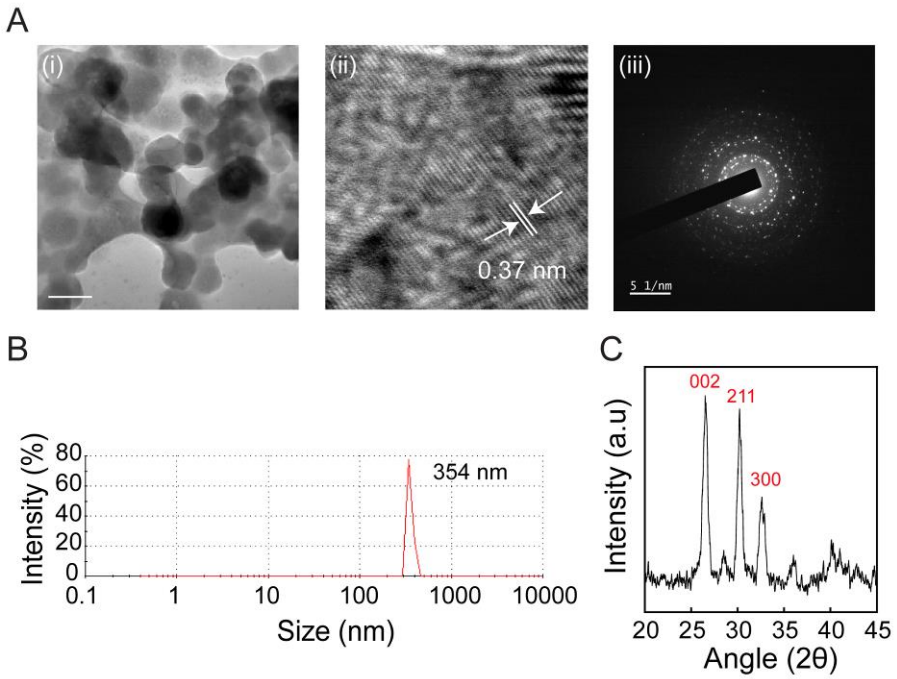


**Figure 3.3.** Characterization of HANPs synthesized from PF3 obtained from *L. plantarum* MTCC 1325. (A) (i) FETEM image analysis. Scale bar is 100 nm. (ii) HR-TEM analysis. (iii) SAED analysis. (B) DLS analysis. (C) powder XRD analysis.

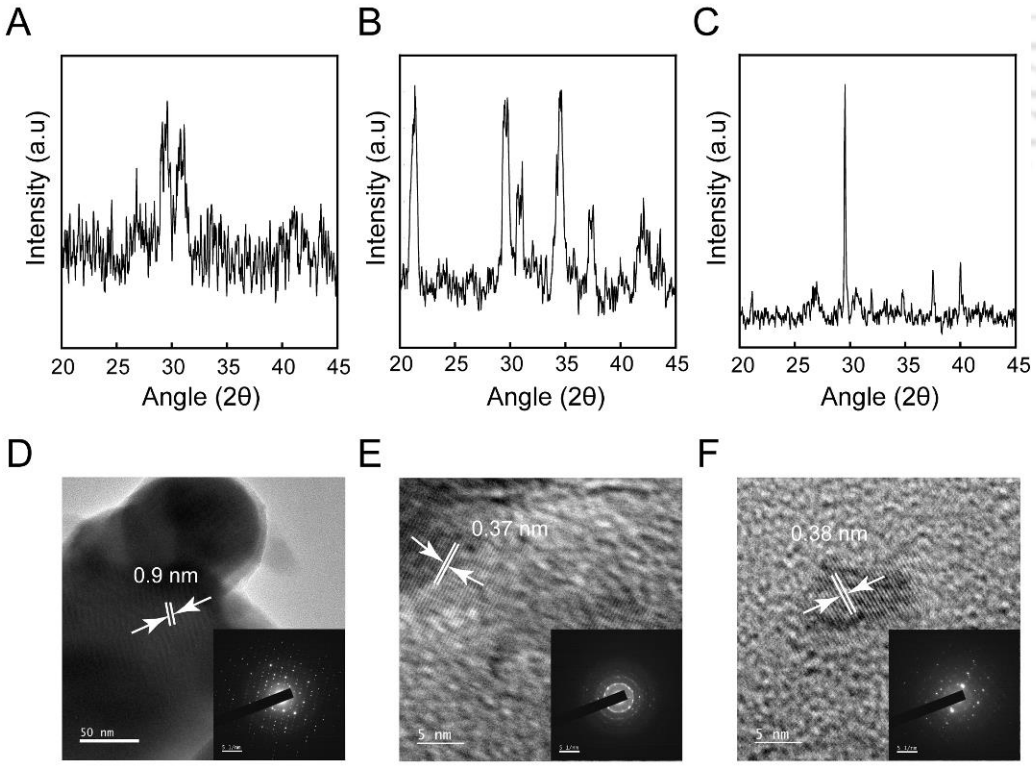


**Figure 3.4.** (A-C) Powder XRD analysis and (D-F) HR-TEM and SAED analysis (inset) of HANPs obtained from (A and D) SLP extract, (B and E) ~95 kDa protein fraction, (C and F) ~43 kDa protein fraction of *P. pentosaceus* CRA51.

(Figure 3.3C) corresponded to (002), (211) and (300) lattice planes, respectively (Gao *et al*., 2016). The major proteins (~95 kDa and ~43 kDa) present in *P. pentosaceus* CRA51 SLP extract were also eluted and used as template for HANP synthesis. Powder XRD analysis indicated that crystalline HANPs were obtained from SLP and ~43 kDa protein fraction (Figure 3.4A-C). HR-TEM analysis indicated that the HANPs obtained from SLP extract, ~95 kDa protein fraction and ~43 kDa fraction of *P. pentosaceus* CRA51 were oval in shape with lattice distances of 0.9 nm, 0.37 nm and 0.38 nm, respectively (Figure 3.4D-F). SAED patterns also indicated that HANPs obtained from SLP and ~43 kDa protein fraction were crystalline (Figure 3.4D-F, inset).

*3.3.3. Generation of Polymyxin B-loaded Hydroxyapatite Nanocomposite (PB-HNC)*

Nanoscale hydroxyapatite holds considerable potential for various biomedical applications such as bone tissue engineering scaffold, implant coating and as a drug delivery system (Szczes *et al*., 2017). In particular, owing to their biocompatibility, HANPs are of great interest as a drug delivery vehicle. For instance, generation of antibiotic-loaded HANPs can be perceived to render effective antibacterial applications and may thus hold merit as an implant coating. Based on this rationale, in the present study a polymyxin B (PB)-loaded hydroxyapatite nanocomposite (PB-HNC) was generated and its potential to hinder *Pseudomonas aeruginosa* biofilm formation was ascertained. *Pseudomonas aeruginosa* is an opportunistic human pathogen, that can cause a number of serious diseases (Breidenstein *et al.*, 2011; Ang *et al.*, 2016). Polymyxin B (PB) is a cationic peptide, with an established activity against Gram-negative bacteria (Zavascki *et al.*, 2007; Viljanen *et al.*, 1984) and PB is largely used to target *P. aeruginosa* (Tam *et al.* 2005; Berditsch *et al.*, 2015). In the present study, PB-HNC was generated by incubating HANPs obtained by mineralization of the SLP extract of *L. plantarum* MTCC 1325 with varying concentrations of PB for 12 h to render adsorption of the antibiotic. The adsorption of PB on HANPs measured in terms of the strength of adsorption ($q_e$) revealed a saturation effect at antibiotic concentrations in excess of 300 mg/L (Figure 3.5A). The adsorption isotherm parameters $Q_m$ and $b$ were around 500 mg/g and 10965 L/mg, respectively. It was also evident that adsorption of polymyxin B on HANPs followed a Langmuir isotherm model (Figure 3.5B). Prior to testing the potential of PB-HNC as an antibacterial agent, it was pertinent to determine whether the nanocomposite rendered favorable release of the antibiotic in a physiological buffer system. In this regard, a rapid release of the

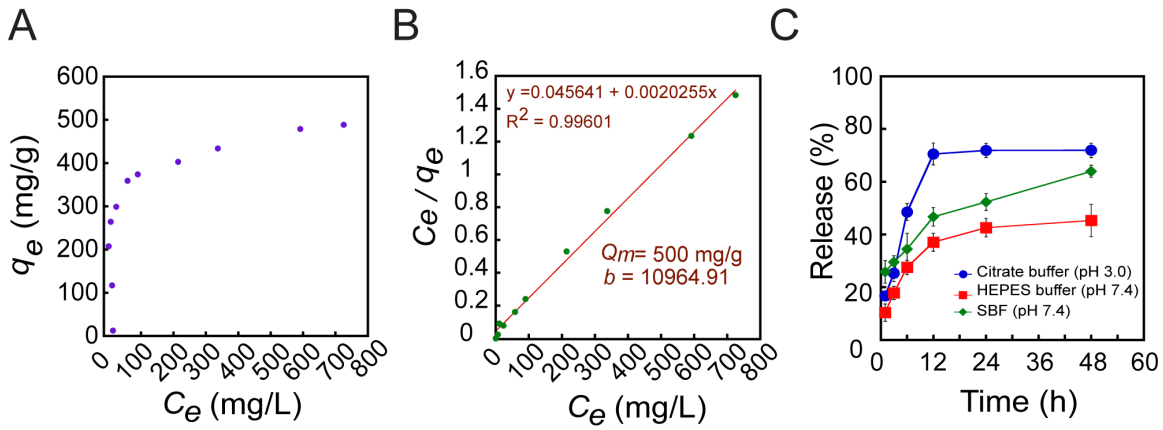


**Figure 3.5.** (A) Adsorption isotherm of polymyxin B on HANP. (B) Linear regression plot for estimation of adsorption isotherm parameters for polymyxin B. (C) *In vitro* release kinetics of polymyxin B from PB-HNC incubated in various buffers and simulated body fluid (SBF).

antibiotic, with a plateau of around 70% release was observed upon incubation of PB-HNC in citrate buffer (pH 3.0) for 48 h (Figure 3.5C). It may be mentioned that a sustained release profile of PB was observed with a cumulative release of around 40% following 48 h of incubation of PB-HNC in a buffer of physiological pH (HEPES buffer, pH 7.4) (Figure 3.5C). Akin to the release profile observed in HEPES buffer, a sustained release profile was also evident when PB-HNC was incubated in simulated body fluid (SBF) at pH 7.4, wherein a plateau was observed at around 50% release of PB (Figure 3.5C).

### *3.3.4. Antibacterial Activity of PB-HNC*

The MIC and MKC of polymyxin B against *P. aeruginosa* MTCC 2488 was 0.75 µM and 3.125 µM, respectively, while the MIC and MKC of PB-HNC against *P. aeruginosa* MTCC 2488 was 6.25 µM and 25 µM, respectively (Figure A3.2 and Table A3.1, Appendix). Treatment of *P. aeruginosa* cells with PB-HNC loaded with 10 µM PB resulted in a systematic reduction in the viability of the target cells (up to 2.0 $Log_{10}$ CFU) (Figure 3.6A). However, viability of *P. aeruginosa* cells was not hampered on treatment with only HANPs (Figure 3.6A). The antibacterial activity of PB-HNC was corroborated by FETEM analysis, wherein notable cellular damage and disintegration was observed in *P. aeruginosa* MTCC 2488 cells treated with PB-HNC as compared to the untreated cells (Figure 3.6B). In a cFDA-SE dye leakage assay, the fluorescence intensity of effluxed dye from *P. aeruginosa* MTCC 2488 cells treated with PB-HNC (loaded with 10 µM polymyxin B) or polymyxin B alone (10 µM) was

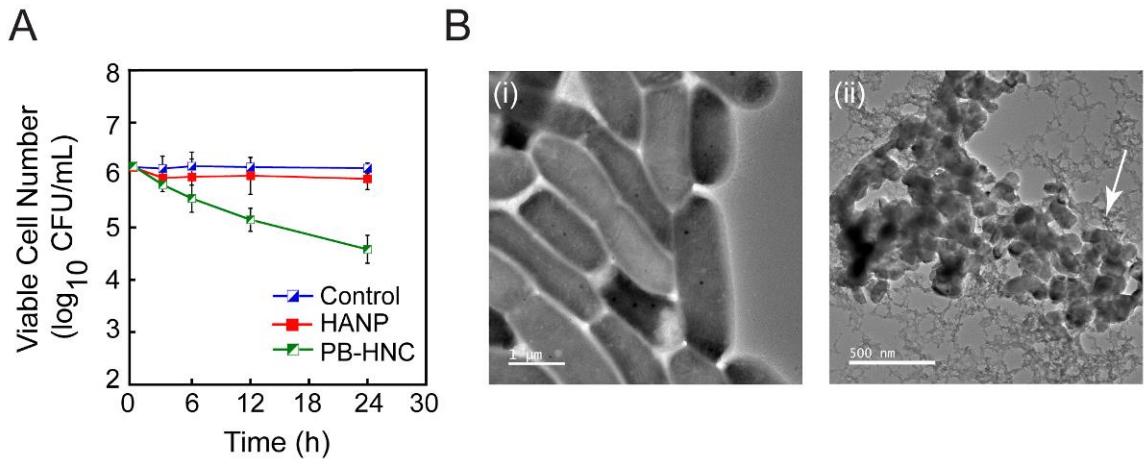


**Figure 3.6.** (A) Effect of PB-HNC on the viability of *P. aeruginosa* MTCC 2488 cells. (B) FETEM analysis of (i) *P. aeruginosa* MTCC 2488 cells and (ii) *P. aeruginosa* MTCC 2488 cells treated with 10 µM PB-HNC. Scale bar in (i) and (ii) are 1.0 µm and 500 nm, respectively. Arrow in (ii) indicates disintegration of *P. aeruginosa* MTCC 2488 cells treated with PB-HNC.

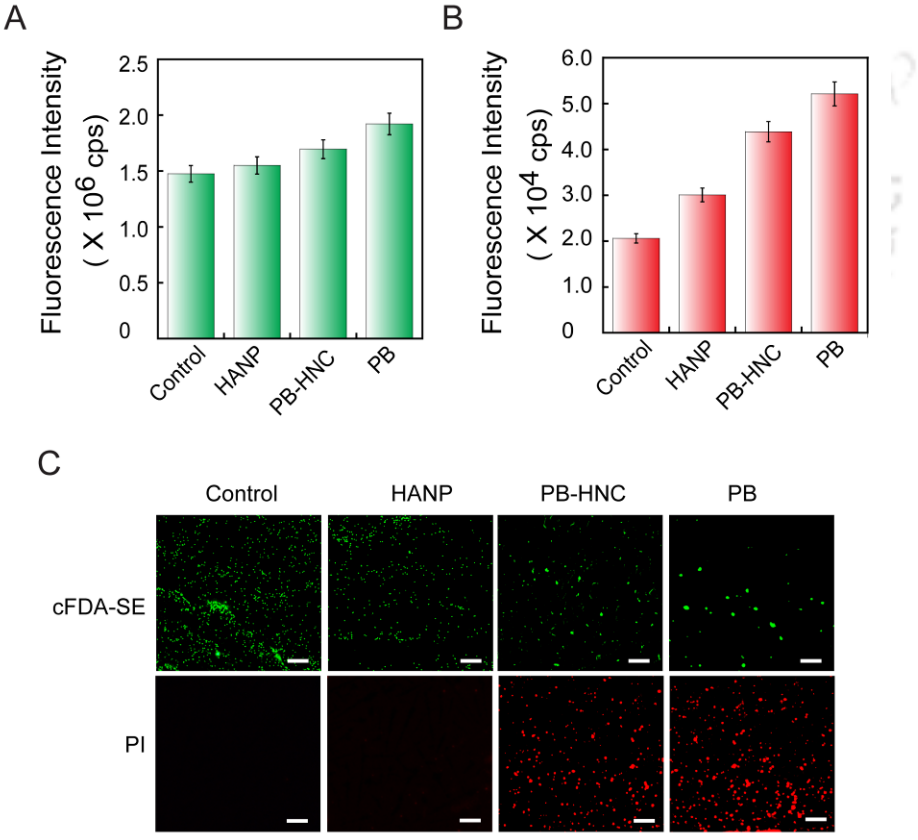


**Figure 3.7.** (A) cFDA-SE leakage assay and (B) PI uptake assay in *P. aeruginosa* MTCC 2488 cells treated with 10 µM PB-HNC. (C) Fluorescence microscope-based live/dead assay with PB-HNC-treated *P. aeruginosa* MTCC 2488 cells using cFDA-SE and PI. Scale bar for the images is 50 µm.

higher than control cells and cells treated with HANP (Figure 3.7A), which suggested that treatment with PB-HNC and PB resulted in membrane perforation and leakage of the entrapped dye. The membrane-directed activity of PB-HNC was also captured in a PI uptake assay, wherein the fluorescence intensity of cell-associated PI was higher for *P. aeruginosa* MTCC 2488 cells treated with PB-HNC and polymyxin B as compared to control cells and cells treated with HANP (Figure 3.7B). Fluorescence microscopic analysis with cFDA-SE and PI also validated the membrane-directed activity of PB-HNC (Figure 3.7C).

*3.3.5. Antibiofilm Activity and In Vitro Cytotoxic Effect of PB-HNC*

A systematic reduction in metabolic activity of *P. aeruginosa* MTCC 2488 biofilm was evident in presence of PB-HNC loaded with an increasing concentration of polymyxin B. The minimal biofilm inhibitory concentration ($BIC_{50}$) and minimal biofilm eradication concentration ($BEC_{50}$) of PB-HNC against *P. aeruginosa* MTCC 2488 was 75 μM (Figure 3.8A) and 150 μM (Figure 3.8B), respectively. Inhibition of *P. aeruginosa* biofilm growth by PB-HNC was also validated by crystal violet staining, wherein a dose-dependent decrease of biofilm biomass was apparent (Figure A3.3 in Appendix). Further, fluorescence microscope analysis with cFDA-SE and congo red indicated a reduction in biofilm viability and matrix formation upon treatment with 100 μM PB-HNC (Figure 3.8C).

In order to leverage the bactericidal activity of PB-HNC for potential therapeutic application, it was pertinent to ascertain its cytotoxic effect. To this end, a standard MTT assay was conducted to evaluate the cytotoxic potential of PB-HNC on cultured human embryonic kidney cells (HEK 293 cells). With regard to polymyxin B alone, it was observed that at concentrations equivalent to its $BIC_{50}$ and $BEC_{50}$ against *P. aeruginosa* MTCC 2488 (75 μM and 150 μM, respectively), the antibiotic was toxic as the viability of cultured HEK 293 cells was ~60% (Figure 3.9). However, PB-HNC was essentially non-toxic as the viability of HEK 293 cells was observed to be ~80% even at the highest tested concentration (Figure 3.9). The slow release kinetics of the payload from HANPs likely ensured a low local concentration of polymyxin B and thereby reduced the toxic effect on HEK 293 cells.

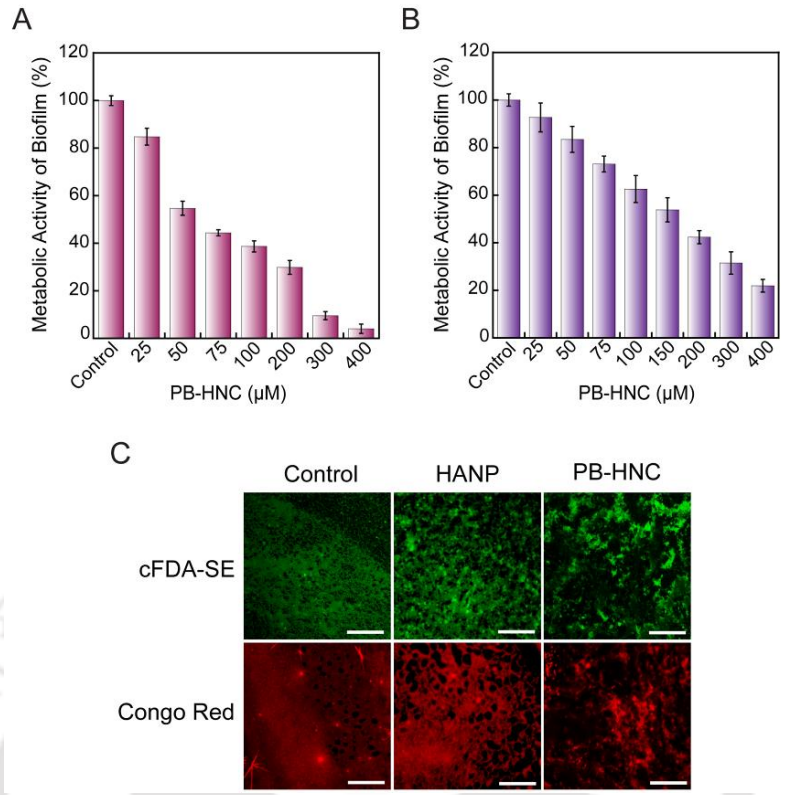


**Figure 3.8.** MTT-based assay for estimating (A) inhibition and (B) eradication of *P. aeruginosa* MTCC 2488 biofilm grown in the presence of PB-HNC. (C) Fluorescence microscopic analysis to ascertain inhibition of *P. aeruginosa* MTCC 2488 biofilm grown in the presence of PB-HNC. Scale bar for the images is 100 μm.

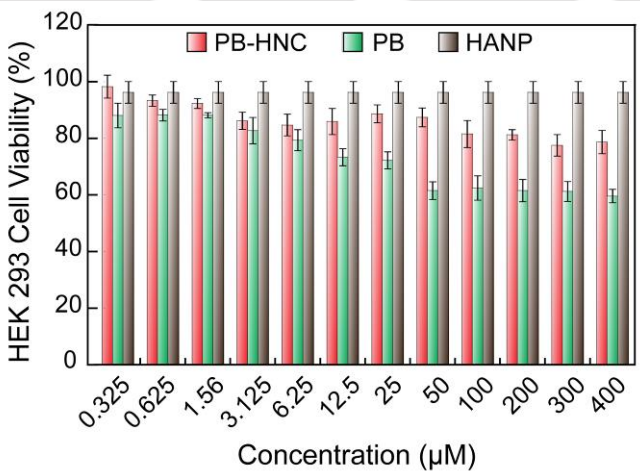


**Figure 3.9.** MTT assay to determine cytotoxic effect of PB-HNC on HEK 293 cells. The concentration of polymyxin B loaded in PB-HNC or used singularly is indicated. The concentration of HANP is 1.0 mg/mL. Each data point represents mean ± standard deviation from six samples.

### 3.4. Significant Findings

The salient findings of the present study are as follows:

1. The major proteins present in the SLP extract of *L. plantarum* MTCC 1325, *L. plantarum* CRA52 and *P. pentosaceus* CRA51 were detected by SDS-PAGE analysis.

2. The purified ~20 kDa protein present in the SLP extract of *L. plantarum* MTCC 1325 and ~43 kDa protein present in the SLP extract of *P. pentosaceus* CRA51 was majorly involved as a mineralization template and supported the formation of hydroxyapatite nanoparticles.

3. HANPs generated by mineralization of the SLP extract of *L. plantarum* MTCC 1325 was used to generate a polymyxin B loaded nanocomposite (PB-HNC), which rendered a sustained release of the antibiotic in buffer systems having physiological pH.

4. Standard antibacterial assays indicated the bactericidal and antibiofilm potential of PB-HNC against *P. aeruginosa* MTCC 2488.

5. The biogenic HANPs and PB-HNC were non-toxic to cultured HEK 293 cells at concentrations relevant for antibiofilm activity.

The present study could thus demonstrate the potential of secreted protein(s) from LAB as a mineralization template for facile synthesis of HANPs. The investigation could also identify the key protein present in the SLP extract for nucleation and mineralization. Although, the study demonstrated a green synthesis route for generating biocompatible HANPs, the recovery of the extracellular secreted protein templates from LAB entails the use of arduous steps. Further, the yield of these protein templates from the LAB cultures is also moderate. As an alternate strategy, the next chapter discusses the potential of using cell surface-associated proteins (CSPs) of LAB as a viable template for biomineralization and generation of HANPs.

# Chapter 4

## Generation of HANPs Using Cell Surface-Associated Protein (CSP) and Whole Cell of Probiotic *Lactobacillus rhamnosus* GG

*This chapter describes the potential of cell surface-associated protein (CSP) from probiotic LAB L. rhamnosus GG as well as the whole cell of the LAB to synthesis hydroxyapatite nanoparticles. The characterization of the material followed by mechanistic studies are presented herein.*

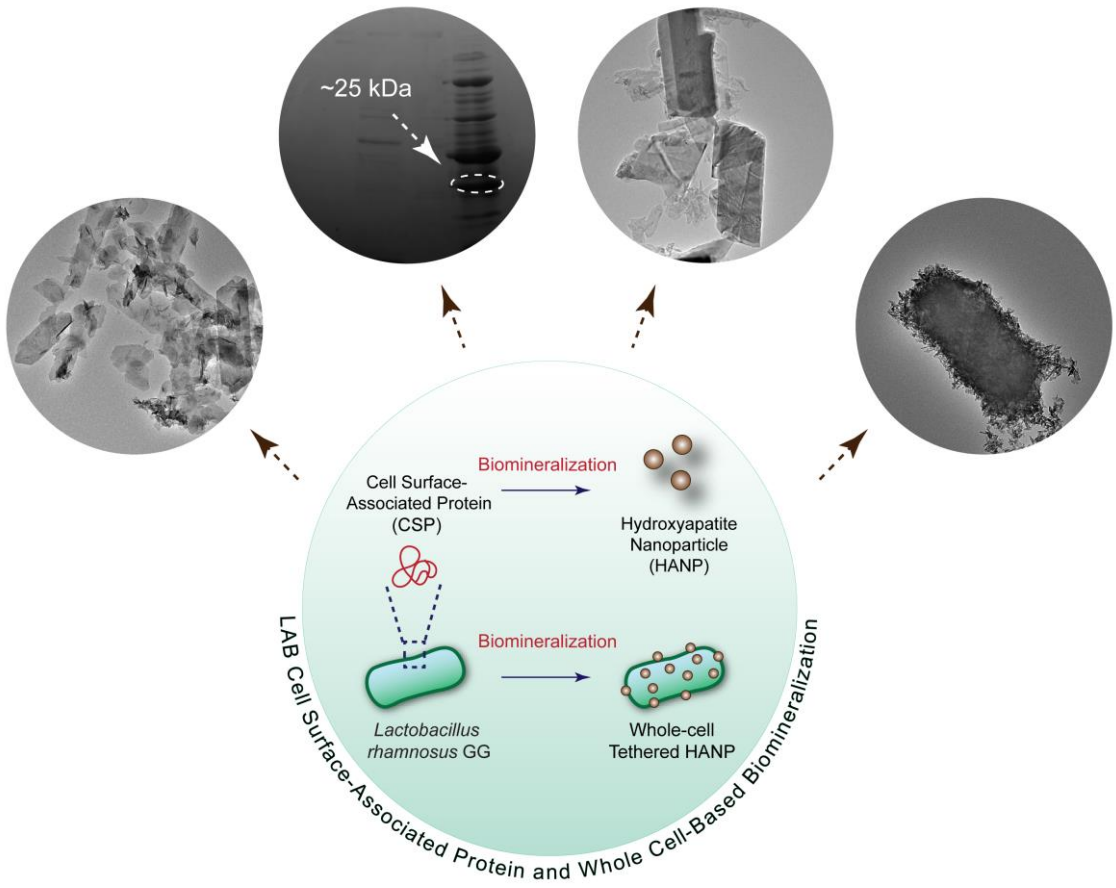

# ABSTRACT

This chapter describes the role of cell surface-associated protein (CSP) from LAB as a nucleation scaffold in biomineralization for the generation of HANPs and also illustrates whole-cell based HANP synthesis by the probiotic LAB *Lactobacillus rhamnosus* GG. Initially, five strains of LAB were screened for the presence of cell surface-associated protein, wherein prominent bands (~66 kDa, ~47 kDa, ~40 kDa and ~25 kDa) were evident in SDS-PAGE analysis for *L. rhamnosus* GG. The aggregated nature of the CSP extract from *L. rhamnosus* GG was evident in FETEM and AFM analysis. CSP extract from *L. rhamnosus* GG was mineralized to yield spindle-shaped HANPs having an average particle length of 371 nm as evidenced in FETEM analysis. CSP-mineralized HANPs (CSP-HANPs) were also characterized by FTIR and BET analysis, while XRD and SAED analysis indicated their crystalline nature. Mechanistic studies suggested the key role of ~25 kDa CSP (F4SP) in mineralization. In contrast to CSP-HANPs, F4SP-mineralized crystalline hydroxyapatite (HA) was plate-shaped having an average length of 1.68 µm and breadth of 0.95 µm. HANP mineralization at the whole-cell (WC) level resulted in clusters of aggregated HANPs (WC-HANPs) adhering onto *L. rhamnosus* GG cells, which was evident in FETEM, FESEM and AFM analysis. FETEM analysis revealed that the desorbed WC-HANPs recovered by cell lysis were needle-shaped, with a particle size distribution of 70-110 nm.

### 4.1. Introduction

Microbial proteins or peptides, which are abundant can be harnessed for biomineralization-based synthesis of nanoparticles (Arakaki *et al*., 2003; Ahmadzadeh *et al*., 2016). Since microbes are amicable to large-scale cultivation, a viable and persistent source of the template protein or peptide is available. However, considering biomedical applications, it is paramount that the microbial protein or peptide templates not only favour nucleation, but are also non-toxic and biocompatible. In this context, the choice of lactic acid bacteria (LAB) as a source of such templates is an interesting prospect given the GRAS (generally regarded as safe) status of LAB. Earlier studies highlighted in Chapter 2 and Chapter 3 have demonstrated the feasibility of using extracellular secreted protein(s) extract of LAB as a template for generating HANPs. Although the secreted LAB protein(s) could readily serve as mineralization templates, their recovery from a large volume of LAB culture filtrate involved a tedious concentration step. This quandary can be a bottle-neck to routine large-scale use of secreted LAB protein(s) as mineralization templates.

To circumvent this problem, it was conceived that the cell surface-associated proteins (CSPs) of LAB can be a viable template for biomineralization. To validate this hypothesis in the current study, *Lactobacillus rhamnosus* GG was selected as a host cell owing to its widely recognized probiotic status, safety profile and health promoting attributes (Stage *et al*., 2020; Goldin *et al*., 1992; Guarino *et al*., 2009). Given that LAB CSPs are acidic, hydrophobic in nature and can self-assemble (Deepika *et al*., 2009; Hynonen and Palva, 2013), it was envisioned that the CSP of *L. rhamnosus* GG can serve as a nucleation scaffold, facilitate metal chelation and HANP mineralization thereof as depicted in Scheme 4.1. Metal-chelating groups (like $COO^-$ and $PO_4^{3-}$), are present in the cell envelope of Gram-positive bacteria (French *et al*., 2013; Kern *et al*., 2010; Weidenmaier and Peschel, 2008). Thus, besides CSP, the metal-chelating groups of the cell envelope of the Gram-positive *L. rhamnosus* GG can perhaps be leveraged at the whole-cell level, wherein the large surface area of bacterial cells can ensure high density nucleation sites and efficient metal chelation, leading to enhanced biomineralization of HANPs (Scheme 4.1). The inherent heterogeneity of the two distinct routes of synthesis (LAB CSP vis-à-vis whole cell) is also likely to yield a fundamental understanding of the mechanistic aspect of template-directed biomineralization and provide a guideline for generation of HANPs of controlled size and shape.

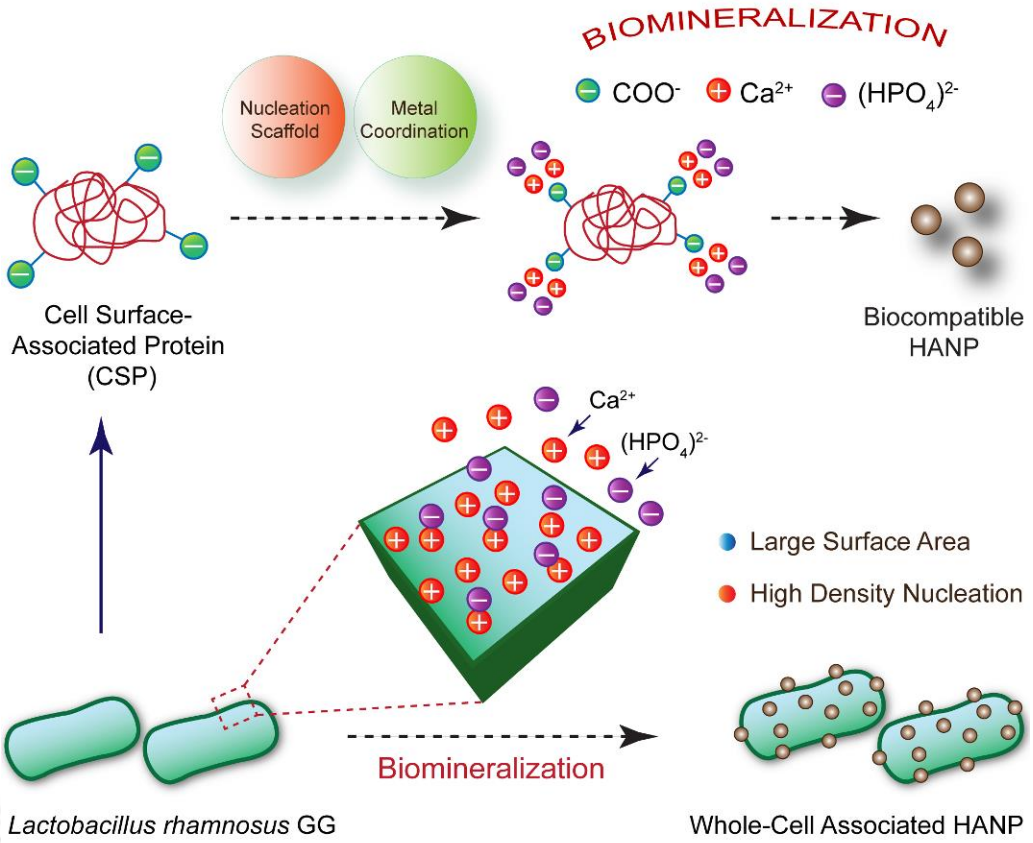


**Scheme 4.1.** Schematic representation illustrating the rationale of using *Lactobacillus rhamnosus* GG cell surface-associated protein (CSP) and whole cell for HANP synthesis by biomineralization.

Based on the aforementioned rationale, the present investigation illustrates the use of *L. rhamnosus* GG CSP as well as whole-cell as a nucleation centre in biomineralization for the generation of HANPs. In this study, the role of the LAB CSP protein(s) is deciphered to acquire a mechanistic insight on the biomineralization process.

## 4.2. Materials and Methods

### *4.2.1. Reagents and Growth Media*

Lactobacillus MRS broth (MRS) broth and lithium chloride were purchased from HiMedia (India). Dimethyl sulfoxide (DMSO), acetic acid glacial and methanol were obtained from Merck (India). High range protein ladder, Coomassie Brilliant Blue R-250 were procured from Sisco Research Laboratories (India). Potassium bromide, glycine and SDS were procured from Sigma-Aldrich.

### *4.2.2. Bacterial Strains and Growth Conditions*

*Lactobacillus plantarum* NCIM 2592, *Lactobacillus rhamnosus* GG, *Lactobacillus* sp. CuAk9, *Enterococcus faecium* CRA21, *Lactobacillus plantarum* MTCC 1325 were cultured in MRS broth at 37°C for 18 h in static condition. The bacterial strains were sub-cultured prior to their use in experiments.

### *4.2.3. Isolation of LAB Cell Surface-Associated Protein (CSP)*

The cell surface-associated protein (CSP) from *Lactobacillus plantarum* NCIM 2592, *Lactobacillus rhamnosus* GG, *Lactobacillus sp.* CuAk9, *Enterococcus faecium* CRA21 and *Lactobacillus plantarum* MTCC 1325 was extracted by using 6.0 M LiCl as reported in a previous study (Avall-Jaaskelainen *et al*., 2002). LAB cells were grown in 100 mL MRS media for 24 h at 37°C in static condition. The cells were then harvested by centrifugation at 8000 rpm for 5 min and washed twice with sterile PBS. The pellet was resuspended in 20 mL of 6.0 M LiCl and incubated for 1 h at 30ºC, 180 rpm followed by centrifugation at 11000 rpm for 20 min. The supernatant was dialyzed against distilled water overnight at 4°C in a 12,000 MWCO dialysis bag (Sigma Aldrich, USA) followed by lyophilization to obtain CSP extract. For each LAB strain, the concentration of protein in CSP was quantified by Bradford assay (Bradford, 1976). The CSP from the LAB strains were then subjected to SDS-PAGE analysis. Following electrophoresis, the gel was stained with Coomassie Brilliant Blue R-250 for 4 h, destained in methanol:acetic solution (25:10 v/v) and its image was captured in a Geldoc system (BioRad, USA). A schematic representation of the CSP extraction is shown in Scheme 4.2.

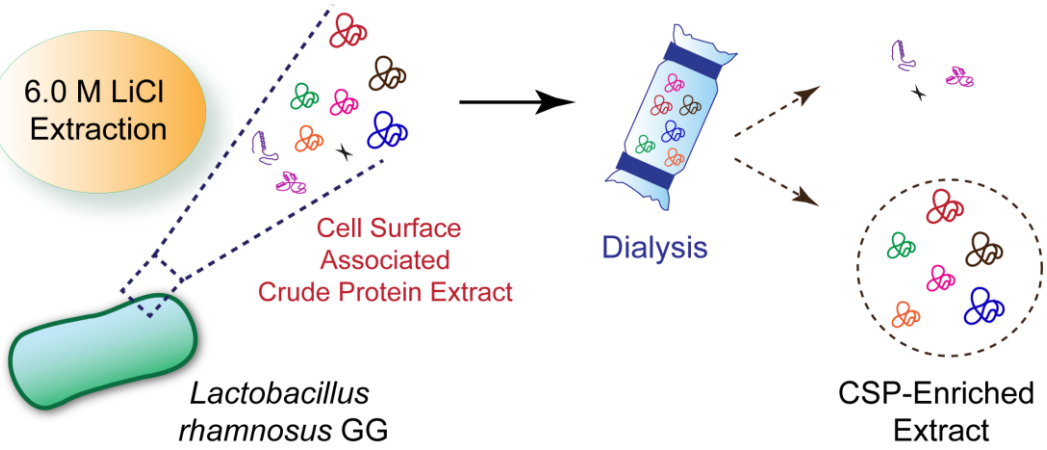


**Scheme 4.2.** Schematic representation illustrating extraction of cell surface-associated protein (CSP) from *Lactobacillus rhamnosus* GG using lithium chloride.

*4.2.4. Fractionation of the Cell Surface-Associated Protein L. rhamnosus GG*

The prominent bands observed for *L. rhamnosus* GG CSP on an SDS-PAGE gel were eluted using the IN-Gel digest protocol (Sigma-Aldrich, USA) without using trypsin enzyme. The eluted protein fractions (F1SP-F4SP) were lyophilized and the amount of the protein was again quantified by Bradford assay (Bradford, 1976).

*4.2.5. Characterization of Cell Surface-Associated Protein (CSP) and CSP Fraction 4 (F4SP) of L. rhamnosus GG*

*4.2.5.1. AFM Analysis*

The CSP extract and F4SP isolated from *L. rhamnosus* GG was resuspended in sterile MilliQ water. The concentration of the proteins was estimated by Bradford method (Bradford 1976). A 10 µl aliquot of the sample was drop casted onto a sterile glass cover slip (18 mm × 18 mm) and air dried overnight in a laminar hood. Atomic force microscopic images were acquired in non-contact mode for a 10 µm × 10 µm area at a scan rate of 0.5-1.0 line/s (Cypher, Oxford). Analysis of the amplitude channel and topographic images was accomplished by using the WSxM v5.0 Develop 6.5 image viewer software.

*4.2.5.2. FETEM Analysis*

CSP extract and F4SP isolated from *L. rhamnosus* GG was negatively stained using 2.0 % uranyl acetate. Equal quantities of sample and stain were mixed thoroughly and drop-casted onto a carbon-coated copper grid and incubated for 30 seconds. Excess sample in the vicinity of the grid was removed carefully by capillary suction using a filter paper and the sample on the grid was dried completely. The sample was then analysed by FETEM (Model 2100F, JEOL) operating at 200 kV and the images were recorded.

*4.2.5.3. MALDI-TOF Analysis*

The ~25 kDa protein band corresponding to F4SP was excised from the SDS-polyacrylamide gel and subjected to IN-Gel digestion using trypsin enzyme. The resulting peptide was subjected to MALDI-TOF analysis (Autoflex Speed, Bruker). The protein was identified using MS search module from MASCOT software (http://www.matrixscience.com) against the Swiss-Prot database. The search parameters were set as one allowed missed cleavage, carbamidomethyl modification of cysteine as a fixed modification, oxidation of methionine as a variable modification and a peptide tolerance of 200 ppm. Identification was considered when a significant match ($p$ value < 0.05) was registered with a Mascot ion score of ≥ 40 (Espino *et al.*, 2015).

*4.2.6. Synthesis of Hydroxyapatite Nanoparticles (HANPs) using L. rhamnosus GG CSP and CSP Fractions*

HANPs were synthesized by essentially following a wet precipitation method (Dasgupta *et al*., 2010). CSP extract or CSP fractions (F1SP-F4SP) from *L. rhamnosus* GG was used as a nucleating agent for biomineralization. Initially, a 5.0 M aqueous solution of $Ca(NO_3)_2.4H_2O$ was prepared in separate sets in a beaker. Subsequently, $NH_4OH$ was added dropwise into 6.0 mL of 5.0 M $Ca(NO_3)_2.4H_2O$ to adjust the pH to 9.0 following which 5.0 mL of either CSP extract (10 µg/mL) or CSP fractions (F1SP-F4SP, 0.80 µg/mL each) were slowly added to the pH adjusted calcium salt solution in separate sets with constant stirring at room temperature. Then 0.018 molar $(NH_4)_2HPO_4$ solution was added to the $Ca^{2+}$-protein solution to achieve a Ca: P molar ratio of 1.67:1 in the reaction blend and the pH of the solution was again adjusted to 9.0 by dropwise addition of $NH_4OH$. The mixture was incubated for 24 h at room temperature in static condition, followed by centrifugation at 10,000 rpm for 5 min. The supernatant was

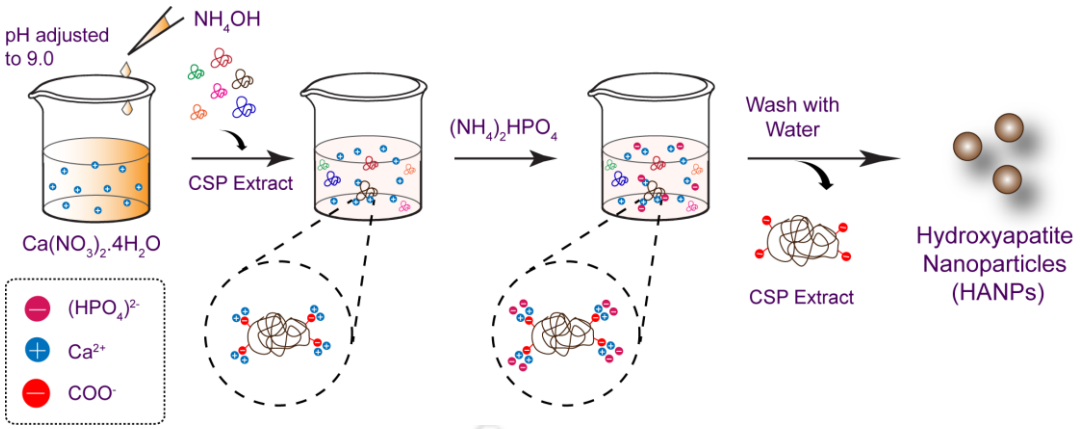


**Scheme 4.3.** Schematic representation illustrating generation of HANPs using cell surface-associated protein (CSP) from *Lactobacillus rhamnosus* GG.

discarded and the pellet was then washed twice with sterile MilliQ water to remove $NO_3^-$ ions and loosely bound CSP. The pellets were lyophilized and then subjected to calcination at 600°C for 2 h to obtain HANPs, which were stored at -20°C prior to further use. A schematic representation HANP generation using CSP extract is shown in Scheme 4.3

*4.2.7. Synthesis of Hydroxyapatite Nanoparticles (HANPs) using L. rhamnosus GG Whole Cell*

*L. rhamnosus* GG cell ($10^8$ cells/ml) was used as a template for whole cell mediated hydroxyapatite nanoparticle (WC-HANP) synthesis. WC-HANPs were prepared by wet precipitation process (Dasgupta *et al.*, 2010). $NH_4OH$ was added dropwise into 2.3 mL of 0.8675 M $Ca(NO_3)_2.4H_2O$ to adjust the pH to 9.0, following which 0.5 mL of *L. rhamnosus* GG cells suspended in sterile MilliQ water ($10^8$ cells/ml) were slowly added to the pH adjusted calcium salt solution with constant stirring at room temperature. Subsequently, 0.003 molar $(NH_4)_2HPO_4$ solution was added to the solution to achieve a Ca: P molar ratio of 1.67:1 in the reaction blend and the pH of the solution was again adjusted to 9.0 by dropwise addition of $NH_4OH$. The mixture was incubated for 24 h at room temperature in static condition, followed by centrifugation at 10,000 rpm for 5 min. The supernatant was carefully aspirated and the cell pellet was then washed twice with sterile MilliQ water.

In order to separate the HANPs from the cells of *L. rhamnosus* GG, the cells were lysed by incubating with 1.0 ml 1% Triton X-100 in a rocker for 30 min at room

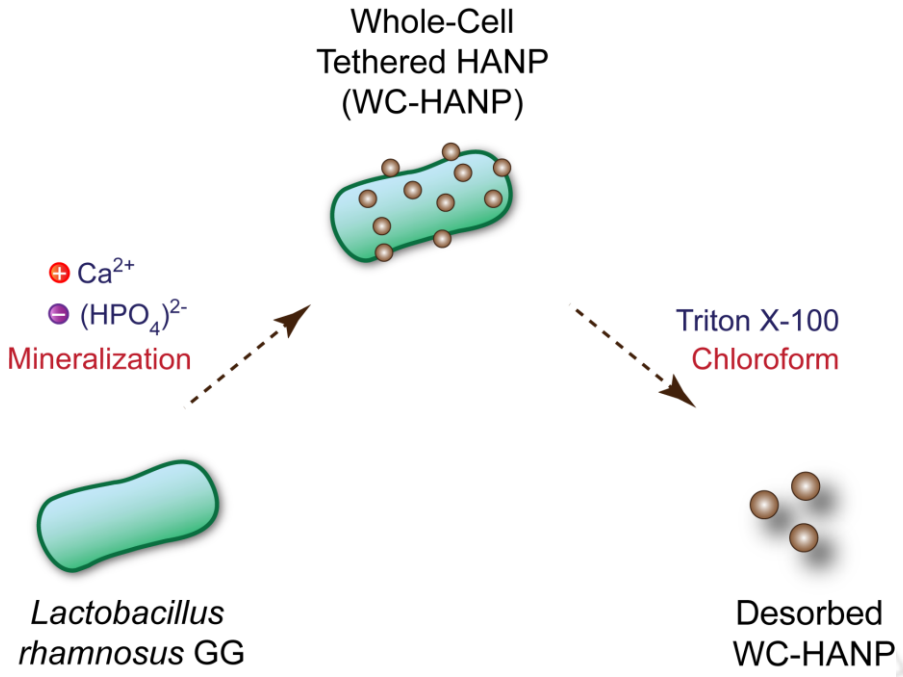


**Scheme 4.4.** Cartoon illustrating (A) generation of *L. rhamnosus* GG whole cell-associated HANPs (WC-HANPs) and (B) desorption of WC-HANPs following cell lysis using Triton X-100 and chloroform.

temperature followed by centrifugation at 10,000 rpm for 5 min. The pellet containing the HANPs was washed twice with sterile MilliQ water, followed by washing with sterile distilled water and 1.0 ml chloroform to remove the lipids and proteins from the suspension. The resulting HANPs (desorbed WC-HANPs) were lyophilized and both the CSP-HANPs, F4SP-HA and desorbed-HANPs were characterized by various methods as mentioned in the following section. A schematic representation of the whole cell LAB associated HANP synthesis and desorption process is shown in Scheme 4.4.

### *4.2.8. Characterization of Biogenic HANPs*

The HANPs obtained through mineralization of *L. rhamnosus* GG CSP, F4SP and desorbed WC-HANP were characterized by the following methods:

#### *4.2.8.1. FTIR Analysis*

FTIR spectra of HANPs were recorded in KBr pellets at 4.0 $cm^{-1}$ resolution in an infrared spectrometer (Spectrum One, Perkin-Elmer). Eight scans were performed for

each sample in the wavenumber range of 4000 $cm^{-1}$ to 500 $cm^{-1}$. A background spectrum for pure KBr was also measured.

*4.2.8.2. Powder XRD Analysis*

Powder X-ray diffraction (D2 Phaser, Bruker, Germany) data of the HANPs were recorded at room temperature over the 2θ range of 20°- 45° at a step size of 0.02° and a count time of 2s/step.

*4.2.8.3. BET Surface Area Analysis*

The specific surface area and average pore size of the HANPs were measured using BET surface area analyser and $N_2$ adsorption-desorption isotherm (Quantachrome, Autosorb-IQ MP).

*4.2.8.4. Atomic Force Microscope Analysis*

HANP samples were initially sonicated for 10 min and 10 µl of each sample was spotted onto sterile glass cover slips (18 mm × 18 mm) and air dried in a laminar hood overnight. Atomic force microscopic images were acquired in non-contact mode for a 10 µm × 10 µm area at a scan rate of 0.5-1.0 line/s (Cypher, Oxford). Analysis of the amplitude channel and topographic images was accomplished by using the WSxM v5.0 Develop 6.5 image viewer software.

*4.2.8.5. FESEM, FETEM, HR-TEM and SAED Analysis*

The HANP samples were sonicated for 10 mins and an aliquot of each sample was added on a clean sterile aluminium foil. The samples were air dried in a laminar hood overnight and visualized under Field Emission Scanning Electron Microscope (Zeiss Sigma 300, USA). Separate drops of the samples were also spotted onto carbon-coated Cu TEM grid (Pacific Grid, USA) followed by air drying in laminar hood. The dried samples were loaded onto specimen holder and their images were recorded under Field Emission Transmission Electron Microscope (JEOL 2100F, Japan) operating 200 kV. The samples were also subjected to High Resolution Transmission Electron Microscope (HR-TEM) analysis and the Selected Area Electron Diffraction (SAED) pattern was recorded.

*4.2.9. Isothermal Calorimetry Studies*

ITC measurements were made at 37°C using a VP-ITC device (MicroCal, Northampton, USA). To prevent the formation of air bubbles, the buffers were degassed under vacuum prior to the experiment. The CSP extract from *L. rhamnosus* GG (10 µg/mL) and 5.0 mM aqueous solution of $Ca(NO_3)_2.4H_2O$ were taken in sterile MilliQ water to minimize heats of dilution. In order to study binding of ammonified Ca-protein complex and $(NH_4)_2HPO_4$, the Ca-protein complex was dissolved in sterile MilliQ-grade water (final protein and Ca concentrations were nearly 8.8 µg/mL and 0.72 µM, respectively), loaded onto the cell and titrated against $(NH_4)_2HPO_4$. Integrated heat effects, after correction for heats of dilution, were analyzed by non-linear regression using a sequential-binding model (Microcal Origin, version 5.0).

## 4.3. Results and Discussion

*4.3.1. Isolation of Cell Surface-Associated Protein (CSP) from L. rhamnosus GG*

Extraction of *L. rhamnosus* GG CSP was accomplished by LiCl method, based on the notion that this salt is likely to disrupt only the non-covalent interactions between surface proteins and bacterial cells without denaturing the proteins (Grosu-Tudor *et al.*, 2016). SDS-PAGE analysis of *L. rhamnosus* GG CSP extract revealed four major protein bands having a molecular weight of ~66 kDa, ~47 kDa, ~40 kDa and ~25 kDa, respectively (Figure 4.1A). Based on the intensity of the protein bands in SDS-PAGE analysis, it was apparent that the expression of CSP in *L. rhamnosus* GG was relatively more as compared to other LAB strains (Figure 4.1A). In FETEM analysis, *L. rhamnosus* GG CSP extract appeared as a lattice of aggregated proteins (Figure 4.1B). AFM analysis of the CSP extract revealed that the proteins were disc-shaped, aggregated and displayed an average height profile of ~17.21 nm (Figure 4.1C-D). Aggregation of *L. rhamnosus* GG CSP extract suggested that the protein(s) present in the CSP extract likely display self-assembly or protein-protein interactions.

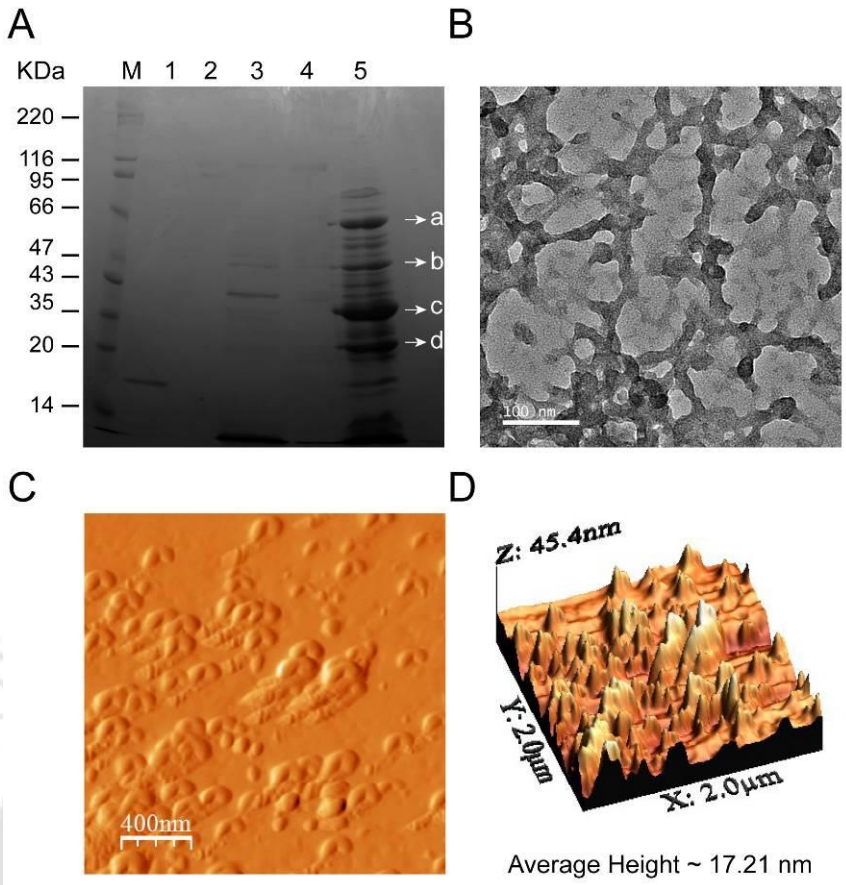


**Figure 4.1.** (A) SDS-PAGE analysis of cell surface-associated protein extract from LAB. Lanes 1-5: *Lactobacillus* sp. CuAk9, *L. plantarum* NCIM 2592, *L. plantarum* CRA21 *L. plantarum* MTCC 1325 and *L. rhamnosus* GG. Major protein bands in *L. rhamnosus* GG (lane 5) CSP are labelled as a-d. (B) FETEM analysis of CSP from *L. rhamnosus* GG. (C) Amplitude channel image and (D) 3D topography in AFM analysis of CSP extract from *L. rhamnosus* GG.

*4.3.2. Synthesis of HANP Using CSP as a Mineralization Scaffold*

HANPs were synthesized by wet precipitation method using the CSP extract (10 µg/mL) from *L. rhamnosus* GG as a mineralization template. FETEM and FESEM analysis indicated that the CSP-derived HANPs were spindle-shaped with an average particle length of ~370 nm (Figure 4.2A-B) and a lattice distance of 0.4 nm (Figure 4.2C). AFM analysis also revealed that the HANPs were spindle-shaped (Figure 4.2D) with an average height profile of ~0.6 nm (Figure 4.2D, inset). The crystalline nature of CSP-HANPs was apparent in powder XRD analysis, wherein sharp peaks were observed at $2\theta = 26^0$, $31^0$ and $33^0$ (Figure 4.3A), which correspond to (002), (211) and (300) lattice planes, respectively (Gao *et al.*, 2016). SAED pattern analysis further

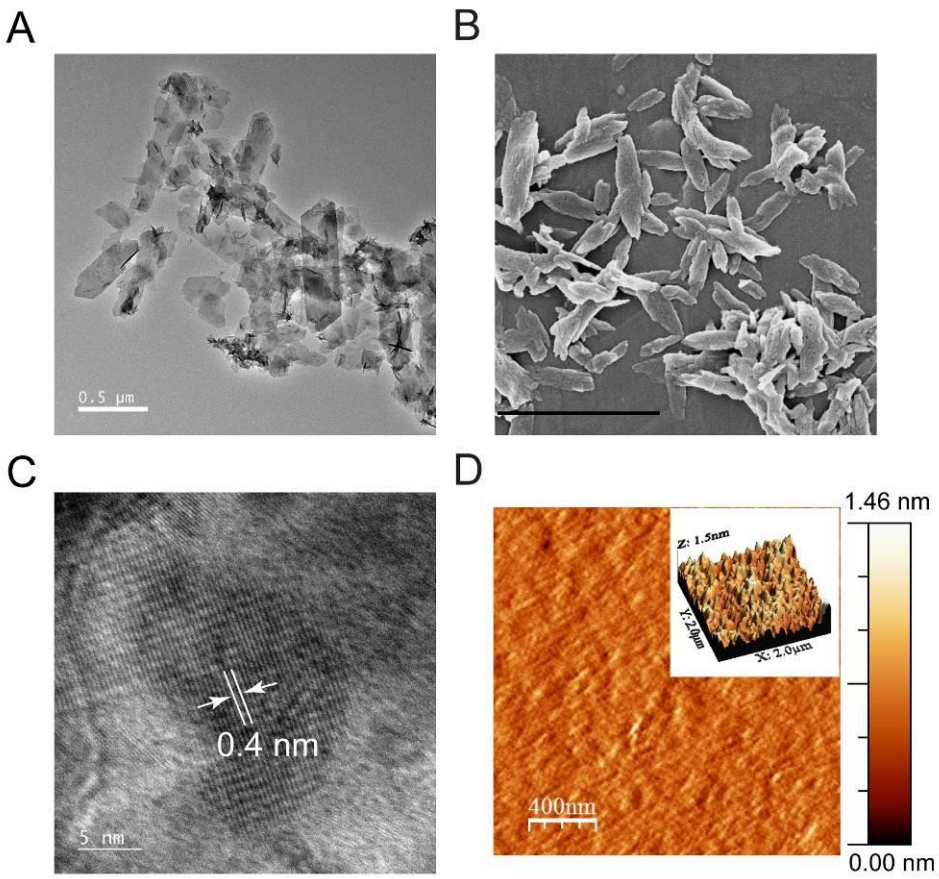


**Figure 4.2.** Characterization of HANPs obtained from CSP extract of *L. rhamnosus* GG by (A) FETEM, (B) FESEM, (C) HR-TEM and (D) 2D topography-based AFM analysis (Inset indicates 3D topography image). Scale bar for the image in (B) is 500 nm.

supported the crystalline nature of the HANPs (Figure 4.3B). FTIR analysis of HANPs indicated the presence of characteristic peaks at 3568 $cm^{-1}$, 1461 $cm^{-1}$ and 1041 $cm^{-1}$ corresponding to $OH^-$, $CO_3^{2-}$ and $PO_4^{3-}$ stretching frequencies, respectively (Figure 4.3C). The adsorption-desorption isotherm observed for CSP-mineralized HANPs in BET analysis (Figure 4.3D) indicated a type IV adsorption isotherm with a hysteresis loop (Huang *et al.*, 2019), wherein the surface area and the average pore size of HANPs was 16.7 $m^2/g$ and 2.8 nm, respectively.

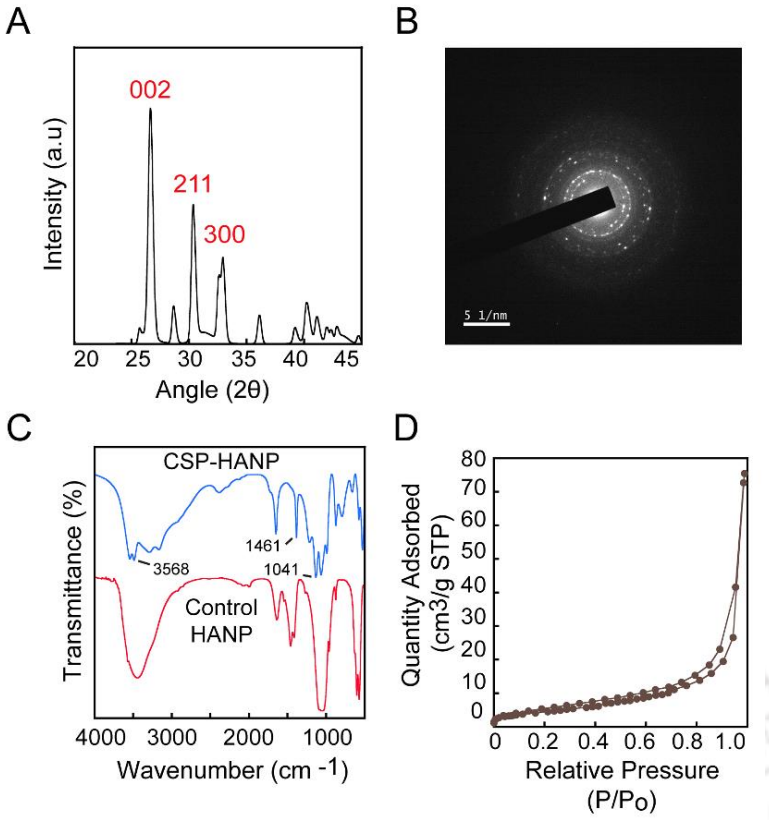


**Figure 4.3.** Characterization of HANPs obtained from CSP extract of *L. rhamnosus* GG by (A) Powder XRD, (B) SAED pattern, (C) FTIR and (D) BET analysis.

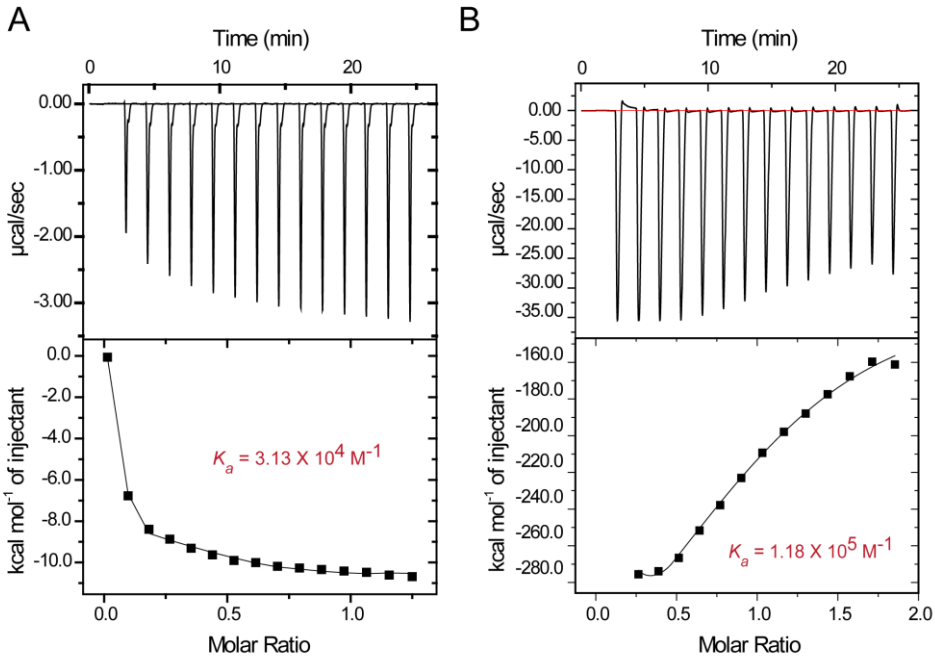


**Figure 4.4.** ITC studies to ascertain interaction between (A) *L. rhamnosus* GG CSP and $Ca^{2+}$ and (B) CSP-$Ca^{2+}$ complex and $PO_4^{3-}$.

In order to validate the role of *L. rhamnosus* GG CSP extract in the biomineralization process, ITC studies were conducted. ITC studies revealed that the interaction between CSP extract and $Ca^{2+}$ ion was strong ($K_a$ = 3.13 × $10^4$ $M^{-1}$) (Figure 4.4A). Subsequently, binding between $Ca^{2+}$-CSP complex and $PO_4^{3-}$ ions was favorable ($K_a$ = 1.18 × $10^5$ $M^{-1}$) (Figure 4.4B). Thus, ITC experiments indicated a significant role of the proteinaceous CSP template in the nucleation process during HANP mineralization.

*4.3.3. Synthesis of HANP with L. rhamnosus GG CSP Fraction*

In order to precisely decipher the role of the individual proteins of *L. rhamnosus* GG CSP extract in biomineralization, the major protein bands encompassing ~66 kDa, ~47 kDa, ~40 kDa and ~25 kDa proteins (Figure 4.1A) were separately eluted from the gel and designated as fractions F1SP, F2SP, F3SP and F4SP, respectively. The yield of F1SP, F2SP, F3SP and F4SP eluted from the gel was low, amounting 0.62 µg/mL, 0.26 µg/mL, 0.48 µg/mL and 0.76 µg/mL, respectively. These fractions were further concentrated and then used in separate sets (~0.80 µg/mL each) as mineralization templates for generation of HANPs. FTIR analysis of HANPs obtained from fraction F4SP (~25 kDa protein) showed peaks at 3568 $cm^{-1}$, 1461 $cm^{-1}$ and 1041 $cm^{-1}$ corresponding to $OH^-$, $CO_3^{2-}$ and $PO_4^{3-}$ stretching frequencies, respectively (Figure 4.5A). These characteristics peaks were not obtained when the other CSP fractions namely F1SP, F2SP and F3SP were used for HANP synthesis (Figure A4.1 in Appendix). Thus, amongst the proteins present in *L. rhamnosus* GG CSP, F4SP (~25 kDa protein) seems to play a key role in HA biomineralization. However, FETEM analysis indicated that HA obtained from F4SP was plate-shaped and formed aggregates having a length of 1.68 µm and breadth of 0.95 µm (Figure 4.5B). Powder XRD analysis indicated the crystalline nature of F4SP-HA (Figure 4.5C), which was further validated by SAED pattern (Figure 4.5C, Inset). Analogous to CSP-HANPs, a type IV adsorption isotherm with a hysteresis loop was evident in BET analysis for HA derived from F4SP (Figure 4.5D). BET analysis also revealed that the surface area and average pore size of F4SP-HA was 7.4 $m^2/g$ and 2.7 nm, respectively. FETEM and AFM analysis revealed that the gel eluted and purified F4SP formed spherical aggregates of ~105 nm size (Figure 4.6), indicating self-assembly nature of the protein. Identification of F4SP was accomplished by MALDI-TOF followed by MASCOT analysis using Swiss-Prot database, which suggested that F4SP shared homology with

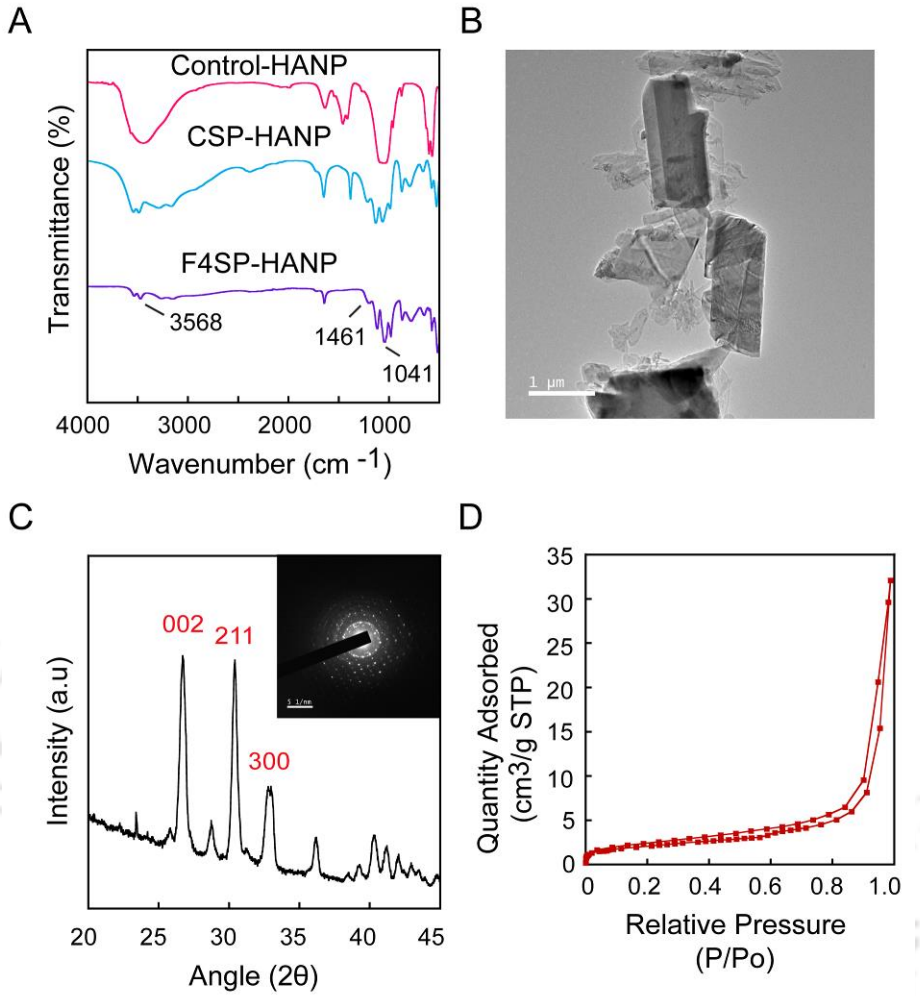


**Figure 4.5.** Characterization of HANPs by mineralization of gel-eluted F4SP (fraction 4) protein present in *L. rhamnosus* GG CSP extract. (A) FTIR analysis, (B) FETEM analysis, (C) Powder XRD analysis (Inset showing SAED pattern) and (D) BET analysis.

50S ribosomal L5 protein of *L. plantarum* WCFS1, which has been shown to be cell surface-associated and is known to have metal binding amino acid residues such as histidine (one residue), aspartic acid (12 residues) and glutamic acid (13 residues) (NCBI Reference Sequence: WP_063204017.1). Hence, based on the homology, it can be presumed that F4SP is likely to have metal binding amino acid residues, which can render effective calcium entrapment during mineralization and generate HA crystals. Although F4SP could function as a mineralization template, it failed to yield HA of nanoscale dimensions. It is plausible that the other associated proteins namely F1SP, F2SP, F3SP, which were present in *L. rhamnosus* GG CSP (Figure 4.1A) may not be central to metal binding and mineralization per se, but likely play a role in restricting the growth of the mineral in a confined space, resulting in spindle-shaped HA of

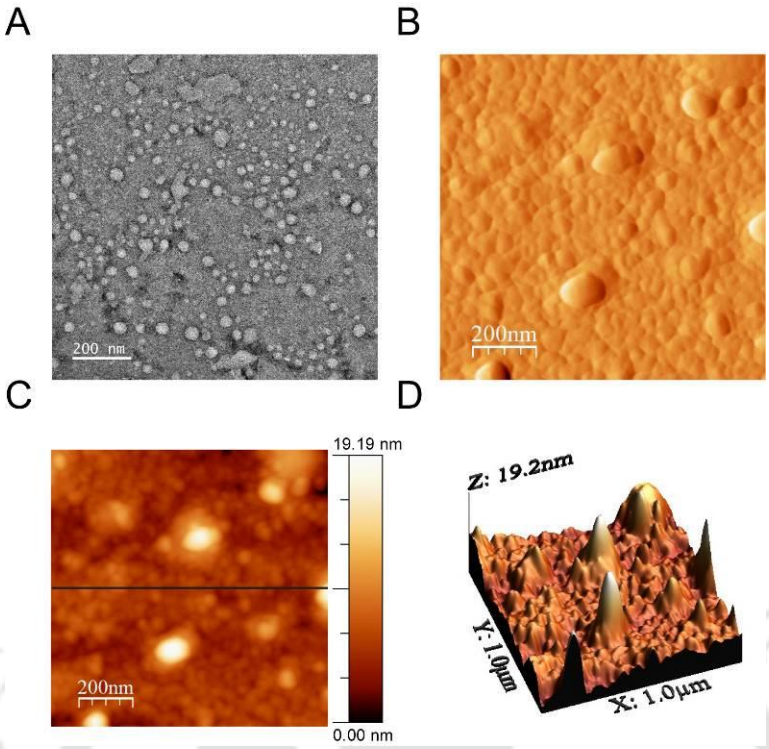


**Figure 4.6.** Characterization of purified F4SP (fraction 4) protein present in *L. rhamnosus* GG CSP extract by (A) FETEM analysis, (B) Amplitude channel, (C) 2D topography and (D) 3D topography-based AFM analysis.

nanoscale dimension as evident in the case of HANPs derived by CSP-mineralization (Figure 4.2A-B). Further mechanistic studies in future can precisely define the role of the other proteins (F1SP, F2SP and F3SP) in the mineralization process.

*4.3.4. Characterization of HANPs obtained from Whole Cell of L. rhamnosus GG*

Based on the leads that CSP as well as the ~25 kDa protein (F4SP) of *L. rhamnosus* GG could support mineralization and generate HANPs, it was pertinent to assess whether whole cells of the probiotic *L. rhamnosus* GG could also direct mineralization for HANP synthesis. FETEM and FESEM analysis revealed that dense clusters of aggregated HANPs were tethered on elongated cells of *L. rhamnosus* GG (Figure 4.7A-B). Clusters of whole cell-associated HANPs (WC-HANPs) adhering onto the cells was also evident in AFM analysis, wherein an average height profile of ~140.35 nm was obtained (Figure 4.7C-D). Although the size of the WC-HANPs could not be ascertained by microscopic methods owing to the high aggregation and coalescence of

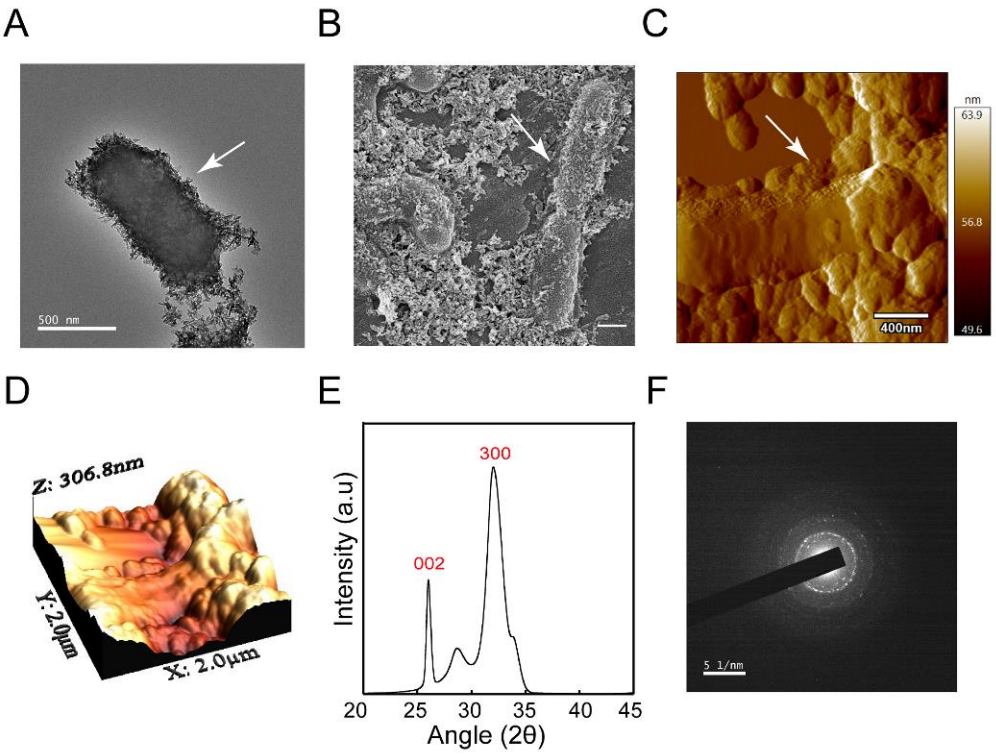


**Figure 4.7.** Characterization of *L. rhamnosus* GG whole cell-associated HANPs (WC-HANPs) by (A) FETEM analysis, (B) FESEM analysis, (C) 2D topography-based AFM analysis, (D) 3D topography-based AFM analysis. White arrow in (A-C) indicates the presence of HANPs on the cell surface of *L. rhamnosus* GG. (E) Powder XRD analysis, (F) SAED pattern analysis.

nanoparticles, the crystalline nature of WC-HANPs was validated based on the salient peaks obtained at 2θ = 26° and 33° in powder XRD analysis indicating the corresponding (002) and (300) lattice planes of HA (Figure 4.7E) and the SAED pattern (Figure 4.7F). Thus, the ability of CSP as well as the ~25 kDa protein (F4SP) of *L. rhamnosus* GG to serve as a nucleation scaffold and support HANP mineralization could be leveraged even at the whole cell level. However, additional surface ligands present in the cell may also contribute to the mineralization process, which warrants further investigation in the future. For instance, metal reactive groups (MRGs) are likely to be present on the cell envelope of the Gram-positive bacteria *L. rhamnosus* (French *et al.*, 2013; Kern *et al.*, 2010; Weidenmaier *et al.*, 2008) and these groups may render metal coordination, which is critical in biomineralization.

*4.3.5. Desorption of HANPs from the Surface of L. rhamnosus GG Whole Cell*

The WC-HANPs were recovered by cell lysis in presence of Triton X-100 and chloroform. FETEM analysis revealed that the desorbed or recovered HANPs were needle-shaped (Figure 4.8A) and had a particle size distribution ranging from 70-110 nm, which was relatively less than HANPs obtained using CSP (~200-530 nm) or F4SP (~0.9-4.5 µm). The difference in the particle size of HANPs is perhaps due to the inherent differences in the biomineralization process. The bacterial cell lends a large surface area for high density display of ligands and functional groups relevant for biomineralization. The high density of nucleation sites and mineralization ligands present on the surface of the cell may lead to spatial restriction of the mineralization process, which can then lead to generation of HANPs of smaller size as opposed to mineralization on an organic matrix such as *L. rhamnosus* GG CSP or F4SP. HR-TEM analysis indicated that the lattice distance in desorbed WC-HANPs was 0.28 nm (Figure 4.8B). The needle-shaped desorbed WC-HANPs were also evident in AFM analysis, wherein an average height profile of ~80.03 nm was obtained (Figure 4.8C-D). SAED pattern and powder XRD analysis revealed that WC-HANPs were crystalline in nature (Figure 4.8E-F).

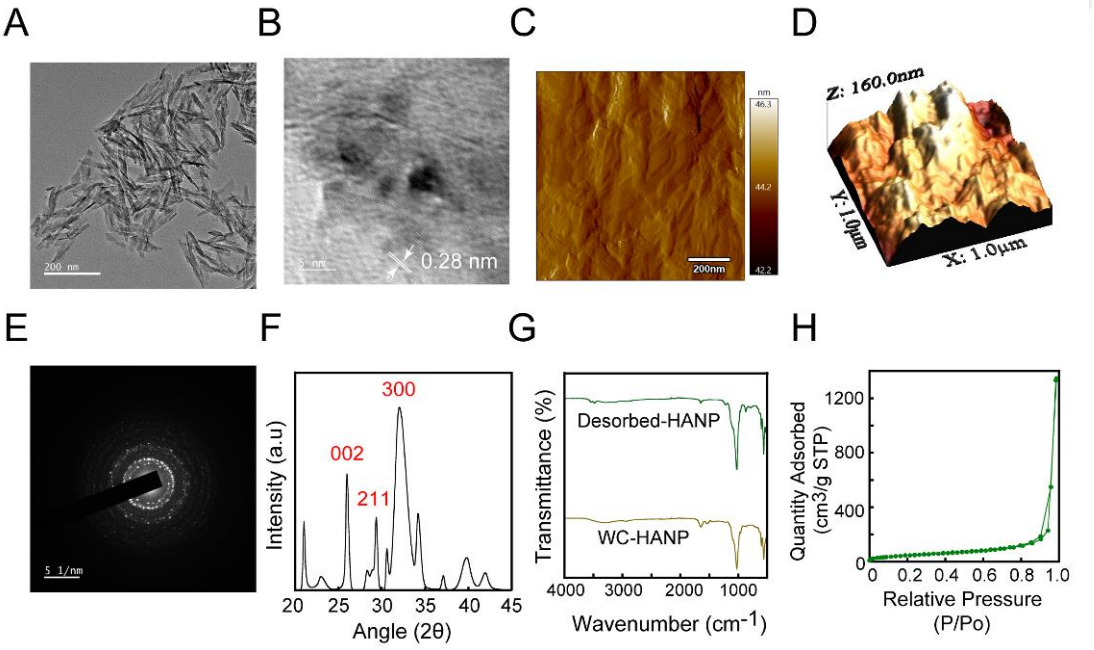


**Figure 4.8.** Characterization of desorbed WC-HANPs by (A) FETEM analysis, (B) HR-TEM analysis, (C) 2D topography-based AFM analysis, (D) 3D topography-based AFM analysis, (E) SAED pattern, (F) Powder XRD analysis, (G) FTIR analysis and (H) BET analysis.

The characteristic peaks observed at 3568 $cm^{-1}$, 1461, and 1041 $cm^{-1}$ observed in FTIR analysis confirmed the identity of desorbed HANPs (Figure 4.8G), while BET analysis indicated a type IV adsorption isotherm with a hysteresis loop for the desorbed WC-HANPs (Figure 4.8H). BET analysis also revealed that the desorbed WC-HANPs had a surface area of 170.47 $m^2/g$ and an average pore size of 4.9 nm.

The comparatively small particle size (70-110 nm) and large surface area (170.47 $m^2/g$) of desorbed WC-HANPs as compared to that obtained using *L. rhamnosus* GG CSP or F4SP extract indicates the benefit of using a whole cell-based biomineralization process. However, recovery of the cell-associated HANPs entails an arduous cell treatment process with harsh chemicals such as chloroform and Triton X-100 followed by extensive washing, unlike a simple washing step in case of HANPs obtained from *L. rhamnosus* GG CSP. Hence, in order to leverage the whole cell-associated biomineralization for large-scale HANP synthesis, a facile method of HANP recovery needs to be developed in future.

### 4.4. Significant Findings

The salient findings of this chapter are as follows:

1. Cell surface-associated protein (CSP) of *L. rhamnosus* GG was isolated by lithium chloride extraction.
2. Spindle-shaped crystalline HANPs with an average particle size distribution of ~200-530 nm was synthesized by using CSP of *L. rhamnosus* GG as a biomineralization template.
3. The F4SP (~25 kDa) purified fraction protein present in the CSP extract of *L. rhamnosus* GG supported biomineralization process and rendered generation of plate-shaped and crystalline HA of micron scale dimension.
4. Whole cell (WC) of *L. rhamnosus* GG could also render biomineralization and support synthesis of HANPs.
5. Desorbed WC-HANPs recovered by cell lysis were needle shaped and 70-110 nm in size.

Based on the leads obtained in the present study, it is evident that the CSP extract from the probiotic *L. rhamnosus* GG rendered facile synthesis of HANPs. It is well established that HANPs can enhance the osteoconductive and osteointegrative attribute of polymeric scaffolds and hold considerable potential in bone tissue engineering applications. Based on this notion, the next chapter describes the generation of CSP-HANP-grafted scaffold for supporting bone cell growth and differentiation.

# Chapter 5

## *L. rhamnosus* GG Cell Surface-Associated Protein (CSP)-Mineralized HANP Incorporated in Polymeric Scaffold for Bone Cell Growth

*This chapter describes the generation of chitosan-gelatin scaffold incorporated with L. rhamnosus GG CSP-mineralized HANP and its in vitro evaluation for bone cell growth and differentiation.*

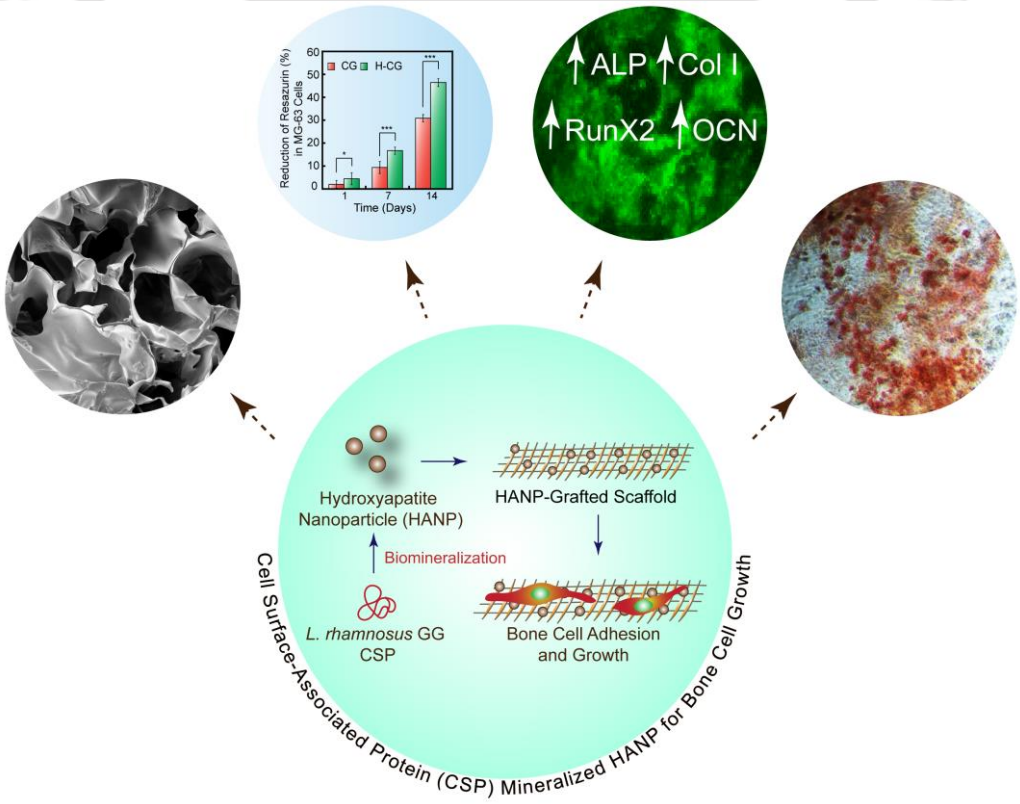

# ABSTRACT

This chapter describes the use of HANPs obtained by mineralization of *L. rhamnosus* GG cell surface-associated protein (CSP) for the development of an osteogenic chitosan-gelatin (CG)-based scaffold. CG scaffold incorporated with 15% w/v CSP-HANP (H-CG) was generated. FESEM analysis clearly indicated that both CG as well as H-CG scaffolds had interconnected pores, wherein the pore size ranged between 140-300 µm and 160-230 µm, respectively. HANP deposition in H-CG lead to the formation of rough edges that could be visualized under higher magnification in FESEM. HANP deposition within H-CG was evidenced by EDX analysis, which clearly indicated the presence of the elements Ca, P and O. CG was brownish-yellow in color, whereas H-CG had a milky white appearance. CG and H-CG were also characterized by FTIR and powder XRD. CG and H-CG scaffolds showed nearly 90% and 84% porosity, respectively, while the swelling ratios of CG and H-CG were 10.09% ± 0.4 and 9.79% ± 0.44, respectively. The degradation rate of H-CG scaffold was comparable with CG and ~ 69% lysozyme-mediated degradation was observed for H-CG over a time period of 21 days. Based on % resazurin reduction, the proliferation of MG-63 cells (osteoblast-like cells) seeded onto H-CG scaffold was higher (46.46 ± 0.76) as compared to CG scaffold (30.88 ± 0.56) after 14 days of cell proliferation. Calcein AM staining indicated a higher density of viable MG-63 cells growing on H-CG as compared to CG scaffold. The H-CG scaffold rendered superior alkaline phosphatase (ALP) activity in seeded MG-63 cells, while alizarin red S staining indicated that calcium mineral formation was higher in case of MG-63 cells seeded onto H-CG as compared to CG scaffold after 14 days of cell growth. The potential of H-CG in bone cell growth and differentiation was substantiated in gene expression studies, wherein expression of the osteogenic marker genes ALP, Col I, Runx2 and OCN was unequivocally higher in MG-63 cells seeded in H-CG as compared to CG scaffold.

## 5.1. Introduction

Hydroxyapatite (HA) holds significant prospect in bone tissue engineering based on its biocompatible and osteoconductive attributes (Haider *et al*., 2017; Brokesh and Gaharwar, 2020). Bone fracture and defects are major concerns in orthopedic healthcare. Standard methods of restoring bone defects include autografts, allografts and demineralized bone matrix. However, these methods are fraught with limitations as they can be associated with post-operative complications, host immune reactions and infections (Giannoudis *et al*., 2005). In this context, bone tissue engineering has emerged as a viable alternative and entails the use of functional substitutes or scaffolds as well as implants (Bose *et al.*, 2012; Ohgushi *et al.*, 2005; Srouji and Livne, 2005). Ideally, a bone scaffolding matrix should render mechanical support, display favorable biodegradation and possess porous structure for cellular infiltration and optimal oxygen and nutrient supply to the cells (Wang *et al.*, 2017; Khaled *et al.*, 2011; Ngiam *et al.*, 2011). Further, the scaffolds should promote osteointegration and osteoconduction. Several techniques are used to fabricate bone tissue engineering scaffolds, which include solvent casting and particulate leaching, gas foaming, freeze drying, phase separation, electrospinning and 3D bioprinting (Almirall *et al.*, 2004; Turnbull *et al.*, 2018; Kang *et al.*, 2006).

Hydroxyapatite (HA), which constitutes the mineral phase of natural bone renders hardness and stiffness to the bone matrix (Thein-Han *et al.*, 2009; Kim *et al.*, 2006; Frohbergh *et al.*, 2012). Hence, synthetic HA, and in particular, nanoscale HA in osteogenic grafts has yielded superior bioactivity, enhanced cell adhesion, proliferation, and integration (Zhou and Lee, 2011; Li *et al*., 2019; Anitha *et al*., 2017). Despite its prospect in osteogenesis, the intrinsic hardness, brittleness and slow degradation of HA is a limitation (Sun *et al*., 2011). In this context, integration of HANPs in scaffolds made of chitosan and other polymers have led to enhanced properties and fulfilled several functional requirements in scaffolds used for bone tissue engineering (Dai *et al*., 2020; Kim *et al*., 2006; Yu *et al*., 2020; Farokhi *et al*., 2018; Veiga *et al*., 2020).

Based on the aforementioned rationale, this chapter describes the generation of chitosan gelatin (CG) scaffolds incorporated with HANPs derived by mineralization of *L. rhamnosus* GG CSP. The characterization of HANP-incorporated CG scaffold (H-CG scaffold) is presented. Further, the potential of the developed H-CG scaffold to support bone cell growth and differentiation in a cell culture model is also demonstrated.

## 5.2. Materials and Methods

### *5.2.1. Growth Media and Chemicals*

Gelatin and alizarin red S were purchased from Himedia (India). Dimethyl sulfoxide (DMSO) was obtained from Merck (India). Alkaline phosphatase (ALP) enzyme and p-nitrophenyl phosphate (PNPP) were procured from Sisco Research Laboratories (India). Dulbecco's Modified Eagle Medium (DMEM), trypsin-EDTA, 3-(4,5-dimethyl-2-thiazolyl)-2,5-diphenyl-2H-tetrazolium bromide (MTT), chitosan, alamar blue and Calcein-AM were procured from Sigma-Aldrich. TRIzol reagent, SYBR Green qRT-PCR one step kit was obtained from Invitrogen.

### *5.2.2. MG-63 Cell Culture*

Human osteosarcoma cells (MG-63 cells) were procured from National Animal Cell Repository, National Centre of Cell Sciences (NCCS) Pune, India. MG-63 cells were grown in 25 $cm^2$ tissue culture flasks in DMEM supplemented with 10% (v/v) FBS, 100 units/mL penicillin, and 100 µg/mL streptomycin at 37°C in a humidified atmosphere of 5% $CO_2$ until the cells were approximately 90% confluent.

### *5.2.3. Cytotoxic Effect of L. rhamnosus GG CSP and CSP-HANPs*

The cytotoxic effect of CSP extract from *L. rhamnosus* GG and HANPs obtained from CSP (CSP-HANP) were tested on human embryonic kidney (HEK 293) cell lines and human osteosarcoma (MG-63) cell lines by an MTT assay, following the manufacturer instruction (Sigma-Aldrich, MO, USA). HEK 293 and MG-63 cells were initially propagated in Dulbecco's Modified Eagle Medium (DMEM) supplemented with 10% fetal bovine serum (FBS), penicillin (100 units/mL) and streptomycin (100 µg/mL) at 37°C in a $CO_2$ incubator under a humidified atmosphere of 5% $CO_2$. The cells were subsequently seeded in 96 well plates ($10^4$ cells/well) and CSP (10 µg/ml) and HANPs (1.0 mg/ml) made in DMEM were added to the cells in separate sets and incubated for 24 h under 5% $CO_2$ at 37°C. Following incubation, the media was aspirated and fresh DMEM containing MTT solution was added to the wells and incubated for 4 h at 37°C. Subsequently, the supernatant was removed and the insoluble formazan product was solubilized in DMSO and its absorbance was measured in a microtitre plate reader (Infinite M200, TECAN, Switzerland) at 550 nm. The absorbance obtained for control

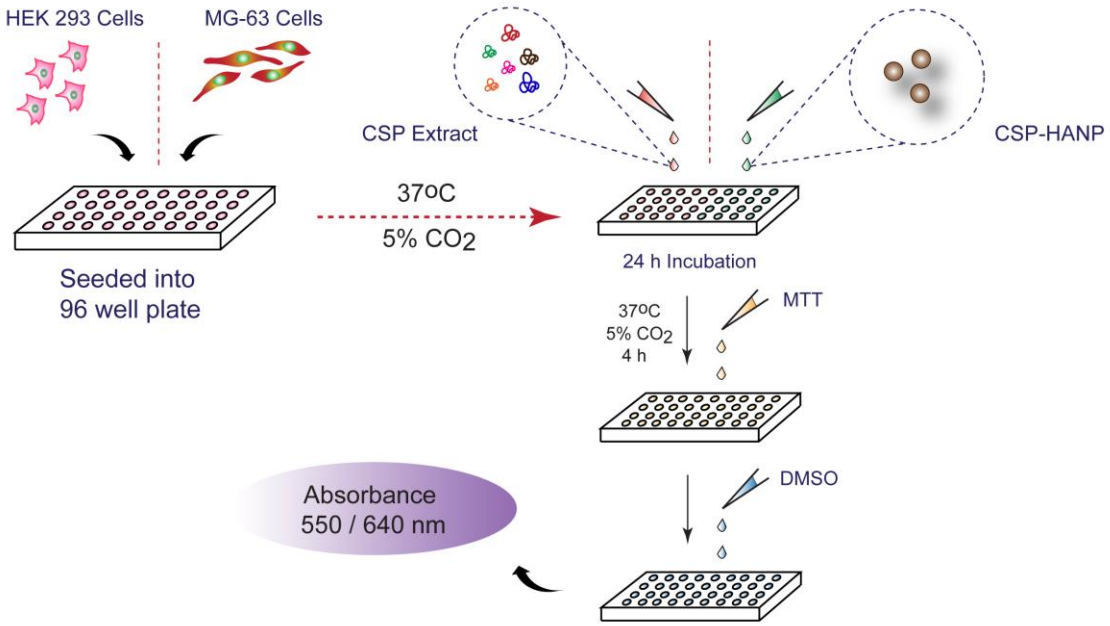


**Scheme 5.1.** Schematic representation of MTT-based assay to ascertain cytotoxic potential of CSP and CSP-HANP on cultured HEK 293 cells and MG-63 cells.

samples (untreated cells) was considered to represent 100% cell viability, whereas the absorbance for treated cells were compared to the untreated control cells to determine % cell viability. MTT assay was performed in six independent sets and each set consisted of three replicates. Data analysis and determination of standard deviation was performed with Microsoft Excel 2010 (Microsoft Corporation, USA). A schematic representation illustrating MTT-based assay to ascertain cytotoxic potential of CSP and CSP-HANP on cultured HEK 293 cells and MG-63 cells is indicated in Scheme 5.1.

*5.2.4. Hydroxyapatite-Incorporated Chitosan-Gelatin (H-CG) Scaffold*

H-CG scaffold was prepared using a stirring and freeze-drying method (Maji *et al.*, 2018). Chitosan, gelatin and CSP-HANPs were mixed to get a homogeneous formulation containing 2% chitosan (w/v), 2% gelatin (w/v) and 15% CSP-HANPs (w/v). Crosslinking was accomplished by adding 0.15% glutaraldehyde. Subsequently, the mixture was kept in -80°C for 12 h and lyophilized for 48 h to obtain porous scaffolds. The lyophilized porous scaffolds were neutralized with 1% NaOH solution and washed with sterile MilliQ water several times. The neutralized scaffolds were lyophilized for further use. Chitosan-gelatin (CG) scaffold devoid of any HANPs was also prepared following the aforementioned steps. Prior to *in vitro* cell culture, sterilization of CG and H-CG scaffold was accomplished by washing with 70% ethanol

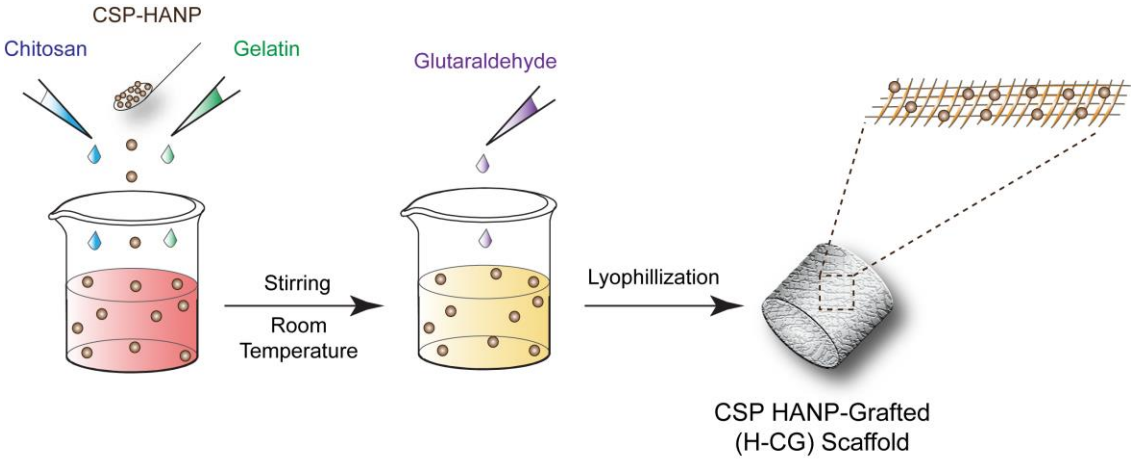


**Scheme 5.2.** Cartoon illustrating generation of CSP-HANP-incorporated chitosan-gelatin (H-CG) scaffold using stirring and freeze-drying method.

followed by UV treatment. A schematic representation of generation of CSP-HANP-incorporated chitosan-gelatin (H-CG) scaffold illustrated in Scheme 5.2.

The prepared scaffolds were characterized by microscopic analysis, FTIR, powder XRD, determination of porosity, swelling ratio and enzymatic degradation. These methods are described in the following section.

*5.2.4.1. Morphological Analysis*

The surface morphology of a thin section of CG and H-CG scaffold was characterized by Field Emission Scanning Electron Microscope (FESEM, Zeiss, Germany) analysis and EDX analysis. NIH Image J software (imagej.nih.gov) was used to determined pore size and its distribution.

*5.2.4.2. FTIR and Powder XRD Analysis of Scaffolds*

FTIR spectra of scaffolds were recorded in ATR mode at 4.0 $cm^{-1}$ resolution in an infrared spectrometer (Perkin-Elmer). Eight scans were performed for every sample in the range of 4000 $cm^{-1}$ to 500 $cm^{-1}$. Powder X-ray diffraction (D2 Phaser, Bruker, Germany) data of CG and H-CG scaffolds were recorded at room temperature over the 2θ range of 10°- 40° at a step size of 0.02° and a count time of 2s/step.

*5.2.4.3. Determination of Scaffold Porosity and Swelling Ratio*

The porosity of the scaffolds was examined by the liquid displacement method (Azizian *et al.*, 2018). The scaffolds were cut into equal size discs

(4 mm diameter × 2 mm thickness). The scaffold discs were carefully dipped in a known volume ($V_1$) of ethanol taken in a graduated measuring cylinder. Air bubble within scaffolds was carefully eliminated by applying a gentle pressure to the scaffolds against the cylinder wall. The volume after scaffold immersion was recorded ($V_2$). Final ethanol volume was recorded after removal of scaffold ($V_3$). To estimate the change in volume due to evaporation during measurement, a second measuring cylinder without scaffold was used as control to normalize the final volume. Scaffold porosity was calculated using the following formula:

$$Scaffold\ Porosity\ (\%) = [(V_1 - V_3)/(V_2 - V_3)] \times 100$$

Swelling ratio of scaffolds was studied using conventional gravimetric procedure (Chi *et al.*, 2019). The weight of lyophilized scaffolds in dried state ($W_d$) was recorded followed by immersion in sterile phosphate buffered saline (PBS, pH 7.4). At predetermined time points, scaffolds were carefully taken out, excess surface liquid was wiped by filter paper, followed by recording swollen weight ($W_s$). The swelling ratio was calculated using the equation:

$$Swelling\ Ratio\ (\%) = [(W_s - W_d)/W_d] \times 100$$

where $W_d$ is the dry weight of the construct and $W_s$ is the swollen weight of the construct.

*5.2.4.4. Enzymatic Degradation of Scaffold*

Enzymatic degradation of CG and H-CG scaffolds was evaluated using lysozyme from chicken egg white (Sigma-Aldrich, U.S.). Briefly, scaffolds were immersed in sterile PBS (pH 7.4) containing 0.01% lysozyme and incubated at 37°C. Enzyme solution was replaced every 3 days with freshly prepared solution. Scaffolds immersed in PBS without enzyme under similar conditions were used as control. On every third day, scaffolds were taken out, air-dried, and weighed to calculate weight loss over a period of 21 days.

*5.2.5. Seeding of MG-63 Cells on Scaffolds*

MG-63 cells were initially grown in a 25 $cm^2$ tissue culture flask in Dulbecco's Modified Eagle's Medium (DMEM) supplemented with 10% (v/v) Fetal bovine serum (FBS), penicillin (100 units/mL) and streptomycin (100 µg/mL) under a humidified atmosphere of 5% $CO_2$ in an incubator until the cells were approximately 80% confluent. CG and H-CG scaffolds of 4.0 mm diameter and 2.0 mm thickness were used for cell seeding. Initially the scaffolds were dipped in DMEM media in 96 well tissue culture plate for 24 h followed by seeding with $3 \times 10^5$ MG-63 cells suspended in 20 µL of DMEM medium. The cell seeded scaffolds were incubated at 37°C incubator with 5% $CO_2$ for 5 h to allow cell adherence. After 5 h, fresh culture media was gently added to each well. Fresh medium was replaced every alternate day, and scaffolds were harvested in separate sets on day 1, 7 and 14, respectively. A schematic representation illustrating the methods used to ascertain the potential of H-CG scaffold in supporting growth and differentiation of seeded MG-63 cells in Scheme 5.3.

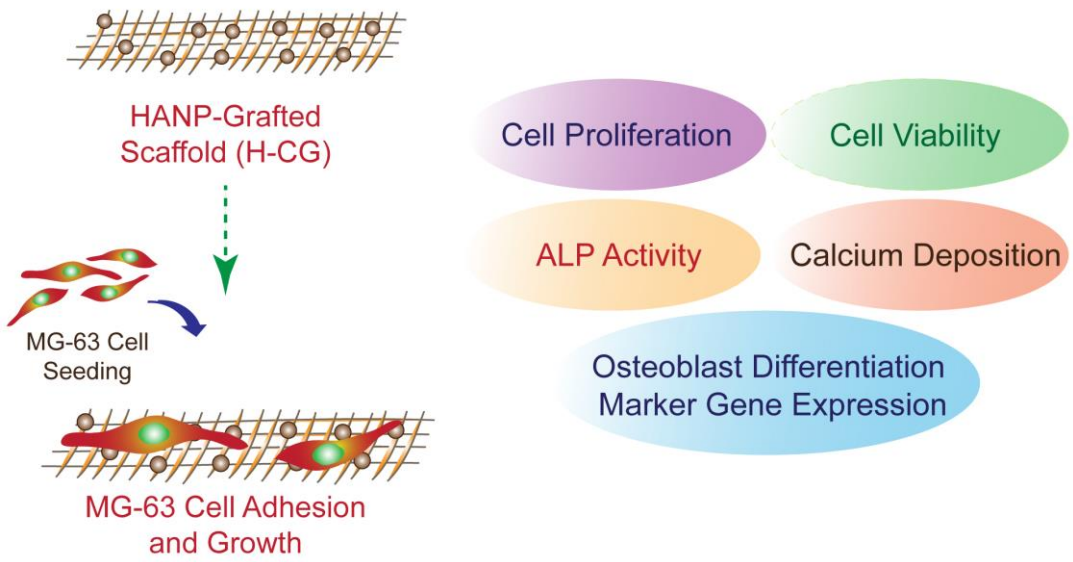


**Scheme 5.3.** Schematic illustrating the methods used to ascertain the potential of H-CG scaffold in supporting growth and differentiation of seeded MG-63 cells.

*5.2.6. Estimation of Cell Proliferation and Viability*

MG-63 cell proliferation was ascertained using alamar blue dye reduction assay. Briefly, CG and H-CG scaffolds with and without MG-63 cells were incubated at 37°C in DMEM medium containing 10% (v/v) alamar blue dye (Sigma, USA). At the end of 4 h incubation, the absorbance of a 100 µL aliquot of medium from each sample was measured at 570 nm as well as 600 nm in a multiplate reader (Infinite M200, TECAN, Switzerland). Scaffolds without cells incubated with 10% alamar blue dye was considered as negative control. Proliferation of MG-63 cells was analysed at predefined time points based on % resazurin reduction (Das *et al.*, 2013). Cell viability was determined by staining MG-63 cells with calcein-AM (Sigma-Aldrich, U.S.). Briefly, the cell-seeded scaffolds, harvested after 7 and 14 days of cell culture, were initially washed with sterile PBS to remove cellular debris. Cell seeded scaffolds were stained with calcein-AM solution (working concentration 4.0 µM in sterile PBS) for 20 min and visualized under fluorescence microscope (Eclipse Ti-U, Nikon) with an excitation filter of 450-490 nm (Maji *et al.*, 2018).

*5.2.7. Alkaline Phosphatase Assay and DNA Quantification*

Alkaline phosphatase (ALP) activity was determined by an assay based on hydrolysis of p-nitrophenyl phosphate (pNPP) to p-nitrophenol. Initially, MG-63 cell seeded scaffolds were washed twice with sterile PBS followed by lysis with 0.1% Triton X-100 for 30 min. The lysate was centrifuged at 5000 rpm for 10 min and the obtained supernatant was used to measure ALP activity. Briefly, 50 µl supernatant was incubated with 125 µl of active reagent (0.012 M pNPP in 0.05 M diethanolamine) solution at 37°C for 1 h in the dark. Following incubation, the reaction was terminated by adding 50 µL of 2.5 M NaOH. Subsequently, the absorbance of p-nitrophenol was measured at 405 nm in a multimode reader (Infinite M200, TECAN, Switzerland), which corresponds to alkaline phosphatase activity (Pramanik *et al.*, 2009). DNA content of MG-63 cells seeded in CG and H-CG scaffold was measured using a Quant iT PicoGreen ds reagent (Molecular Probes, Life Technologies, U.S.) by following the manufacturer's protocol. Briefly, after different days of culture, cells seeded in scaffolds were lysed by incubating the scaffolds in sterile PBS containing 0.1% Triton X-100. The lysate was centrifuged at 11000 rpm for 2 min. A 25 µl aliquot of the supernatant was added to PicoGreen premixed with 175 µl of TE buffer (10 mM Tris-HCl, pH 7.5, 1 mM EDTA) and incubated for 5 min. Fluorescence emission of the

solution was measured at 520 nm in a multiplate reader (Infinite M200, TECAN, Switzerland) at an excitation wavelength of 490 nm and was considered as an index of DNA content in the cell. ALP activity obtained by hydrolysis of pNPP was finally normalized against the fluorescence emission of PicoGreen-DNA complex obtained for MG-63 cells.

*5.2.8. Mineral Deposition*

The degree of mineralization in MG-63 cells was estimated by Alizarin red S staining. Briefly, a staining solution containing 1.0 mg/mL of Alizarin Red S (prepared in sterile MilliQ water and adjusted to pH 4.5) was added to the scaffolds wherein the MG-63 cells were grown for 14 days. After 15 min incubation, the staining solution was thoroughly washed with sterile MilliQ water followed by visualization of the cell-seeded scaffolds under a bright field microscope.

*5.2.9. Gene Expression Studies*

Real-time PCR was used to determine expression of collagen I (Col I), alkaline phosphatase (ALP), Runt-related transcript 2 (Runx2), osteocalcin (OCN) and glyceraldehyde-3-phosphate-dehydrogenase (GAPDH) mRNA transcripts. The sequence of the primers for these genes is indicated in Table 5.1. Separate sets of CG and H-CG scaffolds wherein MG-63 cells were seeded and grown for 1, 7 and 14 days were treated with 500 µL TRIzol reagent (Invitrogen, U.S.) for 5 min followed by 100 µL chloroform treatment. Chloroform treated samples were centrifuged at 12000 rpm for 15 min at 4°C. Subsequently, the upper aqueous phase containing RNA was mixed with 250 µL isopropanol followed by centrifugation at 12000 rpm for 10 min at 4°C to obtain RNA pellet. RNA concentration was quantified by measuring the absorbance at 260 nm (NanoPhotometer NP80, IMPLEN). Following RNA isolation, 150 ng of isolated RNA was used as template for real-time PCR reactions. The PCR reaction was set up using SYBR 1-STEP qRT-PCR kit and the tubes were incubated in a 36-Well Rotor, QIAGEN Rotor-Gene Q qRT-PCR machine. Expression of each target gene was normalized against GAPDH. Reverse transcription was accomplished by incubating the reaction mixture at 50°C for 3 min. The subsequent PCR conditions were as follows: (1) initial hold temperature at 94°C for 2 min, (2) denaturation step at 94°C for 30 sec, (3) annealing at 59°C for 30 sec, (4) extension at 72°C for 30 sec for a

**Table 5.1.** Sequence of primers used in gene expression studies.

| Sl. No. | Gene | Primer Sequence (5' to 3') | Amplicon Size (bp) |
|---|---|---|---|
| 1. | Collagen I (Col I) | Forward: CCCTGGAAAGAATGGAGATGAT<br>Reverse: ACTGAAACCTCTGTGTCCCTTCA | 139 |
| 2. | Alkaline Phosphatase (ALP) | Forward: CCACGTCTTCACATTTGGTG<br>Reverse: AGACTGCGCCTGGTAGTTGT | 196 |
| 3. | Runx2 | Forward: TCTGGCCTTCCACTCTCAGT<br>Reverse: GACTGGCGGGGTGTAAGTAA | 161 |
| 4. | Osteocalcin (OCN) | Forward: CAGCGAGGTAGTGAAGAGAC<br>Reverse: GCCAACTCGTCACAGTCC | 126 |
| 5. | GAPDH | Forward: GACCTGACCTGCCGTCTA<br>Reverse: GTTGCTGTAGCCAAATTCGTT | 237 |

total of 50 cycles. Analysis of RT-PCR data was accomplished using the LinReg PCR (2014.x) software and the cycle threshold ($C_T$) values were calculated after baseline correction. The fold change in gene expression values was determined by the $\Delta C_T$ method (Livak *et al.*, 2001).

## 5.3. Results and Discussion

### *5.3.1. Cytotoxic Potential of L. rhamnosus GG CSP-derived HANP (CSP-HANP)*

Based on the results highlighted in the previous chapter (Chapter 4), it was apparent that CSP extract from the probiotic *L. rhamnosus* GG rendered facile synthesis of HANPs. It is widely acknowledged that HANPs can enhance the osteoconductive and osteointegrative attribute of polymeric scaffolds and hence hold considerable promise in bone tissue engineering applications (Brokesh and Gaharwar, 2020; Wang *et al.*, 2007; Bhattacharjee *et al.*, 2016). Hence, the subsequent objective in the present investigation was to incorporate CSP-HANPs into a chitosan-gelatin based scaffold and ascertain the potential of the scaffold to support growth and differentiation of bone cells in an *in vitro* cell culture model. To this end, the cytotoxic effect of CSP-HANP on cultured human embryonic kidney cells (HEK 293 cells) and human osteosarcoma cells (MG-63 cells) was initially ascertained. It was encouraging to observe that both *L. rhamnosus* GG CSP extract (10 µg/mL), which was used as a mineralization template as well as the CSP-mineralized HANPs (1.0 mg/mL) were non-toxic against

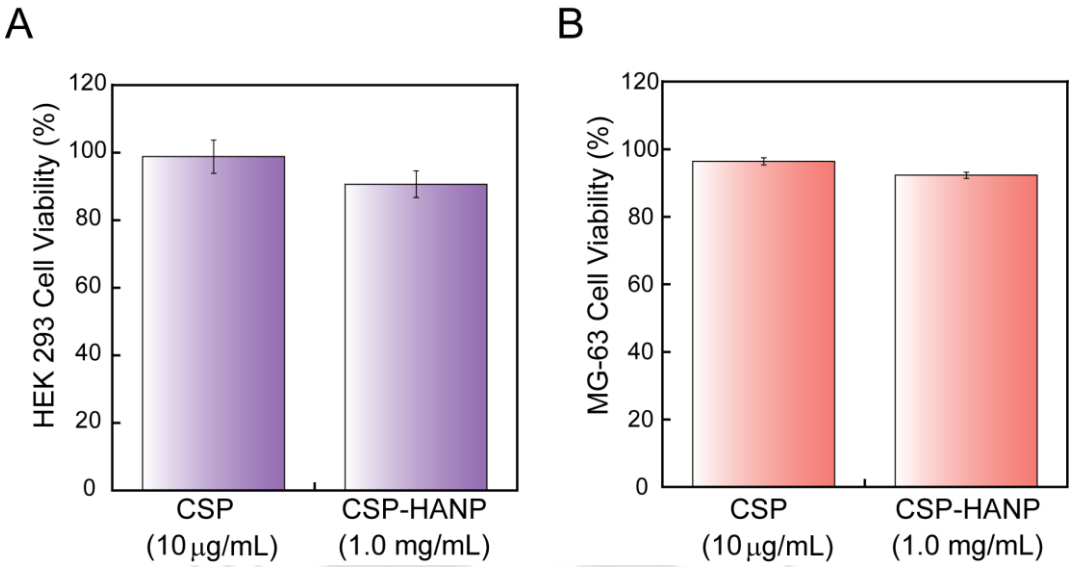


**Figure 5.1.** MTT assay to determine the cytotoxic effect of CSP of *L. rhamnosus* GG and HANPs obtained from mineralized-CSP against (A) HEK 293 cells and (B) MG-63 cells.

HEK 293 cells and MG-63 cells (Figure 5.1). This indicated that the CSP-HANPs were biocompatible and amicable for bone cell engineering application.

*5.3.2. CSP-HANP Incorporated Chitosan-Gelatin (H-CG) Scaffold*

In order to ascertain the potential of *L. rhamnosus* GG CSP derived HANPs in bone cell growth and differentiation, chitosan-gelatin (CG) scaffold incorporated with 15% w/v CSP-HANP (H-CG) was generated by following a standard method (Maji *et al.*, 2018) FESEM analysis indicated that both CG and H-CG scaffolds were porous and displayed interconnected pore structure (Figure 5.2A-B). During scaffold generation, the bubbles formed by a rigorous stirring process perhaps retained their stability and did not collapse during subsequent lyophilization, leading to the formation of an interconnected porous network (Maji *et al.*, 2018). The pore size distribution of CG and H-CG scaffold ranged between 140-300 µm and 160-230 µm, respectively, while the average pore size of CG and H-CG scaffold was 214.77 ± 59.84 µm and 193.49 ± 44.22 µm, respectively. Based on the obtained pore size, the H-CG scaffold is conducive for bone cell growth (Alonso-Sierra *et al.*, 2017; Babaie and Bhaduri, 2018). The CG scaffold appeared brownish-yellow in color (Figure 5.2A, inset), whereas H-CG scaffold had a milky white appearance (Figure 5.2B, inset). The presence of HANPs within H-CG scaffold was confirmed by EDX analysis, which clearly indicated the presence of Ca, P and O (Figure 5.2C). In FTIR analysis, the characteristic peaks

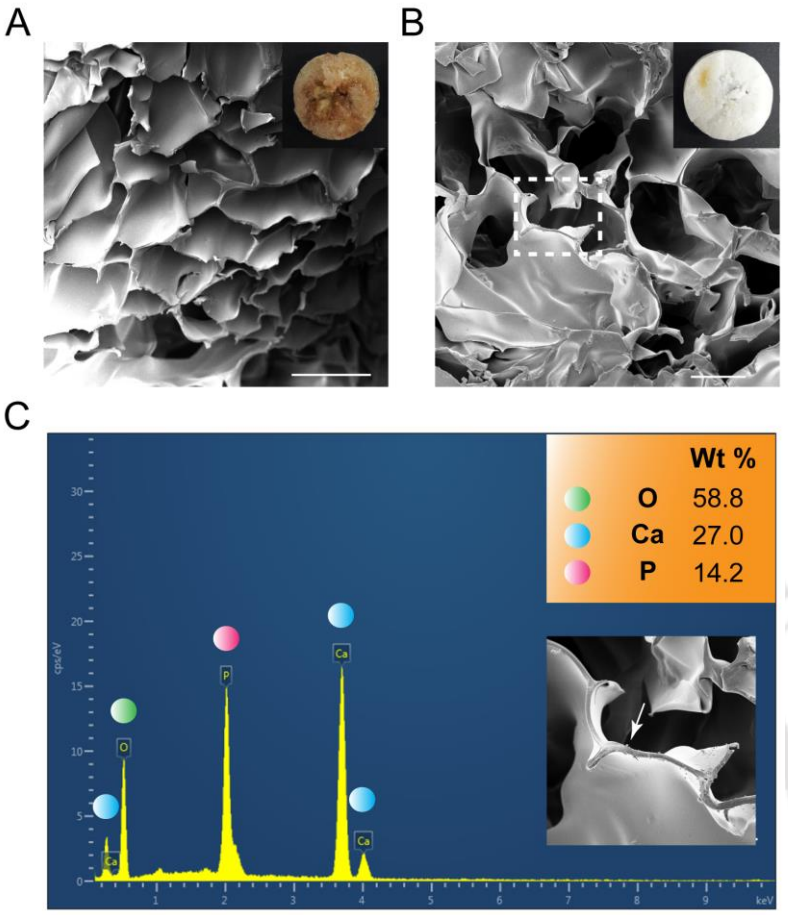


**Figure 5.2.** FESEM analysis of (A) CG scaffold and (B) H-CG scaffold. Scale bar for the images is 100 µm. Inset in (A) and (B) indicates the physical appearance of the respective scaffolds, (C) EDX analysis of H-CG scaffold. Inset: White arrow indicates the well-defined sharp edge in H-CG scaffold.

for chitosan (1325 $cm^{-1}$, 1150 $cm^{-1}$ and 1063 $cm^{-1}$) and gelatin (1650 $cm^{-1}$, 1525 $cm^{-1}$, 1235 $cm^{-1}$) (Maji *et al.*, 2018) were evident in both the scaffolds (Figure 5.3A). The presence of significant peaks at 3568 $cm^{-1}$, 1461 $cm^{-1}$ and 1041 $cm^{-1}$ corresponding to $OH^-$, $CO_3^{2-}$ and $PO_4^{3-}$ stretching frequencies, respectively, supported the incorporation of HANPs in H-CG scaffold (Figure 5.3A). Powder XRD analysis revealed sharp peaks at $2\theta = 26^0$, $31^0$ and $33^0$, which correspond to (002), (211) and (300) lattice planes, respectively, reiterating the presence of HANPs in H-CG scaffold (Figure 5.3B).

CG scaffold exhibited significant overall porosity, amounting to ~90% (Figure 5.4A). Upon incorporation of HANPs the porosity of H-CG scaffold was still high (~84%), which suggested that HANPs perhaps did not occupy much of the internal space and occlude the pores of the scaffold. The high porosity of H-CG scaffold augers well for bone tissue engineering applications (Chen *et al.*, 2019; Akay *et al.*, 2004). The

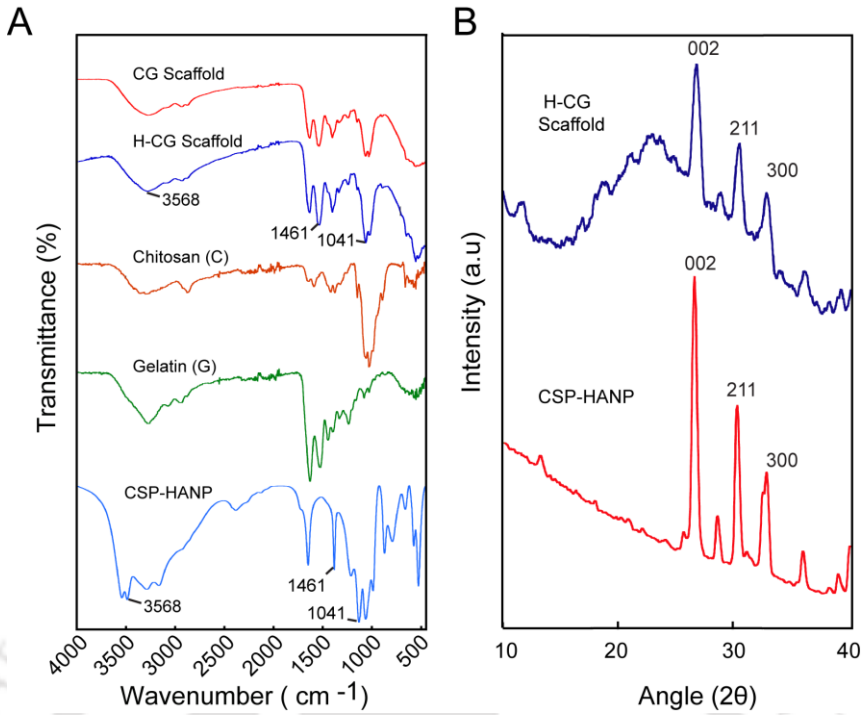


**Figure 5.3.** Characterization of CG and H-CG scaffolds by (A) FTIR analysis. (B) Powder XRD analysis.

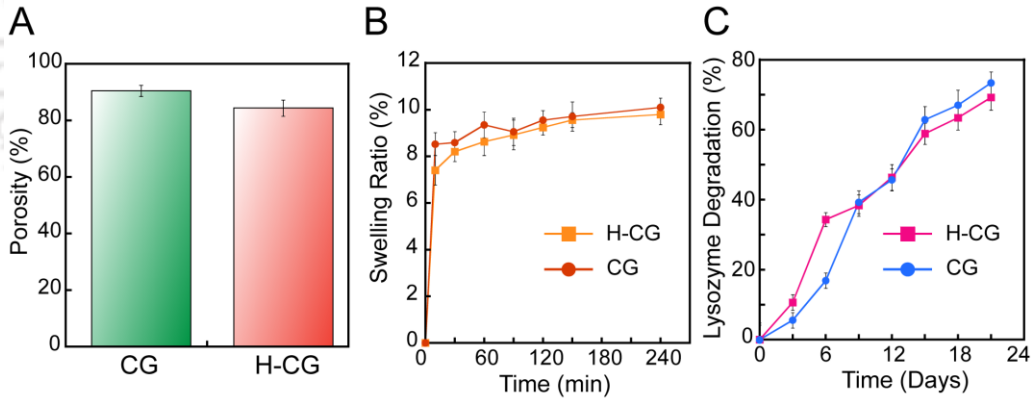


**Figure 5.4.** Characterization of CG and H-CG scaffolds by measuring (A) Porosity, (B) Swelling ratio (%) and (C) Enzymatic degradation in presence of lysozyme.

overall hydration (swelling ratio) of the scaffold reduced marginally from ~10.09% in CG scaffold to ~9.79% in H-CG (Figure 5.4B), suggesting that the diffusive nature was essentially retained in H-CG scaffold. Reduction in hydration and swelling ratio of scaffold owing to HANP incorporation in scaffold has been reported earlier (Maji *et al.*, 2018; Pawelec *et al.*, 2017). Biodegradation of H-CG scaffolds in presence of lysozyme was marginally less (~69%) than CG scaffold (~77%) over a period of 21 days (Figure 5.4C) and was similar to the observation in an earlier study (Dan *et al.*, 2016).

The sustained degradation profile of H-CG observed over 21 days augers well as it is acknowledged that bone cell regeneration is a slow process and a scaffold degradation rate that complements the turnover of new tissue will likely provide optimal benefit in bone tissue engineering applications. Based on this premise, the observed sustained degradation enhances the scope of H-CG scaffold in bone tissue engineering.

*5.3.3. Cellular Viability and Proliferation in H-CG Scaffold*

The ability of H-CG scaffold to support the growth and differentiation of MG-63 cells (osteoblast-like cells) was evaluated. The proliferation of MG-63 cells was ascertained by Alamar blue assay, wherein % resazurin reduction observed for cells grown on H-CG scaffold was significantly higher than that observed for CG scaffold (Figure 5.5A). This difference became even more prominent with increasing period of cell growth, wherein % resazurin reduction was higher in MG-63 cell seeded H-CG scaffold (~46%) than CG scaffold (~30%) after 14 days of cell growth (Figure 5.5A). Resazurin reduction can be correlated with the metabolic activity of healthy cells (Borra *et al.*, 2009). Apart from the inherent porosity observed in both the scaffolds, which likely ensured high nutrient diffusion and gas transport, the presence of HANPs presumably enhanced the osteoconductive and osteointegrative attribute of the H-CG scaffold. This, in turn, enabled robust cell growth and higher metabolic activity in

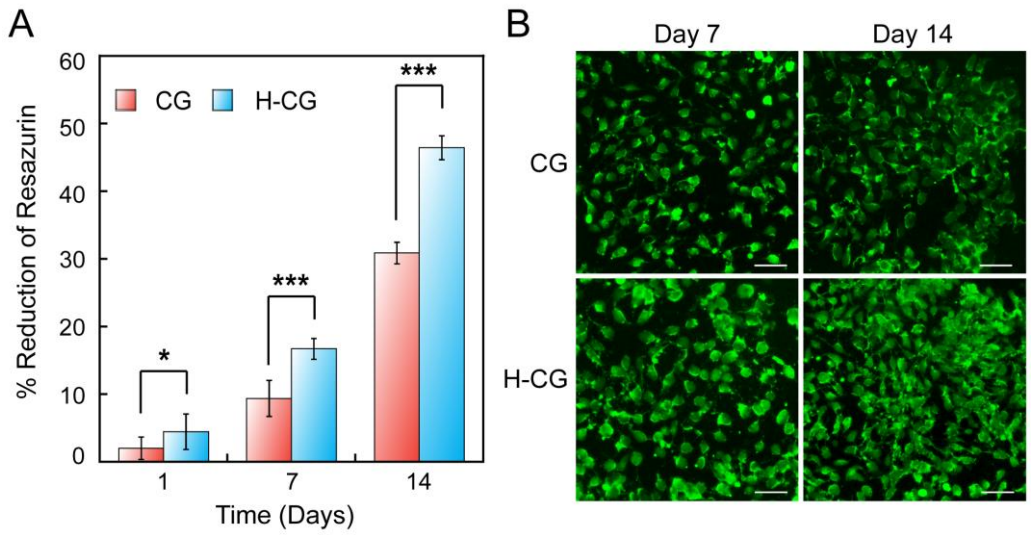


**Figure 5.5.** (A) Measurement of proliferation of MG-63 cells seeded in CG and H-CG scaffolds by Alamar blue assay. * and *** indicate $p$ value < 0.05 and < 0.001, respectively in one-way ANOVA. (B) Calcein-AM staining of MG-63 cells grown on CG and H-CG scaffolds. Scale bar for the images is 100 µm.

MG-63 cells seeded in H-CG, which is manifested herein as higher % resazurin reduction. Calcein-AM staining indicated a large number of viable cells growing on the scaffolds and the density of MG-63 cells growing on H-CG scaffold appeared higher than that observed in case of CG scaffold (Figure 5.5B). Presence of HANPs in the scaffold may promote superior osteoblast adhesion and proliferation as suggested earlier (Zhou and Lee, 2011). Importantly, the large number of viable cells observed in calcein-AM staining also revealed that the scaffolds were cytocompatible to osteoblast cells.

*5.3.4. Estimation of ALP Activity and Mineral Deposition*

A systematic increase in ALP activity was observed till 7 days for MG-63 cells seeded in both the scaffolds followed by a substantial drop in ALP activity thereafter (Figure 5.6A). Alkaline phosphatase (ALP) is an enzyme, which is recognized as an early osteogenic marker and is involved in extracellular matrix mineralization (Frohbergh *et al.*, 2012). Hence, the surge in ALP activity in H-CG seeded MG-63 cells till 7 days seems to corroborate this notion. Further, it is worth mentioning that the ALP activity in MG-63 cells seeded in H-CG scaffold was significantly higher on day 1 (~1.83 fold higher) and day 7 (~1.55 fold higher) as compared to cells grown on CG scaffold alone (Figure 5.6A). The enhanced ALP activity is an indicator of a higher

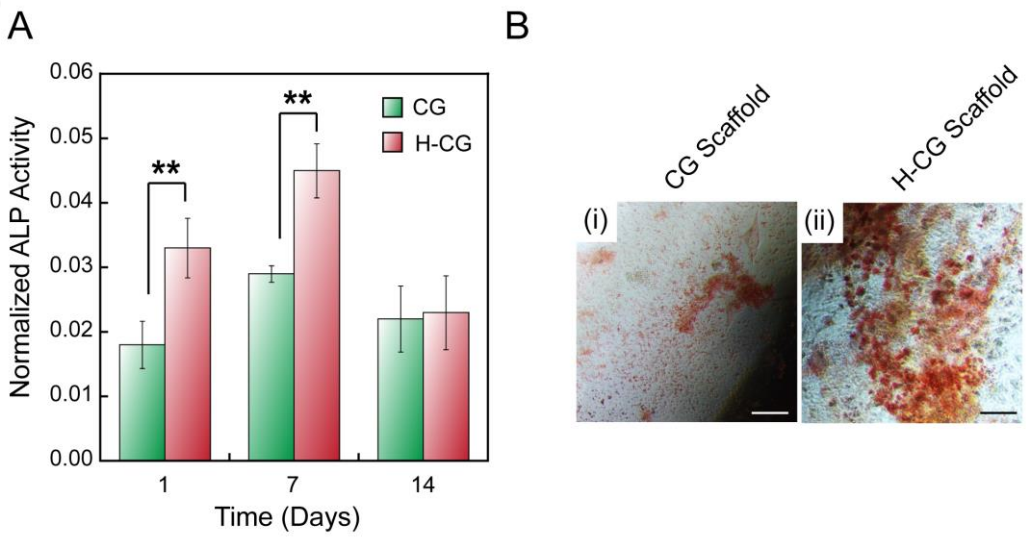


**Figure 5.6.** (A) Normalized alkaline phosphatase activity of MG-63 cells grown on CG and H-CG scaffolds. ** indicates *p* value < 0.01 in one-way ANOVA. (B) Visualization of calcium deposition by Alizarin red S staining in MG-63 cells cultured on CG and H-CG scaffolds for 14 days. Scale bar for the images is 100 µm.

number of osteogenic committed progenitor cells in the seeded H-CG scaffold (Golub and Boesze-Battaglia, 2007). Alizarin red S staining revealed that calcium deposition was superior in cells seeded in H-CG scaffold as compared to CG scaffold (Figure 5.6B). Based on a higher calcium deposition, it can be surmised that in comparison to CG scaffold, the H-CG scaffold contained a relatively larger population of MG-63 cells, which displayed a propensity to differentiate into osteoblast lineage cells and hence the H-CG scaffold was more conducive to induce osteogenic differentiation.

*5.3.5. Expression of Osteogenic Markers*

In order to check the influence of the scaffolds in osteogenic differentiation of MG-63 cells, expression of ALP, Col I, Runx2 and OCN osteogenic marker genes were ascertained. A quantitative real-time PCR analysis illustrated that the expression of ALP and Col I genes enhanced on day 14 as compared to day 7 (Figure 5.7A-B). Both ALP and Col I are early marker genes implicated in extracellular matrix mineralization and synthesis, respectively (Barrere *et al.*, 2006). Hence, a systematic increase in the turnover of ALP and Col I transcripts as evident from the gene expression studies presumably ensures early osteogenic differentiation and efficient mineralization in MG-63 cells. It was noteworthy that on Day 14, the fold change in the expression of ALP and Col I was significantly higher ($p$ value < 0.01) in H-CG scaffold (~1.69 and ~1.26 fold, respectively) as compared to the fold change observed in CG scaffold (~1.45 and ~1.34 fold, respectively) (Figure 5.7A-B), validating the benefit of HANP incorporation in scaffolds used for bone cell growth and differentiation as reported in earlier studies (Wang *et al.*, 2007; Bhattacharjee *et al.*, 2016). The expression of Runx2 and OCN marker genes was also higher on day 14 as compared to day 7 in seeded MG-63 cells (Figure 5.7C-D). Given that Runx2 is a transcription factor implicated in osteogenesis (Franceschi and Xiao, 2003; Salhotra *et al.*, 2020), high expression of Runx2 in seeded MG-63 cells would likely enhance expression of other osteoblast-specific genes and promote cell differentiation. The upregulation of OCN in seeded MG-63 cells on Day 14 as observed in gene expression studies (Figure 5.7D) is in support of the premise that OCN is a late osteoblast differentiation marker, implicated in extracellular matrix mineralization (Barrere *et al.*, 2006; Robler *et al.*, 2020). Akin to the results obtained for ALP and Col I, it was observed that on Day 14, the fold change in the expression of Runx2 and OCN was significantly higher ($p$ value < 0.001) in H-CG scaffold (~1.62 and ~1.36 fold, respectively) as compared to the fold change

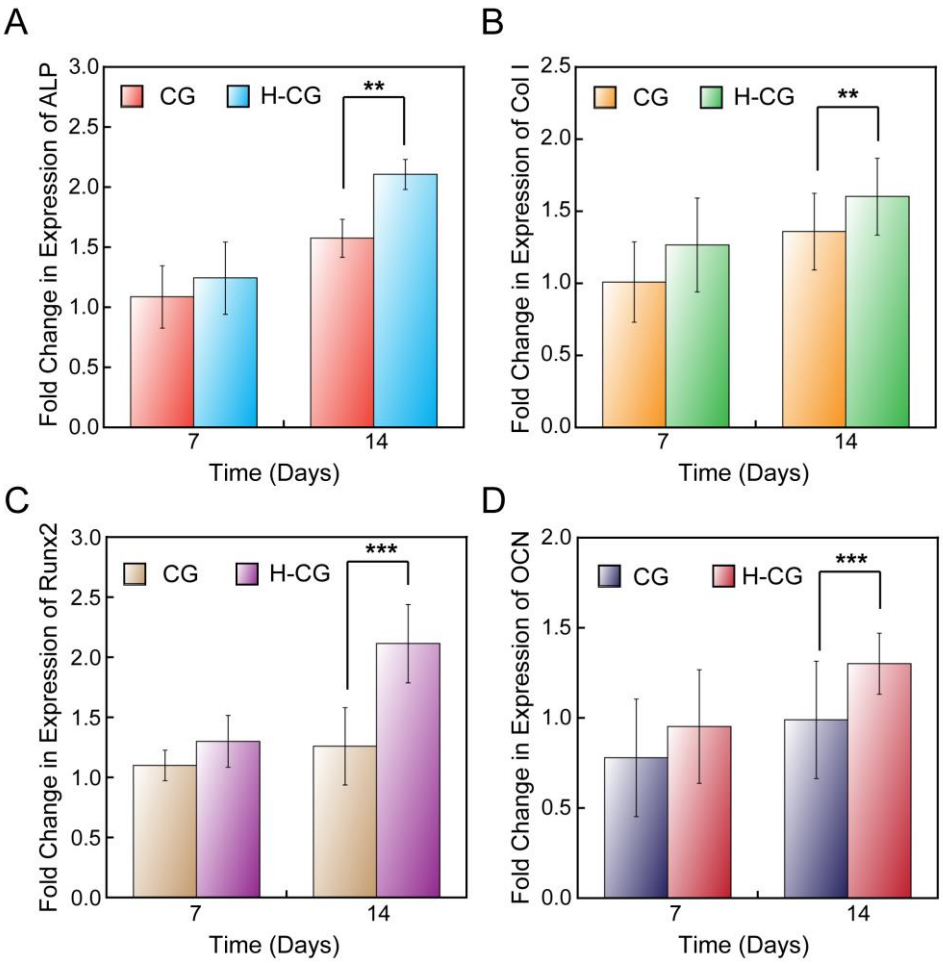


**Figure 5.7.** Quantitative real-time PCR analysis to ascertain the fold change in the expression of osteogenic genes in MG-63 cells grown on CG and H-CG scaffolds. (A) ALP. (B) Col I. (C) Runx2. (D) OCN. ** and *** indicate a *p* value of <0.01 and <0.001, respectively, in one-way ANOVA.

observed in CG scaffold (~1.14 and ~1.26 fold, respectively) (Figure 5.7C-D). This observation reiterated that CSP-HANP incorporation in CG scaffold distinctly enhanced bone cell growth and differentiation. It may be mentioned here that the results obtained in the present study pertaining to osteogenic differentiation of bone cells seeded on hydroxyapatite incorporated scaffold is comparable to the results reported for various types of synthetic hydroxyapatite (Yu *et al.*, 2017; Ding *et al.*, 2019; Wei *et al.*, 2020; Li *et al.*, 2020).

## 5.4. Significant Findings

The salient findings of this chapter are as follows:

1. Chitosan-gelatin scaffold incorporated with *L. rhamnosus* GG CSP-mineralized HANPs (H-CG) displayed favorable porosity, swelling property and biodegradation profile, thus rendering H-CG as an amicable scaffold for osteogenesis.

2. MG-63 osteoblast-like cells grown in H-CG scaffold displayed higher cell proliferation, alkaline phosphatase activity, and calcium mineral deposition after 14 days of cell culture.

3. The potential of H-CG in bone tissue engineering was substantiated in marker gene expression studies, wherein the seeded MG-63 cells displayed enhanced expression of ALP, Col I, Runx2 and OCN genes after 14 days of cell growth.

It was evident from the cumulative results obtained in Chapters 4-5 that *L. rhamnosus* GG CSP is a viable mineralization template for synthesis of biocompatible HANPs, which can be leveraged for bone cell growth and differentiation. However, given the labile nature of proteins as templates, there is also an interesting scope to explore rationally designed synthetic ligands that can mimic the protein/peptide template actions in the mineralization process and generate HANPs for biomedical applications. Based on this tenet, the following chapter describes the generation of HANPs using a low molecular weight 2-dodecylmalonic acid (MA) amphiphile and demonstrates their potential as a coating on titanium wire for supporting bone cell growth.

# Chapter 6

## Biomineralization Inspired Synthesis of HANPs Using Synthetic Amphiphile for Orthopaedic Implant Application

*This chapter illustrates a bio-inspired mineralization process for synthesis of hydroxyapatite nanoparticles using malonic acid amphiphile as a template. The HANPs were used to generate a type I collagen-HANP coated titanium wire implant that could support bone cell growth and differentiation.*

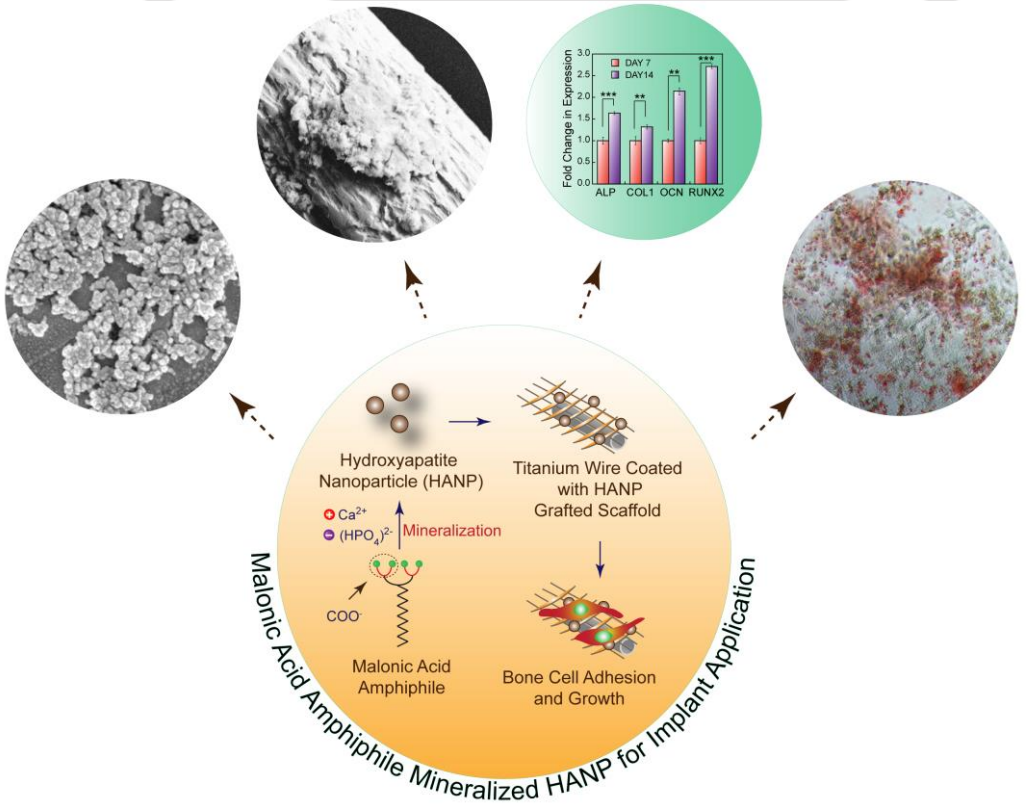

# ABSTRACT

This chapter highlights a biomineralization-inspired approach for the generation of hydroxyapatite nanoparticles (HANPs) using a low molecular weight amphiphilic ligand 2-dodecylmalonic acid (MA). HANPs synthesized by wet precipitation method in presence of various concentrations of MA were observed to vary in their particle size and also displayed heterogenous shapes. The smallest particle size of HANPs with stable size distribution was obtained in presence of 37 µM MA, wherein the nanoparticles referred to as $MA_2$-HANPs were 22-27 nm in size. The sharp peaks observed in powder XRD analysis at around $2\theta = 26^o$ and $31^o$ suggested the presence of crystalline hydroxyapatite, which was also corroborated by SAED analysis. The presence of HANPs was also evidenced through the characteristic stretching frequency at 3568, 1461 and 1041 $cm^{-1}$ obtained in FTIR analysis. In order to leverage the generated HANPs in orthopaedic application, titanium wire (TW) was coated with $MA_2$-HANPs incorporated collagen type I (H-TW). FESEM analysis revealed the presence of a thick corrugated surface coating on TW, indicating coating of the HANP-grafted collagen onto TW. The characteristic stretching frequency observed in FTIR analysis validated the presence of HANPs in the coated TW. The metabolic activity of osteoblast-like MG-63 cells grown on H-TW increased progressively as evidenced by the heightened resazurin reduction after 14 days of cell growth (~ 48%) in comparison to the cells grown for 7 days (~32%). Robust cell proliferation and high viability of MG-63 cells grown on H-TW was also captured through calcein-AM staining. Interestingly, the early marker genes (Col I, ALP), late marker gene (OCN) and master regulatory gene (Runx2) implicated in osteogenic differentiation showed significantly higher expression in MG-63 cells grown on H-TW for 14 days as compared to the cells grown for 7 days. Alizarin red S staining clearly indicated copious calcium mineral deposition in MG-63 cells grown on H-TW for 14 days. It is envisaged that the malonic acid amphiphile used herein can serve as a prototype to design synthetic ligands that can drive biomineralization-inspired synthesis of HANPs for their application in orthopaedic implants.

## 6.1. Introduction

In recent times, hydroxyapatite (HA) has assumed tremendous importance and emerged as a key material for developing bone graft substitutes. In particular, the use of hydroxyapatite nanoparticles (HANPs) in synthetic osteogenic grafts has rendered significant edge in terms of enhanced bioactivity, superior cell adhesion, proliferation, and integration (Zhou and Lee, 2011; Li *et al*., 2019; Anitha *et al*., 2017). In order to fulfill this requirement of HANPs for orthopaedic applications, there is a distinct need to streamline efforts towards developing facile methods of synthesizing biocompatible HANPs. In this context, biomineralization-based method of nanoparticle (NP) synthesis assumes importance as it enables green synthesis and precise control of size and shape of NPs. There are previous reports that highlight the use of natural as well as engineered proteins and peptides as biomineralization templates for synthesis of NPs (Yang *et al*., 2017; Ghorbani *et al*., 2019; Li *et al*., 2012). In line with these findings, in the current investigation, cell-free proteins or cell surface-associated protein from LAB were successfully used as biomineralization templates for synthesis of biocompatible HANPs as evident from the results shown in Chapter 2 and Chapter 4. It may be mentioned here that the size of HANPs were 50-100 nm and 371 nm when cell-free proteins or cell surface-associated protein from LAB was used as a mineralization template (Chapter 2 and Chapter 4). This indicated the inherent heterogeneity of the two contrasting routes of synthesis. Moreover, given the complex and labile nature of proteins, it may be challenging to exploit the cell-free proteins or cell surface-associated protein from LAB as a mineralization template for routine and large-scale synthesis of HANPs.

In order to address the aforementioned challenge, there is a scope to engage synthetic mimics of proteins and explore their potential in biomimetic mineralization. Further, such synthetic ligands can be rationally designed, which not only supports bioinspired mineralization but also enhances the scope of generating materials having superior attributes such as high surface area for regenerative medicine and tissue engineering applications. In the context of synthetic ligands, self-assembling peptide amphiphiles have been used as templates for biomineralization (Hartgerink *et al*., 2001; Zhao *et al*., 2010). Additional studies have demonstrated that self-assemblies of amphiphilic dendrons, phosphorylated dendronized poly(amido amine)s and tyrosine phosphate containing tetraphenylethylene can be engaged for mineralization of hydroxyapatite (Yang *et al*., 2011; Xin *et al*., 2014; Liu *et al*., 2013).

In the current investigation, the tenet of using amphiphilic ligands as mineralization template was adopted and a rationally designed 2-dodecylmalonic acid (MA) amphiphile was used for template-directed synthesis of HANPs. Akin to a protein template, which can self-assemble to form a stable nucleation scaffold, chelate metal through acidic amino acid residues and initiate biomineralization (Scheme 6.1A), it was envisaged that the malonic acid amphiphile can also self-assemble through hydrophobic interactions of alkyl chains, chelate metals owing to the presence of the carboxyl groups and thereby render bio-inspired mineralization of HANPs as envisaged in Scheme 6.1B. In this study, the HANPs generated by mineralization of MA are extensively characterized. The potential of the HANPs to support bone cell growth and differentiation in an *in vitro* titanium-based implant model is also reported.

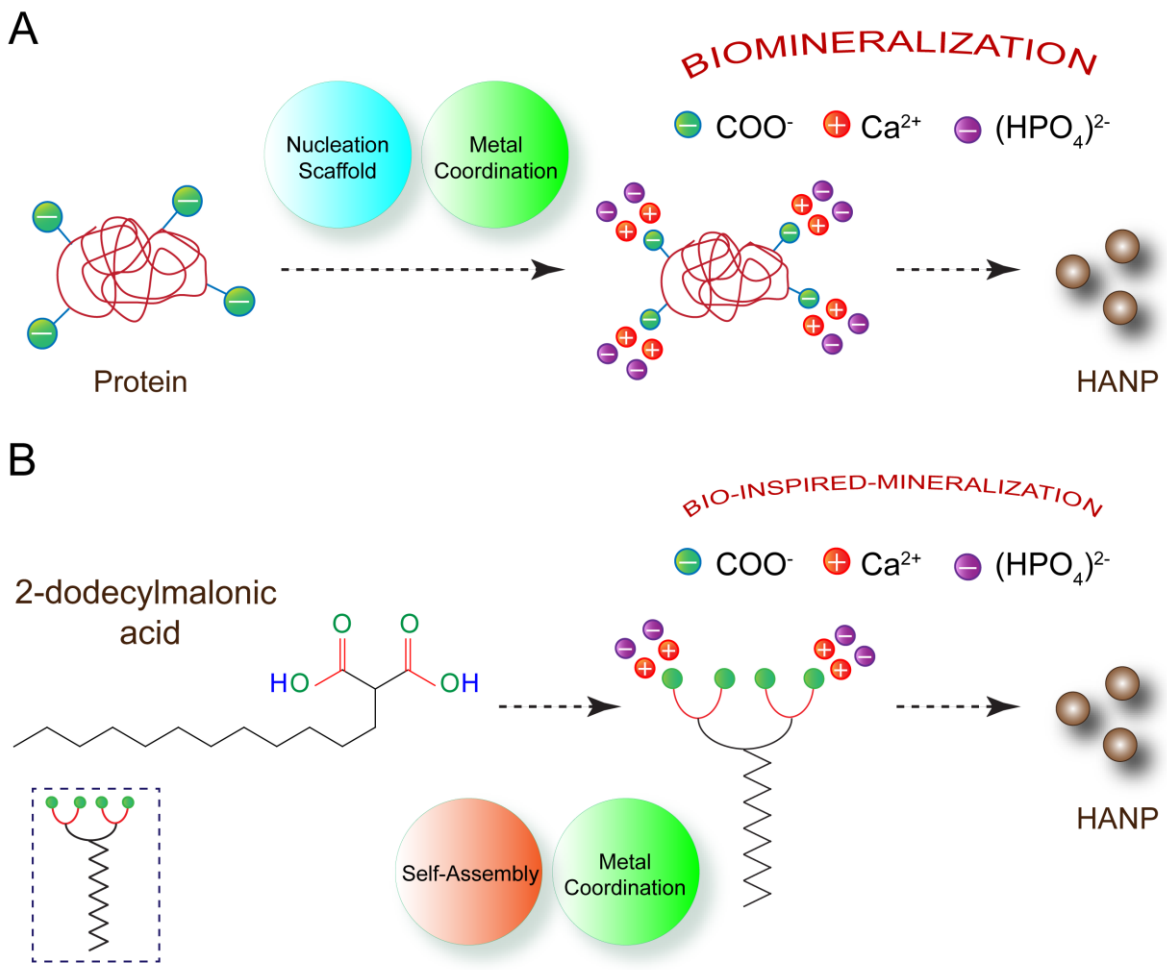


**Scheme 6.1.** Schematic illustrating the rationale of using 2-dodecylmalonic acid amphiphile for HANP synthesis by bioinspired mineralization.

## 6.2. Materials and Methods

### *6.2.1. Growth Media and Chemicals*

Calcium nitrate, di-ammonium hydrogen phosphate, alizarin red S were purchased from HiMedia (India). Dimethyl sulfoxide (DMSO) was obtained from Merck (India). Alkaline phosphatase (ALP) enzyme and p-nitrophenyl phosphate (pNPP) were procured from Sisco Research Laboratories (India). Dulbecco's Modified Eagle Medium (DMEM), trypsin-EDTA, 3-(4,5-dimethyl-2-thiazolyl)-2,5-diphenyl-2H-tetrazolium bromide (MTT), alamar blue, potassium bromide, 4',6-Diamidino-2-phenylindole (DAPI), paraformaldehyde, phalloidin-TRITC, collagen type I and titanium wire (0.25 mm diameter) was procured from Sigma-Aldrich. TRIzol reagent and SYBR Green qRT-PCR one step kit was obtained from Invitrogen.

### *6.2.2. Cell Culture and Maintenance*

Human osteosarcoma cells (MG-63) were procured from NCCS (National Center for Cell Science, Pune, India) and initially grown in a 25 $cm^2$ tissue culture flask in Dulbecco's Modified Eagle's Medium (DMEM) supplemented with 10% (v/v) Fetal bovine serum (FBS), penicillin (100 units/mL) and streptomycin (100 µg/mL) under a humidified atmosphere of 5% $CO_2$ in an incubator until the cells were approximately 90% confluent.

### *6.2.3. Synthesis of Hydroxyapatite Nanoparticles using Malonic Acid Amphiphile*

Hydroxyapatite nanoparticles (HANPs) were synthesized by using the wet precipitation method. 2-dodecylmalonic acid (MA) amphiphile was used as a template for biomineralization. MA was synthesized by following a previously described method (Ojha *et al*., 2010). Synthesis of HANP was accomplished by following the method described in Chapter 2 where Ca: P molar ratio was maintained as 1.67:1. Briefly, varying concentrations of MA (7.0 µM, 37 µM, 80 µM, 184 µM, 400 µM and 1200 µM, respectively) constituted in DMSO solution were added in separate sets to pH adjusted $Ca(NO_3)_2.4H_2O$ solution followed by addition of $(NH_4)_2HPO_4$ solution to maintain a Ca: P molar ratio of 1.67:1. Since MA solutions were prepared in DMSO, two control experiments were also set up having the lowest and highest concentration of DMSO (0.04% and 3%, respectively) were also used as template. The reaction blend was incubated for 24 h at room temperature in static condition. Subsequently, HANPs

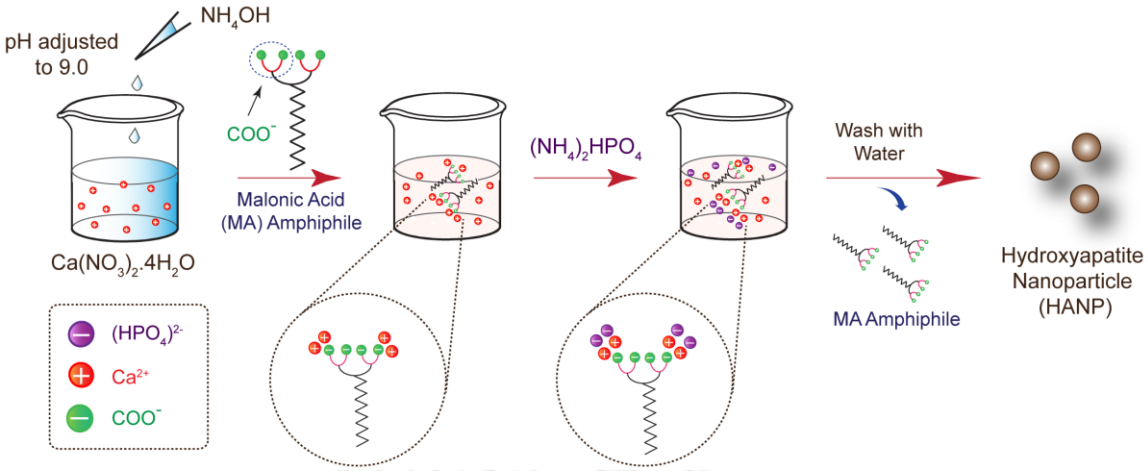


**Scheme 6.2.** Schematic illustration of the essential steps followed for the synthesis of HANPs by using 2-dodecylmalonic acid (MA) as a mineralization template.

were recovered by centrifugation at 10000 rpm followed by washing and lyophilization. A schematic representation of the essential steps in the synthesis of MA-mediated HANP is shown in Scheme 6.2.

### *6.2.4. Characterization of HANPs*

#### *6.2.4.1. FTIR Analysis*

FTIR spectra of HANPs obtained from malonic acid amphiphile were recorded in KBr pellets at 4.0 $cm^{-1}$ resolution in an infrared spectrometer (Spectrum One, Perkin-Elmer). Eight scans were performed for each sample in the wavenumber range of 4000 $cm^{-1}$ to 500 $cm^{-1}$.

#### *6.2.4.2. Powder XRD Analysis*

Powder X-ray diffraction (D2 Phaser, Bruker, Germany) data of the HANPs were recorded at room temperature over the 2θ range of 20°- 45° at a step size of 0.02° and a count time of 2s/step.

#### *6.2.4.3.BET Surface Area Analysis*

The specific surface area, pore volume and pore diameter of HANPs were analysed using BET surface area analyser (Quantachrome, Autosorb-IQ MP) followed by measuring $N_2$ adsorption-desorption isotherm.

*6.2.4.4. Atomic Force Microscope Analysis*

Samples were sonicated for 10 mins and 10 µl of each sample was spotted onto sterile glass cover slips (18 mm × 18 mm) and air dried inside a laminar hood overnight. Images were captured with Cypher AFM (Oxford). The images were acquired in non-contact mode, with 10 µm × 10 µm area at a scan rate of 0.5-1.0 line/s. Analysis of the topographic images of the surface was accomplished by using the WSxM v5.0 Develop 6.5 image viewer software.

*6.2.4.5. FESEM and FETEM Analysis*

Samples were sonicated for 10 mins and an aliquot of HANPs was added on a clean sterile aluminium foil. The samples were air dried in a laminar hood overnight and visualized under Field Emission Scanning Electron Microscope (Zeiss Sigma 300, USA). Separate drops of the sample were spotted onto carbon coated Cu TEM grid (Pacific Grid, USA) and air dried in laminar hood before loading them onto specimen holder. Microscopic images along with selected area electron diffraction (SAED) pattern were recorded under Field Emission Transmission Electron Microscope (JEOL 2100F, Japan) operating at 200 kV.

*6.2.4.6. Thermal Gravimetric (TG) Analysis*

TGA of HANPs was performed in TG thermal analyzer (NETZSCH, STA 449F3). The measurements were performed at a heating rate of 10K/min in an argon atmosphere with a flow rate of 60 ml/min and heating range was 25°C-1150°C. Samples were placed on an alumina crucible for analysis with an empty crucible as reference.

*6.2.5. In Vitro Cytotoxicity Studies by MTT Assay*

The cytotoxic effect of HANPs obtained by using varying concentration of malonic acid amphiphile were tested on human osteosarcoma (MG-63) cell lines by an MTT assay following the manufacturer instruction (Sigma-Aldrich, MO, USA). MG-63 cells were initially propagated in Dulbecco's Modified Eagle Medium (DMEM) supplemented with 10% fetal bovine serum (FBS), penicillin (100 units/mL) and streptomycin (100 µg/mL) at 37 °C in a $CO_2$ incubator under a humidified atmosphere of 5% $CO_2$. The cells were subsequently seeded in 96 well plates ($10^4$ cells/well) and HANPs made in DMEM were added to the cells in separate sets and incubated for 24 hours under 5% $CO_2$ at 37°C. Following incubation, the media was aspirated and

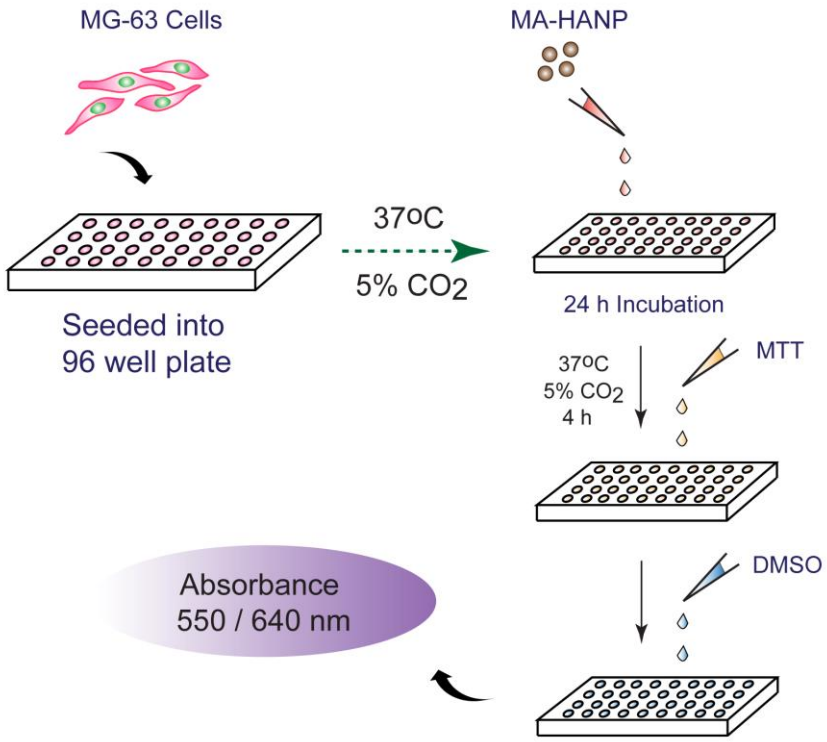


**Scheme 6.3.** Schematic representation of the essential steps followed to ascertain the *in vitro* cytotoxic effect of MA-HANPs on cultured MG-63 cells.

fresh DMEM containing MTT solution was added to the wells and incubated for 4 h at 37°C. Subsequently, the supernatant was removed and the insoluble formazan product was solubilized in DMSO and its absorbance was measured in a microtitre plate reader (Infinite M200, TECAN, Switzerland) at 550 nm. The absorbance obtained for control samples (untreated cells) was considered to represent 100% cell viability, whereas the absorbance for treated cells were compared to the untreated control cells to determine % cell viability. MTT assay was performed in six independent sets and each set consisted of three replicates. Data analysis and determination of standard deviation was performed with Microsoft Excel 2010 (Microsoft Corporation, USA). A schematic representation of the MTT assay used for ascertaining the cytotoxic potential of malonic acid amphiphile-derived HANP (MA-HANP) is indicated in Scheme 6.3.

*6.2.6. Preparation of Titanium Wire Coated with MA-HANP Grafted Collagen (H-TW)*

Titanium (Ti) wire was cut into several pre-defined pieces of 1.5 cm length each. The wire surface was ultrasonically cleaned sequentially with acetone, ethanol and deionized water for 10 minutes in each solvent. Subsequently, the wires were sterilized by exposure under UV light for 30 min. The sterilized pieces of Ti wires were placed

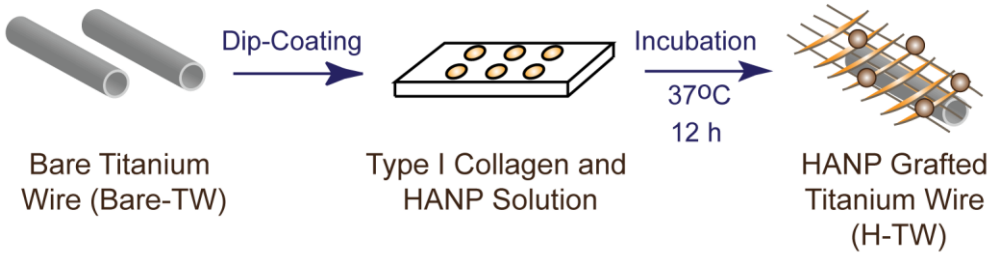


**Scheme 6.4.** Schematic representation of the protocol followed for generating HANP-grafted titanium wire (H-TW). The HANPs used herein were obtained by using 37 µM MA as a mineralization template.

into 6 well tissue culture plate containing type I collagen (1.0 mg/mL in sterile tissue culture grade water) and HANPs (1.0 mg/mL). The HANPs selected herein were obtained by using 37 µM MA as mineralization template. The plate was incubated at 37°C in static condition overnight. Then the solution was discarded and the plate was kept in a laminar hood for overnight drying of the coated Ti wires (H-TW). The coated Ti wires were subsequently subjected to 1h UV treatment. A schematic highlighting the salient steps for generation of the coated Ti wire is indicated in Scheme 6.4. The coated (H-TW) and bare titanium wires (TW) were characterized by FESEM (Zeiss, Germany) and EDX analysis. FTIR spectra of the wires were recorded in ATR mode at 4.0 $cm^{-1}$ resolution in an infrared spectrometer (Spectrum One, Perkin-Elmer). Eight scans were performed for every sample in the range of 4000 $cm^{-1}$ to 500 $cm^{-1}$.

*6.2.7. Cell Seeding onto Coated Ti Wire*

Prior to cell seeding, the coated wires were dipped in DMEM media for 24 h followed by seeding with $3 \times 10^5$ MG-63 cells suspended in DMEM medium. The cell seeded Ti wires were incubated at 37 °C incubator with 5% $CO_2$ for 3 h to allow cell adherence. After 3 h, 1 mL of culture media was gently added to each well. Fresh medium was replaced every alternate day, and cells were finally harvested on day 7 and 14, respectively. The potential of the coated Ti wire to support growth and differentiation of the seeded MG-63 cells was ascertained by multiple assays, which included determination of cell proliferation and viability, ALP activity, calcium deposition, cell morphology and gene expression studies as represented schematically in Scheme 6.5.

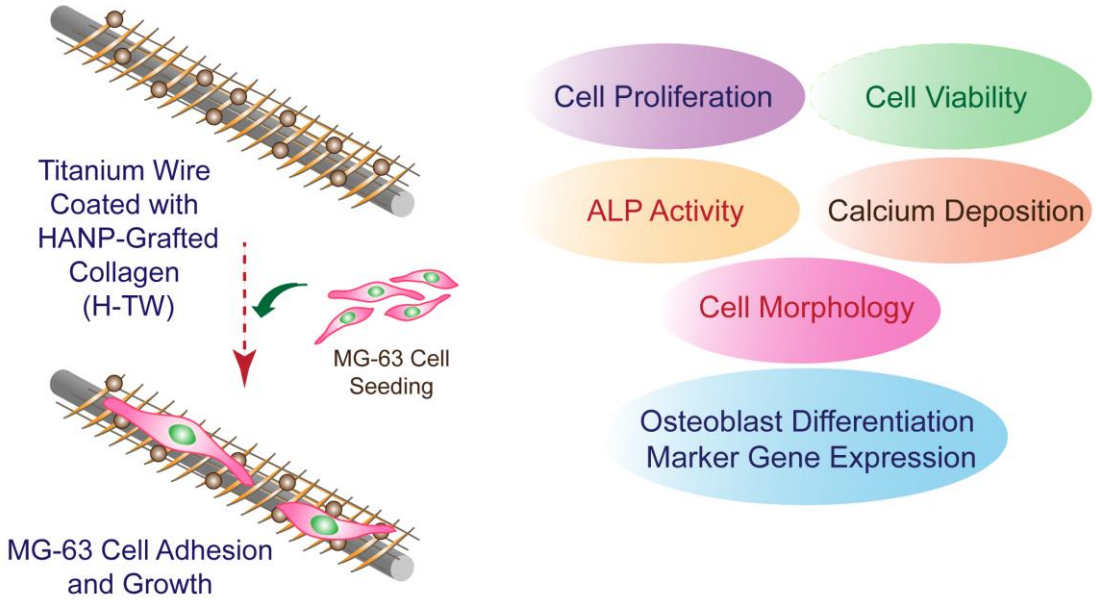


**Scheme 6.5.** Schematic representation of assays used to evaluate the potential of HANP-grafted titanium wire (H-TW) to support growth and differentiation of seeded MG-63 cells.

*6.2.8. Estimation of Cell Proliferation and Cell Viability Assay*

MG-63 cell proliferation study was performed using alamar blue dye reduction assay. Briefly, titanium wire with and without cells were incubated at 37 °C in DMEM medium containing 10% (v/v) alamar blue dye (Sigma, USA). At the end of 4 h incubation, the absorbance of a 100 µL aliquot of medium from each sample was read at 570/600 nm in a multiplate reader (Tecan Infinite Pro 200). Ti wire without cells incubated with 10% alamar blue dye was considered as negative control. Proliferation of MG-63 cells was analysed at predefined time points based on % resazurin reduction (Das *et al*., 2013).

*In vitro* cell viability was studied by staining MG-63 cells with calcein-AM (Sigma-Aldrich, U.S.). Briefly, the cell-seeded wires, harvested after 7 days and 14 days of cell culture, were first washed with sterile PBS to remove any nonadherent cell and cell debris. Cell seeded wires were further stained with calcein-AM solution (4.0 µM in PBS) for 20 min and visualized under fluorescence microscope (Eclipse Ti-U, Nikon) with an excitation filter of 450-490 nm (green, calcein-AM) (Maji *et al*., 2018).

*6.2.9. Alkaline Phosphatase Assay and DNA Quantification*

Alkaline phosphatase activity was determined by an assay based on hydrolysis of p-nitrophenyl phosphate to p-nitrophenol. Initially, cell seeded wires (H-TW) were washed with sterile PBS twice followed by cell lysis with 0.1% Triton X-100 for 30 min. The lysate was centrifuged at 5000 rpm for 10 min and the obtained supernatant was used to measure ALP activity. Briefly, 50 µl supernatant was incubated with 125 µl of active reagent (0.012 M pNPP in 0.05 M diethanolamine) solution at 37 °C for 1 h in the dark. After incubation, reaction was terminated by adding 50 µL of 2.5 M NaOH. Subsequently, the absorbance of p-nitrophenol was measured at 405 nm in a multimode reader (Infinite M200, TECAN, Switzerland), which corresponds to alkaline phosphatase activity (Pramanik *et al.,* 2009). DNA content was measured fluorometrically using a Quant iT PicoGreen ds reagent (Molecular Probes, Life Technologies, U.S.) according to the manufacturer's protocol. Briefly, after different days of cell culture, cells were lysed with sterile PBS containing 0.1% Triton X-100. The lysate was centrifuged at 11000 rpm for 2 min. A 25 µl aliquot of the supernatant was added to PicoGreen premixed with 175 µl of TE buffer (10 mM Tris-HCl, pH 7.5, 1 mM EDTA) and incubated for 5 min. Fluorescence emission of the solution was measured at 520 nm in a multiplate reader (Infinite M200, TECAN, Switzerland) at an excitation wavelength of 490 nm and was considered as an index of DNA content in the cell. ALP activity obtained by hydrolysis of pNPP was finally normalized against the fluorescence emission of PicoGreen-DNA complex obtained for MG-63 cells.

*6.2.10. Gene Expression Studies*

Real-time PCR was used to determine expression of collagen I (Col I), alkaline phosphatase (ALP), Runt-related transcript 2 (Runx2), osteocalcin (OCN) and glyceraldehyde-3-phosphate-dehydrogenase (GAPDH) mRNA transcripts. The sequences of the primers used in this study are indicated in Table 5.1 in Chapter 5. Following 7 and 14 days of cell growth, the MG-63 cell seeded Ti wire (H-TW) were treated with 500 µL TRIzol reagent (Invitrogen, U.S.) for 5 min followed by 100 µL chloroform treatment. Chloroform treated samples were centrifuged at 12000 rpm for 15 min at 4°C. Subsequently, the upper aqueous phase containing RNA was mixed with 250 µL isopropanol followed by centrifugation at 12000 rpm for 10 min at 4°C to obtain the RNA pellet. RNA concentration was quantified by measuring the absorbance

at 260 nm (NanoPhotometer NP80, IMPLEN). Following RNA isolation, 150 ng of isolated RNA was used as template for real-time PCR reactions. The PCR reaction was set up using SYBR 1-STEP qRT-PCR kit and the tubes were incubated in a 36-Well Rotor, QIAGEN Rotor-Gene Q qRT-PCR machine. Expression of each target gene was normalized against GAPDH. Reverse transcription was accomplished by incubating the reaction mixture at 50 °C for 3 min. The subsequent PCR conditions were as follows: (1) initial hold temperature at 94 °C for 2 min, (2) denaturation step at 94 °C for 30 sec, (3) annealing at 59 °C for 30 sec, (4) extension at 72 °C for 30 sec for a total of 50 cycles. Analysis of RT-PCR data was accomplished using the LinReg PCR (2014.x) software and the cycle threshold ($C_T$) values were calculated after baseline correction. The fold change in gene expression values was determined by the $\Delta\Delta C_T$ method (Livak *et al.*, 2001).

*6.2.11. Mineral Deposition*

The degree of mineralization in MG-63 cells grown in coated Ti wires (H-TW) was estimated by Alizarin red S staining. Briefly, a staining solution containing 1.0 mg/mL of Alizarin Red S (prepared in sterile MilliQ water and adjusted to pH 4.5) was added to the cell seeded Ti wire. After 15 min incubation, the staining solution was thoroughly washed with sterile MilliQ water followed by imaging under a bright field microscope.

*6.2.12. Morphological Study*

In order to pursue morphological studies and detect F-actin, cell staining was performed using phalloidin-TRITC and DAPI stains. Initially the cells grown on HANP-coated titanium wire for 7 days and 14 days were washed once with sterile PBS. Then the cells were fixed with 4% paraformaldehyde for 10 min. In addition to this, the cell membrane was permeabilized with 0.1% Triton X-100 and the cells were then stained with 0.1 µM Phalloidin-TRITC in sterile PBS for 1h followed by counterstaining with 30 µM DAPI in sterile PBS for 10 min. Finally, cells were washed with sterile PBS followed by imaging using a fluorescence microscope (Eclipse Ti-U, Nikon).

## 6.3. Results and Discussion

*6.3.1. Characterization of HANPs Obtained by Using Malonic Acid (MA) Amphiphile as a Mineralization Template*

2-dodecylmalonic acid (MA) was used as a template for the synthesis of HANPs using a bio-inspired mineralization approach. Synthesis of HANP was carried out by following wet precipitation method. The various concentrations of MA used in the synthesis were 7.0 µM, 37 µM, 80 µM, 184 µM, 400 µM, 1200 µM and the recovered HANPs were denoted as $MA_1$-HANP, $MA_2$-HANP, $MA_3$-HANP, $MA_4$-HANP, $MA_5$-HANP and $MA_6$-HANP, respectively. Since the MA solutions were constituted in DMSO, control experiments were also performed, wherein the corresponding concentration of DMSO present in the reaction blend for $MA_1$-HANP (lowest concentration) and $MA_6$-HANP (highest concentration) was used and these samples were referred to as control 1 and control 2, respectively. Following synthesis, the obtained HANPs were characterized by FESEM, powder XRD and FTIR analysis. FESEM analysis revealed that $MA_1$-HANPs and $MA_2$-HANPs obtained at low MA concentrations corresponding to 7.0 µM and 37 µM, respectively were spherical or

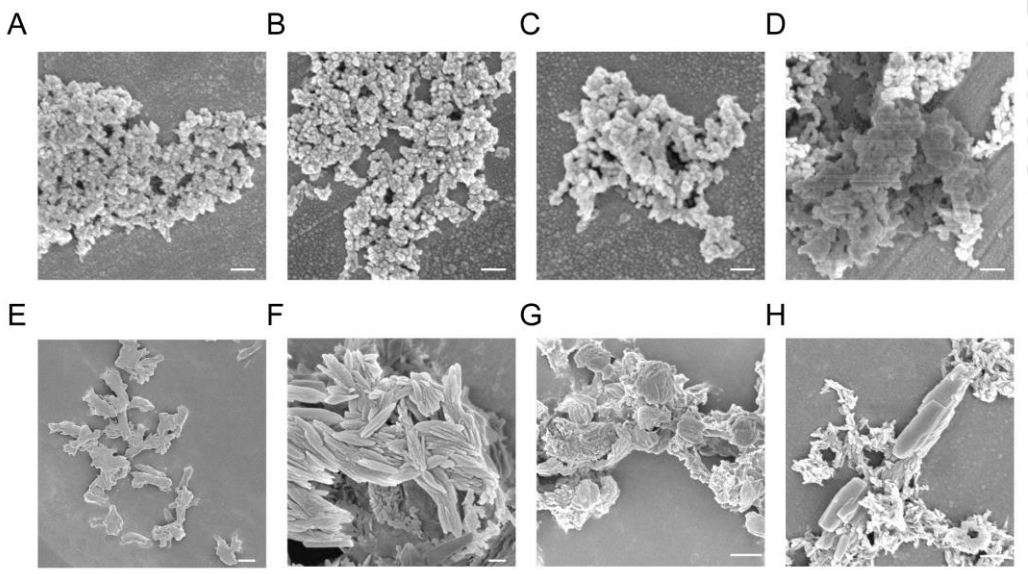


**Figure 6.1.** FESEM image of HANPs generated by mineralization of varying concentrations of 2-dodecylmalonic acid (MA) amphiphile. (A) $MA_1$-HANPs (7.0 µM MA), (B) $MA_2$-HANPs (37 µM MA), (C) $MA_3$-HANPs (80 µM MA), (D) Control 1 (0.04% DMSO), (E) $MA_4$-HANPs (184 µM MA), (F) $MA_5$-HANPs (400 µM MA), (G) $MA_6$-HANPs (1200 µM MA), (H) Control 2 (3% DMSO). Scale bar for the FESEM images are: (A-D) 200 nm and (E-H) 3.0 µm.

**Table 6.1.** Particle size range for HANPs obtained using varying concentrations of 2-dodecylmalonic acid (MA) amphiphile.

| Sl. No. | Sample | Concentration of MA or DMSO | Particle Size Range |
|---|---|---|---|
| 1. | $MA_1$-HANPs | 7.0 µM MA | 30-40 nm |
| 2. | $MA_2$-HANPs | 37 µM MA | 22-27 nm |
| 3. | $MA_3$-HANPs | 80 µM MA | 30-40 nm |
| 4. | $MA_4$-HANPs | 184 µM MA | 410-430 nm |
| 5. | $MA_5$-HANPs | 400 µM MA | 1-1.5 µm |
| 6. | $MA_6$-HANPs | 1200 µM MA | 3.6-5.2 µm |
| 7. | Control 1 | 0.04% DMSO | 35-50 nm |
| 8. | Control 2 | 3% DMSO | 680-740 nm |

oblong-shaped (Figure 6.1A-B). With further increase in the concentration of MA, the obtained HANPs ($MA_3$-HANP, $MA_4$-HANP, $MA_5$-HANP and $MA_6$-HANP) were observed to increasingly agglomerate and coalesce, leading to a change in shape from spherical or oblong observed in case of $MA_1$-HANPs and $MA_2$-HANPs to spindle and plate-shaped structures (Figure 6.1C, Figure 6.1E-G). The HANPs obtained in presence of DMSO alone (control 1 and control 2) were also observed to exhibit a high degree of aggregation and heterogeneity in shape (Figure 6.1D, Figure 6.1H). Image J analysis revealed that the particle size of HANPs obtained at lower concentrations of MA was distinctly less than those obtained at higher concentrations or in presence of high concentration of DMSO alone (Table 6.1). The particle size range for HANPs obtained with low concentration of MA ($MA_1$-HANPs, $MA_2$-HANPs and $MA_3$-HANPs) is comparable to the size of HANPs obtained by various other routes of synthesis (Table 2.1).

Powder XRD analysis of $MA_1$-HANPs, $MA_2$-HANPs and $MA_3$-HANPs revealed the presence of discrete signature peaks for hydroxyapatite phase at $2\theta = 26^{o}$ and $2\theta = 31^{o}$ (Figure 6.2A-C), which correspond to (002) and (211) lattice planes, respectively (Gao *et al*., 2016; Li *et al*., 2012). This also indicated that these HANPs were essentially crystalline in nature. At higher concentrations of MA ($MA_4$-HANPs, $MA_5$-HANPs and $MA_6$-HANPs) and DMSO alone, multiple peaks were observed in

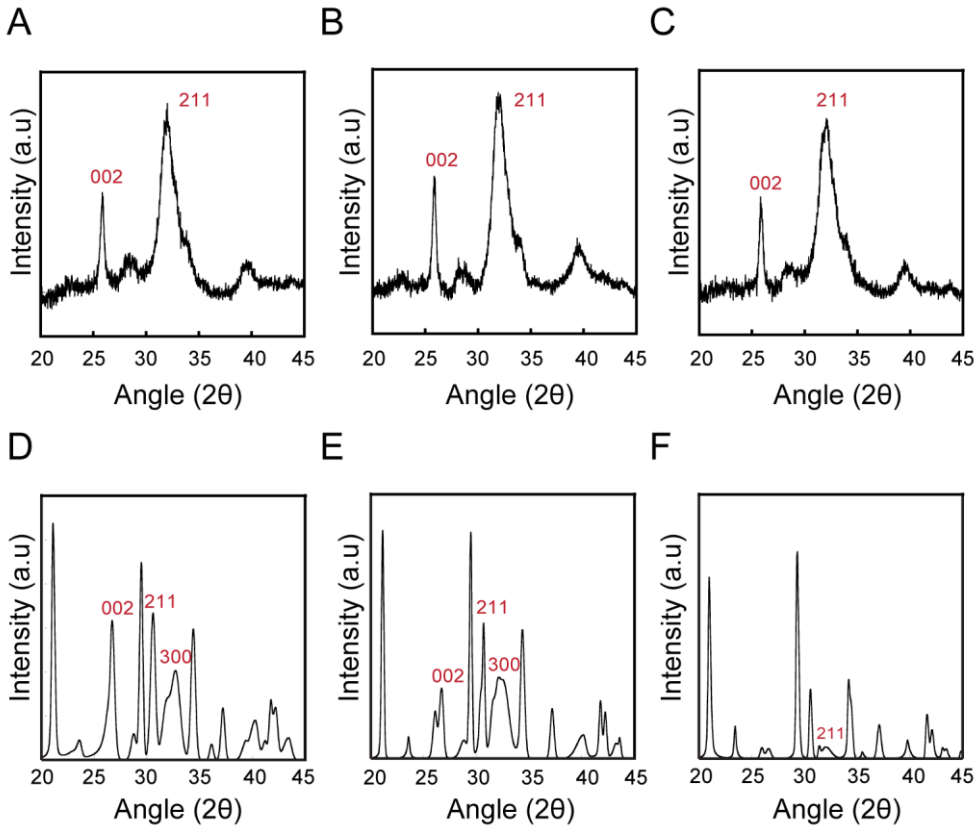


**Figure 6.2.** Powder XRD analysis of HANPs generated by mineralization of varying concentrations of 2-dodecylmalonic acid (MA) amphiphile. (A) $MA_1$-HANPs (7.0 µM MA), (B) $MA_2$-HANPs (37 µM MA), (C) $MA_3$-HANPs (80 µM MA), (D) $MA_4$-HANPs (184 µM MA), (E) $MA_5$-HANPs (400 µM MA) and (F) $MA_6$-HANPs (1200 µM MA).

XRD analysis (Figure 6.2D-F, Figure A6.1B in Appendix), which suggested that the generated material was quite heterogenous in nature. It may be mentioned here that the salient peaks for hydroxyapatite phase at $2\theta = 26^{\circ}$ and $2\theta = 31^{\circ}$ were also observed for HANPs synthesized in presence of lower concentration of DMSO (Figure A6.1A in Appendix). However, the generated material was quite unstable in solution and had a propensity to precipitate rapidly. FTIR analysis of $MA_1$-HANPs, $MA_2$-HANPs and $MA_3$-HANPs indicated the presence of significant peaks at 3568 $cm^{-1}$, 1461 $cm^{-1}$, and 1041 $cm^{-1}$ (Figure A6.2A in Appendix), which correspond to $OH^-$, $CO_3^{2-}$, and $PO_4^{3-}$ stretching frequencies, respectively (Cipreste *et al.*, 2016; Dasgupta *et al.*, 2010). Akin to the results obtained in powder XRD analysis, multiple peaks were observed in FTIR analysis for $MA_4$-HANPs, $MA_5$-HANPs and $MA_6$-HANPs (Figure A6.2B in Appendix), which again suggested the heterogenous nature of the generated material.

Based on the characterization of the HANPs obtained by mineralization of MA, it was evident that lower concentration of MA favoured effective mineralization and led to generation of small size HANPs of uniform shape and high crystallinity. Clearly, inherent differences in the biomineralization process was witnessed upon increasing the concentration of MA. Self-assembly of the amphiphilic MA is perhaps critical for generating the nucleation scaffold and the accessibility of the acidic $COO^-$ groups in the MA-derived scaffold ensures effective metal chelation and spatial restriction of the mineralization process, which perhaps leads to generation of smaller size nanoparticles in case of $MA_1$-HANPs, $MA_2$-HANPs and $MA_3$-HANPs. When higher concentrations of MA were used, aggregation of the amphiphile was presumably very strong, which may hinder the formation of an optimal nucleation scaffold and efficient display of the mineralization ligand ($COO^-$ groups in the MA scaffold). This, in turn, may lead to improper nucleation and crystal growth of HA, resulting in large scale aggregation and precipitation of the mineral, as evidenced in case of $MA_4$-HANPs, $MA_5$-HANPs and $MA_6$-HANPs.

Amongst all the HANPs, it appeared that $MA_2$-HANPs exhibited least heterogenicity in terms of size and shape and was thus further characterized. AFM analysis revealed that $MA_2$-HANPs were mostly oblong-shaped, with an average height profile of ~155.72 nm (Figure 6.3A-B). FETEM analysis of HANPs also indicated the oblong morphology of the HANPs (Figure 6.3C), while SAED pattern analysis supported the crystalline nature of the particles (Figure 6.3C, inset). The lattice distance of the particles was 0.29 nm, as observed from HR-TEM analysis (Figure 6.3D). BET analysis of $MA_2$-HANPs indicated a type IV adsorption isotherm with a hysteresis loop (Huang *et al.*, 2019), wherein the surface area was ~90 $m^2/g$ with average pore size of ~4 nm (Figure 6.3E). TGA analysis showed a two-step degradation of HANPs and the resulting mass obtained at 1150ºC was ~89% (Figure 6.3F). The decrease of mass can be attributed to initial loss of weakly entrapped water molecules and loss of lattice water at higher temperatures (Sheikh *et al.*, 2016; Liang *et al.*, 2012; Ivanova *et al.*, 2001).

### *6.3.2. Titanium Wire Coated with HANP-Grafted Type I Collagen*

Titanium (Ti) wire is a well-recognized orthopaedic implant widely used in bone repair and tissue engineering applications (Geetha *et al.,* 2009; Spriano *et al.,* 2018). However, Ti implants are essentially bioinert in nature and hence demand functional

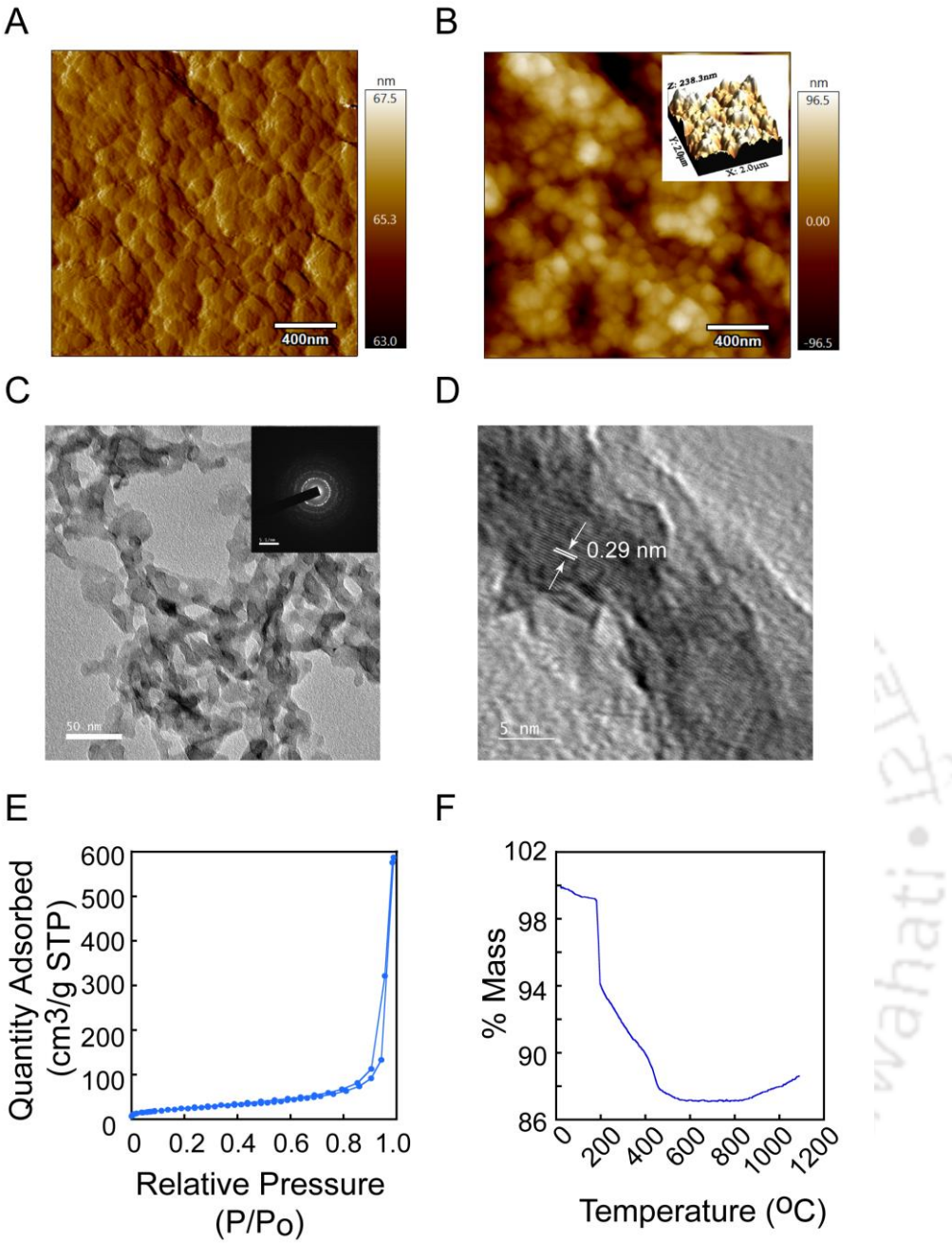


**Figure 6.3.** Characterization of $MA_2$-HANPs. (A) Amplitude channel-based AFM analysis, (B) 2D topography-based AFM analysis. Inset indicates 3D topography, (C) FETEM analysis. Inset indicates SAED pattern, (D) HR-TEM analysis, (E) BET surface area analysis, (F) TGA analysis.

modulation to render bone cell adhesion and differentiation and induce formation of bone at the tissue-implant interface. Collagen Type I is a major component of bone extracellular matrix (ECM), which is implicated in nucleation and growth of bone apatite and hence collagen type I coating on implants has resulted in superior

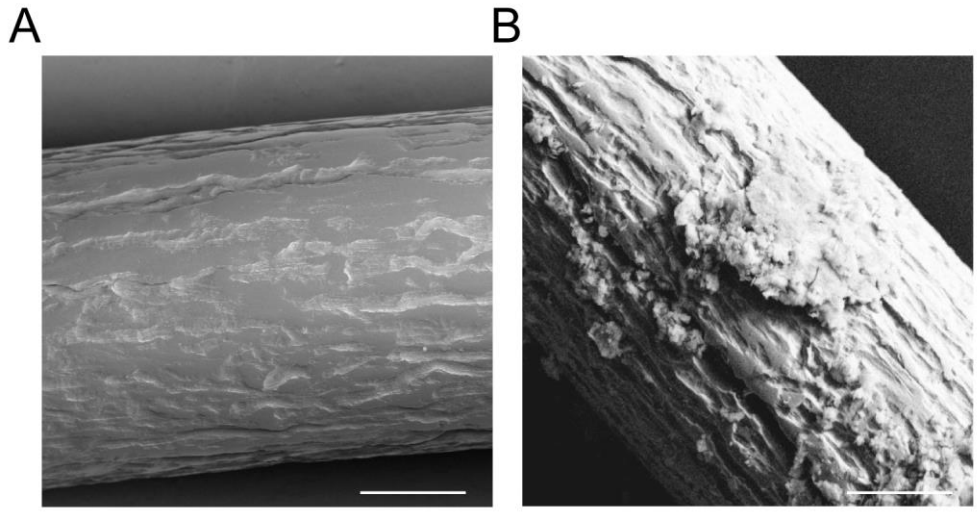


**Figure 6.4.** FESEM analysis of (A) Bare Ti wire, (B) Ti wire coated with collagen type I solution containing $MA_2$-HANPs (H-TW). Scale bar for the images is 100 µm.

osteogenesis around the coating (Wang *et al.*, 2012; Rammelt *et al*., 2004). Further, incorporation of hydroxyapatite as a coating can facilitate efficient osseointegration of implants and effective bone cell growth and differentiation (Haider *et al*., 2017; Arcos and Vallet-Regi, 2020). Based on this premise, in the current study the Ti wire was coated with collagen type I solution containing $MA_2$-HANPs. The bare titanium wire (TW) and type I collagen-HANP coated titanium wire (H-TW) was analysed by FESEM. A rough surface appearance was evident in case of bare titanium wire (Figure 6.4A), whereas in case of H-TW, a thick corrugated surface coating, likely due to coating with HANP-containing collagen type I solution was observed (Figure 6.4B). FESEM-EDX analysis also supported the presence of calcium and phosphate ion deposition, which clearly showed the deposition of hydroxyapatite nanoparticles upon titanium wire surface (Figure 6.5A). In order to check the deposition of HANPs onto titanium wire surface, FTIR analysis was performed. FTIR analysis revealed that the HANPs signature peaks were present in case of hydroxyapatite nanoparticle ($MA_2$-HANPs) coated titanium wire (H-TW) (Figure 6.5B).

*6.3.3. Assessment of MG-63 Cell Proliferation*

It is well established that HANPs hold enornmous potential in bone tissue engineering applications (Brokesh and Gaharwar, 2020; Wang *et al*., 2007; Bhattacharjee *et al*., 2016). Based on this premise, in the present study a potential orthopaedic implant was

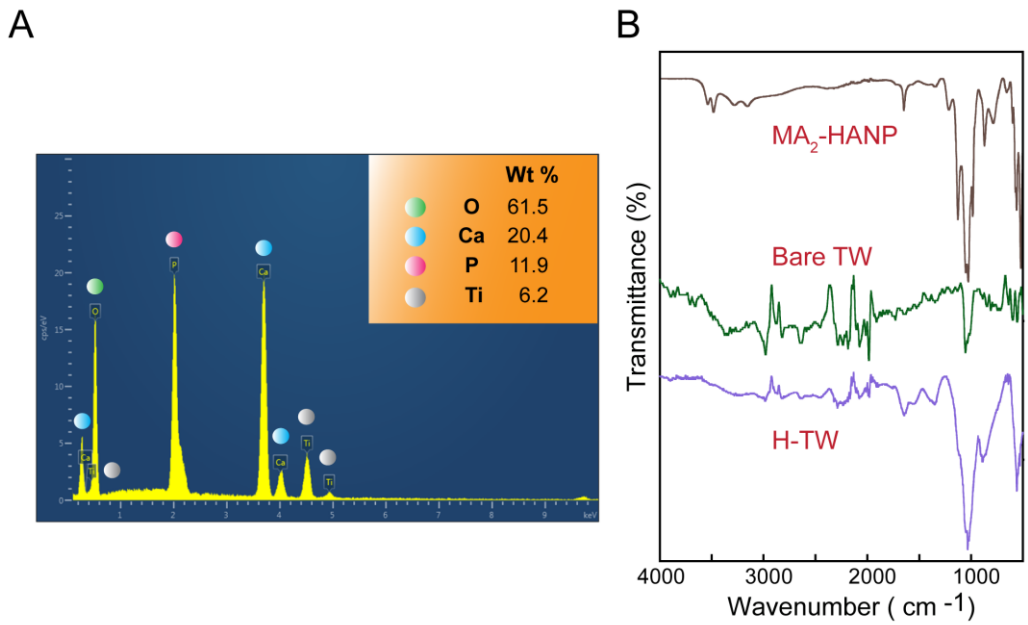


**Figure 6.5.** (A) EDX analysis of Ti wire coated with collagen type I solution containing $MA_2$-HANPs (H-TW). (B) FTIR analysis of (i) $MA_2$-HANPs, (ii) Bare Ti wire and (iii) Ti wire coated with collagen type I solution containing $MA_2$-HANPs (H-TW).

generated by coating a Ti wire with collagen type I containing $MA_2$-HANPs and this functionalized implant was characterized. In order to leverage the implant for bone tissue engineering applications, it was imperative to initially ascertain the cytotoxic effect of the malonic acid amphiphile-derived HANPs (MA-HANPs) on bone cells. To this end, an *in vitro* MTT assay was conducted to determine the cytotoxicity of MA-HANPs on cultured MG-63 cells. The essential observation was that the samples $MA_1$-HANP to $MA_5$-HANP (wherein the MA concentration used for mineralization of HANPs varied from 7.0 µM to 400 µM, respectively) were non-toxic to MG-63 cells, with the cell viability being more than 80% (Figure 6.6A). In case of HANPs generated from 1200 µM MA ($MA_6$-HANP), a nominal toxicity was manifested as the viability of MG-63 cells was less than 80% (Figure 6.6A). It may be mentioned here that both the control samples were essentially non-toxic as the viability of cultured MG-63 cells was in excess of 80% (Figure 6.6A).

The proliferation of MG-63 cells was determined by alamar blue assay. Resazurin is an active component present in the alamar blue dye, which is converted into its reduced state by the activity of oxidoreductase enzyme of proliferating cells, which in turn can also be considered as an index of the metabolic activity of live cells (Borra *et al.*, 2009). The percentage of resazurin reduction observed for MG-63 cells

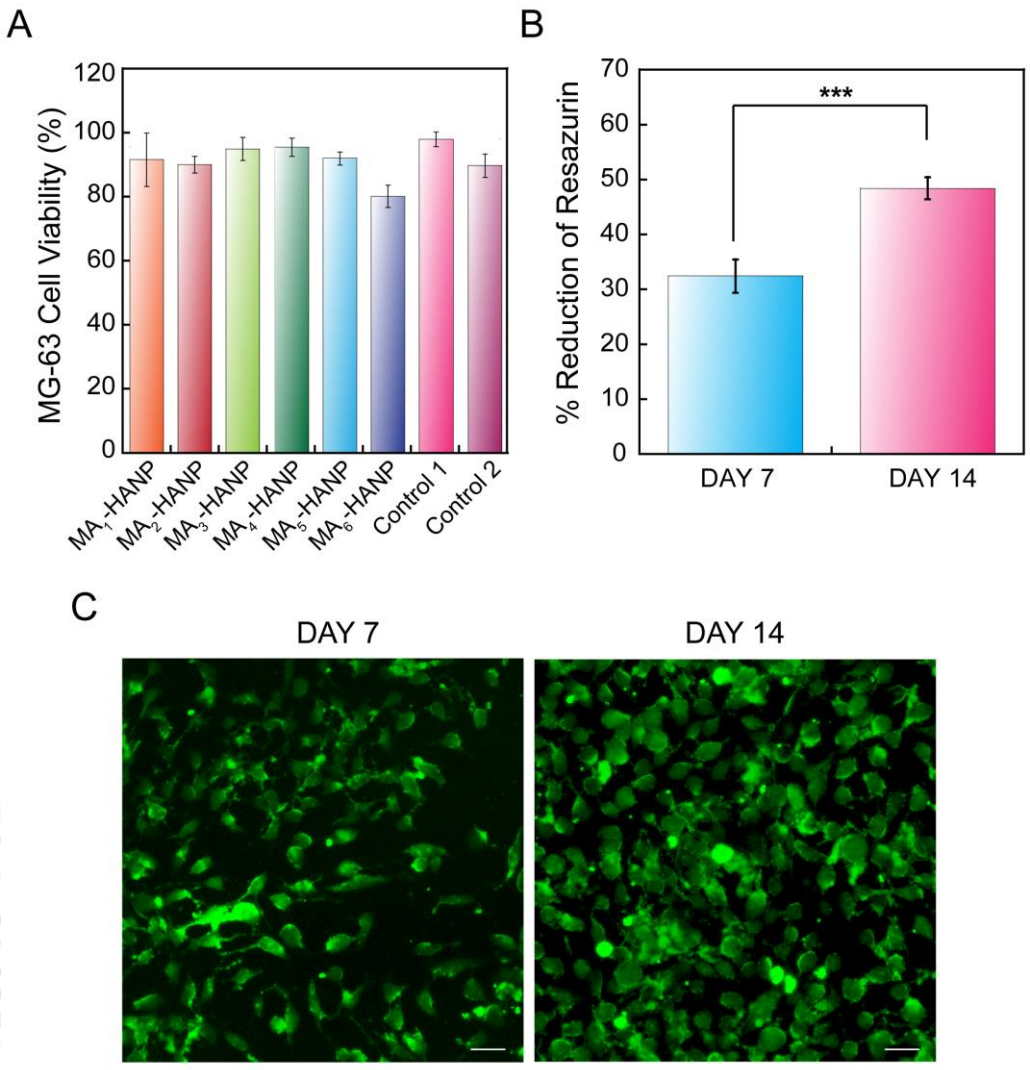


**Figure 6.6.** (A) MTT assay to determine the cytotoxic effect of malonic acid amphiphile -derived HANPs ($MA_1$-HANPs to $MA_6$-HANPs) against cultured MG-63 cells. Control 1 and Control 2 represent samples having low (0.04%) and high (3%) content of DMSO. (B) Measurement of proliferation of MG-63 cells seeded in H-TW by Alamar blue assay. *** indicates *p* value of < 0.001, in one-way ANOVA. (C) Calcein-AM staining of MG-63 cells grown on H-TW for 7 and 14 days. Scale bar for the images is 100 µm.

grown for 14 days on HANP-grafted-Ti wire was higher (48.38%) as compared to the cells grown for 7 days (32.4%) (Figure 6.6B). Calcein AM staining indicated a large number of viable cells growing on H-TW and the density of MG-63 cells appeared to be higher on 14 days of cell growth as compared to 7 days of cell growth (Figure 6.6C). Based on the results, it was apparent that the Ti wire coated with collagen type I containing $MA_2$-HANPs may hold considerable potential in bone tissue engineering applications as it was cytocompatible and rendered robust growth of MG-63 cells.

*6.3.4. ALP Activity, Osteogenic Gene Expression, Mineralization and Cytoskeleton Organization in MG-63 Cells Seeded in Coated Ti Wire*

ALP activity was observed to be higher for MG-63 cells seeded in H-TW after 7 days of cell growth as compared to the cells grown for 14 days (Figure 6.7A). Alkaline phosphatase (ALP) is an early osteogenic marker, which is involved in extracellular matrix mineralization (Frohbergh *et al.*, 2012). The higher ALP activity in MG-63 cells seeded in H-TW after 7 days of cell growth supports this notion. In order to verify the effect of HANP-coated Ti wire on the differentiation of MG-63 cells, expression of ALP, Col I, Runx2 and OCN osteogenic marker genes were ascertained by a quantitative real-time PCR analysis. It was observed that expression of ALP and Col I genes were higher on day 14 as compared to day 7 (Figure 6.7B). ALP and Col I are early marker genes implicated in extracellular matrix mineralization and synthesis, respectively (Barrere *et al.*, 2006). Hence, an enhancement in the expression of ALP and Col I transcripts suggested early osteogenic differentiation and mineralization in MG-63 cells. It may be mentioned that the fold change in the expression of ALP and Col I was significantly higher for cells grown in HANP-coated Ti wire for 14 days as compared to the fold change observed in case of cells grown for 7 days (Figure 6.7B. The expression of Runx2 and OCN marker genes was also higher on day 14 as compared to day 7 in MG-63 cells grown on HANP-coated Ti wire (Figure 6.7B). Runx2 is a transcription factor implicated in osteogenesis (Franceschi and Xiao, 2003; Salhotra *et al.*, 2020). Hence, higher expression of Runx2 in MG-63 cells on day 14 perhaps is likely to ensure enhanced expression of other osteoblast-specific genes and thereby promote cell differentiation. Further, higher expression of OCN in MG-63 cells grown for 14 days substantiates the notion that OCN is a late osteoblast differentiation marker, implicated in extracellular matrix mineralization (Barrere *et al.*, 2006; Robler *et al.*, 2020). Alizarin red S staining revealed that calcium deposition was copious in MG-63 cells grown on HANP-coated Ti wire for 14 days (Figure 6.7C). Based on the high calcium deposition, it was apparent that a substantial proportion of MG-63 cells grown on the HANP-coated Ti wire exhibited a propensity to differentiate into osteoblast lineage cells and hence the developed implant material was conducive to induce osteogenic differentiation. Significant detection of actin could be achieved in MG-63 cells grown on HANP-coated Ti wire for 7 and 14 days and the cells appeared elongated (Figure 6.7D), which suggested that H-TW was biocompatible and could promote cytoskeletal organization and differentiation in MG-63 cells.

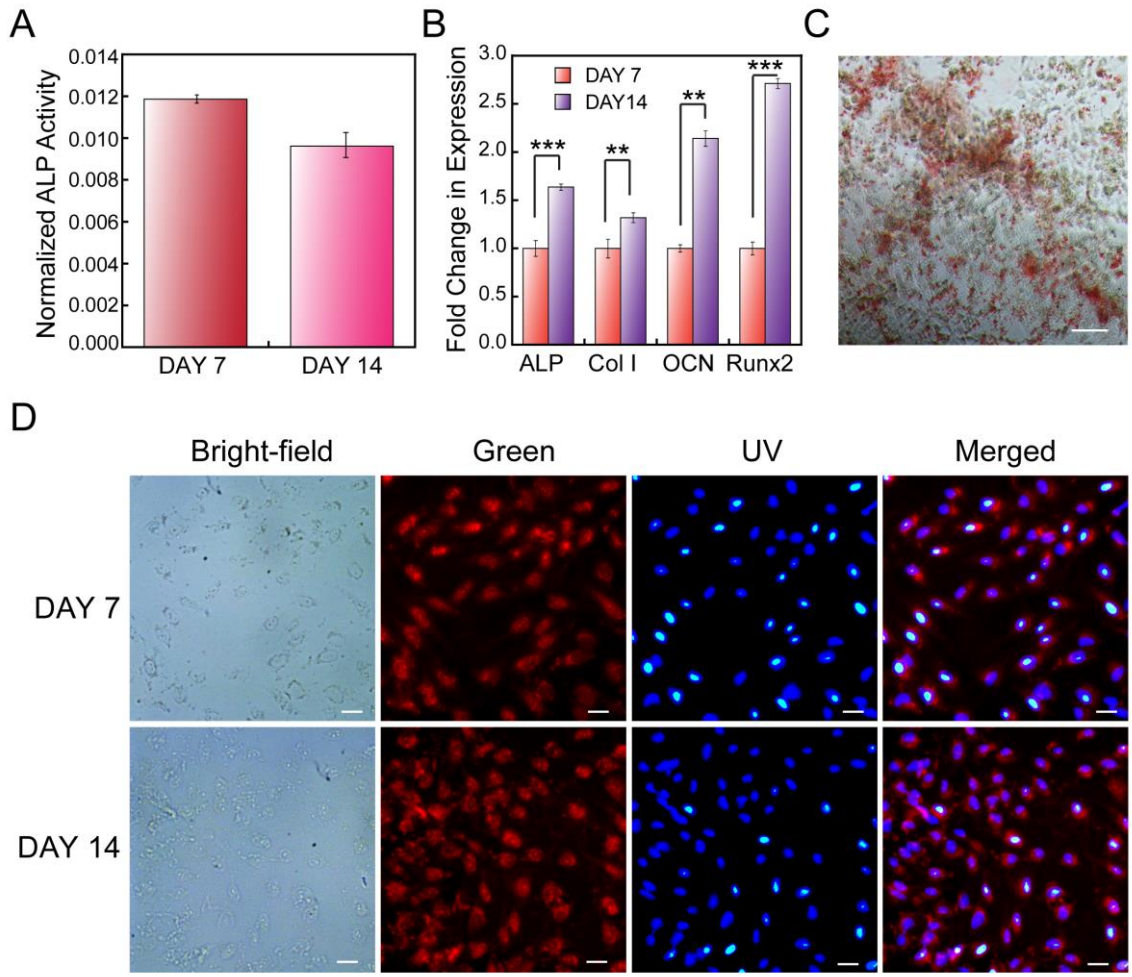


**Figure 6.7.** (A) Normalized alkaline phosphatase activity of MG-63 cells grown on HANP-coated Ti wire (H-TW) for 7 and 14 days. (B) Quantitative real-time PCR analysis to ascertain the fold change in the expression of the osteogenic genes in MG-63 cells grown on HANP-coated Ti wire (H-TW) for 7 and 14 days. ** and *** indicate a *p* value of <0.01 and <0.001, respectively, in one-way ANOVA. (C) Visualization of calcium deposition by Alizarin red S staining in MG-63 cells cultured on HANP-coated Ti wire (H-TW) for 14 days. Scale bar for the images is 100 µm. (D) Actin staining for cytoskeletal reorganization and cell morphology studies in MG-63 cells grown on HANP-coated Ti wire (H-TW) for 7 and 14 days. Scale bar for the images is 100 µm.

## 6.4. Significant Findings

The salient findings of this chapter are as follows:

1. The small amphiphilic ligand 2-dodecylmalonic acid (MA) can be used as a template for synthesis of HANPs. Amongst various concentrations of MA used for HANP synthesis, it was observed that 37 µM MA was the optimal concentration and the HANPs obtained thereof ($MA_2$-HANPs) were uniform in size and shape.

2. FESEM and Image J analysis revealed that $MA_2$-HANPs were oblong-shaped with a particle size ranging from 22-27 nm. Powder XRD and SAED pattern analysis revealed that $MA_2$-HANPs were crystalline in nature.

3. FESEM and EDX analysis indicated that titanium (Ti) wire could be functionalized with $MA_2$-HANP-grafted Type I collagen to yield a potential orthopedic implant (H-TW) following a dip coating method.

4. H-TW rendered growth, proliferation, osteogenic marker gene expression, calcium deposition and cytoskeletal organization in osteosarcoma MG-63 cells. Hence, H-TW is a potentially biocompatible implant, which can be leveraged for bone cell growth and differentiation.

In the subsequent section, the salient findings emerging from the thesis work is summarized and the future perspective is highlighted.

# SUMMARY AND FUTURE PERSPECTIVE

# SUMMARY AND FUTURE PERSPECTIVE

Hydroxyapatite nanoparticles (HANPs) are in great demand owing to their immense translational potential in bone tissue engineering, orthopaedic implant coating and drug delivery applications. Given the use of toxic reagents in chemical synthesis of HANPs, alternate methods of generating biocompatible HANPs and leverage their biomedical prospect are warranted. The current investigation addresses this issue and illustrates a novel biomineralization-based method of HANP synthesis using secreted as well as cell surface-associated proteins from lactic acid bacteria (LAB), which has a GRAS status. The scope of the biomineralization process was further strengthened as a rationally designed malonic acid synthetic amphiphile could also be explored in biomimetic mineralization for HANP synthesis. The salient advancements of the study and the future prospects are as follows:

1. The secreted extracellular acidic proteins (SLPs) from various LAB strains served as a mineralization template for synthesis of HANPs through biomineralization approach. In a biomineralization-derived synthesis strategy, it is paramount that the proteins or peptide templates not only favor nucleation, but are also non-toxic and biocompatible. In this regard, the choice of secreted proteins from LAB is vindicated given the GRAS status of LAB and their established probiotic attributes. The present investigation demonstrated that the use of secreted LAB protein as a mineralization template is a promising conduit for synthesis of HANPs. However, given the demand of HANPs, the synthesis procedure requires to be facile and economically viable. Hence in future, it will be worthwhile to ascertain the feasibility of recovering the LAB protein template for successive rounds of mineralization.

2. Given the inherent heterogeneity of the SLP extracts of LAB, it was pertinent to analyze the role of the individual protein(s) in the template-directed mineralization process in order to acquire an insight and identify the key protein templates for nucleation and generation of HANPs. In the current investigation, this premise was evaluated, wherein a purified fraction consisting of a low molecular weight protein from *L. plantarum* MTCC 1325 strain could be

leveraged for HANP synthesis. Based on the leads obtained in the present study, there is a scope in the future to conduct a proteomics-based study with the secreted LAB proteins and identify key residues in the protein which render effective mineralization and synthesis of HANPs. Further, it is envisaged that the process of biomineralization can perhaps be fine-tuned by tweaking the LAB template protein structure, in conjunction with physico-chemical conditions or introduction of additives and stabilizers in order to enable size and shape controlled- synthesis of HANPs.

3. It is critical that the therapeutic merit of a biogenic nanomaterial should be validated by demonstrating its potential in mitigating a real clinical problem. In this context, the current investigation illustrates a significant application of the HANPs derived by biomineralization and demonstrates that a polymyxin B-loaded hydroxyapatite nanocarrier (PB-HNC) could be generated that could hinder the formation *Pseudomonas aeruginosa* biofilm, which represents a grave problem in the clinics. In future, the prospect of using the biocompatible HANPs for delivery of an antibacterial payload can be validated through *in vivo* biofilm infection models.

4. Although the secreted LAB protein(s) could readily support template-mediated synthesis of HANPs, their recovery from the extracellular culture filtrate can be tedious and a hindrance for large-scale synthesis of HANPs. In order to circumvent this problem, in the current investigation, the prospect of cell surface-associated proteins (CSPs) of the well-known probiotic *Lactobacillus rhamnosus* GG as a template for biomineralization was ascertained. Based on the evidence that LAB CSPs are acidic and hydrophobic nature in growth medium and display the propensity to self-assemble, the CSP of *L. rhamnosus* GG served as a nucleation scaffold to facilitate HANP mineralization. The key protein involved in the mineralization process was also identified by conducting mechanistic studies. Interestingly, the whole cell of *L. rhamnosus* GG could also direct mineralization and yield HANPs of uniform size and shape. In order to leverage the whole cell-associated biomineralization for large-scale HANP synthesis, a facile method of HANP recovery can be developed in future.

5. The excellent biocompatibility, osteoconductivity and osteoinductive properties of HANPs enhance their prospect in developing scaffolds for bone tissue engineering. This premise was validated in the current study by generating a chitosan-gelatin scaffold reinforced with CSP-mineralized HANPs (H-CG), which exhibited favorable porosity, swelling property and biodegradation profile. Further, the osteogenic potential of H-CG was validated in an *in vitro* cell culture model wherein the scaffold could support bone cell proliferation, mineralization and osteogenic marker gene expression. In future, it will be worthwhile to leverage the developed H-CG scaffolds to deliver growth factors for efficient osteogenesis and to ascertain this tenet in an *in vivo* model.

6. It was encouraging to observe in the current investigation that the LAB secreted and cell surface-associated proteins as well as whole cell could render facile mineralization to generate HANPs. However, given the heterogenous and labile nature of the LAB proteins, there is a scope to rationally design synthetic mimics of the protein templates and explore their potential in bio-inspired mineralization for synthesis of HANPs. Based on this notion, the present study highlights a biomineralization-inspired approach for the generation of HANPs using a low molecular weight malonic acid (MA) amphiphile. In order to leverage the generated HANPs in orthopaedic application, titanium wire (TW) was coated with collagen type I incorporated with the generated HANPs. Interestingly, the HANP-coated titanium wire (H-TW) rendered significant bone cell growth, mineralization and osteogenic marker gene expression. It would be interesting to tweak the functional groups of the amphiphile to obtain enhanced material characteristics and the potential of H-TW for bone tissue engineering application can be evaluated in future in a suitable *in vivo* model.

A graphical representation of the significant findings emerging from the present investigation is indicated in Scheme 1.

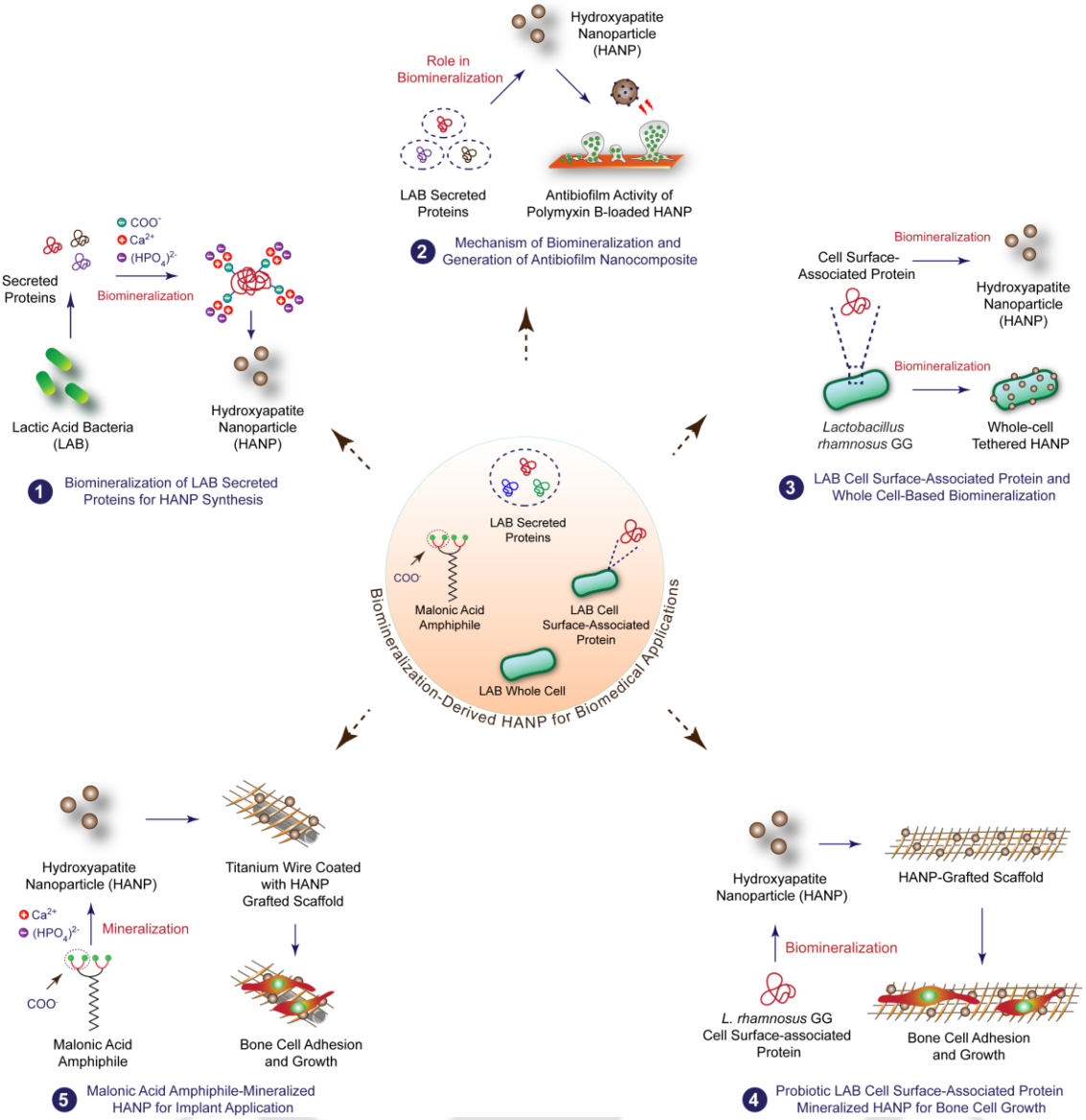


**Scheme 1.** Graphical representation of the significant findings of the present investigation.

# BIBLIOGRAPHY

1. Abdali, Z.; Aminzare, M.; Zhu, X.; DeBenedictis, E.; Xie, O.; Keten, S.; Dorval Courchesne, N. M. Curli-Mediated Self-Assembly of a Fibrous Protein Scaffold for Hydroxyapatite Mineralization. *ACS Synthetic Biology*, **2020**, *9*, 3334-3343.
2. Addadi, L.; Raz, S.; Weiner, S. Taking advantage of disorder: Amorphous calcium carbonate and its roles in biomineralization. *Advanced Materials*, **2003,** *15*, 959–970.
3. Aghaei, H.; Nourbakhsh, A.A.; Karbasi, S.; JavadKalbasi, R.; Rafienia, M.; Nourbakhsh, N.; Bonakdar, S.; Mackenzie, K.J. Investigation on bioactivity and cytotoxicity of mesoporous nano-composite MCM-48/hydroxyapatite for ibuprofen drug delivery. *Ceramics International*, **2014**, *40*, 7355-7362.
4. Ahmadzadeh, E.; Talebnia, F.; Tabatabaei, M.; Ahmadzadeh, H.; Mostaghaci, B. Osteoconductive composite graft based on bacterial synthesized hydroxyapatite nanoparticles doped with different ions: From synthesis to in vivo studies. *Nanomedicine: Nanotechnology, Biology and Medicine*, **2016**, *12*, 1387-1395.
5. Akay, G.; Birch, M. A.; Bokhari, M. A. Microcellular polyHIPE polymer supports osteoblast growth and bone formation in vitro. *Biomaterials*, **2004**, *25*, 3991-4000.
6. Almirall, A.; Larrecq, G.; Delgado, J. A.; Martınez, S.; Planell, J. A.; Ginebra, M. P. Fabrication of low temperature macroporous hydroxyapatite scaffolds by foaming and hydrolysis of an α-TCP paste. *Biomaterials*, **2004**, *25*, 3671-3680.
7. Alonso-Sierra, S.; Velázquez-Castillo, R.; Millán-Malo, B.; Nava, R.; Bucio, L.; Manzano-Ramírez, A.; Cid-Luna, H.; Rivera-Muñoz, E.M. Interconnected porosity analysis by 3D X-ray microtomography and mechanical behavior of biomimetic organic-inorganic composite materials. *Materials Science and Engineering: C*, **2017**, *80*, 45-53.
8. Alves, N. M.; Leonor, I. B.; Azevedo, H. S.; Reis, R. L.; Mano, J. F. Designing biomaterials based on biomineralization of bone. *Journal of Materials Chemistry*, **2010**, *20*, 2911-2921.
9. Amemiya, Y.; Arakaki, A.; Staniland, S. S.; Tanaka, T.; Matsunaga, T. Controlled formation of magnetite crystal by partial oxidation of ferrous hydroxide in the presence of recombinant magnetotactic bacterial protein Mms6. *Biomaterials*, **2007**, *28*, 5381-5389.
10. Amini, A. R.; Laurencin, C. T.; Nukavarapu, S. P. Bone tissue engineering: recent advances and challenges. *Critical Review in Biomedical Engineering*, **2012**, *40*, 363–408.

11. Anbu, P.; Kang, C. H.; Shin, Y. J.; So, J. S. Formations of calcium carbonate minerals by bacteria and its multiple applications. *Springer plus*, **2016**, *5*, 1-26.
12. Andrés, N. C.; D'Elía, N. L.; Ruso, J. M.; Campelo, A. E.; Massheimer, V. L.; Messina, P. V. Manipulation of $Mg^{2+}$–$Ca^{2+}$ switch on the development of bone mimetic hydroxyapatite. *ACS Applied Materials & Interfaces*, **2017**, *9*, 15698-15710.
13. Ang, J. Y.; Abdel-Haq, N.; Zhu, F.; Thabit, A. K.; Nicolau, D. P.; Satlin, M. J.; van Duin, D. Multidrug-resistant *Pseudomonas aeruginosa* infection in a child with cystic fibrosis. *Antimicrobial Agents and Chemotherapy*, **2016**, *60*, 5627–5630.
14. Anitha, A.; Menon, D.; Sivanarayanan, T. B.; Koyakutty, M.; Mohan, C. C.; Nair, S. V.; Nair, M. B. Bioinspired composite matrix containing hydroxyapatite-silica core-shell nanorods for bone tissue engineering. *ACS Applied Materials & Interfaces*, **2017**, *9*, 26707-26718.
15. Arakaki, A.; Shimizu, K.; Oda, M.; Sakamoto, T.; Nishimura, T.; Kato, T. Biomineralization-inspired synthesis of functional organic/inorganic hybrid materials: organic molecular control of self-organization of hybrids. *Organic & Biomolecular Chemistry*, **2015**, *13*, 974-989.
16. Arakaki, A.; Webb, J.; Matsunaga, T. A novel protein tightly bound to bacterial magnetic particles in *Magnetospirillum magneticum* strain AMB-1. *Journal of Biological Chemistry*, **2003**, *278*, 8745-8750.
17. Arcos, D.; Vallet-Regí, M. Substituted hydroxyapatite coatings of bone implants. *Journal of Materials Chemistry B*, **2020**, *8*, 1781-1800.
18. Arevalo-Ferro, C.; Hentzer, M.; Reil, G.; Görg, A.; Kjelleberg, S.; Givskov, M.; Riedel, K.; Eberl, L. Identification of quorum-sensing regulated proteins in the opportunistic pathogen *Pseudomonas aeruginosa* by proteomics. *Environmental Microbiology*, **2003**, *5*, 1350–1369.
19. Arias, J. L.; Fernández, M. S. Polysaccharides and proteoglycans in calcium carbonate-based biomineralization. *Chemical Reviews*, **2008**, *108*, 4475-4482.
20. Åvall-Jääskeläinen, S.; Kylä-Nikkilä, K.; Kahala, M.; Miikkulainen-Lahti, T.; Palva, A. Surface display of foreign epitopes on the *Lactobacillus brevis* S-layer. *Applied and Environmental Microbiology*, **2002**, *68*, 5943-5951.
21. Azizian, S.; Hadjizadeh, A.; Niknejad, H. Chitosan-gelatin porous scaffold incorporated with Chitosan nanoparticles for growth factor delivery in tissue engineering. *Carbohydrate Polymers*, **2018**, *202*, 315-322.

22. Babaie, E.; Bhaduri, S. B. Fabrication aspects of porous biomaterials in orthopedic applications: a review. *ACS Biomaterials Science & Engineering*, **2018**, *4*, 1-39.
23. Bansal, V.; Rautaray, D.; Ahmad, A.; Sastry, M. Biosynthesis of zirconia nanoparticles using the fungus *Fusarium oxysporum*. *Journal of Materials Chemistry*, **2004**, *14*, 3303–3305.
24. Barrère, F.; van Blitterswijk, C. A.; de Groot, K. Bone regeneration: molecular and cellular interactions with calcium phosphate ceramics. *International Journal of Nanomedicine*, **2006**, *1*, 317-332.
25. Bentzmann, S.; Plésiat, P. The *Pseudomonas aeruginosa* opportunistic pathogen and human infections. *Environmental Microbiology*, **2011**, *13*, 1655–1665.
26. Berditsch, M.; Jäger, T.; Strempel, N.; Schwartz, T.; Overhage, J.; Ulrich, A. S. Synergistic effect of membrane-active peptides polymyxin B and gramicidins on multidrug-resistant strains and biofilms of *Pseudomonas aeruginosa*. *Antimicrobial Agents and Chemotherapy*, **2015**, *59*, 5288–5296.
27. Bertran, O.; del Valle, L.J.; Revilla-López, G.; Chaves, G.; Cardús, L.; Casas, M.T.; Casanovas, J.; Turon, P.; Puiggalí, J.; Alemán, C. Mineralization of DNA into nanoparticles of hydroxyapatite. *Dalton Transactions*, **2014**, *43*, 317-327.
28. Bhattacharjee, P.; Naskar, D.; Maiti, T. K.; Bhattacharya, D.; Kundu, S. C. Non-mulberry silk fibroin grafted poly (Є-caprolactone)/nano hydroxyapatite nanofibrous scaffold for dual growth factor delivery to promote bone regeneration. *Journal of Colloid and Interface Science*, **2016**, *472*, 16-33.
29. Billings, N.; Ramirez Millan, M.; Caldara, M.; Rusconi, R.; Tarasova, Y.; Stocker, R.; Ribbeck, K. The Extracellular Matrix Component Psl Provides Fast-Acting Antibiotic Defense in *Pseudomonas aeruginosa* Biofilms. *PLoS Pathogens*, **2013**, *9*, e1003526.
30. Bird, S. M.; Rawlings, A. E.; Galloway, J. M.; Staniland, S. S. Using a biomimetic membrane surface experiment to investigate the activity of the magnetite biomineralisation protein Mms6. *RSC Advances*, **2016**, *6*, 7356-7363.
31. Borah, B. M.; Singh, A. K.; Ramesh, A.; Das, G. Lactic Acid Bacterial Extract as a Biogenic Mineral Growth Modifier. *Journal of Crystal Growth*, **2009**, *311*, 2664−2672.
32. Borowitzka, M. A. Morphological and cytological aspects of algal calcification. *International Review of Cytology*, **1982**, *74*, 127-162.

33. Borowitzka, M. A.; Larkum, A. W. D.; Nockolds, C. E. A scanning electron microscope study of the structure and organization of the calcium carbonate deposits of algae. *Phycologia*, **1974**, *13*, 195-203.
34. Borra, R. C.; Lotufo, M. A.; Gagioti, S. M.; Barros, F. D. M.; Andrade, P. M. A simple method to measure cell viability in proliferation and cytotoxicity assays. *Brazilian Oral Research*, **2009**, *23*, 255-262.
35. Bosak, T. Calcite precipitation, microbially induced. In: Reitner J, Thiel V (eds) Encyclopedia of earth sciences series. *Springer*, Netherlands, **2011**, 223–227.
36. Bose, S.; Roy, M.; Bandyopadhyay, A. Recent advances in bone tissue engineering scaffolds. *Trends in Biotechnology*, **2012**, *30*, 546-554.
37. Bradford, M. M. A rapid and sensitive method for the quantitation of microgram quantities of protein utilizing the principle of protein-dye binding. *Analytical Biochemistry*, **1976**, *72*, 248-254.
38. Braem, A.; De Brucker, K.; Delattin, N.; Killian, M.S.; Roeffaers, M.B.; Yoshioka, T.; Hayakawa, S.; Schmuki, P.; Cammue, B.P.; Virtanen, S.; Thevissen, K. Alternating current electrophoretic deposition for the immobilization of antimicrobial agents on titanium implant surfaces. *ACS Applied Materials & Interfaces*, **2017**, *9*, 8533-8546.
39. Breidenstein, E. B. M.; de la Fuente-Núñez, C.; Hancock, R. E. W. *Pseudomonas aeruginosa*: All roads lead to resistance. *Trends in Microbiology*, **2011**, *19*, 419–426.
40. Brokesh, A. M.; Gaharwar, A. K. Inorganic Biomaterials for Regenerative Medicine. *ACS Applied Materials & Interfaces*, **2020**, *12*, 5319-5344.
41. Bu, S.; Yan, S.; Wang, R.; Xia, P.; Zhang, K.; Li, G.; Yin, J. In Situ Precipitation of Cluster and Acicular Hydroxyapatite onto Porous Poly (γ-benzyl-l-glutamate) Microcarriers for Bone Tissue Engineering. *ACS Applied Materials & Interfaces*, **2020**, *12*, 12468-12477.
42. Cai, Y.; Tang, R. Calcium phosphate nanoparticles in biomineralization and biomaterials. *Journal of Materials Chemistry*, **2008**, *18*, 3775-3787.
43. Cao, H.; Zhang, L.; Zheng, H.; Wang, Z. Hydroxyapatite nanocrystals for biomedical applications. *The Journal of Physical Chemistry C*, **2010**, *114*, 18352-18357.

44. Cardoso, J. C.; Félix, R. C.; Ferreira, V.; Peng, M.; Zhang, X.; Power, D. M. The calcitonin-like system is an ancient regulatory system of biomineralization. *Scientific Reports*, **2020**, *10*, 1-18.
45. Chan, C. S.; Fakra, S. C.; Edwards, D. C.; Emerson, D.; Banfield, J. F. Iron oxyhydroxide mineralization on microbial extracellular polysaccharides. *Geochimica et Cosmochimica Acta*, **2009**, *73*, 3807-3818.
46. Chen, P.; Liu, L.; Pan, J.; Mei, J.; Li, C.; Zheng, Y. Biomimetic composite scaffold of hydroxyapatite/gelatin-chitosan core-shell nanofibers for bone tissue engineering. *Materials Science and Engineering: C*, **2019**, *97*, 325-335.
47. Chen, X.; Zhou, R.; Chen, B.; Chen, J. Nanohydroxyapatite/Cellulose Nanocrystals/Silk Fibroin Ternary Scaffolds for Rat Calvarial Defect Regeneration. *RSC Advances*, **2016**, *6*, 35684-35691.
48. Chi, H.; Song, X.; Song, C.; Zhao, W.; Chen, G.; Jiang, A., Wang, X.; Tailong, Y.; Zheng, L., Yan, J. Chitosan-Gelatin Scaffolds Incorporating Decellularized Platelet-Rich Fibrin Promote Bone Regeneration. *ACS Biomaterials Science & Engineering*, **2019**, *5*, 5305-5315.
49. Cipreste, M.F.; Gonzalez, I.; da Mata Martins, T.M.; Goes, A.M.; de Almeida Macedo, W.A.; de Sousa, E.M.B. Attaching folic acid on hydroxyapatite nanorod surfaces: an investigation of the HA–FA interaction. *RSC Advances*, **2016**, *6*, 76390-76400.
50. Coleman, R. J.; Jack, K. S.; Perrier, S.; Grøndahl, L. Hydroxyapatite mineralization in the presence of anionic polymers. *Crystal Growth & Design*, **2013**, *13*, 4252-4259.
51. Collier, J. H.; Messersmith, P. B. Phospholipid strategies in biomineralization and biomaterials research. *Annual Review of Materials Research*, **2001**, *31*, 237-263.
52. Contreras-Montoya, R.; Jabalera, Y.; Blanco, V.; Cuerva, J. M.; Jimenez-Lopez, C.; Alvarez de Cienfuegos, L. Lysine as size-control additive in a bioinspired synthesis of pure superparamagnetic magnetite nanoparticles. *Crystal Growth & Design*, **2020**, *20*, 533-542.
53. Crookes-Goodson, W. J.; Slocik, J. M.; Naik, R. R. Bio-Directed Synthesis and Assembly of Nanomaterials. *Chemical Society Reviews*, **2008**, *37*, 2403−2412.
54. Cunniffe, G. M.; O'Brien, F. J.; Partap, S.; Levingstone, T. J.; Stanton, K. T.; Dickson, G. R. The synthesis and characterization of nanophase hydroxyapatite using a novel dispersant-aided precipitation method. *Journal of Biomedical Materials Research Part A*, **2010**, *95*, 1142-1149.

55. Cunniffe, G.M.; Curtin, C.M.; Thompson, E.M.; Dickson, G.R.; O'Brien, F.J. Content-Dependent Osteogenic Response of Nanohydroxyapatite: An *In Vitro* and *In Vivo* Assessment within Collagen-Based Scaffolds. *ACS Applied Materials & Interfaces*, **2016**, *8*, 23477-23488.
56. Da Silva Carvalho, T.; Perez, L. R. R. Impact of biofilm production on polymyxin B susceptibility among *Pseudomonas aeruginosa* clinical isolates. *Infection Control & Hospital Epidemiology*, **2019**, *40*, 739-740.
57. Dai, C.; Li, Y.; Pan, W.; Wang, G.; Huang, R.; Bu, Y.; Liao, X.; Guo, K.; Gao, F. Three-dimensional high-porosity chitosan/honeycomb porous carbon/hydroxyapatite scaffold with enhanced osteoinductivity for bone regeneration. *ACS Biomaterials Science & Engineering*, **2020**, *6*, 575-586.
58. Dan, Y.; Liu, O.; Liu, Y.; Zhang, Y.Y.; Li, S.; Feng, X.B.; Shao, Z.W.; Yang, C.; Yang, S.H.; Hong, J.B. Development of novel biocomposite scaffold of chitosan-gelatin/nanohydroxyapatite for potential bone tissue engineering applications. *Nanoscale Research Letters*, **2016**, *11*, 487.
59. Das, B.; Chattopadhyay, P.; Mishra, D.; Maiti, T. K.; Maji, S.; Narayan, R.; Karak, N. Nanocomposites of bio-based hyperbranched polyurethane/funtionalized MWCNT as non-immunogenic, osteoconductive, biodegradable and biocompatible scaffolds in bone tissue engineering. *Journal of Materials Chemistry B*, **2013**, *1*, 4115-4126.
60. Das, S. K.; Dickinson, C.; Lafir, F.; Brougham, D. F.; Marsili, E. Synthesis, characterization and catalytic activity of gold nanoparticles biosynthesized with *Rhizopus oryzae* protein extract. *Green Chemistry*, **2012**, *14*, 1322-1334.
61. Das, S. K.; Liang, J.; Schmidt, M.; Laffir, F.; Marsili, E. Biomineralization mechanism of gold by zygomycete fungi *Rhizopous oryzae*. *ACS Nano*, **2012**, *6*, 6165-6173.
62. Dasgupta, S.; Banerjee, S. S.; Bandyopadhyay, A.; Bose, S. Zn- and Mg-doped hydroxyapatite nanoparticles for controlled release of protein. *Langmuir*, **2010**, *26*, 4958–4964.
63. Deepika, G.; Green, R. J.; Frazier, R. A.; Charalampopoulos, D. Effect of growth time on the surface and adhesion properties of *Lactobacillus rhamnosus* GG. *Journal of Applied Microbiology*, **2009**, *107*, 1230-1240.
64. Degli Esposti, L.; Adamiano, A.; Tampieri, A.; Ramirez-Rodriguez, G.B.; Siliqi, D.; Giannini, C.; Ivanchenko, P.; Martra, G.; Lin, F.H.; Delgado-López, J.M.; Iafisco, M.

Combined effect of citrate and fluoride ions on hydroxyapatite nanoparticles. *Crystal Growth & Design*, **2020**, *20*, 3163−3172.

65. Deshmukh, K.; Shaik, M.M.; Ramanan, S.R.; Kowshik, M. Self-activated fluorescent hydroxyapatite nanoparticles: a promising agent for bioimaging and biolabeling. *ACS Biomaterials Science & Engineering*, **2016**, *2*, 1257-1264.
66. Dinarvand, P.; Seyedjafari, E.; Shafiee, A.; Babaei Jandaghi, A.; Doostmohammadi, A.; Fathi, M.H.; Farhadian, S.; Soleimani, M. New approach to bone tissue engineering: simultaneous application of hydroxyapatite and bioactive glass coated on a poly (L-lactic acid) scaffold. *ACS Applied Materials & Interfaces*, **2011**, *3*, 4518-4524.
67. Ding, X.; Li, X.; Li, C.; Qi, M.; Zhang, Z.; Sun, X.; Wang, L.; Zhou, Y. Chitosan/dextran hydrogel constructs containing strontium-doped hydroxyapatite with enhanced osteogenic potential in rat cranium. *ACS Biomaterials Science & Engineering*, **2019**, *5*, 4574-4586.
68. Egan, T.J.; Chen, J.Y.; de Villiers, K.A.; Mabotha, T.E.; Naidoo, K.J.; Ncokazi, K.K.; Langford, S.J.; McNaughton, D.; Pandiancherri, S.; Wood, B.R. Haemozoin (β-haematin) biomineralization occurs by self-assembly near the lipid/water interface. *FEBS Letters*, **2006**, *580*, 5105-5110.
69. El hadad, A. A.; Barranco, V.; Jimenez-Morales, A.; Peon, E.; Hickman, G. J.; Perry C. C.; Galvan, J. C. Enhancing in vitro biocompatibility and corrosion protection of organic–inorganic hybrid sol–gel films with nanocrystalline hydroxyapatite. *Journal of Materials Chemistry B*, **2014**, *2*, 3886-3896.
70. Elangomannan, S.; Louis, K.; Dharmaraj, B. M.; Kandasamy, V. S.; Soundarapandian, K.; Gopi, D. Carbon nanofiber/polycaprolactone/mineralized hydroxyapatite nanofibrous scaffolds for potential orthopedic applications. *ACS Applied Materials & Interfaces*, **2017**, *9*, 6342-6355.
71. Espino, E.; Koskenniemi, K.; Mato-Rodriguez, L.; Nyman, T. A.; Reunanen, J.; Koponen, J.; Ohman, T.; Siljamaki, P.; Alatossava, T.; Varmanen, P.; Savijoki, K. Uncovering surface-exposed antigens of *Lactobacillus rhamnosus* by cell shaving proteomics and two-dimensional immunoblotting. *Journal of Proteome Research*, **2015**, *14*, 1010-1024.
72. Ethirajan, A.; Ziener, U.; Landfester, K. Surface-Functionalized Polymeric Nanoparticles as Templates for Biomimetic Mineralization of Hydroxyapatite. *Chemistry of Materials*, **2009**, *21*, 2218-2225.

73. Fairbrother, L.; Etschmann, B.; Brugger, J.; Shapter, J.; Southam, G.; Reith, F. Biomineralization of gold in biofilms of *Cupriavidus metallidurans*. *Environmental Science & Technology*, **2013**, *47*, 2628-2635.
74. Fan, Z.; Wang, J.; Wang, Z.; Li, Z.; Qiu, Y.; Wang, H.; Xu, Y.; Niu, L.; Gong, P.; Yang, S. Casein phosphopeptide-biofunctionalized graphene biocomposite for hydroxyapatite biomimetic mineralization. *The Journal of Physical Chemistry C*, **2013**, *117*, 10375-10382.
75. Farokhi, M.; Mottaghitalab, F.; Samani, S.; Shokrgozar, M.A.; Kundu, S.C.; Reis, R.L.; Fatahi, Y.; Kaplan, D.L. Silk fibroin/hydroxyapatite composites for bone tissue engineering. *Biotechnology Advances*, **2018**, *36*, 68-91.
76. Franceschi, R. T.; Xiao, G. Regulation of the osteoblast-specific transcription factor, Runx2: Responsiveness to multiple signal transduction pathways. *Journal of Cellular Biochemistry*, **2003**, *88*, 446-454.
77. French, S.; Puddephatt, D.; Habash, M.; Glasauer, S. The dynamic nature of bacterial surfaces: implications for metal–membrane interaction. *Critical reviews in Microbiology*, **2013**, *39*, 196-217.
78. Frohbergh, M. E.; Katsman, A.; Botta, G. P.; Lazarovici, P.; Schauer, C. L.; Wegst, U. G.; Lelkes, P. I. Electrospun hydroxyapatite-containing chitosan nanofibers crosslinked with genipin for bone tissue engineering. *Biomaterials*, **2012**, *33*, 9167-9178.
79. Fulgione, A.; Nocerino, N.; Iannaccone, M.; Roperto, S.; Capuano, F.; Roveri, N.; Lelli, M.; Crasto, A.; Calogero, A.; Pilloni, A.P.; Capparelli, R. Lactoferrin adsorbed onto biomimetic hydroxyapatite nanocrystals controlling-in vivo-the *Helicobacter pylori* infection. *PLOS one*, **2016**, *11*, e0158646.
80. Gao, C.; Peng, S.; Feng, P.; Shuai, C. Bone biomaterials and interactions with stem cells. *Bone Research*, **2017**, *5*, 1-33.
81. Gao, X.; Song, J.; Ji, P.; Zhang, X.; Li, X.; Xu, X.; Wang, M.; Zhang, S.; Deng, Y.; Deng, F.; Wei, S. Polydopamine-templated hydroxyapatite reinforced polycaprolactone composite nanofibers with enhanced cytocompatibility and osteogenesis for bone tissue engineering. *ACS Applied Materials and Interfaces*, **2016**, *8*, 3499–3515.

82. Geetha, M.; Singh, A. K.; Asokamani, R.; Gogia, A. K. Ti based biomaterials, the ultimate choice for orthopaedic implants–a review. *Progress in Materials Science*, **2009**, *54*, 397-425.

83. Ghimire, A.; Skelly, J. D.; Song, J. Micrococcal-Nuclease-Triggered On-Demand Release of Vancomycin from Intramedullary Implant Coating Eradicates *Staphylococcus aureus* Infection in Mouse Femoral Canals. *ACS Central Science*, **2019**, *5*, 1929-1936.

84. Ghorbani, F.; Zamanian, A.; Behnamghader, A.; Joupari, M. D. A facile method to synthesize mussel-inspired polydopamine nanospheres as an active template for in situ formation of biomimetic hydroxyapatite. *Materials Science and Engineering: C*, **2019**, *94*, 729-739.

85. Ghosh, M.; Halperin-Sternfeld, M.; Grigoriants, I.; Lee, J.; Nam, K. T.; Adler-Abramovich, L. Arginine-presenting peptide hydrogels decorated with hydroxyapatite as biomimetic scaffolds for bone regeneration. *Biomacromolecules*, **2017**, *18*, 3541-3550.

86. Giannoudis, P. V; Dinopoulos, H.; Tsiridis, E. Bone substitutes: an update. *Injury*, **2005**, *36*, S20-S27.

87. Goldin, B. R.; Gorbach, S. L.; Saxelin, M.; Barakat, S.; Gualtieri, L.; Salminen, S. Survival of *Lactobacillus* species (strain GG) in human gastrointestinal tract. *Digestive Diseases and Sciences*, **1992**, *37*, 121-128.

88. Golub, E. E.; Boesze-Battaglia, K. The role of alkaline phosphatase in mineralization. *Current opinion in Orthopaedics*, **2007**, *18*, 444-448.

89. Goswami, S.; Adhikari, M. D.; Kar, C.; Thiyagarajan, D.; Das, G.; Ramesh, A. Synthetic amphiphiles as therapeutic antibacterials: lessons on bactericidal efficacy and cytotoxicity and potential application as an adjuvant in antimicrobial chemotherapy. *Journal of Materials Chemistry B*, **2013**, *1*, 2612-2623.

90. Goswami, S.; Thiyagarajan, D.; Das, G.; Ramesh, A. Biocompatible nanocarrier fortified with a dipyridinium-based amphiphile for eradication of biofilm. *ACS Applied Materials & Interfaces*, **2014**, *6*, 16384-16394.

91. Grosu-Tudor, S. S.; Brown, L.; Hebert, E. M.; Brezeanu, A.; Brinzan, A.; Fadda, S.; Mozzi, F.; Zamfir, M. S-layer production by *Lactobacillus acidophilus* IBB 801 under environmental stress conditions. *Applied Microbiology and Biotechnology*, **2016**, *100*, 4573-4583.

92. Guarino, A.; Vecchio, A. L.; Canani, R. B. Probiotics as prevention and treatment for diarrhea. *Current Opinion in Gastroenterology*, **2009**, *25*, 18-23.

93. Gungormus, M.; Branco, M.; Fong, H.; Schneider, J. P.; Tamerler, C.; Sarikaya, M. Self-assembled bi-functional peptide hydrogels with biomineralization-directing peptides. *Biomaterials*, **2010**, *31*, 7266-7274.

94. Habraken, W. J. E. M.; Wolke, J. G. C.; Jansen, J. A. Ceramic composites as matrices and scaffolds for drug delivery in tissue engineering. *Advanced Drug Delivery Reviews*, **2007**, *59*, 234-248.

95. Hadagalli, K.; Panda, A. K.; Mandal, S.; Basu, B. Faster biomineralization and tailored mechanical properties of marine-resource-derived hydroxyapatite scaffolds with tunable interconnected porous architecture. *ACS Applied Bio Materials*, **2019**, *2*, 2171-2184.

96. Haider, A.; Haider, S.; Han, S. S.; Kang, I. K. Recent advances in the synthesis, functionalization and biomedical applications of hydroxyapatite: a review. *RSC Advances*, **2017**, *7*, 7442-7458.

97. Hartgerink, J. D.; Beniash, E.; Stupp, S. I. Self-assembly and mineralization of peptide-amphiphile nanofibers. *Science*, **2001**, *294*, 1684-1688.

98. Huang, A.; Dai, H.; Wu, X.; Zhao, Z.; Wu, Y. Synthesis and characterization of mesoporous hydroxyapatite powder by microemulsion technique. *Journal of Materials Research and Technology*, **2019**, *8*, 3158-3166.

99. Huang, Z.; Jin, H.; Che, S. Structural roles of amphiphilic peptide tails on silica biomineralization. *Dalton Transactions*, **2014**, *43*, 16169-16172.

100. Hutmacher, D. W.; Schantz, J. T.; Lam, C. X. F.; Tan, K. C.; Lim, T. C. State of the art and future directions of scaffold-based bone engineering from a biomaterials perspective. *Journal of Tissue Engineering and Regenerative Medicine*, **2007**, *1*, 245-260.

101. Hynönen, U.; Palva, A. Lactobacillus surface layer proteins: structure, function and applications. *Applied Microbiology and Biotechnology*, **2013**, *97*, 5225-5243.

102. Iafisco, M.; Quirici, N.; Foltran, I.; Rimondini, L. Electrospun collagen mimicking the reconstituted extracellular matrix improves osteoblastic differentiation onto titanium surfaces. *Journal of Nanoscience and Nanotechnology*, **2013**, *13*, 4720-4726.

103. Irfan, M.; Suprajaa, P. S.; Baraneedharan, P.; Reddy, B. M. A Comparative Study of Nanohydroxyapetite Obtained from Natural Shells and Wet Chemical Process. *Journal of Materials Science and Surface Engineering*, **2020**, *7*, 938-943.
104. Isikli, C.; Hasirci, V.; Hasirci, N. Development of porous chitosan–gelatin/hydroxyapatite composite scaffolds for hard tissue-engineering applications. *Journal of Tissue Engineering and Regenerative Medicine*, **2012**, *6*, 135-143.
105. Ivanova, T. I.; Frank-Kamenetskaya, O. V.; Kol'tsov, A. B.; Ugolkov, V. L. Crystal structure of calcium-deficient carbonated hydroxyapatite. Thermal decomposition. *Journal of Solid State Chemistry*, **2001**, *160*, 340-349.
106. Iwatsubo, T.; Kishi, R.; Miura, T.; Ohzono, T.; Yamaguchi, T. Formation of hydroxyapatite skeletal materials from hydrogel matrices via artificial biomineralization. *The Journal of Physical Chemistry B*, **2015**, *119*, 8793-8799.
107. Jabalera, Y.; Casares Atienza, S.; Fernández-Vivas, A.; Peigneux, A.; Azuaga Fortes, A. I.; Jimenez-Lopez, C. Protein conservation method affects MamC-mediated biomineralization of magnetic nanoparticles. *Crystal Growth & Design*, **2019**, *19*, 1064-1071.
108. Jackson, E.; Ferrari, M.; Cuestas-Ayllon, C.; Fernández-Pacheco, R.; Perez-Carvajal, J.; de la Fuente, J.M.; Grazú, V.; Betancor, L. Protein-templated biomimetic silica nanoparticles. *Langmuir*, **2015**, *31*, 3687-3695.
109. Jain, N.; Bhargava, A.; Majumdar, S.; Tarafdar, J. C.; Panwar, J. Extracellular biosynthesis and characterization of silver nanoparticles using *Aspergillus flavus* NJP08: A mechanism perspective. *Nanoscale*, **2011**, *3*, 635–641.
110. Jain, R.; Khandelwal, G.; Roy, S. Unraveling the Design Rules in Ultrashort Amyloid-Based Peptide Assemblies toward Shape-Controlled Synthesis of Gold Nanoparticles. *Langmuir*, **2019**, *35*, 5878-5889.
111. Javaheri, N.; Dries, R.; Burson, A.; Stal, L. J.; Sloot, P. M. A.; Kaandorp, J. A. Temperature Affects the Silicate Morphology in a Diatom. *Scientific Reports*, **2015**, 5, 11652.
112. Javaid, M. A.; Kaartinen, M. T. Mesenchymal stem cell-based bone tissue engineering. *International Dental Journal of Students Research*, **2013**, *1*, 24-35.
113. Jiang, D.; Zhao, H.; Yang, Y.; Zhu, Y.; Chen, X.; Sun, J.; Yu, K.; Fan, H.; Zhang, X. Investigation of luminescent mechanism: N-rich carbon dots as luminescence centers

in fluorescent hydroxyapatite prepared using a typical hydrothermal process. *Journal of Materials Chemistry B*, **2017**, *5*, 3749-3757.

114. Jiang, H.; Zuo, Y.; Zou, Q.; Wang, H.; Du, J.; Li, Y.; Yang, X. Biomimetic spiral-cylindrical scaffold based on hybrid chitosan/cellulose/nano-hydroxyapatite membrane for bone regeneration. *ACS Applied Materials & Interfaces*, **2013**, *5*, 12036-12044.
115. Jutz, G.; Böker, A. Bio-inorganic microcapsules from templating protein-and bionanoparticle-stabilized Pickering emulsions. *Journal of Materials Chemistry*, **2010**, *20*, 4299-4304.
116. Kang, F.; Qu, X.; Alvarez, P. J.; Zhu, D. Extracellular saccharide-mediated reduction of Au3+ to gold nanoparticles: new insights for heavy metals biomineralization on microbial surfaces. *Environmental Science & Technology*, **2017**, *51*, 2776-2785.
117. Kang, H. G.; Kim, S. Y.; Lee, Y. M. Novel porous gelatin scaffolds by overrun/particle leaching process for tissue engineering applications. *Journal of Biomedical Materials Research Part B*, **2006**, *79*, 388-397.
118. Karunakaran, G.; Cho, E. B.; Kumar, G. S.; Kolesnikov, E.; Janarthanan, G.; Pillai, M. M.; Rajendran, S.; Boobalan, S.; Gorshenkov, M. V.; Kuznetsov, D. Ascorbic Acid-Assisted Microwave Synthesis of Mesoporous Ag-Doped Hydroxyapatite Nanorods from Biowaste Seashells for Implant Applications. *ACS Applied Bio Materials*, **2019**, *2*, 2280–2293.
119. Kern, T.; Giffard, M.; Hediger, S.; Amoroso, A.; Giustini, C.; Bui, N. K.; Joris, B.; Bougault, C.; Vollmer W.; Simorre, J. P. Dynamics characterization of fully hydrated bacterial cell walls by solid-state NMR: evidence for cooperative binding of metal ions. *Journal of the American Chemical Society*, **2010**, *132*, 10911-10919.
120. Khaled, E. G.; Saleh, M.; Hindocha, S.; Griffin, M.; Khan, W. S. Tissue Engineering for Bone Production-Stem Cells, Gene Therapy and Scaffolds. *The Open Orthopaedics Journal*, **2011**, *5*, 289-295.
121. Kim, S. S.; Park, M. S.; Jeon, O.; Choi, C. Y.; Kim, B. S. Poly (lactide-co-glycolide)/hydroxyapatite composite scaffolds for bone tissue engineering. *Biomaterials*, **2006**, *27*, 1399-1409.
122. Koirala, M. B.; Nguyen, T. D. T.; Pitchaimani, A.; Choi, S. O.; Aryal, S. Synthesis and characterization of biomimetic hydroxyapatite nanoconstruct using chemical

gradient across lipid bilayer. *ACS Applied Materials & Interfaces*, **2015**, *7*, 27382-27390.

123. Kokubo, T.; Kushitani, H.; Sakka, S.; Kitsugi, T.; Yamamuro, T. Solutions able to reproduce *in vivo* surface-structure changes in bioactive glass-ceramic A-W3. *Journal of Biomedical Materials Research*, **1990**, *24*, 721-734.
124. Kontrec, J.; Ukrainczyk, M.; Džakula, B. N.; Kralj, D. Precipitation and characterization of hollow calcite nanoparticles. *Crystal Research and Technology*, **2013**, *48*, 622-626.
125. Kotzsch, A.; Gröger, P.; Pawolski, D.; Bomans, P. H.; Sommerdijk, N. A.; Schlierf, M.; Kröger, N. Silicanin-1 is a conserved diatom membrane protein involved in silica biomineralization. *BMC Biology*, **2017**, *15*, 1-16.
126. Kuhrts, L.; Macías-Sánchez, E.; Tarakina, N. V.; Hirt, A. M.; Faivre, D. Shaping magnetite with Poly-L-arginine and pH: from small single crystals to large mesocrystals. *The Journal of Physical Chemistry Letters*, **2019**, *10*, 5514-5518.
127. Kutikov, A. B.; Skelly, J. D.; Ayers, D. C.; Song, J. Templated repair of long bone defects in rats with bioactive spiral-wrapped electrospun amphiphilic polymer/hydroxyapatite scaffolds. *ACS Applied Materials & Interfaces*, **2015**, *7*, 4890-4901.
128. Lambert, P. A. Mechanisms of antibiotic resistance in *Pseudomonas aeruginosa*. *Journal of the Royal Society of Medicine*, **2002**, *95*, 22-26.
129. Lamkhao, S.; Phaya, M.; Jansakun, C.; Chandet, N.; Thongkorn, K.; Rujijanagul, G.; Bangrak, P.; Randorn, C. Synthesis of hydroxyapatite with antibacterial properties using a microwave-assisted combustion method. *Scientific Reports*, **2019**, *9*, 1-9.
130. Lechner, C. C.; Becker, C. F. Silaffins in silica biomineralization and biomimetic silica precipitation. *Marine Drugs*, **2015**, *13*, 5297-5333.
131. Lee, J.; Kim, G. Calcium-deficient hydroxyapatite/collagen/platelet-rich plasma scaffold with controlled release function for hard tissue regeneration. *ACS Biomaterials Science & Engineering*, **2018**, *4*, 278-289.
132. Levengood, S. K. L.; Zhang, M. Chitosan-based scaffolds for bone tissue engineering. *Journal of Materials Chemistry B*, **2014**, *2*, 3161-3184.
133. Levi-Kalisman, Y.; Falini, G.; Addadi, L.; Weiner, S. Structure of the nacreous organic matrix of a bivalve mollusk shell examined in the hydrated state using cryo-TEM. *Journal of Structural Biology*, **2001**, *135*, 8-17.

134. Li, B.; Kan, L.; Zhang, X.; Li, J.; Li, R.; Gui, Q.; Qiu, D.; He, F.; Ma, N.; Wang, Y.; Wei, H. Biomimetic bone-like hydroxyapatite by mineralization on supramolecular porous fiber networks. *Langmuir*, **2017**, *33*, 8493-8502.

135. Li, D.; Huang, X.; Wu, Y.; Li, J.; Cheng, W.; He, J.; Tian, H.; Huang, Y. Preparation of pH-responsive mesoporous hydroxyapatite nanoparticles for intracellular controlled release of an anticancer drug. *Biomaterials Science*, **2016**, *4*, 272-280.

136. Li, D.; Newton, S. M.; Klebba, P. E.; Mao, C. Flagellar display of bone-protein-derived peptides for studying peptide-mediated biomineralization. *Langmuir*, **2012**, *28*, 16338-16346.

137. Li, H.; Song, X.; Li, B.; Kang, J.; Liang, C.; Wang, H.; Yu, Z.; Qiao, Z. Carbon nanotube-reinforced mesoporous hydroxyapatite composites with excellent mechanical and biological properties for bone replacement material application. *Materials Science and Engineering: C*, **2017**, *77*, 1078-1087.

138. Li, L.; Shi, X. Wang, Z.; Guo, M.; Wang, Y.; Jiao, Z.; Zhang, P. Porous Scaffolds of Poly (lactic-co-glycolic acid) and Mesoporous Hydroxyapatite Surface Modified by Poly (γ-benzyl-l-glutamate) (PBLG) for *in vivo* Bone Repair. *ACS Biomaterials Science & Engineering*, **2019**, *5*, 2466-2481.

139. Li, Q.; Csetenyi, L.; Gadd, G. M. Biomineralization of metal carbonates by Neurospora crassa. *Environmental Science & Technology*, **2014**, *48*, 14409-14416.

140. Li, Q.; Li, M.; Zhu, P.; Wei, S. *In vitro* synthesis of bioactive hydroxyapatite using sodium hyaluronate as a template. *Journal of Materials Chemistry*, **2012**, *22*, 20257–20265.

141. Li, Q.; Zhang, J.; Wang, Y.; Qi, W.; Su, R.; He, Z. Peptide-Templated Synthesis of TiO2 Nanofibers with Tunable Photocatalytic Activity. *Chemistry–A European Journal*, **2018**, *24*, 18123-18129.

142. Li, Y.; Hao, H.; Zhong, Z.; Li, M.; Li, J.; Du, Y.; Wu, X.; Wang, J.; Zhang, S. Assembly mechanism of highly crystalline selenium-doped hydroxyapatite nanorods via particle attachment and their effect on the fate of stem cells. *ACS Biomaterials Science & Engineering*, **2019**, *5*, 6703-6714.

143. Li, Y.; Liu, Y.; Xun, X.; Zhang, W.; Xu, Y.; Gu, D. Three-dimensional porous scaffolds with biomimetic microarchitecture and bioactivity for cartilage tissue engineering. *ACS Applied Materials & Interfaces*, **2019**, *11*, 36359-36370.

144. Li, Y.; Wang, Y.; Li, Y.; Luo, W.; Jiang, J.; Zhao, J.; Liu, C. Controllable Synthesis of Biomimetic Hydroxyapatite Nanorods with High Osteogenic Bioactivity. *ACS Biomaterials Science & Engineering*, **2019**, *6*, 320-328.

145. Lian, B.; Hu, Q.; Chen, J.; Ji, J.; Teng, H. H. Carbonate biomineralization induced by soil bacterium *Bacillus megaterium*. *Geochimica et Cosmochimica Acta*, **2006**, *70*, 5522-5535.

146. Liang, Y.H.; Liu, C.H.; Liao, S.H.; Lin, Y.Y.; Tang, H.W.; Liu, S.Y.; Lai, I.R.; Wu, K.C.W. Cosynthesis of cargo-loaded hydroxyapatite/alginate core–shell nanoparticles (HAP@ Alg) as pH-responsive nanovehicles by a pre-gel method. *ACS Applied Materials & Interfaces*, **2012**, *4*, 6720-6727.

147. Lim, T. P.; Lee, W.; Tan, T. Y.; Sasikala, S.; Teo, J.; Hsu, L. Y.; Tan, T. T.; Syahidah, N.; Kwa, A. L. Effective antibiotics in combination against extreme drug-resistant *Pseudomonas aeruginosa* with decreased susceptibility to polymyxin B. *PLoS ONE*, **2011**, *6*, 8–14.

148. Lin, H. R.; Yeh, Y. J. Porous alginate/hydroxyapatite composite scaffolds for bone tissue engineering: preparation, characterization, and in vitro studies. *Journal of Biomedical Materials Research Part B*, **2004**, *71*, 52-65.

149. Liu, B.; Cao, Y.; Huang, Z.; Duan, Y.; Che, S. Silica biomineralization via the self-assembly of helical biomolecules. *Advanced Materials*, **2015**, *27*, 479-497.

150. Liu, H.; Chen, F.; Xi, P.; Chen, B.; Huang, L.; Cheng, J.; Shao, C.; Wang, J.; Bai, D.; Zeng, Z. Biocompatible fluorescent hydroxyapatite: synthesis and live cell imaging applications. *The Journal of Physical Chemistry C*, **2011**, *115*, 18538-18544.

151. Liu, H.; Cheng, J.; Chen, F.; Hou, F.; Bai, D.; Xi, P.; Zeng, Z. Biomimetic and cell-mediated mineralization of hydroxyapatite by carrageenan functionalized graphene oxide. *ACS Applied Materials & Interfaces*, **2014**, *6*, 3132-3140.

152. Liu, H.; Lv, Z.; Ding, K.; Liu, X.; Yuan, L.; Chen, H.; Li, X. Incorporation of tyrosine phosphate into tetraphenylethylene affords an amphiphilic molecule for alkaline phosphatase detection, hydrogelation and calcium mineralization. *Journal of Materials Chemistry B*, **2013**, *1*, 5550-5556.

153. Liu, L.; Pu, X.; Yin, G.; Chen, X.; Yin, J.; Wu, Y. Biomimetic Mineralization of Magnetic Iron Oxide Nanoparticles Mediated by Bi-Functional Copolypeptides. *Molecules*, **2019**, *24*, 1401.

154. Liu, Q.; Huang, S.; Matinlinna, J. P.; Chen, Z.; Pan, H. Insight into biological apatite: physiochemical properties and preparation approaches. *BioMed Research International*, **2013**, 929748.

155. Liu, W.; Wang, J.; Jiang, G.; Guo, J.; Li, Q.; Li, B.; Wang, Q.; Cheng, M.; He, G.; Zhang, X. The improvement of corrosion resistance, biocompatibility and osteogenesis of the novel porous Mg–Nd–Zn alloy. *Journal of Materials Chemistry B*, **2017**, *5*, 7661-7674.

156. Liu, X.; Wei, D.; Zhong, J.; Ma, M.; Zhou, J.; Peng, X.; Ye, Y.; Sun, G.; He, D. Electrospun nanofibrous P (DLLA–CL) balloons as calcium phosphate cement filled containers for bone repair: In vitro and in vivo studies. *ACS Applied Materials & Interfaces*, **2015**, *7*, 18540-18552.

157. Livak, K. J.; Schmittgen, T. D. Analysis of relative gene expression data using real-time quantitative PCR and the $2^{-\Delta\Delta}$CT method. *Methods*, **2001**, *25*, 402-408.

158. Long, T.; Guo, Y. P.; Liu, Y. Z.; Zhu, Z. A. Hierarchically nanostructured mesoporous carbonated hydroxyapatite microspheres for drug delivery systems with high drug-loading capacity. *RSC Advances*, **2013**, *3*, 24169-24176.

159. Lopez-Moreno, R.; Fernández-Vivas, A.; Valverde-Tercedor, C.; Azuaga Fortes, A.I.; Casares Atienza, S.; Rodriguez-Navarro, A.B.; Zarivach, R.; Jimenez-Lopez, C. Magnetite nanoparticles biomineralization in the presence of the magnetosome membrane protein MamC: effect of protein aggregation and protein structure on magnetite formation. *Crystal Growth & Design*, **2017**, *17*, 1620-1629.

160. Lowenstam, H. A. Minerals Formed by Organisms. *Science*, **1981**, *211*, 1126− 1131.

161. Lu, H.; Lutz, H.; Roeters, S.J.; Hood, M.A.; Schäfer, A.; Muñoz-Espí, R.; Berger, R.; Bonn, M.; Weidner, T. Calcium-induced molecular rearrangement of peptide folds enables biomineralization of vaterite calcium carbonate. *Journal of the American Chemical Society*, **2018**, *140*, 2793-2796.

162. Ma, J.; Qin, J. Graphene-like zinc substituted hydroxyapatite. *Crystal Growth & Design*, **2015**, *15*, 1273-1279.

163. Ma, M. G. Hierarchically nanostructured hydroxyapatite: hydrothermal synthesis, morphology control, growth mechanism, and biological activity. *International journal of Nanomedicine*, **2012**, *7*, 1781-1791.

164. Maji, S.; Agarwal, T.; Das, J.; Maiti, T. K. Development of gelatin/carboxymethyl chitosan/nano-hydroxyapatite composite 3D macroporous scaffold for bone tissue engineering applications. *Carbohydrate Polymers*, **2018**, *189*, 115-125.
165. Mann, S. Biomineralization and Biomimetic Materials Chemistry. *Journal of Material Chemistry*, **1995**, *5*, 935−946.
166. Mann, S. Mineralization in biological systems. *Inorganic Elements in Biochemistry*, Springer, **1983**, 125-174.
167. Mann, S. Biomineralization: principles and concepts in bioinorganic materials chemistry, *Oxford University*, **2001**, *5*.
168. Marycz, K.; Smieszek, A.; Targonska, S.; Walsh, S. A.; Szustakiewicz, K.; Wiglusz, R. J. Three dimensional (3D) printed polylactic acid with nano-hydroxyapatite doped with europium (III) ions (nHAp/PLLA@ Eu3+) composite for osteochondral defect regeneration and theranostics. *Materials Science and Engineering: C*, **2020**, *110*, 110634.
169. Mehta, A.; Sidhu, C.; Pinnaka, A. K.; Choudhury, A. R. Extracellular polysaccharide production by a novel osmotolerant marine strain of *Alteromonas macleodii* and its application towards biomineralization of silver. *PloS one*, **2014**, *9*, e98798.
170. Melcher, M.; Facey, S. J.; Henkes, T. M.; Subkowski, T.; Hauer, B. Accelerated nucleation of hydroxyapatite using an engineered hydrophobin fusion protein. *Biomacromolecules*, **2016**, *17*, 1716-1726.
171. Mirabello, G.; Lenders, J. J.; Sommerdijk, N. A. Bioinspired synthesis of magnetite nanoparticles. *Chemical Society Reviews*, **2016**, *45*, 5085-5106.
172. Mobasherpour, I.; Heshajin, M. S.; Kazemzadeh, A.; Zakeri, M. Synthesis of nanocrystalline hydroxyapatite by using precipitation method. *Journal of Alloys and Compounds*, **2007**, *430*, 330-333.
173. Mukherjee, K.; Ruan, Q.; Nutt, S.; Tao, J.; De Yoreo, J. J.; Moradian-Oldak, J. Peptide-based bioinspired approach to regrowing multilayered aprismatic enamel. *ACS Omega*, **2018**, *3*, 2546-2557.
174. Munir, M.U.; Ihsan, A.; Javed, I.; Ansari, M.T.; Bajwa, S.Z.; Bukhari, S.N.A.; Ahmed, A.; Malik, M.Z.; Khan, W.S. Controllably biodegradable hydroxyapatite nanostructures for cefazolin delivery against antibacterial resistance. *ACS Omega*, **2019**, *4*, 7524-7532.

175. Nagarajan, S.; Belaid, H.; Pochat-Bohatier, C.; Teyssier, C.; Iatsunskyi, I.; Coy, E.; Balme, S.; Cornu, D.; Miele, P.; Kalkura, N.S.; Cavaillès, V. Design of boron nitride/gelatin electrospun nanofibers for bone tissue engineering. *ACS Applied Materials & Interfaces*, **2017**, *9*, 33695-33706.

176. Nair, B.; Pradeep, T. Coalescence of nanoclusters and formation of submicron crystallites assisted by *Lactobacillus* strains. *Crystal Growth & Design*, **2002**, *2*, 293-298.

177. Narayanan, T. S.; Lee, M. H. A simple strategy to modify the porous structure of plasma electrolytic oxidation coatings on magnesium. *RSC Advances*, **2016**, *6*, 16100-16114.

178. Neubauer, V. J.; Scheibel, T. Spider Silk Fusion Proteins for Controlled Collagen Binding and Biomineralization. *ACS Biomaterials Science & Engineering*, **2020**, *6*, 5599-5608.

179. Ngiam, M.; Nguyen, L. T.; Liao, S.; Chan, C. K.; Ramakrishna, S. Biomimetic nanostructured materials—potential regulators for osteogenesis? *Annals Academy of Medicine*, **2011**, *40*, 213-222.

180. Nielsen, J. W.; Sand, K. K.; Pedersen, C. S.; Lakshtanov, L. Z.; Winther, J. R.; Willemoës, M.; Stipp, S. L. S. Polysaccharide effects on calcite growth: the influence of composition and branching. *Crystal Growth & Design*, **2012**, *12*, 4906-4910.

181. Nosrati, H.; Sarraf-Mamoory, R.; Le, D. Q. S.; Perez, M. C.; Bünger, C. E. Evaluation of Argon-Gas-Injected Solvothermal Synthesis of Hydroxyapatite Crystals Followed by High-Frequency Induction Heat Sintering. *Crystal Growth & Design*, **2020**, *20*, 3182-3189.

182. Ohgushi, H.; Kotobuki, N.; Funaoka, H.; Machida, H.; Hirose, M.; Tanaka, Y.; Takakura, Y. Tissue engineered ceramic artificial joint—ex vivo osteogenic differentiation of patient mesenchymal cells on total ankle joints for treatment of osteoarthritis. *Biomaterials*, **2005**, *26*, 4654-4661.

183. Ojha, B.; Singh, A. K.; Adhikari, M. D.; Ramesh, A.; Das, G. 2-Alkylmalonic acid: amphiphilic chelator and a potent inhibitor of metalloenzyme. *The Journal of Physical Chemistry B*, **2010**, *114*, 10835-10842.

184. Öner, M.; Yetiz, E.; Ay, E.; Uysal, U. Ibuprofen release from porous hydroxyapatite tablets. *Ceramics International*, **2011**, *37*, 2117-2125.

185. Padmanabhan, V.P.; Balakrishnan, S.; Kulandaivelu, R.; TSN, S.N.; Lakshmipathy, M.; Sagadevan, S.; Mohammad, F.; Al-Lohedan, H.A.; Paiman, S.; Oh, W.C. Nanoformulations of core–shell type hydroxyapatite-coated gum acacia with enhanced bioactivity and controlled drug delivery for biomedical applications. *New Journal of Chemistry*, **2020**, *44*, 7175-7185.

186. Palazzo, B.; Iafisco, M.; Laforgia, M.; Margiotta, N.; Natile, G.; Bianchi, C.L.; Walsh, D.; Mann, S.; Roveri, N. Biomimetic hydroxyapatite–drug nanocrystals as potential bone substitutes with antitumor drug delivery properties. *Advanced Functional Materials*, **2007**, *17*, 2180-2188.

187. Pandey, A.; Midha, S.; Sharma, R. K.; Maurya, R.; Nigam, V. K.; Ghosh, S.; Balani, K. Antioxidant and antibacterial hydroxyapatite-based biocomposite for orthopedic applications. *Materials Science and Engineering: C*, **2018**, *88*, 13-24.

188. Pawelec, K. M.; Kluijtmans, S. G. Biomineralization of recombinant peptide scaffolds: Interplay among chemistry, architecture, and mechanics. *ACS Biomaterials Science & Engineering*, **2017**, *3*, 1100-1108.

189. Peigneux, A.; Valverde-Tercedor, C.; Lopez-Moreno, R.; Perez-Gonzalez, T.; Fernandez-Vivas, M. A.; Jimenez-Lopez, C. Learning from magnetotactic bacteria: A review on the synthesis of biomimetic nanoparticles mediated by magnetosome-associated proteins. *Journal of Structural Biology*, **2016**, *196*, 75-84.

190. Pohl, A.; Berger, F.; Sullan, R.M.; Valverde-Tercedor, C.; Freindl, K.; Spiridis, N.; Lefèvre, C.T.; Menguy, N.; Klumpp, S.; Blank, K.G.; Faivre, D. Decoding biomineralization: interaction of a Mad10-derived peptide with magnetite thin films. *Nano Letters*, **2019**, *19*, 8207-8215.

191. Pohnert, G. Biomineralization in diatoms mediated through peptide-and polyamine-assisted condensation of silica. *Angewandte Chemie International Edition*, **2002**, *41*, 3167-3169.

192. Poulsen, N.; Kröger, N. Silica morphogenesis by alternative processing of silaffins in the diatom *Thalassiosira pseudonana*. *Journal of Biological Chemistry*, **2004**, *279*, 42993-42999.

193. Prakash, K. H.; Kumar, R.; Ooi, C. P.; Cheang, P.; Khor, K. A. Conductometric study of precursor compound formation during wet-chemical synthesis of nanocrystalline hydroxyapatite. *The Journal of Physical Chemistry B*, **2006**, *110*, 24457-24462.

194. Pramanik, N.; Mishra, D.; Banerjee, I.; Maiti, T. K.; Bhargava, P.; Pramanik, P. Chemical synthesis, characterization, and biocompatibility study of hydroxyapatite/chitosan phosphate nanocomposite for bone tissue engineering applications. *International Journal of Biomaterials*, **2009**, 512417.

195. Priyam, A.; Das, R. K.; Schultz, A.; Singh, P. P. A new method for biological synthesis of agriculturally relevant nanohydroxyapatite with elucidated effects on soil bacteria. *Scientific Reports*, **2019**, *9*, 1-14.

196. Purdy Drew, K. R.; Sanders, L. K.; Culumber, Z. W.; Zribi, O.; Wong, G. C. Cationic amphiphiles increase activity of aminoglycoside antibiotic tobramycin in the presence of airway polyelectrolytes. *Journal of the American Chemical Society*, **2009**, *131*, 486-493.

197. Qi, M.L.; Yao, S.; Liu, X.C.; Wang, X.; Cui, F. Nanosheet-assembled carbonated hydroxyapatite microspheres prepared by an EDTA-assisted hydrothermal homogeneous precipitation route. *CrystEngComm*, **2020**, *22*, 2884-2888.

198. Qin, J.; Yang, D.; Maher, S.; Lima-Marques, L.; Zhou, Y.; Chen, Y.; Atkins, G.J.; Losic, D. Micro-and nano-structured 3D printed titanium implants with a hydroxyapatite coating for improved osseointegration. *Journal of Materials Chemistry B*, **2018**, *6*, 3136-3144.

199. Qiu, Y.; Xu, X.; Guo, W.; Zhao, Y.; Su, J.; Chen, J. Mesoporous Hydroxyapatite Nanoparticles Mediate the Release and Bioactivity of BMP-2 for Enhanced Bone Regeneration. *ACS Biomaterials Science & Engineering*, **2020**, *6*, 2323-2335.

200. Rammelt, S.; Schulze, E.; Bernhardt, R.; Hanisch, U.; Scharnweber, D.; Worch, H.; Zwipp, H.; Biewener, A. Coating of titanium implants with type-I collagen. *Journal of Orthopaedic Research*, **2004**, *22*, 1025-1034.

201. Rawlings, A.E.; Somner, L.A.; Fitzpatrick-Milton, M.; Roebuck, T.P.; Gwyn, C.; Liravi, P.; Seville, V.; Neal, T.J.; Mykhaylyk, O.O.; Baldwin, S.A.; Staniland, S.S. Artificial coiled coil biomineralisation protein for the synthesis of magnetic nanoparticles. *Nature Communications*, **2019**, *10*, 1-9.

202. Roohani-Esfahani, S. I.; Newman, P.; Zreiqat, H. Design and fabrication of 3D printed scaffolds with a mechanical strength comparable to cortical bone to repair large bone defects. *Scientific Reports*, **2016**, *6*, 19468.

203. Rößler, S.; Unbehau, R.; Gemming, T.; Kruppke, B.; Wiesmann, H. P.; Hanke, T. calcite incorporated in silica/collagen xerogels mediates calcium release and enhances osteoblast proliferation and differentiation. *Scientific Reports*, **2020**, *10*, 1-13.

204. Ryabenkova, Y.; Jadav, N.; Conte, M.; Hippler, M.F.; Reeves-McLaren, N.; Coates, P.D.; Twigg, P.; Paradkar, A. Mechanism of hydrogen-bonded complex formation between ibuprofen and nanocrystalline hydroxyapatite. *Langmuir*, **2017**, *33*, 2965-2976.

205. Ryu, J.; Ku, S. H.; Lee, M.; Park, C. B. Bone-like peptide/hydroxyapatite nanocomposites assembled with multi-level hierarchical structures. *Soft Matter*, **2011**, *7*, 7201-7206.

206. Sadat-Shojai, M.; Khorasani, M. T.; Dinpanah-Khoshdargi, E.; Jamshidi, A. Synthesis methods for nanosized hydroxyapatite with diverse structures. *Acta Biomaterialia*, **2013**, *9*, 7591-7621.

207. Saeidi, N.; Wong, C. K.; Lo, T. M.; Nguyen, H. X.; Ling, H.; Leong, S. S. J.; Poh, C. L.; Chang, M. W. (2011). Engineering microbes to sense and eradicate *Pseudomonas aeruginosa*, a human pathogen. *Molecular Systems Biology*, **2011**, *7*, 1–11.

208. Saha, B.; Das, S.; Saikia, J.; Das, G. Preferential and enhanced adsorption of different dyes on iron oxide nanoparticles: a comparative study. *The Journal of Physical Chemistry C*, **2011**, *115*, 8024-8033.

209. Salhotra, A.; Shah, H. N., Levi, B., & Longaker, M. T. Mechanisms of bone development and repair. *Nature Reviews Molecular Cell Biology*, **2020**, *21*, 696-712.

210. Salinas, A. J.; Esbrit, P.; Vallet-Regí, M. A tissue engineering approach based on the use of bioceramics for bone repair. *Biomaterials Science*, **2013**, *1*, 40-51.

211. Sand, K. K.; Pedersen, C. S.; Sjoberg, S.; Nielsen, J. W.; Makovicky, E.; Stipp, S. L. S. Biomineralization: long-term effectiveness of polysaccharides on the growth and dissolution of calcite. *Crystal Growth & Design*, **2014**, *14*, 5486-5494.

212. Sano, K. I.; Sasaki, H. Shiba, K. Specificity and biomineralization activities of Ti-binding peptide-1 (TBP-1). *Langmuir*, **2005**, *21*, 3090-3095.

213. Santos, C.; Almeida, M. M.; Costa, M. E. Morphological evolution of hydroxyapatite particles in the presence of different citrate: calcium ratios. *Crystal Growth & Design*, **2015**, *15*, 4417-4426.

214. Sathishkumar, S.; Louis, K.; Shinyjoy, E.; Gopi, D. Tailoring the Sm/Gd-substituted hydroxyapatite coating on biomedical AISI 316L SS: exploration of corrosion resistance, protein profiling, osteocompatibility, and osteogenic differentiation for orthopedic implant applications. *Industrial & Engineering Chemistry Research*, **2016**, *55*, 6331-6344.

215. Schröder, H.C.; Schloßmacher, U.; Boreiko, A.; Natalio, F.; Baranowska, M.; Brandt, D.; Wang, X.; Tremel, W.; Wiens, M.; Müller, W.E. Silicatein: nanobiotechnological and biomedical applications. In *Biosilica in Evolution, Morphogenesis, and Nanobiotechnology*, **2009**, *47*, 251-273.

216. Selvakumar, M.; Kumar, P. S.; Das, B.; Dhara, S.; Chattopadhyay, S. Structurally tuned antimicrobial mesoporous hydroxyapatite nanorods by cyclic oligosaccharides regulation to release a drug for osteomyelitis. *Crystal Growth & Design*, **2017**, *17*, 433-445.

217. Shao, F.; Liu, L.; Fan, K.; Cai, Y.; Yao, J. Ibuprofen loaded porous calcium phosphate nanospheres for skeletal drug delivery system. *Journal of Materials Science*, **2012**, *47*, 1054-1058.

218. Sheikh, L.; Tripathy, S.; Nayar, S. Biomimetic matrix mediated room temperature synthesis and characterization of nano-hydroxyapatite towards targeted drug delivery. *RSC Advances*, **2016**, *6*, 62556-62571.

219. Shen, T.; Yang, W.; Shen, X.; Chen, W.; Tao, B.; Yang, X.; Yuan, J.; Liu, P.; Cai, K. Polydopamine-assisted hydroxyapatite and lactoferrin multilayer on titanium for regulating bone balance and enhancing antibacterial property. *ACS Biomaterials Science & Engineering*, **2018**, *4*, 3211-3223.

220. Shu, X.; Liao, J.; Wang, L.; Shi, Q.; Xie, X. Osteogenic, Angiogenic, and Antibacterial Bioactive Nano-Hydroxyapatite Co-Synthesized Using γ-Polyglutamic Acid and Copper. *ACS Biomaterials Science & Engineering*, **2020**, *6*, 1920-1930.

221. Simkiss, K. The processes of biomineralization in lower plants and animals-an overview. *Biomineralization in lower plants and animals*, **1986**, *30*, 19-37.

222. Spriano, S.; Yamaguchi, S.; Baino, F.; Ferraris, S. A critical review of multifunctional titanium surfaces: New frontiers for improving osseointegration and host response, avoiding bacteria contamination. *Acta Biomaterialia*, **2018**, *79*, 1-22.

223. Sprio, S.; Preti, L.; Montesi, M.; Panseri, S.; Adamiano, A.; Vandini, A.; Pugno, N.M.; Tampieri, A. Surface Phenomena Enhancing the Antibacterial and Osteogenic

Ability of Nanocrystalline Hydroxyapatite, Activated by Multiple-Ion Doping. *ACS Biomaterials Science & Engineering*, **2019**, *5*, 5947-5959.

224. Srouji, S.; Livne, E. Bone marrow stem cells and biological scaffold for bone repair in aging and disease. *Mechanisms of Ageing and Development*, **2005**, *126*, 281-287.
225. Stage, M.; Gustafsson, A. W.; Jørgensen, M.; Vera-Jimenéz, N. I.; Wielje, M.; Nielsen, D. S.; Sandelin, A.; Chen, Y.; Baker, A. Genomic and phenotypic stability of *Lactobacillus rhamnosus* GG in an industrial production process. *Applied and Environmental Microbiology*, **2020**, *86*, e02780-19.
226. Sugawara, A.; Nishimura, T.; Yamamoto, Y.; Inoue, H.; Nagasawa, H.; Kato, T. Self-organization of oriented calcium carbonate/polymer composites: effects of a matrix peptide isolated from the exoskeleton of a crayfish. *Angewandte Chemie International Edition*, **2006**, *45*, 2876-2879.
227. Sun, F.; Zhou, H.; Lee, J. Various preparation methods of highly porous hydroxyapatite/polymer nanoscale biocomposites for bone regeneration. *Acta Biomaterialia*, **2011**, *7*, 3813-3828.
228. Sun, T. W.; Zhu, Y. J.; Chen, F. Hydroxyapatite nanowire/collagen elastic porous nanocomposite and its enhanced performance in bone defect repair. *RSC Advances*, **2018**, *8*, 26218-26229.
229. Sun, T.W.; Yu, W.L.; Zhu, Y.J.; Yang, R.L.; Shen, Y.Q.; Chen, D.Y.; He, Y.H.; Chen, F. Hydroxyapatite Nanowire@ Magnesium Silicate Core–Shell Hierarchical Nanocomposite: Synthesis and Application in Bone Regeneration. *ACS Applied Materials & Interfaces*, **2017**, *9*, 16435-16447.
230. Suzuki, M.; Saruwatari, K.; Kogure, T.; Yamamoto, Y.; Nishimura, T.; Kato, T.; Nagasawa, H. An acidic matrix protein, Pif, is a key macromolecule for nacre formation. *Science*, **2009**, *325*, 1388-1390.
231. Szcześ, A.; Hołysz, L.; Chibowski, E. Synthesis of hydroxyapatite for biomedical applications. *Advances in Colloid and Interface Science*, **2017**, *249*, 321-330.
232. Tam, V. H.; Schilling, A. N.; Vo, G.; Kabbara, S.; Kwa, A. L.; Wiederhold, N. P.; Lewis, R. E. Pharmacodynamics of polymyxin B against *Pseudomonas aeruginosa*. *Antimicrobial Agents and Chemotherapy*, **2005**, *49*, 3624–3630.
233. Tang, S.; Tian, B.; Ke, Q. F.; Zhu, Z. A.; Guo, Y. P. Gentamicin-loaded carbonated hydroxyapatite coatings with hierarchically porous structures: drug delivery

properties, bactericidal properties and biocompatibility. *RSC Advances*, **2014**, *4*, 41500-41509.

234. Thein-Han, W. W.; Saikhun, J.; Pholpramoo, C.; Misra, R. D. K.; Kitiyanant, Y. Chitosan–gelatin scaffolds for tissue engineering: Physico-chemical properties and biological response of buffalo embryonic stem cells and transfectant of GFP–buffalo embryonic stem cells. *Acta Biomaterialia*, **2009**, *5*, 3453-3466.

235. Torgbo, S.; Sukyai, P. Bacterial cellulose-based scaffold materials for bone tissue engineering. *Applied Materials Today*, **2018**, *11*, 34-49.

236. Tseng, B. S.; Zhang, W.; Harrison, J. J.; Quach, T. P.; Song, J. L.; Penterman, J.; Singh, P. K.; Chopp, D. L.; Packman, A. I.; Parsek, M. R. The extracellular matrix protects *Pseudomonas aeruginosa* biofilms by limiting the penetration of tobramycin. *Environmental Microbiology*, **2013**, *15*, 2865-2878.

237. Turnbull, G.; Clarke, J.; Picard, F.; Riches, P.; Jia, L.; Han, F.; Li, B.; Shu, W. 3D bioactive composite scaffolds for bone tissue engineering. *Bioactive Materials*, **2018**, *3*, 278-314.

238. Ubago-Rodríguez, A.; Casares Atienza, S.; Fernández-Vivas, A.; Peigneux, A.; Jabalera, Y.; de la Cuesta-Rivero, M.; Jimenez-Lopez, C.; Azuaga Fortes, A.I. Structure–function of MamC loop and its effect on the in vitro precipitation of biomimetic magnetite nanoparticles. *Crystal Growth & Design*, **2019**, *19*, 2927-2935.

239. Uchida, M.; Klem, M.T.; Allen, M.; Suci, P.; Flenniken, M.; Gillitzer, E.; Varpness, Z.; Liepold, L.O.; Young, M.; Douglas, T. Biological containers: protein cages as multifunctional nanoplatforms. *Advanced Materials*, **2007**, *19*, 1025-1042.

240. Ullah, I.; Gloria, A.; Zhang, W.; Ullah, M.W.; Wu, B.; Li, W.; Domingos, M.; Zhang, X., Synthesis and characterization of sintered Sr/Fe-modified hydroxyapatite bioceramics for bone tissue engineering applications. *ACS Biomaterials Science & Engineering*, **2019**, *6*, 375-388.

241. Ustundag, C. B.; Avciata, O.; Kaya, F.; Kaya, C. Hydrothermally mixed hydroxyapatite–multiwall carbon nanotubes composite coatings on biomedical alloys by electrophoretic deposition. *The Journal of Physical Chemistry B*, **2013**, *117*, 1571-1576.

242. Valarmathi, N.; Sumathi, S. Biomimetic hydroxyapatite/silkfibre/methylcellulose composites for bone tissue engineering applications. *New Journal of Chemistry*, **2020**, *44*, 4647-4663.

243. Valverde-Tercedor, C.; Montalbán-López, M.; Perez-Gonzalez, T.; Sanchez-Quesada, M.S.; Prozorov, T.; Pineda-Molina, E.; Fernandez-Vivas, M.A.; Rodriguez-Navarro, A.B.; Trubitsyn, D.; Bazylinski, D.A.; Jimenez-Lopez, C. Size control of in vitro synthesized magnetite crystals by the MamC protein of *Magnetococcus marinus* strain MC-1. *Applied Microbiology and Biotechnology*, **2015**, *99*, 5109-5121.

244. Veiga, A.; Castro, F.; Rocha, F.; Oliveira, A. L. Protein-Based Hydroxyapatite Materials: Tuning Composition toward Biomedical Applications. *ACS Applied Bio Materials* **2020**, *3*, 3441−3455.

245. Viljanen, P.; Vaara, M. Susceptibility of gram-negative bacteria to polymyxin B nonapeptide. *Antimicrobial Agents and Chemotherapy*, **1984**, *25*, 701–705.

246. Walters, M. C.; 3rd; Roe, F.; Bugnicourt, A.; Franklin, M. J.; Stewart, P. S. Contributions of antibiotic penetration, oxygen limitation, and low metabolic activity to tolerance of *Pseudomonas aeruginosa* biofilms to ciprofloxacin and tobramycin. *Antimicrobial Agents and Chemotherapy*, **2003**, *47*, 317-323.

247. Wang, G.; Zhang, H.; He, Q.; Tong, D.; Ding, C.; Liu, P.; Zhang, Z.; Xie, Y.; Ji, F. Micro-patterned titanium coatings with a grid-like structure doped with vancomycin against bacteria and affecting osteogenic differentiation. *RSC Advances*, **2017**, *7*, 19565-19575.

248. Wang, G.; Zheng, L.; Zhao, H.; Miao, J.; Sun, C.; Liu, H.; Huang, Z.; Yu, X.; Wang, J.; Tao, X. Construction of a fluorescent nanostructured chitosan-hydroxyapatite scaffold by nanocrystallon induced biomimetic mineralization and its cell biocompatibility. *ACS Applied Materials & Interfaces*, **2011**, *3*, 1692-1701.

249. Wang, H.; Li, Y.; Zuo, Y.; Li, J.; Ma, S.; Cheng, L. Biocompatibility and osteogenesis of biomimetic nano-hydroxyapatite/polyamide composite scaffolds for bone tissue engineering. *Biomaterials*, **2007**, *28*, 3338-3348.

250. Wang, K.; Wang, X.; Li, H.; Zheng, S.; Ren, Q.; Wang, Y.; Niu, Y.; Li, W.; Zhou, X.; Zhang, L. A statherin-derived peptide promotes hydroxyapatite crystallization and in situ remineralization of artificial enamel caries. *RSC Advances*, **2018**, *8*, 1647-1655.

251. Wang, X.; Kong, R.; Pan, X.; Xu, H.; Xia, D.; Shan, H.; Lu, J. R. Role of ovalbumin in the stabilization of metastable vaterite in calcium carbonate biomineralization. *The Journal of Physical Chemistry B*, **2009**, *113*, 8975-8982.

252. Wang, X.; Sun, Y.; Lin, K. Facile synthesis of dental enamel-like hydroxyapatite nanorod arrays via hydrothermal transformation of hillebrandite nanobelts. *Journal of Materials Chemistry B*, **2015**, *3*, 7334-7339.

253. Wang, X.; Yu, T.; Chen, G.; Zou, J.; Li, J.; Yan, J. Preparation and characterization of a chitosan/gelatin/extracellular matrix scaffold and its application in tissue engineering. *Tissue Engineering Part C: Methods*, **2017**, *23*, 169-179.

254. Wang, Y. Y.; Yao, Q. Z.; Li, H.; Zhou, G. T.; Sheng, Y. M. Formation of vaterite mesocrystals in biomineral-like structures and implication for biomineralization. *Crystal Growth & Design*, **2015**, *15*, 1714-1725.

255. Wang, Y.; Azaïs, T.; Robin, M.; Vallée, A.; Catania, C.; Legriel, P.; Pehau-Arnaudet, G.; Babonneau, F.; Giraud-Guille, M.M.; Nassif, N. The predominant role of collagen in the nucleation, growth, structure and orientation of bone apatite. *Nature Materials*, **2012**, *11*, 724-733.

256. Wang, Y.; Li, X.; Chen, M.; Zhao, Y.; You, C.; Li, Y.; Chen, G. In vitro and in vivo degradation behavior and biocompatibility evaluation of microarc oxidation-fluoridated hydroxyapatite-coated Mg–Zn–Zr–Sr alloy for bone application. *ACS Biomaterials Science & Engineering*, **2019**, *5*, 2858-2876.

257. Watabe, N.; Kingsley, R. J. Extra-, inter-, and intracellular mineralization in invertebrates and algae. *Origin, evolution, and modern aspects of biomineralization in plants and animals*, **1989**, 209-223.

258. Weaver, J.C.; Milliron, G.W.; Miserez, A.; Evans-Lutterodt, K.; Herrera, S.; Gallana, I.; Mershon, W.J.; Swanson, B.; Zavattieri, P.; DiMasi, E.; Kisailus, D. The stomatopod dactyl club: a formidable damage-tolerant biological hammer. *Science*, **2012**, *336*, 1275-1280.

259. Wei, S.; Cui, H.; Jiang, Z.; Liu, H.; He, H.; Fang, N. Biomineralization processes of calcite induced by bacteria isolated from marine sediments. *Brazilian Journal of Microbiology*, **2015**, *46*, 455-464.

260. Wei, Y.; Liu, L.; Gao, H.; Shi, X.; Wang, Y. In situ formation of hexagon-like column array hydroxyapatite on 3D-plotted hydroxyapatite scaffolds by hydrothermal method and its effect on osteogenic differentiation. *ACS Applied Bio Materials*, **2020**, *3*, 1753-1760.

261. Wei, Y.; Liu, L.; Gao, H.; Shi, X.; Wang, Y. In Situ Formation of Hexagon-like Column Array Hydroxyapatite on 3D-Plotted Hydroxyapatite Scaffolds by

Hydrothermal Method and Its Effect on Osteogenic Differentiation. *ACS Applied Bio Materials*, **2020**, *3*, 1753-1760.

262. Weidenmaier, C.; Peschel, A. Teichoic acids and related cell-wall glycopolymers in Gram-positive physiology and host interactions. *Nature Reviews Microbiology*, **2008**, *6*, 276-287.

263. Weiner, S.; Dove, P. M. An overview of biomineralization processes and the problem of the vital effect. *Reviews in Mineralogy and Geochemistry*, **2003**, *54*, 1-29.

264. Xie, C.; Lu, X.; Wang, K.; Yuan, H.; Fang, L.; Zheng, X.; Chan, C.; Ren, F.; Zhao, C. Pulse electrochemical driven rapid layer-by-layer assembly of polydopamine and hydroxyapatite nanofilms via alternative redox in situ synthesis for bone regeneration. *ACS Biomaterials Science & Engineering*, **2016**, *2*, 920-928.

265. Xie, C.M.; Lu, X.; Wang, K.F.; Meng, F.Z.; Jiang, O.; Zhang, H.P.; Zhi, W.; Fang, L.M. Silver nanoparticles and growth factors incorporated hydroxyapatite coatings on metallic implant surfaces for enhancement of osteoinductivity and antibacterial properties. *ACS Applied Materials & Interfaces*, **2014**, *6*, 8580-8589.

266. Xin, J.; Chen, T.; Lin, Z.; Dong, P.; Tan, H.; Li, J. Phosphorylated dendronized poly (amido amine) s as protein analogues for directing hydroxylapatite biomineralization. *Chemical Communications*, **2014**, *50*, 6491-6493.

267. Xiong, H.; Du, S.; Ni, J.; Zhou, J.; Yao, J. Mitochondria and nuclei dual-targeted heterogeneous hydroxyapatite nanoparticles for enhancing therapeutic efficacy of doxorubicin. *Biomaterials*, **2016**, *94*, 70-83.

268. Xiong, Z. C.; Yang, Z. Y.; Zhu, Y. J.; Chen, F. F.; Zhang, Y. G.; Yang, R. L. Ultralong hydroxyapatite nanowires-based paper co-loaded with silver nanoparticles and antibiotic for long-term antibacterial benefit. *ACS Applied Materials & Interfaces*, **2017**, *9*, 22212-22222.

269. Xu, Z.; Shi, L.; Hu, D.; Hu, B.; Yang, M.; Zhu, L. Formation of hierarchical bone-like apatites on silk microfiber templates via biomineralization. *RSC Advances*, **2016**, *6*, 76426-76433.

270. Xue, B.; Zhang, C.; Wang, Y.; Wang, J.; Zhang, J.; Lu, M.; Li, G.; Cao, Z.; Huang, Q. A novel controlled-release system for antibacterial enzyme lysostaphin delivery using hydroxyapatite/chitosan composite bone cement. *PLoS One*, **2014**, *9*, e113797.

271. Yang, C.; Huan, Z.; Wang, X.; Wu, C.; Chang, J. 3D printed Fe scaffolds with HA nanocoating for bone regeneration. *ACS Biomaterials Science & Engineering*, **2018**, *4*, 608-616.

272. Yang, C.; Li, Y.; Nan, K. Biologically inspired growth of hydroxyapatite crystals on bio-organics-defined scaffolds. *Materials Research Bulletin*, **2013**, *48*, 1128-1131.

273. Yang, L.; Huang, J.; Yang, S.; Cui, W.; Wang, J.; Zhang, Y.; Li, J.; Guo, X. Bone Regeneration Induced by Local Delivery of a Modified PTH-Derived Peptide from Nanohydroxyapatite/Chitosan Coated True Bone Ceramics. *ACS Biomaterials Science & Engineering*, **2018**, *4*, 3246-3258.

274. Yang, M.; Zhou, G.; Shuai, Y.; Wang, J.; Zhu, L.; Mao, C. $Ca^{2+}$-induced self-assembly of Bombyx mori silk sericin into a nanofibrous network-like protein matrix for directing controlled nucleation of hydroxylapatite nano-needles. *Journal of Materials Chemistry B*, **2015**, *3*, 2455-2462.

275. Yang, Q.; Wang, J. X.; Guo, F.; Chen, J. F. Preparation of hydroxyaptite nanoparticles by using high-gravity reactive precipitation combined with hydrothermal method. *Industrial & Engineering Chemistry Research*, **2010**, *49*, 9857-9863.

276. Yang, S.; He, H.; Wang, L.; Jia, X.; Feng, H. Oriented crystallization of hydroxyapatite by the biomimetic amelogenin nanospheres from self-assemblies of amphiphilic dendrons. *Chemical Communications*, **2011**, *47*, 10100-10102.

277. Yang, W.; Guo, W.; Chang, J.; Zhang, B. Protein/peptide-templated biomimetic synthesis of inorganic nanoparticles for biomedical applications. *Journal of Materials Chemistry B*, **2017**, *5*, 401-417.

278. Yang, Z.; Luo, S.; Zeng, Y.; Shi, C.; Li, R. Albumin-Mediated Biomineralization of Shape-Controllable and Biocompatible Ceria Nanomaterials. *ACS Applied Materials & Interfaces*, **2017**, *9*, 6839-6848.

279. Yelten-Yilmaz, A.; Yilmaz, S. Wet chemical precipitation synthesis of hydroxyapatite (HA) powders. *Ceramics International*, **2018**, *44*, 9703-9710.

280. Yu, J.; Xu, Y.; Li, S.; Seifert, G.V; Becker, M.L. Three-dimensional printing of nano hydroxyapatite/poly (ester urea) composite scaffolds with enhanced bioactivity. *Biomacromolecules*, **2017**, *18*, 4171-4183.

281. Yu, L.; Rowe, D. W.; Perera, I. P.; Zhang, J.; Suib, S. L.; Xin, X.; Wei, M. Intrafibrillar Mineralized Collagen–Hydroxyapatite-Based Scaffolds for Bone Regeneration. *ACS Applied Materials & Interfaces*, **2020**, *12*, 18235-18249.

282. Yu, X.; Hu, L.; Wang, G.; Huang, T.; Wei, W.; Wang, M. Xia, Z. DNA-mediated biomineralization of calcium-deficient hydroxyapatite for bone tissue engineering. *New Journal of Chemistry*, **2020**, *44*, 4755-4761.

283. Zavascki, A. P.; Goldani, L. Z.; Li, J.; Nation, R. L. Polymyxin B for the treatment of multidrug-resistant pathogens: A critical review. *Journal of Antimicrobial Chemotherapy*, **2007**, *60*, 1206–1215.

284. Zhang, H.; Wang, G.; Liu, P.; Tong, D.; Ding, C.; Zhang, Z.; Xie, Y.; Tang, H.; Ji, F. Vancomycin-loaded titanium coatings with an interconnected micro-patterned structure for prophylaxis of infections: an in vivo study. *RSC Advances*, **2018**, *8*, 9223-9231.

285. Zhang, J.; Liu, W.; Schnitzler, V.; Tancret, F.; Bouler, J. M. Calcium phosphate cements for bone substitution: chemistry, handling and mechanical properties. *Acta Biomaterialia*, **2014**, *10*, 1035-1049.

286. Zhang, L.; Dong, Y.; Xue, Y.; Shi, J.; Zhang, X.; Liu, Y.; Midgley, A.C.; Wang, S. Multifunctional Triple-Layered Composite Scaffolds Combining Platelet-Rich Fibrin Promote Bone Regeneration. *ACS Biomaterials Science & Engineering*, **2019**, *5*, 6691-6702.

287. Zhang, Y.; Liu, X.; Li, Z.; Zhu, S.; Yuan, X.; Cui, Z.; Yang, X.; Chu, P.K.; Wu, S. Nano Ag/ZnO-incorporated hydroxyapatite composite coatings: highly effective infection prevention and excellent osteointegration. *ACS Applied Materials & Interfaces*, **2018**, *10*, 1266-1277.

288. Zhang, Y.; Lu, J. A Mild and Efficient Biomimetic Synthesis of Rodlike Hydroxyapatite Particles with a High Aspect Ratio Using Polyvinylpyrrolidone As Capping Agent. *Crystal Growth & Design*, **2008**, *8*, 2101-2107.

289. Zhao, H.; He, W.; Wang, Y.; Zhang, X.; Li, Z.; Yan, S.; Zhou, W. Biomimetic synthesis and characterization of hydroxyapatite crystal with low phase transformation temperature. *Journal of Chemical & Engineering Data*, **2008**, *53*, 2735-2738.

290. Zhao, X.; Pan, F.; Xu, H.; Yaseen, M.; Shan, H.; Hauser, C.A.; Zhang, S.; Lu, J.R. Molecular self-assembly and applications of designer peptide amphiphiles. *Chemical Society Reviews*, **2010**, *39*, 3480-3498.

291. Zhao, Y.; Han, Z.; Yan, H.; Zhao, H.; Tucker, M.E.; Han, M.; Mao, G.; Yin, J. Intracellular and Extracellular Biomineralization Induced by *Klebsiella pneumoniae* LH1 Isolated from Dolomites. *Geomicrobiology Journal*, **2020**, *37*, 262-278.

292. Zhou, H.; Lee, J. Nanoscale hydroxyapatite particles for bone tissue engineering. *Acta Biomaterialia*, **2011**, *7*, 2769-2781.

293. Zhou, R.; Li, Y.; Xiao, D.; Li, T.; Zhang, T.; Fu, W.; Lin, Y. Hyaluronan-directed fabrication of co-doped hydroxyapatite as a dual-modal probe for tumor-specific bioimaging. *Journal of Materials Chemistry B*, **2020**, *8*, 2107-2114.

294. Zia, I.; Jolly, R.; Mirza, S.; Umar, M.S.; Owais, M.; Shakir, M. Hydroxyapatite Nanoparticles Fortified Xanthan Gum–Chitosan Based Polyelectrolyte Complex Scaffolds for Supporting the Osteo-Friendly Environment. *ACS Applied Bio Materials*, **2020**, *3*, 7133-7146.

# APPENDIX

# APPENDIX

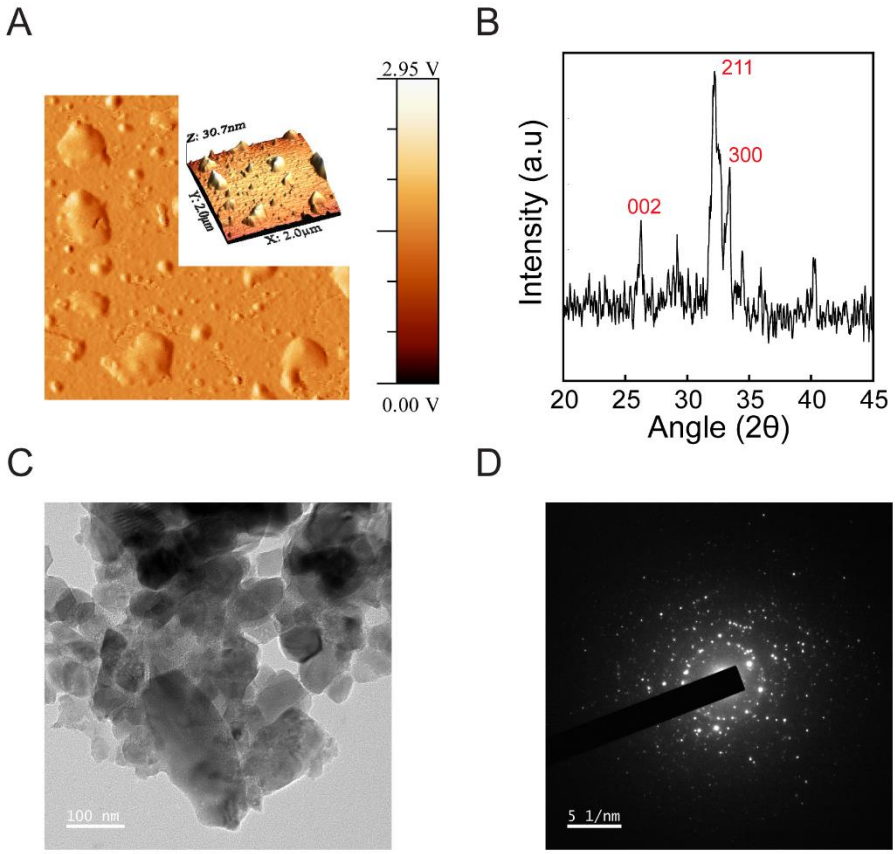


**Figure A2.1.** Characterization of chemically synthesized HANP. (A) AFM analysis indicating amplitude channel (Inset: 3D topography-based image wherein the average height profile was ~10.51 nm). (B) Powder XRD analysis. (C) FETEM analysis. (D) SAED pattern.

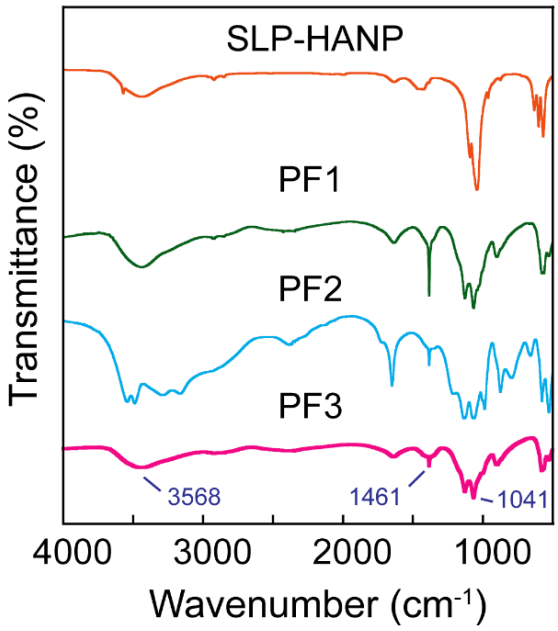


**Figure A3.1.** FTIR analysis of materials obtained from mineralization of purified individual protein fractions (PF1, PF2 and PF3) present in the cell free extract of *L. plantarum* MTCC 1325. For comparison, SLP-HANP was also included.

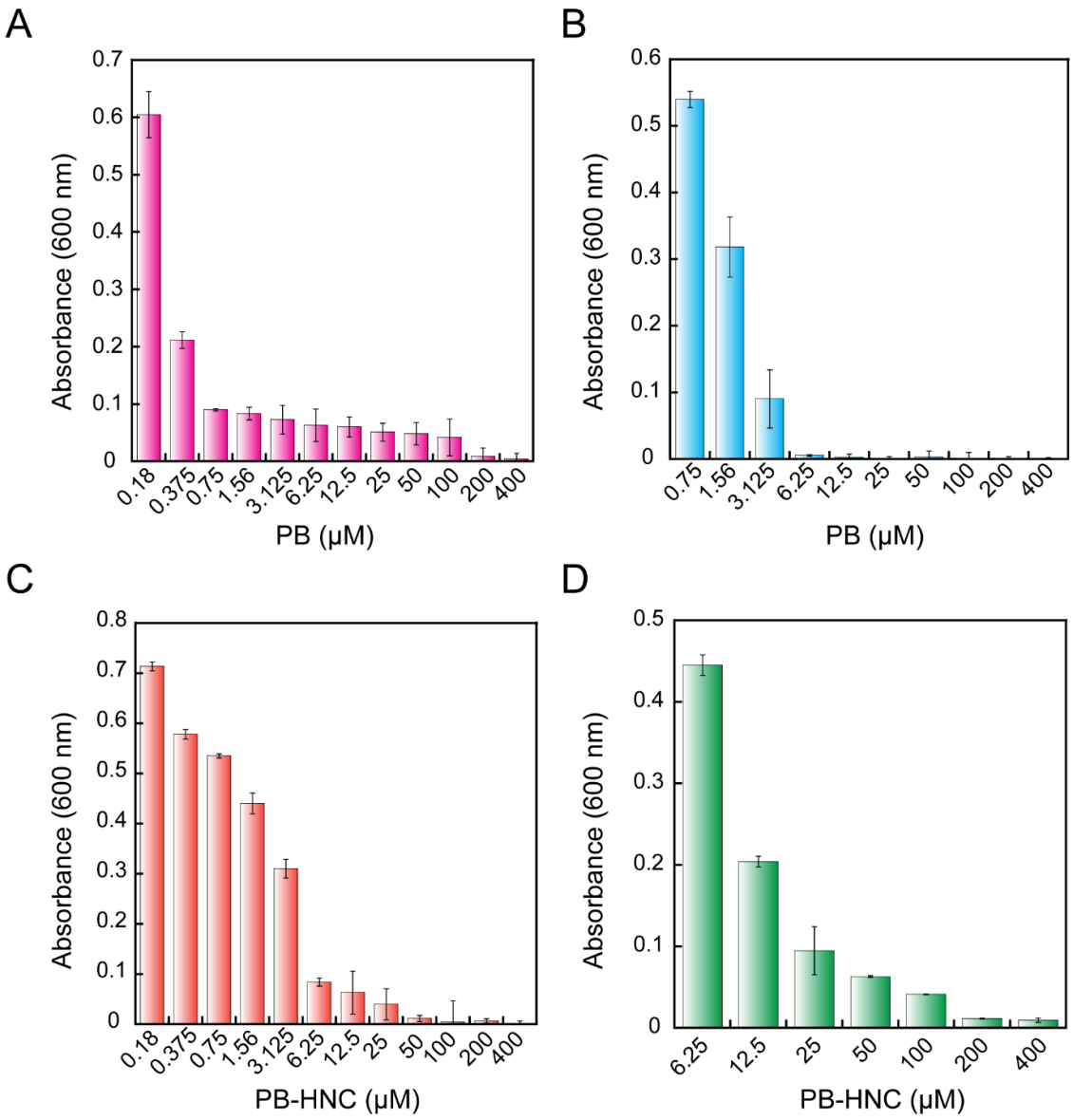


**Figure A3.2.** Concentration-dependent effect of PB and PB-HNC on the growth of *P. aeruginosa* MTCC 2488 cells monitored by measuring absorbance at 600 nm. The minimum inhibitory concentration (MIC) of PB and PB-HNC was estimated from (A) and (C), respectively. The minimum killing concentration (MKC) of PB and PB-HNC was estimated from (B) and (D), respectively.

**Table A3.1.** Minimum inhibitory concentration (MIC) and minimum killing concentration (MKC) of polymyxin B and polymyxin B-loaded hydroxyapatite nanocomposite (PB-HNC) against *Pseudomonas aeruginosa* MTCC 2488.

| Antibacterial Agents | MIC (µM) | MKC (µM) |
|---|---|---|
| Polymyxin B | 0.75 | 3.125 |
| Polymyxin B-loaded Hydroxyapatite Nanocomposite (PB-HNC) | 6.25 | 25 |

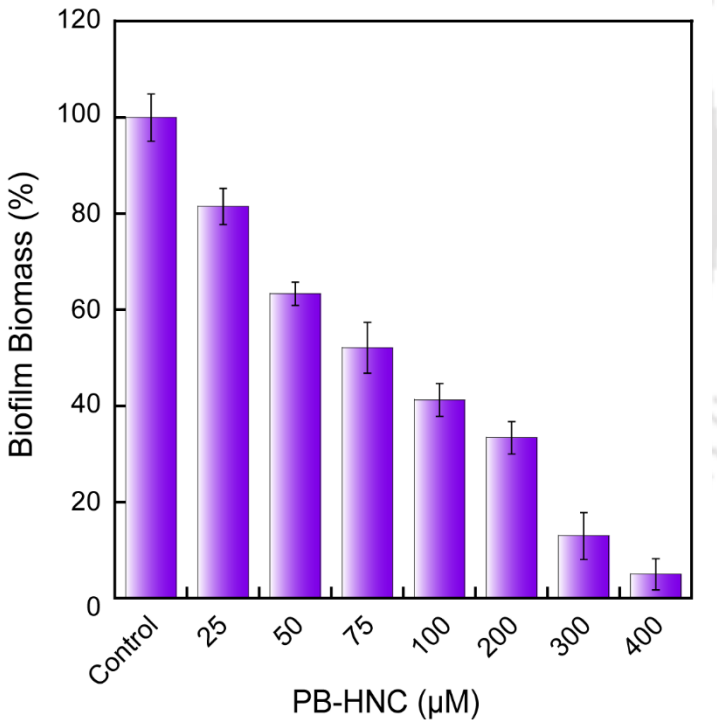


**Figure A3.3.** Crystal violet assay for estimating inhibition of *P. aeruginosa* MTCC 2488 biofilm in presence of varying concentrations of polymyxin B-loaded hydroxyapatite nanocomposite (PB-HNC).

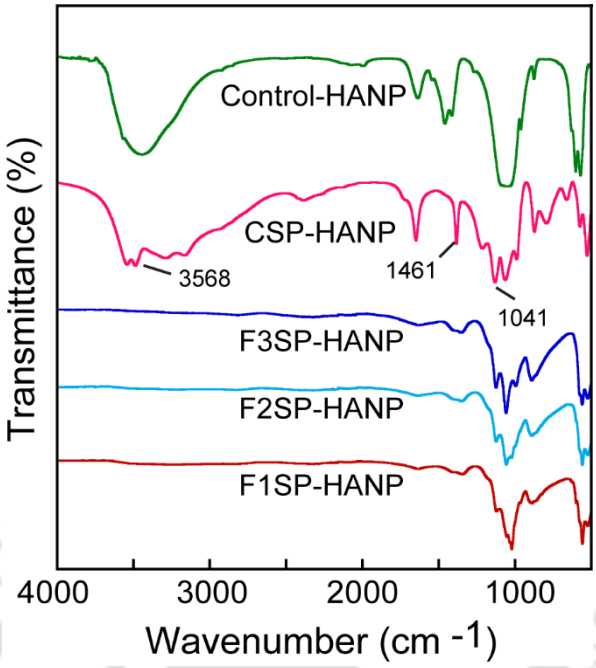


**Figure A4.1.** FTIR analysis of samples obtained by mineralization of gel-eluted F1SP, F2SP and F3SP (fraction 1-3) protein present in *L. rhamnosus* GG CSP extract. For comparison, control HANP (Sigma-Aldrich, USA) and CSP-HANP were also included.

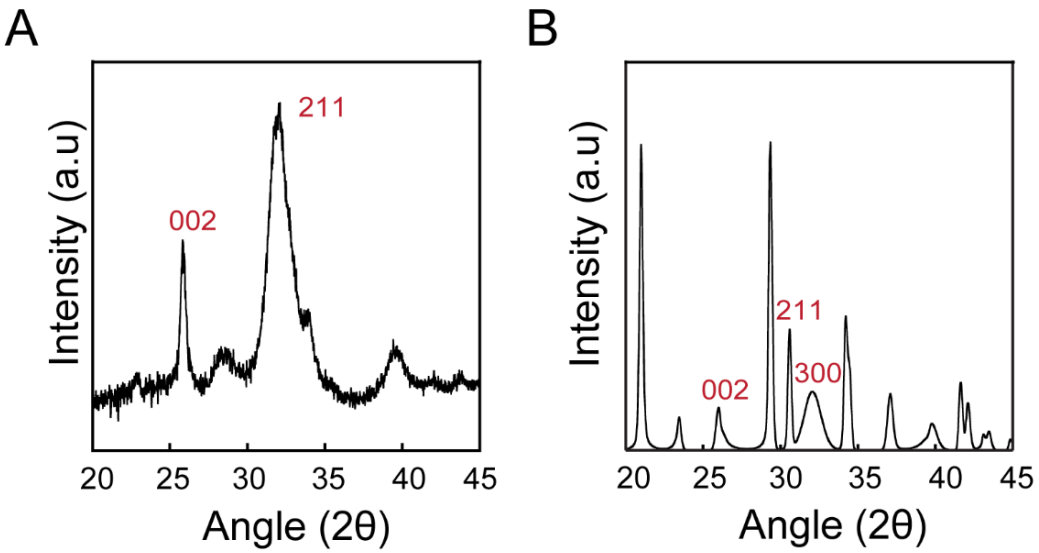


**Figure A6.1.** Powder XRD analysis of HANP generated in presence of (A) 0.04 % DMSO and (B) 3.0 % DMSO.

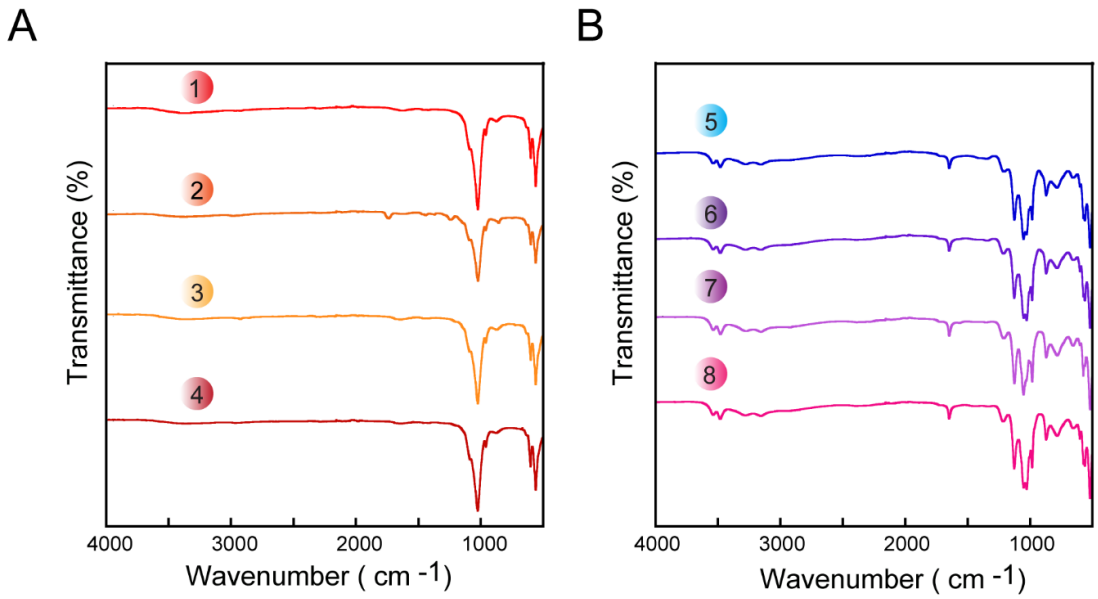


**Figure A6.2.** FTIR analysis of HANPs generated in presence of varying concentrations of 2-dodecylmalonic acid (MA) amphiphile. (A) Traces 1: $MA_1$-HANP, 2: $MA_2$-HANP, 3: $MA_3$-HANP, 4: HANP synthesized in presence of 0.04 % DMSO. (B) Traces 5: $MA_4$-HANP, 6: $MA_5$-HANP, 7: $MA_6$-HANP, 8: HANP synthesized in presence of 3.0 % DMSO.

# LIST OF PUBLICATIONS

# List of Publications

**Publications from Ph.D. Thesis Work:**

**(A) Journal Publications:**

1. **Mullick, P.,** Mukherjee, S., Das, G. and Ramesh, A. (2019). Generation of a Hydroxyapatite Nanocarrier through Biomineralization Using Cell-free Extract of Lactic Acid Bacteria for Antibiofilm Application. *ACS Applied Biomaterials* **2**, 2927-2936.

2. **Mullick, P.**, Das, G. and Ramesh, A. (2021). Probiotic Bacteria Cell Surface-Associated Protein Mineralized Hydroxyapatite Incorporated in Porous Scaffold: *In Vitro* Evaluation for Bone Cell Growth and Differentiation. *Materials Science and Engineering C* **126**, 112101.

3. **Mullick, P.,** Das, G. and Ramesh, A. (2021). 2-Dodecylmalonic Acid-Mediated Synthesis of Mineralized Hydroxyapatite Amicable for Bone Cell Growth on Orthopaedic Implant. *Journal of Colloid and Interface Science* **(Under Revision, Manuscript No. JCIS-21-5229R1)**.

**(B) Conference Presentations:**

1. **Mullick, P.,** Mukherjee, S., Das, G. and Ramesh, A (2016). Biogenic Hydroxyapatite Nanocomposite for Antibacterial Applications. Abstract MMB-62. Presented in 57th Annual Conference of Association of Microbiologists of India (AMI), 24-27 November 2016, Gauhati University, Assam, India.

2. **Mullick, P.,** Das, G and Ramesh, A (2018). Small Synthetic Molecules as Potent Antibacterials. Presented in Research Conclave, 8-11 March 2018, Indian Institute of Technology Guwahati, India.

3. **Mullick, P.,** Das, G and Ramesh, A (2018). Exploring S-layer Protein of Lactic Acid Bacteria for Biomimetic Synthesis of Hydroxyapatite Nanoparticle. Abstract P-078. Presented in 87th Annual Conference of Society of Biological

Chemists (India) (SBCI), 25-27 November 2018, School of Life Sciences, Manipal Academy of Higher Education, Manipal, India.

4. **Mullick, P.,** Das, G and Ramesh, A (2020). Small Amphiphilic Ligand-based Synthesis of Hydroxyapatite Nanoparticle for Orthopaedic Titanium Implant Coating: Characterization and Functional Analysis. Abstract A.P1.12. Presented in 9th European Nanoanalysis Symposium Online Edition, 9 October, 2020, E-MRS, France organized by Dresden Fraunhofer Cluster Nanoanalysis, Dresden, Germany.

5. **Mullick, P.**, Das, G and Ramesh, A (2020). Template-directed Biomineralization of Hydroxyapatite Nanoparticle using Beneficial Microbe and a Low Molecular Weight Amphiphile. Abstract WBC2020-VIR-4552. Presented in 11th World Biomaterials Congress Virtual Event, 11-15 December, 2020, Glasgow, UK.

**(C) Publications from Other Research Projects:**

1. Singh, R., Samanta, S., **Mullick, P.,** Ramesh, A. and Das, G. (2018). $Al^{3+}$ Sensing through Different Turn-On Emission Signals Vis-à-Vis Two Different Excitations: Applications in Biological and Environmental Realms. *Analytica Chimica Acta* **1025**, 172-180.